

University of Windsor

Scholarship at UWindor

Electronic Theses and Dissertations

Theses, Dissertations, and Major Papers

2015

Innovative Membrane Electrode Assemblies For Polymer Electrolyte Membrane Fuel Cells

Esmaeil Navaei Alvar
University of Windsor

Follow this and additional works at: <https://scholar.uwindsor.ca/etd>



Part of the [Mechanical Engineering Commons](#)

Recommended Citation

Navaei Alvar, Esmaeil, "Innovative Membrane Electrode Assemblies For Polymer Electrolyte Membrane Fuel Cells" (2015). *Electronic Theses and Dissertations*. 5696.
<https://scholar.uwindsor.ca/etd/5696>

This online database contains the full-text of PhD dissertations and Masters' theses of University of Windsor students from 1954 forward. These documents are made available for personal study and research purposes only, in accordance with the Canadian Copyright Act and the Creative Commons license—CC BY-NC-ND (Attribution, Non-Commercial, No Derivative Works). Under this license, works must always be attributed to the copyright holder (original author), cannot be used for any commercial purposes, and may not be altered. Any other use would require the permission of the copyright holder. Students may inquire about withdrawing their dissertation and/or thesis from this database. For additional inquiries, please contact the repository administrator via email (scholarship@uwindsor.ca) or by telephone at 519-253-3000ext. 3208.

Innovative Membrane Electrode Assemblies for Polymer Electrolyte Membrane Fuel Cells

By

Esmail Navaei Alvar

A Dissertation
Submitted to the Faculty of Graduate Studies
through the Department of **Mechanical, Automotive, & Materials Engineering**
in Partial Fulfillment of the Requirements for
the Degree of **Doctor of Philosophy**
at the University of Windsor

Windsor, Ontario, Canada

2015

© 2015 Esmail Navaei Alvar

Innovative Membrane Electrode Assemblies for Polymer Electrolyte Membrane Fuel Cells

By

Esmaeil Navaei Alvar

APPROVED BY:

Xueliang Sun, External Examiner
University of Western Ontario, London, Ontario

T. Breen Carmichael, External Program Reader
Chemistry and Biochemistry

Amir Fartaj, Program Reader
Mechanical, Automotive, & Materials Engineering

Nader Zamani, Program Reader
Mechanical, Automotive, & Materials Engineering

S. Holger Eichhorn, Co-Advisor
Chemistry and Biochemistry

Biao Zhou, Advisor
Mechanical, Automotive, & Materials Engineering

21 July, 2015

Declaration of Co-Authorship / Previous Publication

I. Co-Authorship Declaration

I hereby declare that this dissertation incorporates material that is the result of a joint research, as follow:

This dissertation incorporates the outcome of research undertaken at the Clean Powertrain Lab in the Department of Mechanical, Automotive and Materials Engineering under the supervision of my main advisor, Dr. Biao Zhou, in collaboration with my co-advisor, Dr. S. Holger Eichhorn, in the Chemistry and Biochemistry Department, at University of Windsor.

The electrospinning apparatus (used in *Chapters 3 to 6*), and the humidification device and its temperature-controller (used in *Chapter 5 and 6*) added to the existing Clean Powertrain Lab Fuel Cell Test Station were designed and manufactured by the author of this dissertation under the supervision of Dr. Zhou in collaboration with Mr. Sinisa Jezdic (Electronic Technologist at Physics Department of the University of Windsor). All the measurements (except for those of transmission electron microscopy, X-ray photoelectron spectroscopy, and thermal gravimetric analysis) and calculations were performed by the author of this dissertation. The author of this dissertation also had a key role in the experimental designs, data analysis and interpretation of the results under the supervisions of Dr. Zhou and Dr. Eichhorn. Results related to this research are reported in Chapters 2 through 6, inclusive.

I am aware of the University of Windsor's Senate Policy on Authorship and I certify that I have properly acknowledged the contributions of the other researchers to my dissertation, and I have obtained written permission from my co-authors to include the above materials in my dissertation.

I certify that, with the above qualification, this dissertation, and the research to which it refers to, is the product of my own work.

II. Declaration of Previous Publication

This dissertation includes 5 original papers that have been previously published/submitted for publication in peer reviewed journals or proceedings, as follows:

Dissertation Chapter	Publication title/full citation	Publication status*
Chapter 2	<i>E. Navaei Alvar, B. Zhou, S. Holger Eichhorn, "Oxidative Treatment to Improve Coating and Electrochemical Stability of Carbon Fiber Paper with Niobium Doped Titanium Dioxide Sols for Potential Applications in Fuel Cells" (Electrochimica Acta 132 (2014) 347-355.</i>	<i>Published</i>
Chapter 3	<i>E. Navaei Alvar, B. Zhou, S. Holger Eichhorn, "Effect of Reducing Agent on the Dispersion of Pt Nanoparticles on Electrospun Nb_{0.1}Ti_{0.9}O₂ Nanofibers" (MRS Proceedings, 1542 (2013)</i>	<i>Published</i>
Chapter 4	<i>E. Navaei Alvar, B. Zhou, S. Holger Eichhorn, "Carbon-Embedded Mesoporous Nb-doped TiO₂ Nanofibers as Catalyst support for Oxygen Reduction Reaction in PEM Fuel Cells" (Journal of Materials Chemistry A)</i>	<i>To be Submitted</i>
Chapter 5	<i>E. Navaei Alvar, B. Zhou, S. Holger Eichhorn, "Electrosprayed Cathode Catalyst Layer with Composite-Supported Pt Catalyst and Nafion Loading Optimization Strategy for Polymer Electrolyte Membrane Fuel Cell" (Applied Catalysis B: Environmental)</i>	<i>To be Submitted</i>
Chapter 6	<i>E. Navaei Alvar, B. Zhou, S. Holger Eichhorn, "Electrosprayed vs Airsprayed Catalyst Layers with Composite-Supported Pt Catalysts at Optimized Nafion Volume Percentages" (Electrochimica Acta)</i>	<i>To be Submitted</i>

I certify that I have obtained a written permission from the copyright owners to include the above published materials in my dissertation. I certify that the above material describes work completed during my registration as graduate student at the University of Windsor.

I declare that, to the best of my knowledge, my dissertation does not infringe upon anyone's copyright nor violate any proprietary rights and that any ideas, techniques,

quotations, or any other material from the work of other people included in my dissertation, published or otherwise, are fully acknowledged in accordance with the standard referencing practices. Furthermore, to the extent that I have included copyrighted material that surpasses the bounds of fair dealing within the meaning of the Canada Copyright Act, I certify that I have obtained a written permission from the copyright owners to include such materials in my dissertation.

I declare that this is a true copy of my dissertation, including any final revisions, as approved by my dissertation committee and the Graduate Studies office, and that this dissertation has not been submitted for a higher degree to any other University or Institution.

ABSTRACT

Polymer electrolyte membrane fuel cell (PEMFC) is regarded as a promising technology for both automotive and stationary applications. Two significant challenges that hamper its commercialization are its high cost and insufficient durability. Catalyst layer (the region where fuel and oxidant convert to products) has a vital importance to be able to mitigate the above challenges. This dissertation reports a systematic study of using niobium (Nb)-doped titanium dioxide nanofibers as a corrosion-resistance catalyst support for PEMFCs, along with the study on the control of physical and electrochemical properties to create durable and still active platinum catalysts, and a new strategy to optimize ionomer phase (Nafion) loadings in the catalyst layers. It also proposed a simple wet coating process of Nb-doped titanium dioxide (TiO_2) sols onto carbon papers to protect the interface between gas diffusion backing layer and catalyst layer for unitized regenerative fuel cell applications.

Oxidative treatment and dip coating of carbon paper with Nb-doped TiO_2 sol was shown to increase the corrosion resistance of carbon paper at the interface between catalyst layer and gas diffusion backing layer (*Chapter 2*). Anatase phase Nb-doped TiO_2 nanofibers were synthesized by using the upscalable method of electrospinning to find a more durable alternative catalyst support, to substitute not corrosion resistant pure carbon-based catalyst supports (*Chapter 3*). More electronically conductive and high surface area rutile phase Nb-doped TiO_2 nanofibers were synthesized through embedding carbon in between rutile crystallites using an innovative strategy called “in-situ reductive embedment (ISRE)” (*Chapter 4*). However, the ORR mass activities of the Pt catalysts that were supported by carbon-embedded Nb-doped TiO_2 nanofibers were still slightly lower than pure carbon black based Pt catalysts. Instead, electronically more conductive and high surface area catalyst supports were synthesized by physically mixing of commercial carbon blacks with carbon-embedded Nb-doped TiO_2 nanofibers (*Chapter 5*) and the effect of catalyst layer preparation method on the distribution of catalyst layer components has been investigated (*Chapter 6*).

DEDICATION

To my love, Nasim,

To my parents, Ali and Roghieh,

To my beloved sisters, Nazila and Zohreh,

And to my brother, Hassan.

I could not have done it without your unconditional love and constant support.

ACKNOWLEDGEMENTS

I would like to express my deepest gratitude to my advisor, Dr. Biao Zhou, for his relentless guidance, caring and patience. He has constantly challenged me to push my intellectual limits and think on different fundamental limits. I would like to thank my co-advisor, Dr. S. Holger Eichhorn, whom have been always had his door open to listen, advise and enduring question after question and providing a real world perspective. I would also like to thank the rest of my committee members: Dr. Tricia Breen Carmichael, Dr. Nader Zamani, and Dr. Amir Fartaj for their guidance. I must thank Dr. Andy Sun at Western University for taking the responsibility as the external reviewer of my dissertation. I would also like to extend my heartfelt appreciation and thanks to Dr. Paul Charpentier (Western University), Dr. Olivera Kesler (University of Toronto), Dr. Ricardo F. Aroca (Chemistry and Biochemistry Dept.), Dr. Jeremy Rawson (Chemistry and Biochemistry Dept.), and Dr. Tricia Breen Carmichael (Chemistry and Biochemistry Dept.) for providing access to their high temperature tube furnace, TA instrument, Raman Spectrometer, microwave reactor, and four-probe conductivity measurement set-up. I would also like to appreciate a number of people that made possible the successful completion of the adventure that was my dissertation:

- Mr. Sinisa Jezdic (Electronic Technologist at Physics Department), Mr. Andy Jenner (Mechanical Technologist at MAME) and Mr. Bruce Durfy (Automotive Technologist at MAME) whom always went out of their way to assist me, especially when I had a last minute request.
- Mr. Zakir Hussein (From Dr. Charpentier's research group) and Dr. Joel Kuhn (From Dr. Kesler's research group) to take the responsibility to perform pure hydrogen treatment on my samples.
- Ms. Sharon Lackie (Electron microscope technician at Great Lakes Institute for Environmental Research) for her expertise on various materials data collection techniques.
- Mr. Akhil Vohra and Dr. Michael Miller (from Dr. Carmichael's group) for helping me in doing electronic conductivity measurements

- Dr. Igor Osorio Roman (Chemistry and Biochemistry Dept.) for his guidance with the analysis of Raman Spectroscopy results.
- Any one in chemistry and biochemistry department: in particular, Jonathan, Kelong, and Nick for helping me in different ways.

I owe many thanks to my family for their patience, guidance, support and belief in me. Finally, thank you to my lovely wife, Nasim Farahani, for her unwavering love.

TABLE OF CONTENTS

DECLARATION OF CO-AUTHORSHIP / PREVIOUS PUBLICATION	III
ABSTRACT.....	VI
DEDICATION.....	VII
ACKNOWLEDGEMENTS.....	VIII
LIST OF TABLES.....	XVII
LIST OF FIGURES	XX
LIST OF APPENDICES.....	XXVII
CHAPTER 1	1
1.1 GENERAL INTRODUCTION ON POLYMER ELECTROLYTE MEMBRANE FUEL CELLS	2
1.1.1 BASIC CONCEPT AND PRINCIPLES	2
1.1.2 Membrane electrode assembly (MEA).....	4
1.1.3 MEA components and corresponding functions	6
1.2 GENERAL INTRODUCTION ON UNITIZED REGENERATIVE FUEL CELLS (URFCS).....	8
1.3 KEY CHALLENGES TO THE MARKET SUCCESS OF PEMFCS	8
1.3.1 PERFORMANCE AND COST.....	10
1.3.2 Durability.....	11
1.4 CONSTRAINTS ON MATERIAL SELECTION FOR MEA COMPONENTS	13
1.5 OBJECTIVES	15
1.6 OUTLINE OF THE DISSERTATION.....	15
REFERENCES	16
CHAPTER 2	23
2.1 INTRODUCTION	24
2.2 EXPERIMENTALS.....	25

2.2.1 Preparation of functionalized carbon paper.....	26
2.2.2 Preparation of Nb _{0.1} Ti _{0.9} O ₂ coating on carbon paper	27
2.2.3 Physical Characterization	27
2.2.4 Electrochemical Characterization.....	28
2.3 RESULTS AND DISCUSSION	29
2.3.1 Effects of oxidative treatment	29
2.3.2 Nb-doped TiO ₂ coating on carbon paper.....	31
2.3.2.1 Wettability	31
2.3.2.2 Structure and morphology	32
2.3.2.3 Interaction between Nb-doped TiO ₂ coating and carbon surface	36
2.3.3 Electrochemical stability	38
2.4 CONCLUSIONS.....	43
2.5 ACKNOWLEDGMENTS	44
REFERENCES	44
CHAPTER 3	50
3.1 INTRODUCTION	51
3.2 EXPERIMENTAL.....	52
3.2.1 Preparation of Nb _{0.1} Ti _{0.9} O ₂ nanofibers	52
3.2.2 Pt nanoparticle deposition	52
3.2.3 Physical Characterization of Nb _{0.1} Ti _{0.9} O ₂ and Pt/Nb _{0.1} Ti _{0.9} O ₂ nanofibers.....	53
3.2.3 Electrochemical characterization of Pt/Nb _{0.1} Ti _{0.9} O ₂ nanofibers	53
3.3 RESULTS AND DISCUSSION	54
3.4 CONCLUSIONS.....	59
3.5 ACKNOWLEDGMENTS	59

REFERENCES	59
CHAPTER 4	63
4.1 INTRODUCTION	64
4.2 EXPERIMENTAL	66
4.2.1 Synthesis of Nb-doped TiO ₂ nanofibers with embedded carbon and carbon-free	66
4.2.2 Pt catalyst synthesis	67
4.2.3 Physical characterizations	68
4.2.4 Electrochemical characterizations	69
4.3 RESULTS AND DISCUSSION	71
4.3.1 Carbon-embedded/carbon-free Nb-doped TiO ₂ nanofibers as catalyst supports	71
4.3.1.1 Micromorphology	71
4.3.1.2 Crystal structure, electronic conductivity and surface area	72
4.3.1.3 Carbon content and thermal stability	76
4.3.1.4 Atomic structure of embedded carbon	77
4.3.2 Pt catalysts supported by carbon-embedded/carbon-free Nb-doped TiO ₂ nanofibers	80
4.3.2.1 Nanostructure and nanomorphology	80
4.3.2.2 Elemental composition, chemical and electronic state at the surface	82
4.3.3 Electrochemical activity and durability of Pt catalysts for oxygen reduction reaction	87
4.3.3.1 Electrochemical activity of Pt catalysts before durability tests	88
4.3.3.2 Electrochemical activity of Pt catalysts after durability tests	90
4.4 CONCLUSIONS	92

4.5 ACKNOWLEDGMENTS	92
REFERENCES	93
SUPPLEMENTARY INFORMATION (SI) CHAPTER 4.....	101
Koutecky-Levich Equation.....	102
t-plots.....	103
Raman peak analysis parameters and results.....	104
PXRD patterns of Pt-deposited nanofibers	106
Transmission electron microscopy (TEM) and energy dispersive X-ray spectroscopy (EDX) results.....	107
X-ray photoelectron spectroscopy (XPS) survey scans.....	108
High-resolution XPS scans in C 1s region	110
High-resolution XPS scans in O 1s region	112
High-resolution XPS scans in Ti 2p region	114
High-resolution XPS scans in Nb 3d region.....	116
High-resolution XPS scans in Pt 4f region.....	118
Kroger-vink notations.....	120
Electrochemical characterization results	121
References	122
CHAPTER 5	123
5.1 INTRODUCTION	124
5.2 EXPERIMENTAL.....	126
5.2.1 Synthesis and characterization of composite supported Pt catalysts.....	126
5.2.1.1 Synthesis of carbon-embedded Nb-doped TiO ₂ nanofibers	126
5.2.1.2 Synthesis of composite catalyst supports.....	127
5.2.1.3 Pt deposition	127

5.2.1.4	Material characterization of composite supported Pt catalysts.....	128
5.2.1.5	Electrochemical characterization of composite-supported Pt catalysts...	129
5.2.2	Evaluation of composite supported Pt catalysts by optimized H ₂ -air PEMFC performance.....	130
5.2.2.1	NVP vs. NWP in the catalyst layer.....	131
5.2.2.2	Catalyst Layer preparation.....	132
5.2.2.3	Membrane electrode assembly (MEA) fabrication.....	133
5.2.2.4	Polarization curves.....	134
5.3.	RESULTS AND DISCUSSION	134
5.3.1.	Development of composite-supported Pt catalysts.....	134
5.3.1.1	Physical characteristics of composite catalyst supports	134
5.3.1.2	Physical characteristics of composite-supported Pt catalysts.....	138
5.3.1.3	Electrochemical activity and durability of Pt catalysts for oxygen reduction reaction	140
5.3.2	H ₂ -Air PEMFC performance evaluations.....	142
5.3.2.1	Optimized NVP for electrosprayed catalyst layers.....	143
5.3.2.2	Predicted optimized Nafion loadings for composite-supported Pt catalysts	146
5.3.2.3	PEMFC performances at fixed NVP versus fixed NWP	147
5.4	CONCLUSIONS.....	150
5.5	ACKNOWLEDGMENTS	151
	REFERENCES	151
	SUPPLEMENTARY INFORMATION (SI) CHAPTER 5.....	159
	Typical Series of Calculations for Catalyst Ink Preparation	160
	PXRD Patterns of Composite Catalyst Supports	161

Surface Area Analysis and Pore Size Distributions	162
PXRD Patterns of Composite-supported Pt Catalysts.....	163
Survey and High Resolution X-ray Photoelectron Spectroscopy (XPS) Results....	164
Electrochemical Activity and Durability Measurements	168
PEM Fuel Cell Evaluation Tests	170
References	172
CHAPTER 6	173
6.1 INTRODUCTION	174
6.2 EXPERIMENTAL.....	175
6.2.1 Synthesis of composite catalyst supports	175
6.2.2 Synthesis of Pt catalysts	176
6.2.3 Catalyst layer preparation.....	176
6.2.4 Membrane Electrode Assembly (MEA) fabrication.....	178
6.2.5 Polarization Curves	178
6.2.6 AS and ES catalyst layer properties	178
6.3 RESULTS AND DISCUSSION.....	179
6.3.1 H ₂ -Air PEMFC performance evaluation	179
6.3.1.1 Optimized NVP for airsprayed cathode catalyst layers	179
6.3.1.2. Fixed NVP versus fixed NWP for airsprayed catalysts layers	182
6.3.1.3 AS vs. ES CLs at corresponding optimized NVPs	183
6.3.2 AS or ES Catalyst layer Characteristics at optimized NVPs.....	185
6.3.2.1 Morphology and Porosity	185
6.3.2.2 Nafion, Carbon and TiO ₂ distributions.....	187
6.4 CONCLUSIONS.....	191

REFERENCES	191
CHAPTER 7	196
7.1 CONCLUSIONS.....	197
7.2 RECOMMENDATIONS	199
REFERENCES	200
APPENDICES	201
APPENDIX A Basic Operation Principles of various Fuel Cell Types.....	202
APPENDIX B Copyright Permissions	203
VITA AUCTORIS	205

LIST OF TABLES

Table 2.1. The amount of charge per cm^2 measured for the peaks of the Q/HQ redox couples after holding the potential at 1.2 V versus Ag/AgCl for 0, 24, 48, and 72 hours.	42
Table 3.1. Structural and electrochemical properties of Pt/Nb _{0.1} Ti _{0.9} O ₂ catalysts at 50th and 1000th cycles after potential cycling in the range of 0.3 to 1.4V.	56
Table 4.1. Physical Properties of synthesized Nb _x Ti _(1-x) O ₂ nanofibers and Vulcan XC-72R as reference.	72
Table 4.2. Relative surface elemental composition of the synthesized Nb-doped TiO ₂ nanofibers obtained from XPS survey spectra.	83
Table 4.3. Atomic concentration ratios for the supporting NFs obtained from high-resolution XPS spectra shown in Figs. SI-4.11 to SI-4.13, inclusive, and their tabulated peak parameters shown in Tables SI-4.5 to SI-4.7, inclusive.	85
Table 4.4. ECSA and ORR mass activities at 0.9 V measured for 20 wt. % Pt/Nb-doped TiO ₂ nanofiber and 20 wt. % Pt/Vulcan catalysts before and after Durability Tests (potential cycling experiments).	88
Table SI-4.1. Sadezky et al.[5] reported vibration modes and line shapes for the best curve-fitting of first-order Raman bands for carbonaceous materials.	104
Table SI-4.2. Relative band area ratios of the D1-D4 bands to G band, $A_{\text{DX-band}}/A_{\text{G-band}}$ (X = 1, 2, 3, 4).	104
Table SI-4.3. XPS peak parameters and Area % of different components in C 1s region.	111
Table SI-4.4. XPS peak parameters and Area % of different components in O 1s region.	113
Table SI-4.5. XPS peak parameters and Area % of different components in Ti 2p region.	115
Table SI-4.6. XPS peak parameters and Area % of different components in Nb 3d region.	117

Table SI-4.7. XPS peak parameters and Area % of different components in Pt 4f region.	119
Table SI-4.8. Descriptions of Kroger-vink notations used in Eqs. (SI-4.3) and (SI-4.4).	120
Table 5.1. List of investigated Pt catalysts. Samples TC, C25C, C75C and VC were prepared While JM was purchased from Johnson Matthey. CBWP=carbon black weight percentage.	128
Table 5.2. True densities of composite catalyst supports measured through gas pycnometry.	131
Table 5.3. Physical properties of in-house prepared catalyst supports and pure Vulcan XC-72R carbon blacks (purchased from Cabot Corporation).	135
Table 5.4. Predicted optimized Nafion loadings, according to experimentally optimized NVPs, for ES catalyst layers that are employing different catalyst supports.	146
Table SI-5.1. Typical series of calculations to prepare electrosprayed catalyst layers with predetermined Pt loadings and NVPs.	160
Table SI-5.2a. XPS peak parameters and % Area of different chemical states in C 1s region for 20 wt.% Pt/Vul.75 wt.%(C/Nb _{0.1} Ti _{0.9} O ₂) ₂₅ wt.% catalyst.....	166
Table SI-5.2b. XPS peak parameters and % Area of different Chemical states in O 1s region for 20 wt.% Pt/Vul.75 wt.%(C/Nb _{0.1} Ti _{0.9} O ₂) ₂₅ wt.% catalyst.....	166
Table SI-5.2c. XPS peak parameters and % Area of different Chemical states in Ti 2p region for 20 wt.% Pt/Vul.75 wt.%(C/Nb _{0.1} Ti _{0.9} O ₂) ₂₅ wt.% catalyst.....	166
Table SI-5.2d. XPS peak parameters and % Area of different Chemical states in Nb 3d region for 20 wt.% Pt/Vul.75 wt.%(C/Nb _{0.1} Ti _{0.9} O ₂) ₂₅ wt.% catalyst.....	167
Table SI-5.2e. XPS peak parameters and % Area of different Chemical states in Pt 4f region for 20 wt.% Pt/Vul.75 wt.%(C/Nb _{0.1} Ti _{0.9} O ₂) ₂₅ wt.% catalyst.....	167
Table SI-5.3. ECSA and ORR mass activities at 0.9 V measured for different catalysts before and after durability test (1000 full potential cycling experiments).....	169

Table SI-5.4. Converting NWP to NVPs for electrosprayed catalyst layers using 20 wt.% Pt catalysts supported by carbon blacks. The calculations were performed for a Pt loading of $0.2 \text{ mg}_{\text{Pt}}\cdot\text{cm}^{-2}$	170
Table 6.1. List of synthesized Pt catalysts.	176
Table 6.2. True densities of composite catalyst supports measured through gas pycnometry.	177
Table 6.3. Converting proposed NWP [19, 38] in the literature to NVPs for airsprayed catalyst layers using 20 wt. % Pt catalysts supported by pure carbon blacks. The calculations were performed for a Pt loading of $0.2 \text{ mg}_{\text{Pt}}\cdot\text{cm}^{-2}$	179
Table 6.4. Predicted optimized Nafion loadings, according to experimentally optimized NVP, for airsprayed catalyst layers that are employing different catalyst supports.	181
Table A-1. Basic operation principles of various fuel cell types ((Source: http://americanhistory.si.edu/fuelcells/basics.htm).....	202

LIST OF FIGURES

Figure 1.1. Schematic fuel cell polarization (Voltage vs. current density) and power density curves.....	4
Figure 1.2. Schematic view of membrane electrode assemblies and electrochemical reactions.....	5
Figure 1.3. A simplified schematic representation of TPB reaction sites in the catalyst layer.....	7
Figure 1.4. Concept of unitized regenerative fuel cell (URFC) [12].	8
Figure 1.5. Fuel cell targets versus status (the blue line indicates the status as a function of the target in percentage). The figure has been reproduced from [18].	9
Figure 1.6. Schematic representation of Pt agglomeration and carbon corrosion, reprinted from ref. [32]. (a) Mechanism of Pt particle growth by dissolution/precipitation [36]; (b) Degradation of carbon supports and loss of noble-metals [39]......	11
Figure 2.1. Schematic representation of the procedure for oxidative functionalization of carbon paper and its coating with Nb-doped TiO ₂	26
Figure 2.2. Water contact angle of carbon paper. (a) before oxidative functionalization; (b) after oxidative functionalization.....	29
Figure 2.3. Surface characterization of UCP and FCP. (a) FTIR and (b) Raman spectroscopy.....	30
Figure 2.4. Water contact angle of Nb-doped TiO ₂ coated carbon papers. (a) Nb-TiO ₂ -UCP; (b) Nb-TiO ₂ -FCP.....	32
Figure 2.5. X-ray diffraction patterns of different samples. (a) FCP; (b) Nb-doped-FCP; (c) Nb-TiO ₂ -UCP.	33
Figure 2.6. FE-SEM images of different samples at different magnifications. (a-c) Nb-TiO ₂ -CP, (d-f) Nb-TiO ₂ -FCP.....	34
Figure 2.7. FE-SEM images of different Nb-TiO ₂ -FCP samples at different magnifications. (a) and (b) coated after 60% weight loss of the coating solution; (b) and (c)	

exposed to the sol for about 7 hours (during the entire weight reduction process of the sol).	36
Figure 2.8. Surface characterization by FTIR and raman spectroscopy. (a) and (b) FTIR spectra of Nb-doped TiO ₂ , Nb-TiO ₂ -UCP, and Nb-TiO ₂ -FCP; (c) and (d) Raman spectra of Nb-TiO ₂ -UCP taken at different locations; (e) Raman spectra of Nb-TiO ₂ -FCP.	37
Figure 2.9. Cyclic voltammograms of different samples in aqueous 0.5 M H ₂ SO ₄ at a scan rate of 50 mV/s after holding the potential at 1.2 V versus Ag/AgCl for 0, 24, 48, and 72 hours; (a) UCP; (b) FCP; (c) Nb-TiO ₂ -UCP; (d) Nb-TiO ₂ -FCP.	39
Figure 2.10. The amount of charge per cm ² measured for the peaks of the Q/HQ redox couples as a function of time of electrochemical oxidation at 1.2 V.	41
Figure 3.1. FE-SEM images of the Nb _{0.1} Ti _{0.9} O ₂ nanofibers prepared at 1.25 KV/cm electric field.	55
Figure 3.2. Powder X-Ray diffraction patterns of Pt-coated Nb _{0.1} Ti _{0.9} O ₂ nanofibers with EG method and sodium borohydride (NaBH ₄) method.	56
Figure 3.3. Cyclic voltammograms of (a) EG-reduced Pt/Nb _{0.1} Ti _{0.9} O ₂ and (b) NaBH ₄ -reduced Pt/Nb _{0.1} Ti _{0.9} O ₂ catalysts after 50 and 1000 cycles at a scan rate of 100 mV/s. The Pt loading was 100 μgPt.cm ⁻² and the electrolyte was Ar purged 0.5 H ₂ SO ₄ . Insets show the charge integration of the H ₂ desorption peaks for ECSA calculation. ...	57
Figure 3.4. Back scattered FE-SEM images of catalysts reduced by NaBH ₄ (a) and EG (b), respectively. TEM (c) and HRTEM (d) images of Pt nanoparticles on Nb/TiO ₂ nanofibers prepared by the EG method.	58
Figure 4.1. Field emission-SEM images of Nb _x Ti _(1-x) O ₂ (x = 0.1 and 0.25) NFs heat treated under either protocol CF or CE. (a) CF10; (b) CF25; (c) CE10; and (d) CE25. ..	72
Figure 4.2. PXRD patterns collected from Nb _x Ti _(1-x) O ₂ (x = 0.1 and 0.25) NFs heat treated under either protocol CF or CE. (a) Wide-angle patterns; (b) magnified views of the rutile (110) peak.	73

Figure 4.3. Surface area and pore size analysis of $\text{Nb}_x\text{Ti}_{(1-x)}\text{O}_2$ ($x = 0.1$ and 0.25) NFs heat treated under either protocol CF or CE. (a) Nitrogen adsorption/desorption isotherms (BET); and (b) BJH pore size distribution plots. 75

Figure 4.4. TGA data plots obtained for $\text{Nb}_x\text{Ti}_{(1-x)}\text{O}_2$ ($x = 0.1$ and 0.25) NFs heat treated under either protocol CF or CE..... 77

Figure 4.5. Raman Spectra of $\text{Nb}_x\text{Ti}_{(1-x)}\text{O}_2$ ($x = 0.1$ and 0.25) NFs heat treated under either protocol CF or CE along with peak analyses of CE-NFs based on the combination of bands given in Table S1. (a) Raman spectra; (b) peak analyses of first-order bands of ordered/disordered graphite observed for CE10 and CE25. 79

Figure 4.6. Bright field (BF) TEM and HRTEM images from 20 wt. % Pt deposited CE10 NFs. (a) TEM image from a single Pt deposited NF along with collected SAD pattern; (b) HRTEM image from a selected area shown in (a); (c) TEM image from Pt deposited nanofibers with relatively different morphologies; (d) HRTEM image from a selected area shown in (c)..... 81

Figure 4.7. Cyclic voltammograms (CV) and linear sweep voltammograms (LSVs) obtained for different Pt catalysts. (a) CVs obtained in Ar-saturated aqueous solutions of 0.5M H_2SO_4 at a potential scan rate of 50 mV/s; and (b) LSVs obtained in O_2 saturated aqueous solutions of 0.5M H_2SO_4 with a potential sweep rate of 5 mV/s and rotation speed of 1600 rpm..... 89

Figure 4.8. Series of CV and LSV plots obtained for different catalysts during durability experiments. (a, b, and c) Series of CV curves obtained after certain numbers of potential cycling between 0 to 1.2 V in Ar saturated aqueous solutions of 0.5M H_2SO_4 at a potential scan rate of 50 mV/s; (d, e, and f) Oxygen reduction LSVs obtained in O_2 saturated aqueous solutions of 0.5M H_2SO_4 with a potential sweep rate of 5 mV/s and rotation speed of 1600 rpm, before and after 1000 potential cycles..... 91

Figure SI-4.1. t-plots of all synthesized $\text{Nb}_x\text{Ti}_{(1-x)}\text{O}_2$ ($x = 0.1$ and 0.25) nanofibers and a Vulcan XC-72R. 103

Figure SI-4.2. Peak analyses of the ordered/disordered graphite second-order bands observed in the Raman spectra of CE-NFs. (a) CE10; and (b) CE25..... 105

Figure SI-4.3. PXRD patterns of 20 wt. % Pt deposited $\text{Nb}_x\text{Ti}_{(1-x)}\text{O}_2$ ($x = 0.1$ and 0.25) nanofibers.....	106
Figure SI-4.4. BF-TEM and HRTEM images of 20 wt. % Pt deposited CE10 nanofibers at different magnifications.	107
Figure SI-4.5. Dark field-TEM images and collected EDX spectra from 20 wt. % Pt deposited CE10 nanofibers.	107
Figure SI-4.6. XPS survey spectra of 20 wt. % Pt deposited CF10 nanofibers.	108
Figure SI-4.7. XPS survey spectra of 20 wt. % Pt deposited CF25 nanofibers.	108
Figure SI-4.8. XPS survey spectra of 20 wt. % Pt deposited CE10 nanofibers.....	109
Figure SI-4.9. XPS survey spectra of 20 wt. % Pt deposited CE25 nanofibers.....	109
Figure SI-4.10. High resolution XPS spectra of different catalysts along with component fits in C 1s region.....	110
Figure SI-4.11. High resolution XPS spectra of different catalysts along with component fits in O 1s region.....	112
Figure SI-4.12. High resolution XPS spectra of different catalysts along with component fits in Ti 2p region.....	114
Figure SI-4.13. High resolution XPS spectra of different catalysts along with component fits in Nb 3d region..	116
Figure SI-4.14. High resolution XPS spectra of different catalysts along with component fits in Pt 4f region..	118
Figure SI-4.15. ORR Linear sweep voltammograms (LSVs) recorded at a potential scan rate of 5 mV s^{-1} and various rotation speeds along with Koutecky-Levich plots at 0.7 V for different catalysts in O_2 saturated aqueous solution of $0.5\text{M H}_2\text{SO}_4$. LSVs for (a) 20 wt.%Pt/CF10; (b) 20 wt.%Pt/CF25; (c) 20 wt.%Pt/CE10; (d) 20 wt.%Pt/CE25; (e) 20 wt.%Pt/Vulcan; and (f) K-L plots at 0.7V	121
Figure SI-4.16. ORR linear sweep voltammograms of different catalysts recorded in O_2 saturated aqueous solutions of $0.5\text{M H}_2\text{SO}_4$ with a potential sweep rate and rotation speed	

of 5 mV/s and 1600 rpm, respectively, before and after 1000 potential cycles. (a) 20 wt.% Pt/CF10; (b) 20 wt.% Pt/CF25..... 122

Figure 5.1. Weight loss vs Temperature from TGA tests for composite catalyst supports C/Nb_{0.1}Ti_{0.9}O₂, Vul_{25wt.%}-(C/Nb_{0.1}Ti_{0.9}O₂)_{75wt.%} and Vul_{75wt.%}-(C/Nb_{0.1}Ti_{0.9}O₂)_{25wt.%}..... 136

Figure 5.2. Bright filed (BF)-TEM and HRTEM images for the sample of C75C catalyst (20 wt.% Pt/ Vul_{75wt.%}-(C/Nb_{0.1}Ti_{0.9}O₂)_{25wt.%}). (a) and (b) BF-TEM images from different areas; (c) HRTEM image from a representative Pt/C area; and (d) HRTEM image from a representative Pt/NF area. G stands for Graphite and R stands for Rutile..... 139

Figure 5.3. ORR mass activities and ORR activity losses for in-house synthesized Pt catalysts versus the CBWP in composite catalyst supports. The actual carbon contents were obtained from TGA data plots represented in Fig. 5.1. 141

Figure 5.4. Effect of NVP of the cathode CL on H₂/Air PEMFC performance. (a) Polarization curve; (b) Power density curve; and (c) Maximum power density versus NVP values. 143

Figure 5.5. Effect of Pt loading of the ES cathode CL on H₂/Air PEMFC performance at optimized NVP. (a) Polarization curves; (b) Power density curves; and (c) Maximum power density versus Pt loading. 144

Figure 5.6. Performance comparison for PEMFCs with the house-made ES CL (VC catalyst) at optimized NVP with ES CL (E-tek catalyst) reported in literature [54] with the same Pt loading of 0.17 mg_{Pt}·cm⁻². The dashed lines represent the expected H₂/O₂ PEMFC performance based on the model in [70]..... 145

Figure 5.7. Polarization and power density curves of H₂/Air PEMFCs employing electrospayed VC CL on the anode side, with a Pt loading of 0.17 mg_{Pt}·cm⁻² and NVP of 43.7%, and electrospayed TC CL on the cathode side prepared with a Pt loading of 0.17 mg_{Pt}·cm⁻² at different NVPs or NWP. (a) Polarization curves; (b) Power density curves. 147

Figure 5.8. Peak Power densities and ORR activity losses for Pt catalyst with different composite supports..... 149

Figure SI-5.1. Powder X-ray Diffraction patterns of different catalyst supports. C/Nb _{0.1} Ti _{0.9} O ₂ ; Vul. _{25wt.%} -(C/Nb _{0.1} Ti _{0.9} O ₂) _{75wt.%} ; Vul. _{75wt.%} -(C/Nb _{0.1} Ti _{0.9} O ₂) _{25wt.%} ; and Vulcan XC-72.	161
Figure SI-5.2. Surface area, pore size analysis and t-plots of different catalyst supports; (a) Nitrogen adsorption/desorption isotherms; (b) BJH pore size distribution plots; and (c) t-plots.	162
Figure SI-5.3. PXRD patterns of different composite supported-20 wt.% Pt catalysts.	163
Figure SI-5.4. XPS survey spectra of 20 wt. % Pt/Vul. _{75 wt.%} -(C/Nb _{0.1} Ti _{0.9} O ₂) _{25 wt.%} catalyst.	164
Figure SI-5.5. High resolution XPS spectra of 20 wt.% Pt/Vul. _{75 wt.%} -(C/Nb _{0.1} Ti _{0.9} O ₂) _{25 wt.%} catalyst with Chemical state fits at different regions. (a) C 1s region; (b) O 1s region; (c) Ti 2p region; (d) Nb 3d region; and (e) Pt 4f region.	165
Figure SI-5.6. Cyclic and linear-sweep voltammograms obtained from Pt catalysts supported by different composite supports before and after durability test. (before and after applying 1000 potential cycles). (a, c, e, g) Series of CV curves obtained after certain numbers of potential cycling between 0 to 1.2 V. (b, d, f, h) linear sweep voltammograms (LSVs) obtained in O ₂ saturated aqueous solutions of 0.5M H ₂ SO ₄	168
Figure SI-5.7. Effect of lowering Pt on the anode side on the H ₂ /Air PEMFC performances of MEAs prepared using electro sprayed VC catalyst on the cathode side, with a Pt loading of 0.17 mgPt·cm ⁻²	171
Figure SI-5.8. Polarization and power density curves of the H ₂ /Air PEMFCs employing different electro sprayed CLs in their cathode compartments with optimized NVP of 43.7.	171
Figure 6.1. Effect of NVP of the air sprayed cathode CL (VC catalyst) on H ₂ /Air PEMFC performance. (a) Polarization curve; (b) Power density curve; and (c) Maximum power density versus NVP values.	180

Figure 6.2. Effect of NVP of the AS cathode CL (C75C catalyst) on H ₂ /Air PEMFC performance. (a) Polarization curve; (b) Power density curve; and (c) Maximum power density versus NVP values.....	182
Figure 6.3. Comparison of effectiveness in predicting the optimized Nafion loadings through using fixed NVP vs. fixed NWP values. (a) Polarization curve; (b) Power density curve.....	183
Figure 6.4. Effect of catalyst layer preparation methods on the peak power densities of MEAs employing different composite-supported Pt catalysts (Black curves). The increase in the peak power densities through using electro spraying rather than air spraying method were also shown versus CBWP in composite supports (Blue curve).	184
Figure 6.5. Field emission-SEM images of different AS/ES cathode CLs at their corresponding optimized NVPs at 10 μ m scale. a, b, c, and d are for AS CLs; e, f, g, and h are for ES CLs.....	186
Figure 6.6. Pore size distributions for air sprayed/electro sprayed catalyst layers employing C25C catalyst at their corresponding optimized NVPs.	186
Figure 6.7. Back-scattered SEM images and Fluorine X-ray mapping of different AS/ES cathode CLs at their corresponding optimized NVPs. a, b, c, and d are for AS CLs; e, f, g, and h are for ES CLs.	188
Figure 6.8. Back-scattered SEM images and elemental X-ray mappings of AS and ES catalyst layers employing C25C catalyst at their corresponding optimized NVPs.	189
Figure 6.9. Optical images and Raman intensity mappings collected from AS and ES catalysts layers employing C25C catalyst at their corresponding optimized NVPs. Optical images of (a) air sprayed and (b) electro sprayed C25C CLs along with Raman intensity maps of TiO ₂ and carbon.	190

LIST OF APPENDICES

APPENDIX A: Basic Operation Principles of Various Types of Fuel Cells	202
APPENDIX B: Copyright Permissions	203

CHAPTER 1

Introduction

1.1 General introduction on polymer electrolyte membrane fuel cells

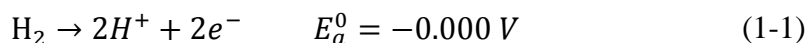
In general, fuel cell is an electrochemical conversion device that takes fuel as input and produces electricity as output. Among five major types of fuel cells (Table A1 in Appendix A), polymer electrolyte membrane fuel cell (PEMFC) converts the chemical energy stored in hydrogen and oxygen directly to electric power through an electrochemical reaction ($\text{H}_2 + \frac{1}{2} \text{O}_2 \rightarrow \text{H}_2\text{O}$), where the only by-product is water. Unlike batteries, PEMFC can be continuously used by refuelling instead of time-consuming charging, easily scalable between power (determined by the fuel cell size) and capacity (determined by the fuel reservoir size), and covers a wide range of applications from 1-W range (cell phone) to the megawatt range (power plant) [1].

1.1.1 Basic concept and principles

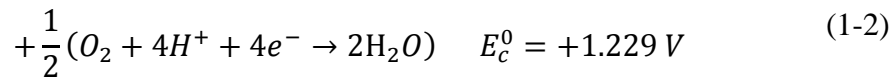
The earth is our home and consists of 90% of hydrogen. There is a tendency to go for energy sources with lower C/H ratio through the history which is maximum in wood and finally converges to zero in pure hydrogen [2]. Hydrogen can offer a sustainable solution for our nation's energy in terms of energy security, near-zero carbon emissions, zero tailpipe emissions, and economic vitality [3]. Among different technologies which are employing hydrogen as fuel, PEMFCs are the key to using hydrogen efficiently for vehicular and portable electronic applications as it have none of tailpipe emissions (e.g. NO_x) inherent to combustion, enabled for lower operation temperatures and fast start-up and dynamic operation [4-8].

PEMFC is always comprised of two electrodes (anode and cathode) which are separated using a proton conducting polymer electrolyte. Accordingly, the overall reaction of a fuel cell ($\text{H}_2 + \frac{1}{2} \text{O}_2 \rightarrow \text{H}_2\text{O}$) has been split into two half electrochemical reactions occurring at anode and cathode electrodes.

The hydrogen oxidation reaction (HOR) on the anode side is



The oxygen reduction reaction (ORR) on the cathode side is



Where E_a^0 and E_c^0 are their corresponding potentials versus standard hydrogen electrode (SHE) under standard conditions. Therefore, the overall steady-state potential of a PEMFC (E_{cell}^0), with an overall reaction of $H_2 + \frac{1}{2} O_2 \rightarrow H_2O$, would be equal to 1.229 V. Although this positive potential difference will create a negative standard free energy change to support thermodynamically the occurrence of spontaneous reaction in PEMFCs, the actual voltage output of a real PEMFC is less than the calculated amount due to the steps that must be taken to produce the electricity in a fuel cell [9]. Sequentially, the steps are reactant delivery (hydrogen to the anode side and oxygen to the cathode side), electrochemical reaction, ionic conduction through the electrolyte and electronic conduction through the external circuit, and product removal on the cathode side [6].

The key performance measure of a fuel cell is the voltage output as a function of the drawn electrical current density (polarization curve) as shown in Figure 1.1. Each step will cause a voltage drop due to the kinetics at the electrode (η_{act} mostly occurred at low current densities), resistivity losses in the electrolyte (η_{iR}), and non-reacting diffusion in gas diffusion layers (η_{diff} mostly occurred at high current densities) [10].

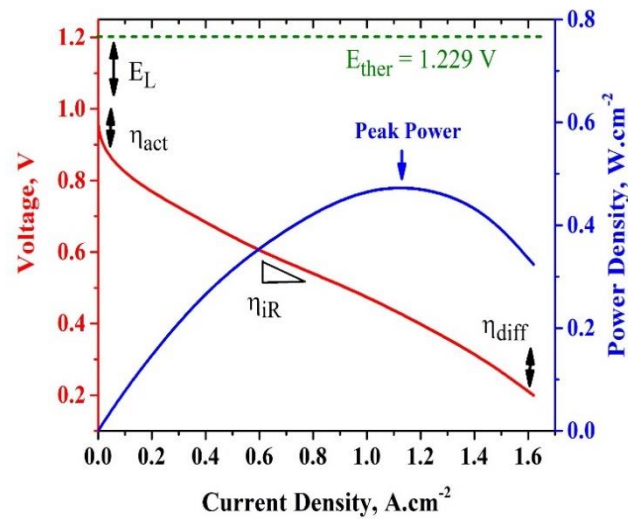


Figure 1.1. Schematic fuel cell polarization (Voltage vs. current density) and power density curves.

Therefore the real voltage output of the fuel cell would be found by the following equation:

$$V = E_{\text{ther}} - E_L - \eta_{\text{act}} - \eta_{iR} - \eta_{\text{diff}} \quad (1-3)$$

Where V is the real voltage output of the fuel cell, E_{ther} is the thermodynamically predicted voltage output (+1.229 V), E_L is the loss in voltage due to leaks across the electrolyte, η_{act} is the activation overpotential due to the kinetics at the electrode, η_{iR} is the overpotential due to ohmic resistances in the system, and η_{diff} is the overpotential due to mass diffusion limitations.

1.1.2 Membrane electrode assembly (MEA)

To convert chemical energy stored in hydrogen and oxygen to electricity, on top of electrochemical reactions, there are other complex phenomena to deal with such as heat transfer and multi-phase flows. Most of these phenomena will happen in the membrane electrode assembly (MEA) of PEMFCs consisting of catalyst layer (CL), proton exchange

membrane, and gas diffusion layers (GDLs). Membrane electrode assembly (MEA) is the assembled stack of different layers in PEMFC which is shown schematically in the section view of Figure 1.2.

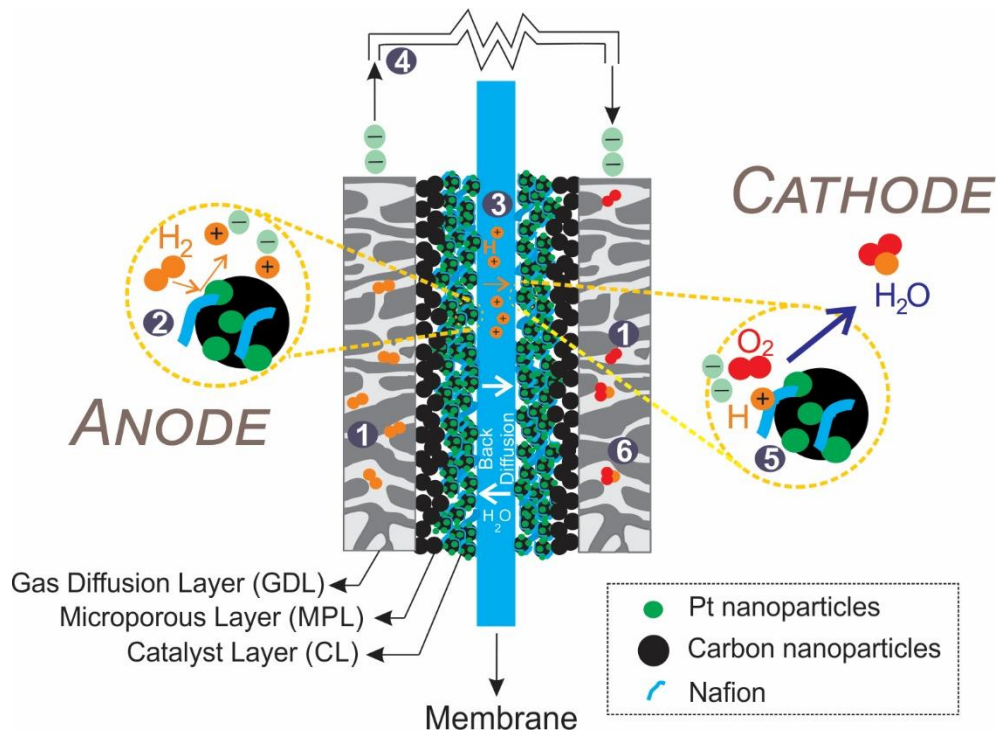


Figure 1.2. Schematic view of membrane electrode assemblies and electrochemical reactions.

MEA turned to be the core technology of PEMFC as all phenomena which are involved to produce electricity are mostly happening through MEAs. As shown in Figure 1.2, the following multi-physics, highly coupled and nonlinear transport and electrochemical phenomena take place in the MEA during fuel cell operation [7]:

(1) H₂ and O₂ flow through the respective porous gas diffusion layer (GDL) and diffuse into the respective catalyst layers (CLs); (2) hydrogen is oxidized at the anode catalyst layer and forms protons and electrons; (3) protons migrate and water is transported through the membrane; (4) electrons are transferred through carbon support to the anode current collector, and then to the cathode current collector through an external circuit; (5) O₂ is

reduced with electrons at the cathode CL to form water; (6) product water is transported out of the cathode CL, through cathode GDL, and eventually out of the cathode gas flow channels. When operating under practical current loads, relatively high inlet humidity, liquid water is present within the fuel cell.

1.1.3 MEA components and corresponding functions

As shown in Fig. 1.2, MEA consists gas diffusion layers, catalyst layers, and proton conducting membrane which all would be explained briefly as follow:

Gas diffusion layer (GDL)

Gas diffusion layer (GDL), gas diffusion media (GDM)-also called gas diffusion backing (GDB) layer- acts as a porous media for the transport of fluids and products from one interface to another. The gas diffusion layer together with catalyst layer is also named as diffusion electrode in the fuel cell community. The main functions are to regulate the reactant gases from the bipolar plate to the catalyst layer, remove the produced products such as water in PEMFC, provide mechanical support for CL, and conduct electrons from CL to bipolar plate and vice versa. Conventional diffusion layer materials for PEMFC applications are carbon cloth and carbon fiber paper.

Proton exchange membrane (PEM)

Proton exchange membrane is one of the key components of PEMFC which should possess high proton conductivity, be impermeable to gases and/or fuel, achieve balanced water transport, and be an electrical insulator. Most popular membrane used in PEMFC applications is a sulfonated polytetrafluoroethylene (PTFE)-known as Nafion. For a polymer to be a good ion conductor it must possess fixed charged sites and sufficient free volume. Nafion has sulfonic acid ($\text{SO}_3^- \text{H}^+$) functional groups attached to a PTFE backbone to create fixed charged sites and free volume for ionic conductivity. Nafion ion conductivity is highly dependent on water content and this requirement necessitates the humidification of reactant gases during PEMFC operation.

Catalyst layers (CLs)

The last but not least important component of PEMFC that requires improvement is the catalyst layer. The electrochemical reaction kinetics and resultant current is highly

dependent on the catalyst layer structure. The current practical catalyst technology for PEMFC applications is Pt nanoparticles supported on high surface area carbon black.

The CL can be coated either on the gas diffusion layer or the membrane and in both cases we need a good interfacial contact between three of them (GDL/CL/PEM). To let both HOR, Eq. (1-1), and ORR, (Eq. (1-2)), happen at their corresponding electrodes, a three phase boundary (TPB) needs to be established to let the three components reactant gas, protons, and electrons come in contact [11]. TPB formation in the catalyst layer of PEMFC has been schematically shown in Figure 1.3.

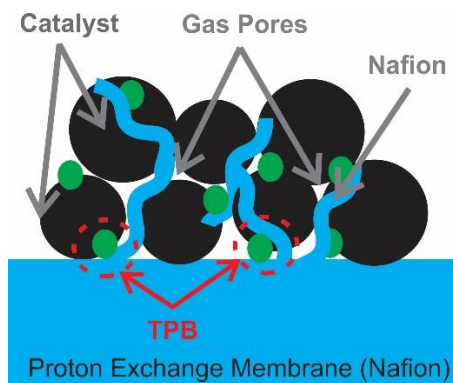


Figure 1.3. A simplified schematic representation of TPB reaction sites in the catalyst layer.

The most sluggish reaction in PEMFC is the oxygen reduction reaction (ORR) which could create a significant limitation for fuel cell performance. In addition to creating a large number of TPB zones, the catalyst layer must effectively remove water generated on the cathode side. So, the basic requirements of the CL in PEMFC are creating large number of TPBs, transport of protons from the anode to the cathode and vice versa, efficient water management especially in the cathode CL, and good electronic current transport.

1.2 General introduction on unitized regenerative fuel cells (URFCs)

A unitized regenerative fuel cell (URFC) is a rather recent technology of PEMFCs which consist of both PEMFC and electrolyser as one unit. Figure 1.4 schematically shows an URFC with combined electrolyser and fuel cell operation modes but only one of the two modes can be operated at any time.

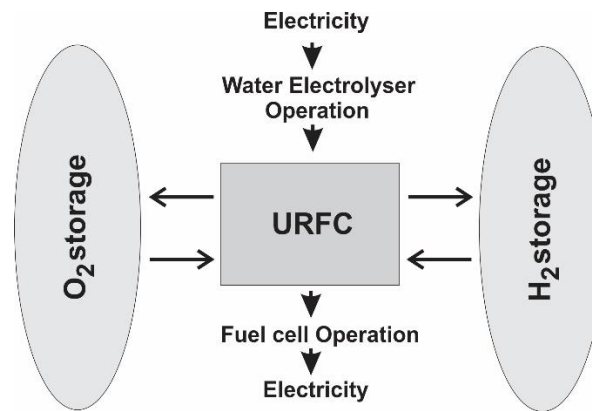


Figure 1.4. Concept of unitized regenerative fuel cell (URFC) [12].

Unitised regenerative PEMFC MEA should have balanced properties to run smoothly in both electrolyser and fuel cell modes. The MEAs for URFCs mainly differ from PEMFC in the type of catalyst they use, i.e. bifunctional catalysts [13], and/or gas diffusion layers [14, 15].

1.3 Key challenges to the market success of PEMFCs

In general, fuel cells must meet three important criteria: sufficient performance, low cost, and high durability. Despite impressive improvements achieved by the fuel cell community to bring the technology to a pre-commercial viability [16-18], there are still key issues that need to be investigated for general acceptance of the technology. For instance, the fuel cell technical team as one of 12 U.S. Drive (Driving Research and Innovation for Vehicle efficiency and Energy sustainability) technical teams identified cost

and durability as the primary challenges to fuel cell commercialization [18], as shown in Figure 1.5.

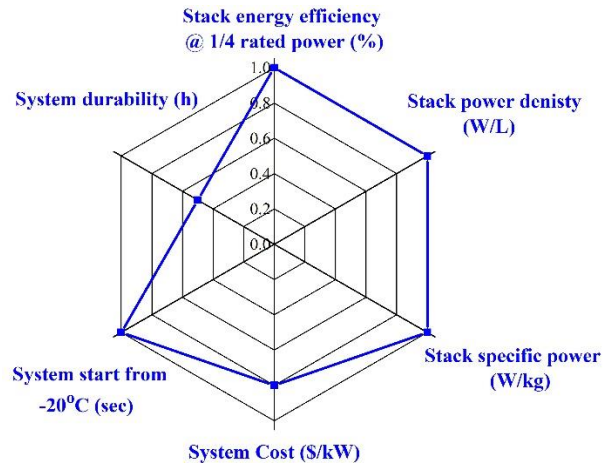


Figure 1.5. Fuel cell targets versus status (the blue line indicates the status as a function of the target in percentage). The figure has been reproduced from [18].

The use of high performance PEMFC for portable applications, i.e. automotive and low duty vehicles, requires membrane electrode assembly (MEA) to be durable under fast start up and shut downs, frequent starts and stops, and dynamic operation. Fuel cells also need to be competitive with gasoline internal combustion engines (ICE) to be economically accepted in the market [19]. Fuel cell research and development (R&D) could be able to successfully reduce the cost of automotive fuel cell more than 80% since 2002 [16]. However, on the road to implement the hydrogen and fuel cell technology a multiyear program has been developed by Department of Energy in United States [17]. The program activities have been planned based on four subprograms including; hydrogen production, hydrogen delivery, hydrogen storage and fuel cell technologies. Among outlined R&D activities by DOE, Fuel cell technology subprogram will focus on developing new materials, novel designs and fabrication methods for different components of a fuel cell including electrolyte, catalyst, gas diffusion media and bipolar plates. For instance, with respect to the development of more durable and active electro-catalysts, DOE has set cost

and durability targets for 2020 [17], as follow: less than $0.125 \text{ mg}_{\text{Pt}}\cdot\text{cm}^{-2}$ total platinum group metal loading (anode + cathode) and less than 40% loss in their initial performance under accelerated stress tests [20].

In the following, I will review required improvements of the membrane electrode assembly components to address the aforementioned performance shortcomings of PEMFC and URFC. Several other components must also be improved but are not discussed here as they are not the main focus of this thesis.

1.3.1 Performance and cost

As stated before in section 1.1.1, the key performance feature of a PEMFC is the amount of current density which can be drawn at a certain voltage. So kinetics of electrochemical half reactions (Eqs. (1-1) and (1-2)) are highly involved in determining the fuel cell performance output. Among these electrochemical half reactions, cathode ORR is six or more orders of magnitude slower than the anode HOR reaction [21]. Moreover, it is well known that the kinetics of electrochemical reactions (charge-transfer reactions) are highly dependent on the electrode material [22]. Accordingly, catalyst development activities are mainly focused on increasing the kinetics of the metal-catalyzed ORR reaction occurring at the cathode side of the MEAs [23, 24].

Nanoparticles of Platinum or Pt-transition metal alloys (i.e. PtCo [25], PtRu [26]) deposited onto pure carbon-based catalyst supports are currently implemented as electro-catalyst for PEMFCs [27]. Due to widespread use of Pt nanoparticles to catalyze the ORR both, its physicochemical and electrochemical properties are very critical to reach DOE 2020 performance and cost targets [18] by a total PGM loading of $0.125 \text{ mg}_{\text{Pt}}\cdot\text{cm}^{-2}$ [21].

Despite great progress achieved to effectively utilize platinum through using Pt-based colloidal nanostructures, e.g. Pt nanowires/nanotubes [28-30], there are still synthetic challenges to develop approaches with high-level controls of uniformity in size, shape and composition of desired Pt or Pt alloy based catalysts [23].

1.3.2 Durability

The proposed highly active Pt nanoparticles must also maintain their performance after 5000 h of operation for automotive fuel cell applications. Current technologically standard catalysts are Pt nanoparticles dispersed onto high surface area carbon blacks such as Vulcan XC-72R or Ketjen Black [31]. Although the current technology has been able to run fuel cell vehicles at the test fleets monitored by DOE (using a Pt loading of $0.4 \text{ mg}_{\text{Pt}}\cdot\text{cm}^{-2}$ or more on the cathode side) [21], its stability is still lower than 5000 hrs of operation and it loses the performance at high potentials. Among proposed mechanisms which can contribute to the degradation of the state of the art catalysts, Platinum dissolution/agglomeration and catalyst support degradation were identified to be the two most important contributors [27, 32-38].

Fig. 1.6 (a) demonstrates the role of electronic transport in Pt agglomeration through Ostwald type of growth or Ostwald ripening [36], whereas Fig. 1.6 (b) shows Pt dissolution due to carbon support corrosion.

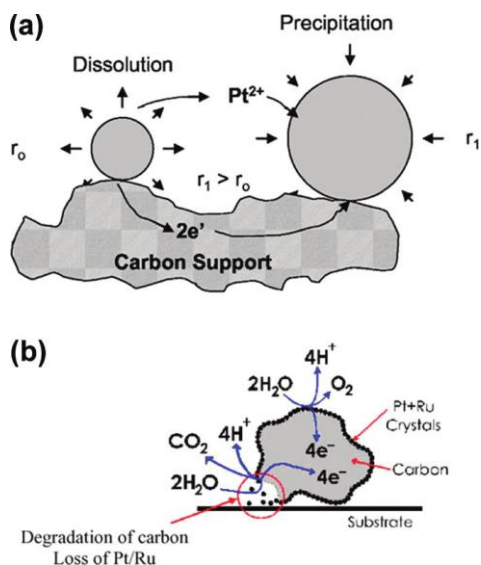


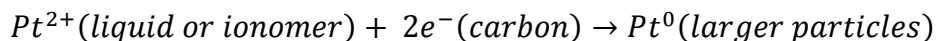
Figure 1.6. Schematic representation of Pt agglomeration and carbon corrosion, reprinted from ref. [32]. (a) Mechanism of Pt particle growth by dissolution/precipitation [36]; (b) Degradation of carbon supports and loss of noble-metals [39].

As shown in Fig. 1.6 (a), by considering a high concentration of free electrons in carbon support, the growth of Pt can be easily explained by Pt dissolution and precipitation as follow [36]:

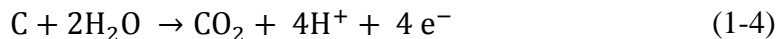
Dissolution



Precipitation



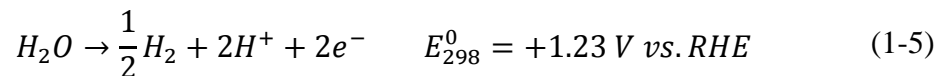
Moreover, during fuel cell operation specifically for conditions of dynamic load operation in automotive applications, the cathode catalyst will be introduced to high electrode potentials in the presence of oxygen. In these start up and shut down conditions (the voltage can go beyond 1.4V [32, 39]), carbon could experience a severe corrosion and oxidation with release of carbon dioxide according to the following equation [33, 40, 41]:



Not surprisingly, the conversion of carbon support to CO₂ (confirmed by doing gas analysis [40]) will cause the catalyst to lose its performance by losing Pt or Pt alloy nanoparticles, loss of Pt/Ru nanoparticles due to carbon corrosion has been shown schematically in Fig. 1.6(b). It has been also speculated that other mechanisms could also contribute to the failure of carbon black supported Pt catalysts [33, 42, 43]. For instance, chemical reduction of dissolved platinum ions in the ionomer phase by crossover H₂ molecules was also observed through examining cycled membrane electrode assemblies [43].

In a recent study of the degradation mechanisms of carbon-supported Pt catalysts [37], the formation of Pt oxide was also found to affect durability of carbon black supported Pt catalysts. Overall among different mechanisms which have been speculated to be responsible for the low durability of carbon black supported Pt catalysts, the corrosion of carbon black supports was identified to be the major contributor.

For URFC applications, on top of the corrosion of carbon based catalyst supports, it has been shown that the corrosion of carbon-based gas diffusion layers (regular hydrophobized carbon paper/clothes) could also contribute significantly to the failure of the MEAs [14]. For URFC applications, under water electrolysis mode, irreversible performance losses could arise from the corrosion of carbon based gas diffusion layers according to the following reactions [44]:



1.4 Constraints on material selection for MEA components

In general, the materials selection for MEA components should be based on an improvement in the efficiency of the whole cell. The overall fuel cell efficiency (η) is given by the following equation [6]:

$$\eta = \frac{nF(E_0 - IR_c)\alpha}{\Delta H} \quad (1-7)$$

Where n is the number of exchanged electrons, F is the Faraday constant, E_0 is the open circuit voltage, R_c is the area-specific resistivity of the cell components, and α is the fraction of fuel used. Eq. (1-7) clearly shows that minimizing the resistivity of the cell components can have a major impact on the overall efficiency. It has been shown that the combined area-specific resistivity (ASR) of the cell components (including MEA) should be below $0.5 \Omega \cdot \text{cm}^{-2}$ (and ideally approach $0.1 \Omega \cdot \text{cm}^{-2}$) to ensure high power densities, e.g. $1 \text{ kW} \cdot \text{kg}^{-1}$, mentioned for transport applications [6].

However, each component of the MEA has its own development criteria on being able to address the key challenges to the market success of PEMFCs. Among MEA components, finding a more durable and more active cathode catalysts for PEMFC applications and durable gas diffusion layers for URFC applications are under development and has been a focus of researcher in the last decade [45].

Because of the instability (low durability) of carbon based materials as a catalyst support under real PEMFC conditions, it is necessary to find an alternative way to catalyze the sluggish ORR reaction on the cathode side. The proposed alternative catalyst supports were achieved through adopting different strategies such as modifications on the current carbon based materials [46, 47]; development of support-less platinum catalysts and/or highly active Pt nanostructures [28, 48]; development of non-noble metal (non PGM) catalysts [49, 50]; and/or development of noncarbon materials [32]. In determining the best candidate to be used as a catalysts support there are a number of factors which are needed to be considered such as excellent electronic conductivity, high corrosion resistivity, high surface area, strong cohesive force to catalyst particles, and uniform particle size distribution [51]. Among the strategies which have been adopted to find alternative catalyst supports, despite astonishing progress achieved through synthesizing metal oxide based (particularly titanium dioxide based [52]) nanostructures as noncarbon catalyst supports [32], it seems to be unlikely for a carbon-free metal oxide based catalyst support to address all requirements (high electronic conductivity, high corrosion resistant, high surface area, and thermal stability) at the same time. Recently, a promising candidate as a catalyst support was identified to be a hybrid or composite of metal oxide based supports (high stability and strong metal-support interaction) with carbon blacks (high surface area and

high conductivity) [53-56]. However, their performances under real fuel cell conditions has not been tested yet and their electrochemical durabilities were not improved significantly versus pure carbon based catalysts supports.

With respect to the instability (low durability) of regular gas diffusion layers (carbon papers/clothes) for URFC applications, among proposed corrosion-resistant alternative GDLs [14, 15], commercially more promising results were obtained through coating corrosion-resistant bifunctional CLs onto carbon papers [57, 58]. The ideal corrosion resistant gas diffusion layer for URFC applications should also have a balanced hydrophilic/hydrophobic properties to operate effectively under both operation modes (electrolyser and fuel cell modes). Despite very promising results through spray coating bifunctional CLs onto carbon-based GDLs, the interface between the CL and gas diffusion layer was still prone to corrosion and is under development.

1.5 Objectives

The objectives of this thesis are twofold, to develop innovative methodologies to make durable and still active membrane electrode assemblies for PEMFCs and protect regular gas diffusion layers from corrosion under URFC applications.

To make durable and still active MEAs, this thesis mainly targeted the development of transition metal doped titanium dioxide based catalyst supports using an easily upscalable method. I also used transition metal doped titanium dioxide sols to create a more uniform corrosion-resistant coating onto regular carbon papers with potential applications in URFCs.

1.6 Outline of the dissertation

Chapter 2 describes how the corrosion resistance of regular carbon papers for URFC applications is increased. This has been done by developing a simple wet coating procedure to protect the interface between carbon papers and bifunctional CLs using a thin film of niobium-doped TiO₂. *Chapter 3* investigates the role of reducing agent to disperse Pt nanoparticles onto anatase phase Nb-doped TiO₂ nanofibers. *Chapter 4* reports an innovative method to address the low durability of carbon-black supported Pt catalysts in

PEMFCs that has been done by an in-situ reductive embedment of carbon into rutile phase Nb-doped TiO₂ nanofibers. The electrochemical stability and activity of both carbon-free and carbon-embedded nanofibers for oxygen reduction reaction in acidic conditions and the effects of heat treatment condition on the chemical processes happening at the surface of Nb-doped TiO₂ nanofibers were also presented in *Chapter 4*. *Chapter 5* focuses on the PEMFC performance evaluation of the MEAs employing composite-supported Pt catalysts and reports an innovative method to prepare cathode CLs with optimized PEMFC performances. The fuel cell performances of the developed Pt catalysts were characterized under real fuel cell conditions using a house-made fully automated fuel cell test station which has been designed and manufactured in the clean Powertrain Lab at the University of Windsor. The H₂/Air PEMFC performances of the MEAs employing composite-supported Pt catalysts on their cathode sides were further optimized though utilizing an innovative method for the preparation of their corresponding cathode CLs. Chapter 6 investigates the effect of catalyst component distribution on the PEMFC performances of composite-supported Pt catalysts. Electron microscopy and Raman mappings were used to investigate how Nafion and other catalyst layer components were distributed in both airsprayed and electrosprayed catalyst layers. Finally, Chapter 7 summarizes the significant findings, draws the conclusions, and suggests some applications of this work to Fuel Cell R&D for the future.

References

1. O'Hayre, R., et al., *Fuel Cell Fundamentals*. 2006, New York: John Wiley & Sons Inc.
2. Sigfusson, T.I., *Pathways to hydrogen as an energy carrier*. Philosophical Transactions of the Royal Society A: Mathematical, Physical and Engineering Sciences, 2007. **365**(1853): p. 1025-1042.
3. *Hydrogen Production Roadmap: Technology Pathways to the Future*. 2009.
4. O'Hayre, R.P., et al., *Fuel cell fundamentals*. 2006: John Wiley & Sons New York.

5. Kirubakaran, A., S. Jain, and R.K. Nema, *A review on fuel cell technologies and power electronic interface*. Renewable and Sustainable Energy Reviews, 2009. **13**(9): p. 2430-2440.
6. Steele, B.C.H. and A. Heinzel, *Materials for fuel-cell technologies*. Nature, 2001. **414**(6861): p. 345-352.
7. Wang, Y., et al., *A review of polymer electrolyte membrane fuel cells: Technology, applications, and needs on fundamental research*. Applied Energy, 2011. **88**(4): p. 981-1007.
8. Erdinc, O. and M. Uzunoglu, *Recent trends in PEM fuel cell-powered hybrid systems: Investigation of application areas, design architectures and energy management approaches*. Renewable and Sustainable Energy Reviews, 2010. **14**(9): p. 2874-2884.
9. Haile, S.M., *Fuel cell materials and components* ☆☆. Acta Materialia, 2003. **51**(19): p. 5981-6000.
10. Ramani, V., *Fuel Cells*. The Electrochemical Society Interface, 2006: p. 41-44.
11. O'Hayre, R., D.M. Barnett, and F.B. Prinz, *The Triple Phase Boundary: A Mathematical Model and Experimental Investigations for Fuel Cells*. Journal of The Electrochemical Society, 2005. **152**(2): p. A439-A444.
12. Pettersson, J., B. Ramsey, and D. Harrison, *A review of the latest developments in electrodes for unitised regenerative polymer electrolyte fuel cells*. Journal of Power Sources, 2006. **157**(1): p. 28-34.
13. Hwang, C.M., et al., *Influence of properties of gas diffusion layers on the performance of polymer electrolyte-based unitized reversible fuel cells*. International Journal of Hydrogen Energy, 2011. **36**(2): p. 1740-1753.
14. Ioroi, T., et al., *Influence of PTFE coating on gas diffusion backing for unitized regenerative polymer electrolyte fuel cells*. Journal of Power Sources, 2003. **124**(2): p. 385-389.

15. Wittstadt, U., E. Wagner, and T. Jungmann, *Membrane electrode assemblies for unitised regenerative polymer electrolyte fuel cells*. Journal of Power Sources, 2005. **145**(2): p. 555-562.
16. DOE, *Progress and accomplishments in hydrogen and fuel cell*. 2014. **<http://energy.gov/eere/fuelcells/downloads/progress-and-accomplishments-hydrogen-and-fuel-cells>**.
17. DOE, *Fuel cell technologies office multi-year research, development, and demonstration plan*. 2014. **<http://energy.gov/eere/fuelcells/downloads/fuel-cell-technologies-office-multi-year-research-development-and-22>**.
18. USDRIVE, *Fuel cell Technical Team Roadmap*. 2013. **<http://www.uscar.org/guest/teams/17/Fuel-Cell-Tech-Team>**.
19. *Fuel Cell Technologies Office Multi-Year Research, Development and Demonstration Plan*, U.S.D.o. Energy, Editor. 2012: Fuel Cell Technologies Office.
20. USDRIVE, *Fuel cell Tech team accelerated stress test and polarization curve protocol for PEMFCS*. 2013. **<http://www.uscar.org/guest/teams/17/Fuel-Cell-Tech-Team>**.
21. Debe, M.K., *Electrocatalyst approaches and challenges for automotive fuel cells*. Nature, 2012. **486**(7401): p. 43-51.
22. Marković, N.M. and P.N. Ross Jr, *Surface science studies of model fuel cell electrocatalysts*. Surface Science Reports, 2002. **45**(4–6): p. 117-229.
23. Peng, Z. and H. Yang, *Designer platinum nanoparticles: Control of shape, composition in alloy, nanostructure and electrocatalytic property*. Nano Today, 2009. **4**(2): p. 143-164.
24. Costamagna, P. and S. Srinivasan, *Quantum jumps in the PEMFC science and technology from the 1960s to the year 2000: Part I. Fundamental scientific aspects*. Journal of Power Sources, 2001. **102**(1–2): p. 242-252.

25. Antolini, E., *Formation of carbon-supported PtM alloys for low temperature fuel cells: a review*. *Materials Chemistry and Physics*, 2003. **78**(3): p. 563-573.
26. Steigerwalt, E.S., G.A. Deluga, and C.M. Lukehart, *Pt–Ru/Carbon Fiber Nanocomposites: Synthesis, Characterization, and Performance as Anode Catalysts of Direct Methanol Fuel Cells. A Search for Exceptional Performance*. *The Journal of Physical Chemistry B*, 2002. **106**(4): p. 760-766.
27. Wu, J., et al., *A review of PEM fuel cell durability: Degradation mechanisms and mitigation strategies*. *Journal of Power Sources*, 2008. **184**(1): p. 104-119.
28. Sun, S., et al., *A Highly Durable Platinum Nanocatalyst for Proton Exchange Membrane Fuel Cells: Multiarmed Starlike Nanowire Single Crystal*. *Angewandte Chemie International Edition*, 2011. **50**(2): p. 422-426.
29. Lee, E.P., et al., *Growing Pt Nanowires as a Densely Packed Array on Metal Gauze*. *Journal of the American Chemical Society*, 2007. **129**(35): p. 10634-10635.
30. Chen, Z., et al., *Supportless Pt and PtPd Nanotubes as Electrocatalysts for Oxygen-Reduction Reactions*. *Angewandte Chemie*, 2007. **119**(22): p. 4138-4141.
31. Soboleva, T., et al., *On the Micro-, Meso-, and Macroporous Structures of Polymer Electrolyte Membrane Fuel Cell Catalyst Layers*. *ACS Applied Materials & Interfaces*, 2010. **2**(2): p. 375-384.
32. Wang, Y.-J., D.P. Wilkinson, and J. Zhang, *Noncarbon Support Materials for Polymer Electrolyte Membrane Fuel Cell Electrocatalysts*. *Chemical Reviews*, 2011. **111**(12): p. 7625-7651.
33. Zhang, S., et al., *A review of platinum-based catalyst layer degradation in proton exchange membrane fuel cells*. *Journal of Power Sources*, 2009. **194**(2): p. 588-600.
34. Huang, S.-Y., et al., *Development of a Titanium Dioxide-Supported Platinum Catalyst with Ultrahigh Stability for Polymer Electrolyte Membrane Fuel Cell Applications*. *Journal of the American Chemical Society*, 2009. **131**(39): p. 13898-13899.

-
35. Yu, X. and S. Ye, *Recent advances in activity and durability enhancement of Pt/C catalytic cathode in PEMFC: Part II: Degradation mechanism and durability enhancement of carbon supported platinum catalyst*. Journal of Power Sources, 2007. **172**(1): p. 145-154.
 36. Virkar, A.V. and Y. Zhou, *Mechanism of Catalyst Degradation in Proton Exchange Membrane Fuel Cells*. Journal of The Electrochemical Society, 2007. **154**(6): p. B540-B547.
 37. Zhang, Y., et al., *Study of the degradation mechanisms of carbon-supported platinum fuel cells catalyst via different accelerated stress test*. Journal of Power Sources, 2015. **273**(0): p. 62-69.
 38. Hitchcock, A.P., et al., *Carbon corrosion of proton exchange membrane fuel cell catalyst layers studied by scanning transmission X-ray microscopy*. Journal of Power Sources, 2014. **266**(0): p. 66-78.
 39. Knights, S.D., et al., *Aging mechanisms and lifetime of PEFC and DMFC*. Journal of Power Sources, 2004. **127**(1-2): p. 127-134.
 40. Baumgartner, W.R.R., et al., *Electrocatalytic Corrosion of Carbon Support in PEMFC at Fuel Starvation*. ECS Transactions, 2006. **3**(1): p. 811-825.
 41. Taniguchi, A., et al., *Analysis of electrocatalyst degradation in PEMFC caused by cell reversal during fuel starvation*. Journal of Power Sources, 2004. **130**(1-2): p. 42-49.
 42. Xu, H., R. Kunz, and J.M. Fenton, *Investigation of Platinum Oxidation in PEM Fuel Cells at Various Relative Humidities*. Electrochemical and Solid-State Letters, 2007. **10**(1): p. B1-B5.
 43. Ferreira, P.J., et al., *Instability of Pt/C Electrocatalysts in Proton Exchange Membrane Fuel Cells: A Mechanistic Investigation*. Journal of The Electrochemical Society, 2005. **152**(11): p. A2256-A2271.

44. Ralph, T.R., S. Hudson, and D.P. Wilkinson, *Electrocatalyst Stability In PEMFCs And The Role Of Fuel Starvation And Cell Reversal Tolerant Anodes*. ECS Transactions, 2006. **1**(8): p. 67-84.
45. Jiang, S.P. and P.K. Shen, *Nanostructured and advanced materials for fuel cells*. The Advances in Materials Science and Engineering, ed. S. Zhang. 2014: CRC Press.
46. Zana, A., et al., *Core-shell TiO₂@C: towards alternative supports as replacement for high surface area carbon for PEMFC catalysts*. Electrochimica Acta, 2014. **139**(0): p. 21-28.
47. Xie, T., et al., *Development of Highly Active and Durable Hybrid Cathode Catalysts for Polymer Electrolyte Membrane Fuel Cells*. Journal of The Electrochemical Society, 2014. **161**(14): p. F1489-F1501.
48. Galbiati, S., A. Morin, and N. Pauc, *Supportless Platinum Nanotubes Array by Atomic Layer Deposition as PEM Fuel Cell Electrode*. Electrochimica Acta, 2014. **125**(0): p. 107-116.
49. Tran, P.D., et al., *A noble metal-free proton-exchange membrane fuel cell based on bio-inspired molecular catalysts*. Chemical Science, 2015. **6**(3): p. 2050-2053.
50. Byon, H.R., J. Suntivich, and Y. Shao-Horn, *Graphene-Based Non-Noble-Metal Catalysts for Oxygen Reduction Reaction in Acid*. Chemistry of Materials, 2011. **23**(15): p. 3421-3428.
51. Chan, K.-Y., et al., *Supported mixed metal nanoparticles as electrocatalysts in low temperature fuel cells*. Journal of Materials Chemistry, 2004. **14**(4): p. 505-516.
52. Abdullah, N. and S.K. Kamarudin, *Titanium dioxide in fuel cell technology: An overview*. Journal of Power Sources, 2015. **278**(0): p. 109-118.
53. Wang, Y.-J., et al., *Ta and Nb co-doped TiO₂ and its carbon-hybrid materials for supporting Pt-Pd alloy electrocatalysts for PEM fuel cell oxygen reduction reaction*. Journal of Materials Chemistry A, 2014. **2**(32): p. 12681-12685.

54. Ignaszak, A., et al., *Carbon–Nb_{0.07}Ti_{0.93}O₂ composite supported Pt–Pd electrocatalysts for PEM fuel cell oxygen reduction reaction*. *Electrochimica Acta*, 2012. **75**(0): p. 220-228.
55. Senevirathne, K., et al., *Nb-doped TiO₂/carbon composite supports synthesized by ultrasonic spray pyrolysis for proton exchange membrane (PEM) fuel cell catalysts*. *Journal of Power Sources*, 2012. **220**(0): p. 1-9.
56. Wang, Y.-J., et al., *Synthesis of Pd and Nb–doped TiO₂ composite supports and their corresponding Pt–Pd alloy catalysts by a two-step procedure for the oxygen reduction reaction*. *Journal of Power Sources*, 2013. **221**(0): p. 232-241.
57. Huang, S.-Y., et al., *Development of supported bifunctional oxygen electrocatalysts and corrosion-resistant gas diffusion layer for unitized regenerative fuel cell applications*. *Journal of Power Sources*, 2012. **198**(0): p. 23-29.
58. Chen, G., et al., *Gas diffusion layer with titanium carbide for a unitized regenerative fuel cell*. *Electrochimica Acta*, 2010. **55**(28): p. 8801-8807.

CHAPTER 2

Oxidative Treatment to Improve Coating and Electrochemical Stability of Carbon Fiber Paper with Niobium Doped Titanium Dioxide Sols for Potential Applications in Fuel Cells

2.1 Introduction

Direct conversion of chemical energy into electrical energy in fuel cells has been broadly developed over several decades because it promises a clean and reliable alternative to combustion engines. The unitized regenerative fuel cell (URFC) is a rather recent technology among the many different kinds of fuel cells, which includes electrolyser and fuel cell in one unit [1]. Its further development is presently limited by the low stability of the bifunctional oxygen electrode for both reduction of oxygen and oxidation of water [2]. Particularly problematic is the commonly used hydrophobized carbon paper (or cloth) as gas diffusion backing (GDB) layer because it quickly corrodes at the high potentials of the oxygen electrode in URFCs [1].

The replacement of carbon paper by more corrosion resistant materials such as titanium fibers [3] and foams [4] has been demonstrated but they cannot compete with the weight and cost advantages of carbon paper. Commercially more promising appears to be the chemical modification of carbon papers. Song et al. [5] and Huang et al. [6] reported a high performance URFC based on a novel bifunctional oxygen electrode that consists of a corrosion-resistant carbon-based gas diffusion layer. They showed that highly active catalysts, such as IrO₂, react with the intermediate free radical oxygen species to less reactive oxygen molecules before they can reach the carbon based GDB layer. IrO₂ and similar coatings of iridium titanium nitride [6] and titanium carbide [7] were spray coated as powders to generate microporous layers on top of carbon paper. Consequently, the interface between the catalyst layer and GDB layer is still prone to corrosion and requires protection of the carbon material.

A possible alternative approach is the direct coating of carbon paper fibers with a corrosion resistant metal oxide layer but this has not been attempted, to the best of our knowledge, and may be challenging due to the hydrophobic nature of the carbon surface and incomplete coating of all carbon fibers. Commercially most promising is the coating with titanium dioxide because of its low cost, low toxicity, high resistance to chemical and photo induced corrosion, and high thermal stability. TiO₂ is widely used not only as white pigment but also as semiconductor in, for example, photovoltaic [8], catalysis [9], and

biomedical applications [10]. Most interesting as semiconductor is the anatase phase of TiO₂ with a band gap of 3.2 eV [11]. Its electronic conductivity can be increased by the introduction of appropriate dopants, such as Nb⁺⁵ [12]. Doping with Nb has also been shown to thermally stabilize the anatase phase and impede grain growth [13]. In fact, highly stable Pt/Nb-doped TiO₂ catalysts have been applied in PEM fuel cells [14, 15]

Our focus is on TiO₂/carbon hybrid materials that combine the advantages of both titanium dioxide and carbon paper [16, 17]. The most cost effective deposition of TiO₂ on carbon paper is deposition from solution, when compared to sputtering [18] and evaporation [19] techniques, but the lack of compatibility between the polar deposition solution and the rather inert and non-polar surface of the carbon paper remains a challenge [20, 21]. Presented here is an oxidative pretreatment of the surface of carbon paper that generates polar groups (e.g. OH, C=O, and COOH) for direct dip coating with Nb-doped TiO₂ sols. This appears to be the first report on the oxidative modification of carbon papers/clothes/felts for a better coating with sol-gels, to the best of our knowledge, but has been widely applied in the functionalization of carbon nanotubes [20, 22]. The presented coating methodology is versatile and not limited to the fabrication of corrosion resistant GDB layers for unitized regenerative fuel cells.

2.2 Experimentals

Figure 2.1 shows the schematic representation of the procedure for oxidative functionalization of carbon paper and its coating with Nb-doped TiO₂. This scheme will be explained in sections 2.2.1 and 2.2.2 and then physical and electrochemical characterization techniques will be explained in sections 2.2.3 and 2.2.4, respectively.

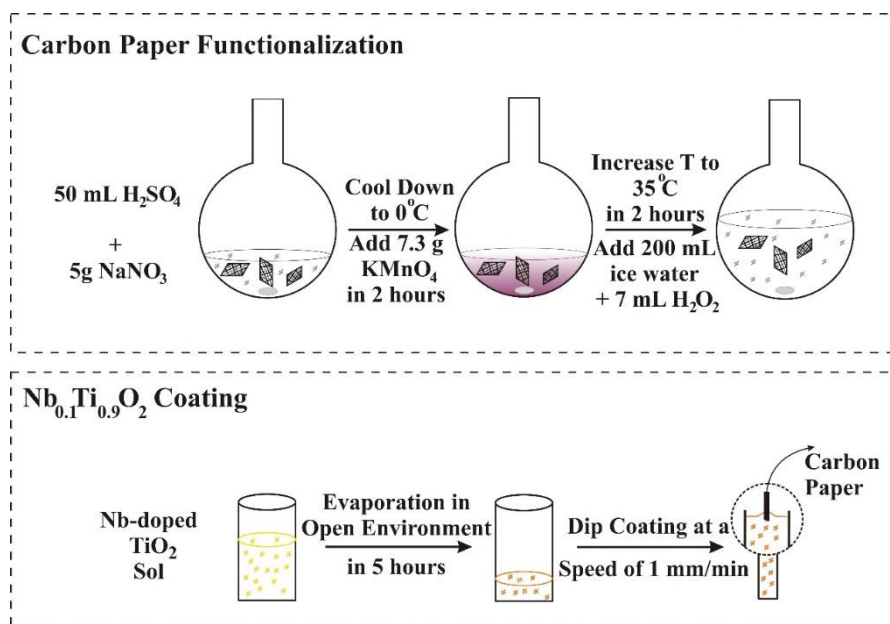


Figure 2.1. Schematic representation of the procedure for oxidative functionalization of carbon paper and its coating with Nb-doped TiO₂.

2.2.1 Preparation of functionalized carbon paper

The surface oxidation of porous carbon paper (Spectracarb™ 2050A-0850 Engineering Fibers Tech. Shelton, CT) was achieved by applying a method previously reported for the oxidation of other carbon materials [23]. Three pieces of carbon fiber papers (15 mm × 15 mm) were thoroughly washed with acetone, dried, and submerged in 50 mL of concentrated sulfuric acid. NaNO₃ (5 g) was added to the sulfuric acid and stirred for an hour before the mixture was cooled down to 0 °C in an ice bath and 7.3 g of KMnO₄ were added in small portions over a period of 2 hours. When the addition was completed the temperature of the stirred mixture was increased to 35 °C for another 2 hours. Finally, the oxidation was completed by the addition of 200 mL of ice water and 7 mL of H₂O₂ (30%). The oxidized carbon paper was thoroughly washed with aqueous HCl (3%) followed by deionized water and dried in a vacuum oven at 50 °C for 24 hours. In the following the untreated carbon paper is denoted as UCP and the oxidatively functionalized carbon paper as FCP.

2.2.2 Preparation of Nb_{0.1}Ti_{0.9}O₂ coating on carbon paper

Nb-doped TiO₂ thin films on carbon paper were prepared by dip coating of the carbon paper into a stabilized Nb-doped TiO₂ sol gel [24, 25]. Acetylacetone was used as stabilizing agent to prevent the rapid hydrolysis of alkoxide precursors with water. Titanium tetraisopropoxide (8 mL, 27 mmol) and niobium ethoxide (680 μ L, 2.7 mmol) (calculated ratio for a final composition of Nb_{0.1}Ti_{0.9}O₂) were added to a vigorously stirred solution of 1.25 mL of acetylacetone in 50 mL of anhydrous ethanol under N₂ atmosphere. The solution was stirred for 2 hours and then acidified to a pH of about 3 by the addition of 8.5 mL of concentrated HCl. Stirring was continued with the solution being open to the environment until 70% of weight loss has occurred due to evaporation of the solvents and the colour of the solution turned to deep yellow (approximately 5 hours). FCP and UCP were submerged into this solution for 1 min and then pulled out vertically at a speed of 1 mm/min. The coated carbon papers were dried in air at 25 °C for 36 hours and then heated to 450 °C at a heating rate of 20 °C/h under N₂ to initiate crystallization of the metal oxide. Nb-doped TiO₂ coated untreated and functionalized carbon papers were denoted as Nb-TiO₂-UCP and Nb-TiO₂-FCP, respectively.

2.2.3 Physical Characterization

XRD measurements were performed on a Bruker D8 Discover diffractometer equipped with a Hi-Star area detector and GADDS software package. The tube is operated at 40 kV and 40 mA with CuK α 1 monochromatized radiation source (wavelength = 1.54187 Å) and an initial beam diameter of 0.5 mm was used. The carbon paper samples were measured in transmission mode and diffraction data were recorded between $2\theta = 20^\circ$ - 55° with θ defined as diffraction angle in degrees.

Contact angle measurements were conducted with a Ramé-Hart goniometer (Model 200) equipped with a CCD camera and an automatic dispenser of water (0.2 μ L). Fourier transform infrared (FTIR) spectra were taken with an ALPHA spectrometer (Bruker Inc.) in the attenuated total reflection (ATR) mode over a spectral range with wave number of 4000 to 400 cm⁻¹. Raman spectroscopy was conducted with a Renishaw inVia Raman microscope by using an argon laser with an excitation wavelength of 514.5 nm and an

objective lens of 50x. Intact carbon paper samples were used for both Raman and FTIR spectroscopy measurements. The morphology of Nb-doped TiO₂ coated carbon paper samples was examined by scanning electron microscopy (FEI Quanta 200 FEG equipped with an energy-dispersive spectrometer EDAX SiLi Detector) in backscatter mode at 15 kV.

2.2.4 Electrochemical Characterization

A conventional three-electrode system (BASi C3) was used for cyclic voltammetry studies. Pt wire and saturated Ag/AgCl electrodes were used as counter and reference electrodes, respectively, and a piece of carbon paper under investigation with an area of 0.5 cm² served as the working electrode. All cyclic voltammetry measurements were conducted in Ar saturated solutions of 0.5 M H₂SO₄ between -0.2 V and 1.2 V versus Ag/AgCl at a scan rate of 50 mV s⁻¹. Sample surfaces were cleaned by running cyclic voltammetry for 20 times in the same solution between -0.2 V and 1.2 V versus Ag/AgCl at a scan rate of 100 mV s⁻¹. A constant voltage of 1.2 V versus Ag/AgCl was applied to the working electrode for up to 72 hours to investigate their corrosion resistance. The degree of corrosion after certain periods of time was monitored by measuring the charge per unit area (mC·cm⁻²) produced by Quinone/Hydroquinone (Q/HQ) redox couple based on the following equation [26, 27]:

$$Q/HQ \text{ charge} = \left(\int_{V_a}^{V_b} i \cdot dV \right) / \dot{V} \quad (2-1)$$

where V_a and V_b define the voltage window of the Q/HQ redox reaction at a scan rate of $\dot{V} = 50$ mV/s and i is the current per unit area produced by Q/HQ redox reaction excluding the pseudo-capacitance current.

2.3 Results and Discussion

2.3.1 Effects of oxidative treatment

The oxidative functionalization of the carbon paper is expected to increase the hydrophilicity of its surface, which was conveniently monitored by the measurement of surface contact angles of water drops (Fig. 2.2). Carbon paper, as purchased, has a hydrophobic surface as illustrated by a contact angle of 124° (Fig. 2.2a). This angle changes to 0° after oxidative treatment, confirming the formation of a hydrophilic surface (Fig. 2.2b).

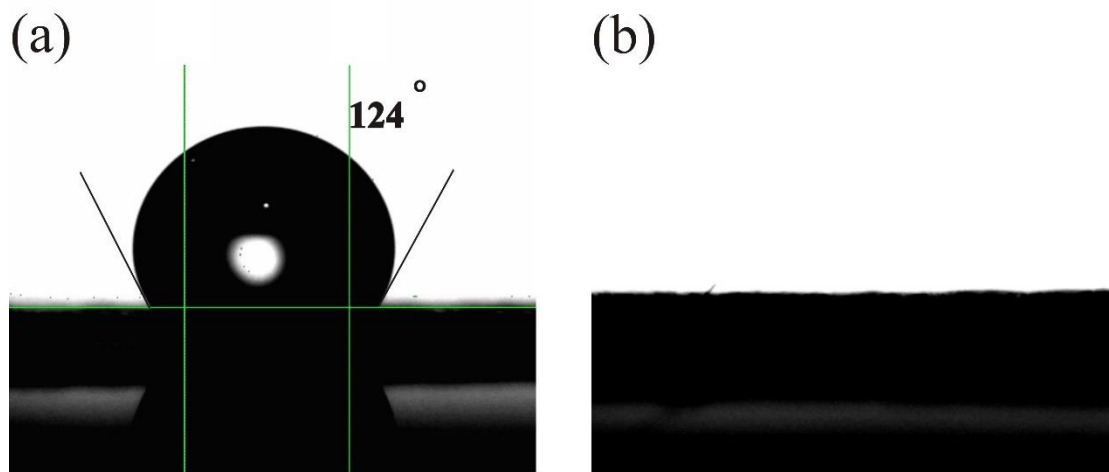


Figure 2.2. Water contact angle of carbon paper. (a) before oxidative functionalization; (b) after oxidative functionalization.

Oxidative functionalization of the carbon paper with alcoholic and carbonyl groups was also confirmed by Infrared (IR) and Raman spectroscopy (Figs. 2.3a and 2.3b, respectively). FTIR spectra of carbon paper after oxidative functionalization clearly exhibit additional absorption bands (Fig. 2.3a). Absorptions at wave numbers of 1005 cm⁻¹ and 1234-1170 cm⁻¹ are assigned to C-O stretching vibrations [28], absorptions at 1705 cm⁻¹ and 1726 cm⁻¹ are attributed to C=O stretching vibrations of carbonyl groups [29-31], and

the absorption at 1400 cm⁻¹ is assigned to the O-H bending deformation of carboxylic acid and phenolic groups [28, 30, 32].

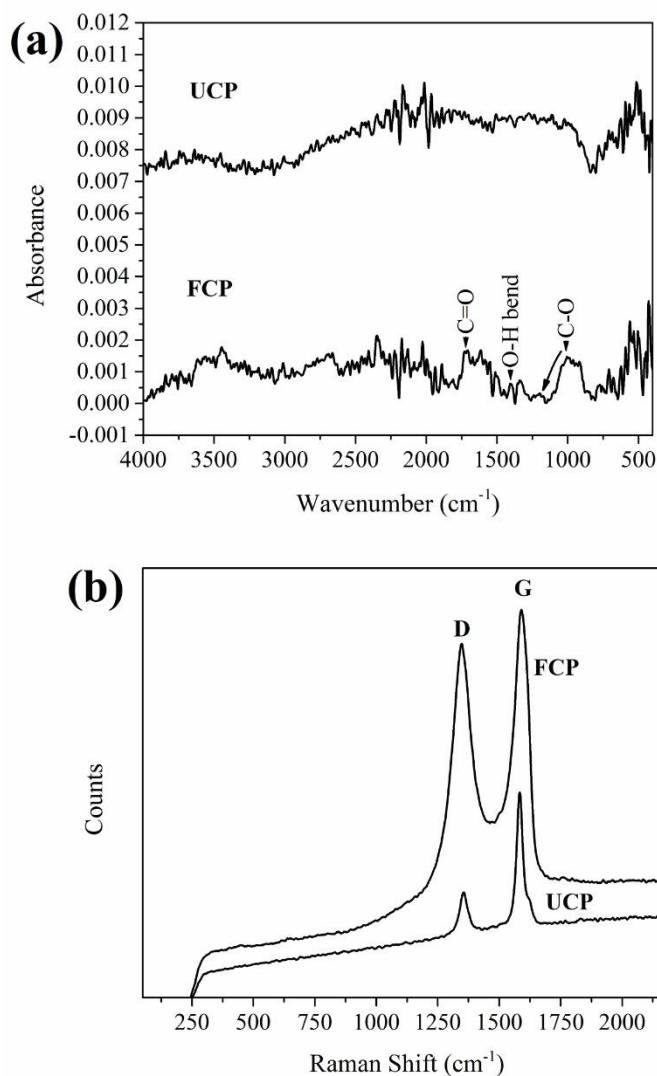


Figure 2.3. Surface characterization of UCP and FCP. (a) FTIR and (b) Raman spectroscopy.

Information about changes to the carbon framework during oxidative functionalization is best obtained by Raman spectroscopy (Fig. 2.3b). Raman spectra of both untreated

carbon paper (UCP) and functionalized carbon paper (FCP) show the characteristic absorption bands of graphite at wave numbers of 1580 cm⁻¹ (G-band) and at 1350 cm⁻¹ (D-band). The G-band is assigned to in plane vibrations of the sp² carbon framework and the D-band (disorder band) is associated with carbon atoms at edges and sp³ carbons [33, 34]. The observed increase in intensity of the D-band relative to the G-band (D/G ratio increases from 0.56 to 0.93) after oxidative functionalization is consistent with the expected increase in sp³ and edge carbons [34, 35]. However, the Raman spectra also confirm that most of the sp² carbon framework remains intact during oxidative functionalization, which is independently supported by XRD data discussed below (see Figure 2.5). These results clearly demonstrate that the oxidation treatment did not destroy the sp² carbon framework, which is important for fuel cell applications.

2.3.2 Nb-doped TiO₂ coating on carbon paper

Characterized UCP and FCP samples were then coated with a sol-gel of Nb-doped TiO₂ and heated to 450 °C under nitrogen to give samples of Nb-TiO₂-UCP and Nb-TiO₂-FCP, respectively.

2.3.2.1 Wettability

Contact angles with water were measured to compare the relative hydrophilicity of the surfaces (Fig. 2.4). As expected, the hydrophilic TiO₂ coating lowers the contact angle of Nb-TiO₂-UCP to 85° in comparison to 124° observed for UCP whereas the contact angles of FCP and Nb-TiO₂-FCP are both 0°. Surprising, however, is the large difference in contact angles between Nb-TiO₂-UCP and Nb-TiO₂-FCP, which must be caused by the incomplete coating on the surface of UCP and thus the larger area of the hydrophobic carbon surface exposed to water.

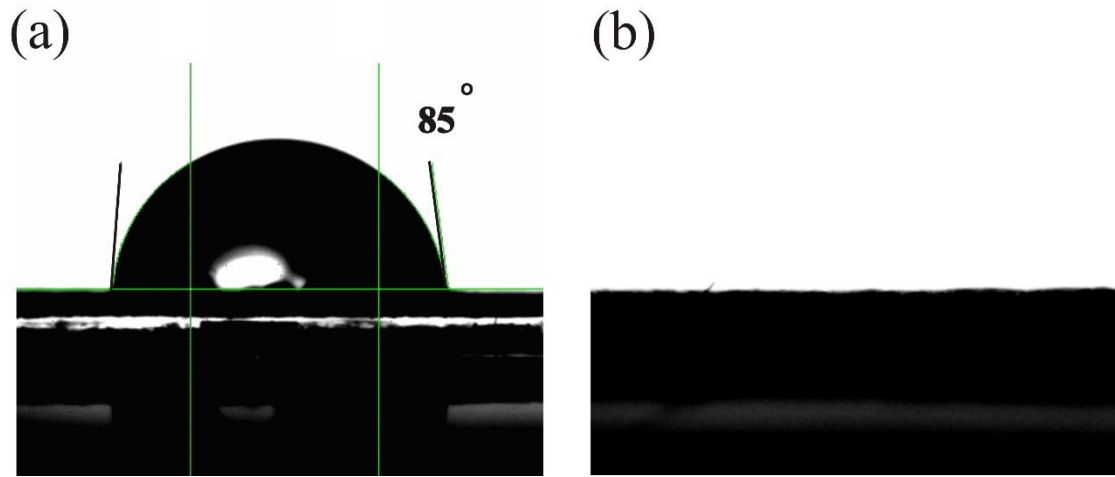


Figure 2.4. Water contact angle of Nb-doped TiO₂ coated carbon papers. (a) Nb-TiO₂-UCP; (b) Nb-TiO₂-FCP.

2.3.2.2 Structure and morphology

Crystallinity and morphology of the Nb-doped TiO₂ coatings were studied by X-ray diffraction (XRD) (transmission mode) and scanning electron microscopy (SEM) (Figs. 2.5 and 2.6). Figure 2.5a shows the presence of strong reflections of the graphitic framework at $2\theta = 27^\circ$ and 44° which verifies the persistence of the predominantly graphitic structure of the carbon paper [36]. The diffraction patterns of Nb-doped TiO₂ coated samples (Figures 2.5b and 2.5c) show the existence of peaks corresponding to (101), (004), (200), (105), and (211) crystallographic planes which were identified as the crystal of anatase phase of TiO₂. Furthermore, the absence of corresponding peaks for Nb oxide confirms an incorporation of Nb into the TiO₂ matrix (Figures 2.5b and 2.5c).

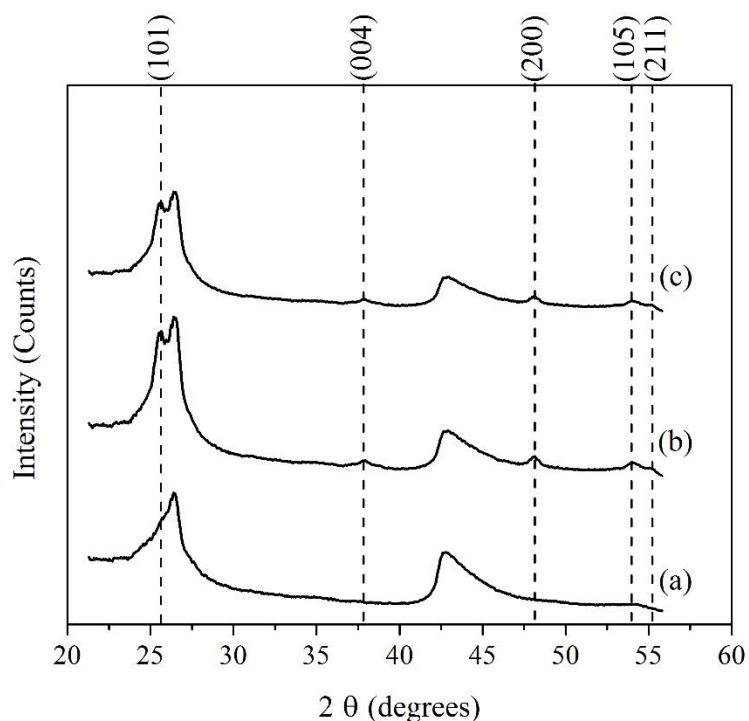


Figure 2.5. X-ray diffraction patterns of different samples. (a) FCP; (b) Nb-doped-FCP; (c) Nb-TiO₂-UCP.

Morphological differences of the TiO₂ coatings of Nb-TiO₂-UCP and Nb-TiO₂-FCP are clearly revealed by SEM studies (Figure 2.6). Both samples contain chunks of TiO₂ but the Nb-TiO₂-FCP sample contains evenly coated carbon fibres (compare Figures 2.6c and 2.6f). This result is in agreement with contact angle measurements described earlier (Figures 2.2 and 2.4) and consistent with our expectation that the carbon surface functionalized with more hydroxyl and carbonyl groups interacts better with the hydrophilic TiO₂ sol. A higher content of Ti at the surface of Nb-TiO₂-FCP in comparison to Nb-TiO₂-UCP is also confirmed by energy dispersive spectroscopy (EDS) that gives Ti contents of 12.77 wt% and 7.17 wt%, respectively. However, the total content of TiO₂ taken by Nb-TiO₂-UCP is 25% larger than that for Nb-TiO₂-FCP. The total content of TiO₂ was simply calculated by weighing either UCP or FCP samples, before and after dipping into the coating solution. This confirms that Nb-TiO₂-FCP is better coated on the surface

with less TiO₂ taken. This difference in the amount of TiO₂ taken is because of the larger chunks of TiO₂ between the fibers in UCP than FCP.

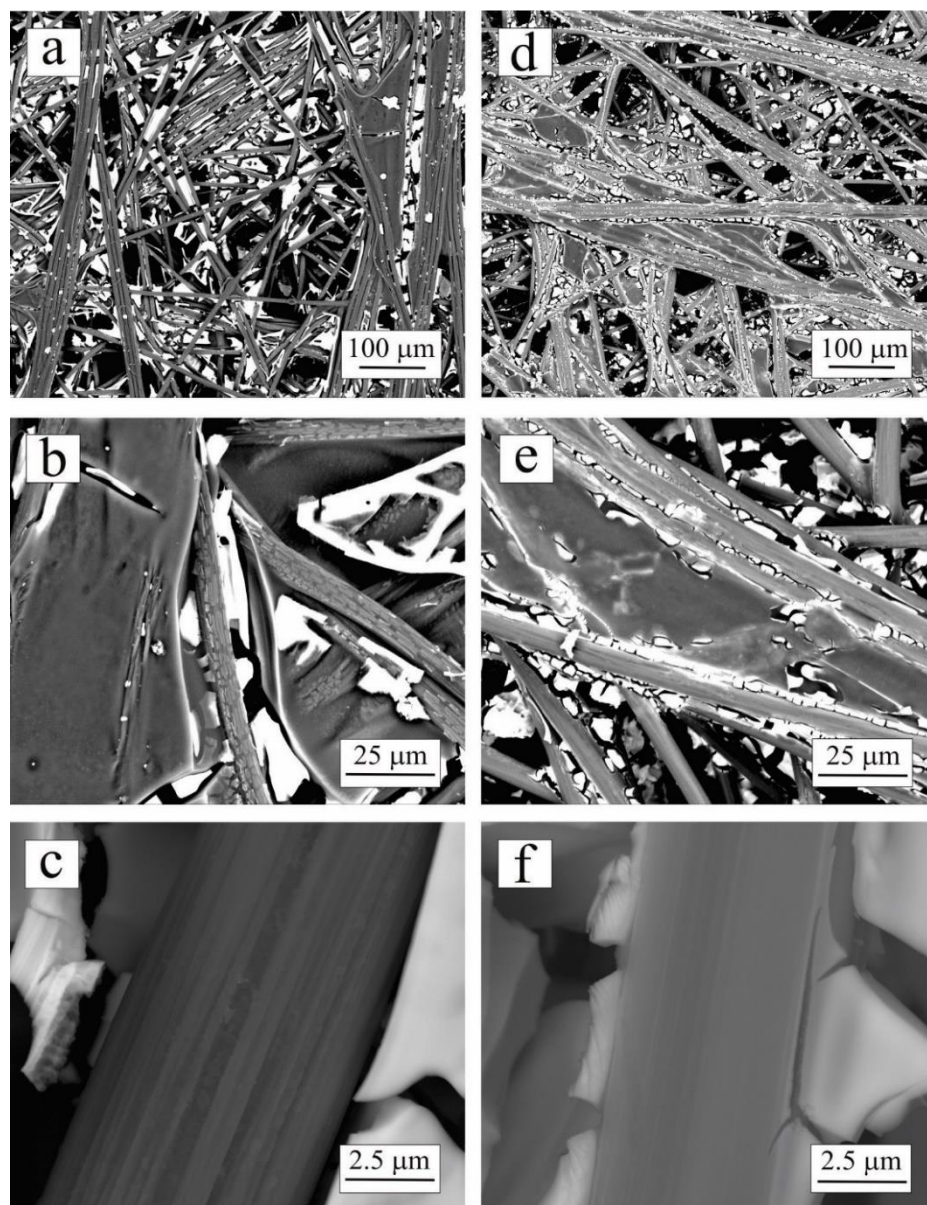


Figure 2.6. FE-SEM images of different samples at different magnifications. (a-c) Nb-TiO₂-CP, (d-f) Nb-TiO₂-FCP.

Optimizations in terms of concentration and viscosity of the deposition solution were also conducted at different amounts of weight loss percentage through evaporation, e.g. 30%, 40%, 70%, and 80%, and increasing the exposure time in the sol to determine the optimum combination to achieve a uniform coating on FCP. Figure 2.7a exemplifies the results at weight losses of the deposition solution lower than 70% ,e.g. 60%, and it demonstrates that the FCP has been less coated than the case for 70% weight loss (Figure 2.6e). EDS results show the Ti contents of 5.39 wt% and 12.77 wt% for 60% and 70% weight loss samples, respectively. The spots indicated by arrows in Figure 2.7b on the surface of FCP represent the locations where Nb-doped TiO₂ is accumulated while the rest is mostly not coated. On the other hand, Figure 2.7c and 2.7d clearly shows that the coating achieved by increasing the exposure time in the sol was also not effective. It create thicker and more complete TiO₂ coatings but the layers delaminated from the fibers during the calcination step, probably due to the different thermal expansion of Nb-doped TiO₂ and carbon paper. Therefore simply by comparing Figures 2.7, and 2.6d-f we can conclude that 70% weight loss is the optimum case among the cases investigated.

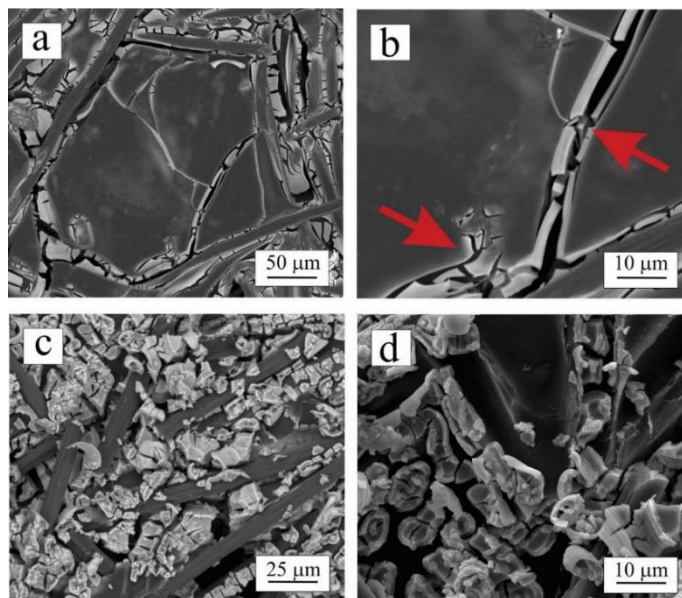


Figure 2.7. FE-SEM images of different Nb-TiO₂-FCP samples at different magnifications. (a) and (b) coated after 60% weight loss of the coating solution; (b) and (c) exposed to the sol for about 7 hours (during the entire weight reduction process of the sol).

2.3.2.3 Interaction between Nb-doped TiO₂ coating and carbon surface

The presence of a Nb-doped TiO₂ coating was also confirmed by infrared (IR) and Raman spectroscopy (Fig. 2.8). Both FTIR spectra of Nb-TiO₂-UCP and Nb-TiO₂-FCP show the characteristic broad absorption band for TiO₂ between wave numbers of 1000 cm⁻¹ and 400 cm⁻¹. A comparison with the IR spectrum of pristine Nb-doped TiO₂ reveals a distinct broadening of the absorption at 440 cm⁻¹ towards larger wave numbers in the spectra of Nb-TiO₂-UCP and Nb-TiO₂-FCP (Fig. 2.8b). This shift is reasoned with a contribution of Ti-O-C vibration modes that are centered at about 620 cm⁻¹ and their combination bands with the vibration mode of the Ti-O-Ti fragment at about 440 cm⁻¹ [37]. The appearance of this broadening towards 620 cm⁻¹ has been interpreted as evidence for the covalent interactions between TiO₂ and the carbon substrate [16]. This broadening is more pronounced in the Nb-TiO₂-FCP than in the Nb-TiO₂-UCP sample, which agrees with the better coating of FCP observed by SEM and the fact that oxidized surface of FCP contains many more functional groups that react with the TiO₂ sol.

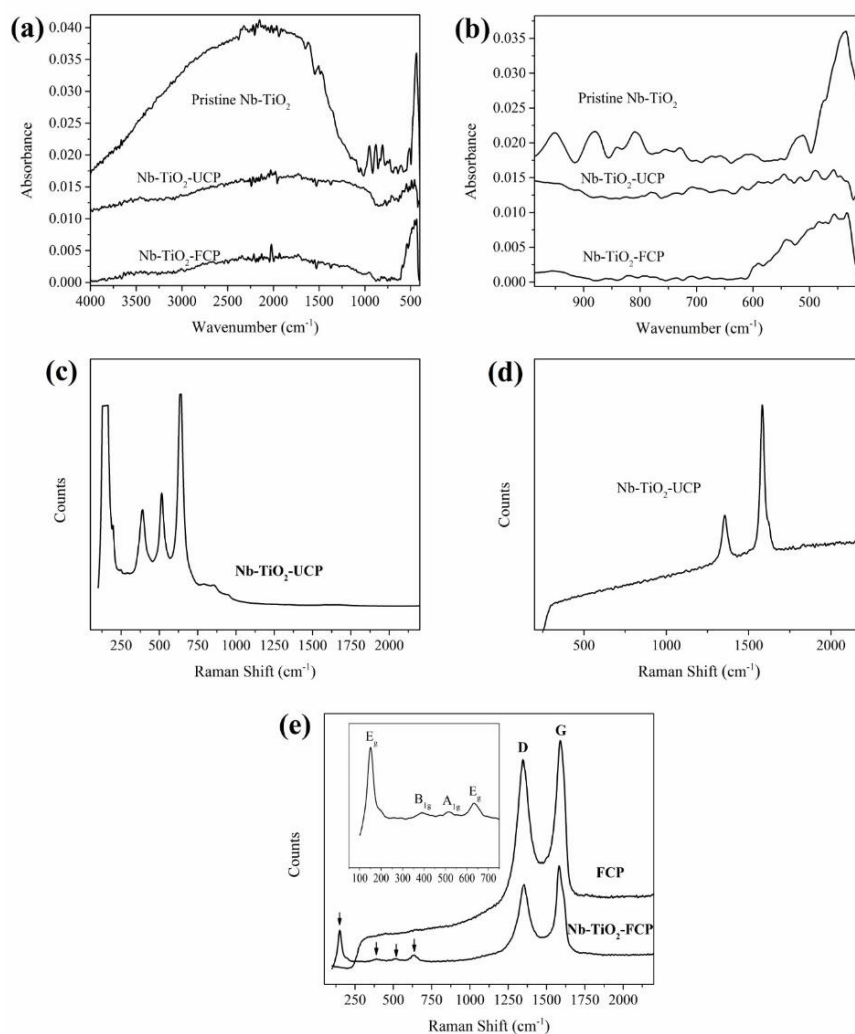


Figure 2.8. Surface characterization by FTIR and Raman spectroscopy. (a) and (b) FTIR spectra of Nb-doped TiO₂, Nb-TiO₂-UCP, and Nb-TiO₂-FCP; (c) and (d) Raman spectra of Nb-TiO₂-UCP taken at different locations; (e) Raman spectra of Nb-TiO₂-FCP.

The Raman spectra of the coated samples were taken at multiple locations to probe for spatial differences with a spot size of 1 μm². No dependence on location was observed for the Nb-TiO₂-FCP sample that always shows both, the characteristic absorptions of the carbon substrate between wave numbers of 1250 and 1650 cm⁻¹ (D- and G-bands) and the anatase phase of TiO₂ (Fig. 2.8e). The Vibrational peaks centered at 149 cm⁻¹, 389 cm⁻¹, 516 cm⁻¹, and 634 cm⁻¹ are well consistent with E_g, B_{1g} and A_{1g} characteristic peaks of the

anatase phase of TiO₂ (see Fig. 2.8e inset) [11, 38]. In contrast, Raman spectra of Nb-TiO₂-UCP sample either showed the absorptions of the anatase phase of TiO₂ or the carbon substrate (Figs. 2.8c and 2.8d, respectively) but never both absorptions together. This is another indication of an uneven coating of UCP and a more uniform coating of FCP. Also of significance is the broadening of the TiO₂ absorptions in the Nb-TiO₂-FCP sample when compared with Nb-TiO₂-UCP. This peak broadening has been attributed to a lower degree of crystallinity (reduced lattice vibration) due to the covalent bonding of TiO₂ to the surface of the oxidized carbon paper [39].

2.3.3 Electrochemical stability

All four samples UCP, FCP, Nb-TiO₂-UCP, and Nb-TiO₂-FCP were studied by cyclic voltammetry (CV) to probe their redox properties and potential for application in URFCs (Fig. 2.9). CV measurements were performed in Ar saturated solutions of aqueous 0.5 M H₂SO₄ between -0.2 V and 1.2 V (versus Ag/AgCl) at a scan rate of 50 mV s⁻¹ to simulate the water electrolysis reaction in URFC applications [5, 40]. The increase in surface oxidation of the carbon paper was evaluated based on an increase in intensity of the redox peaks of the Q/HQ couple at a half potential of about 0.4 V versus Ag/AgCl [40-42] and an increase in pseudo-capacitive current [43, 44].

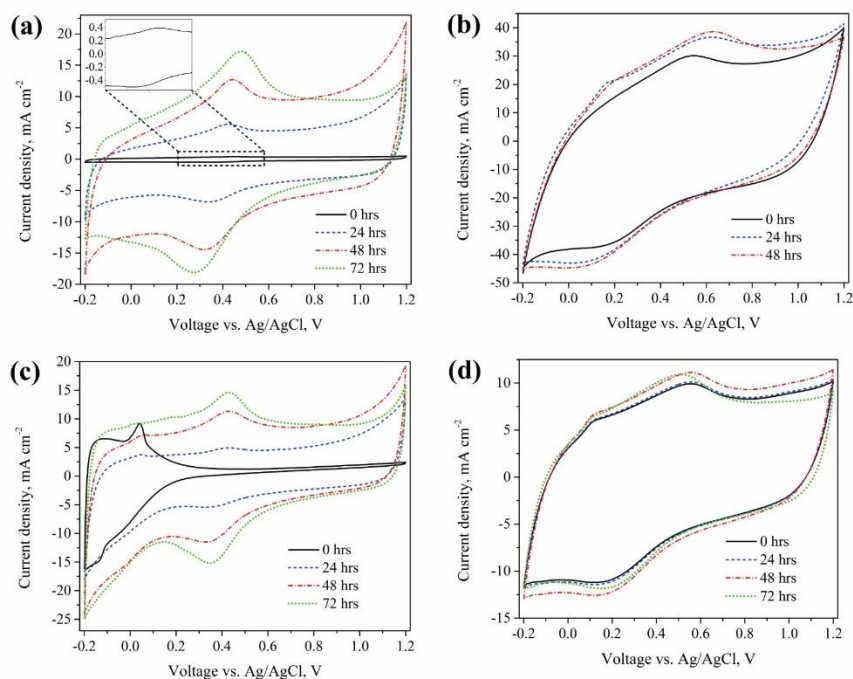


Figure 2.9. Cyclic voltammograms of different samples in aqueous 0.5 M H₂SO₄ at a scan rate of 50 mV/s after holding the potential at 1.2 V versus Ag/AgCl for 0, 24, 48, and 72 hours; (a) UCP; (b) FCP; (c) Nb-TiO₂-UCP; (d) Nb-TiO₂-FCP.

A comparison of the cyclic voltammograms of the four samples as prepared (solid black curves in Fig. 2.9) clearly reveals much larger capacitive currents and more intense peaks of the Q/HQ redox couple for the oxidized FCP samples (Figs. 2.9b and 2.9d) when compared to the UCP samples. This was expected as the oxidative surface treatment generates many more pH and redox active groups (e.g. –OH, C=O, and COOH) on the surface of the FCP samples that also increase the overpotentials for the Q/HQ redox couple (distances between peak potentials). An increase in overpotentials indicates a slower kinetic of the Q/HQ redox reaction and has been reasoned with an increase in local competition for protons when the number of pH active functional groups per unit area increases [40, 44]. The increase in the overpotential for the UCP sample after 72 hours of potential hold at 1.2 V versus Ag/AgCl (Figure 2.9a) also confirms the dependency of overpotential on the degree of oxidation of the carbon paper.

Unexpected was the complete absence of peaks for the Q/HQ redox couple in the as prepared Nb-TiO₂-UCP sample. Two different factors may contribute to the absence of these peaks: first, the uncoated UCP sample contains only a small number of redox active sites that may simply be covered by TiO₂ in the coated Nb-TiO₂-UCP sample. Second, it is likely that some inner Q/HQ redox sites are not reached by the aqueous electrolyte since both samples, UCP and Nb-TiO₂-UCP, are not well wetted by the electrolyte as their contact angles with water of 124° and 85° indicates, respectively. The increase in capacitive current in sample Nb-TiO₂-UCP below 0 V is attributed to a reduction peak of TiO₂ (filling of the conduction-band) [45] whereas the origin of the redox couple with a half potential ($E^{1/2}$) of about -0.05 V remains uncertain.

All four samples were cycled between -0.2 V and 1.2 V versus Ag/AgCl at a scan rate of 50 mV·s⁻¹ for 300 times to monitor the stability towards oxidation but no changes to the peak intensity of the Q/HQ redox couple were observed [5]. Thousand or more cycles are probably required before significant differences in the voltammograms become visible and indicate differences in stability between the samples. To accelerate this process we decided to hold the samples at 1.2 V versus Ag/AgCl for several hours between voltammograms (Figs. 2.9 and 2.10).

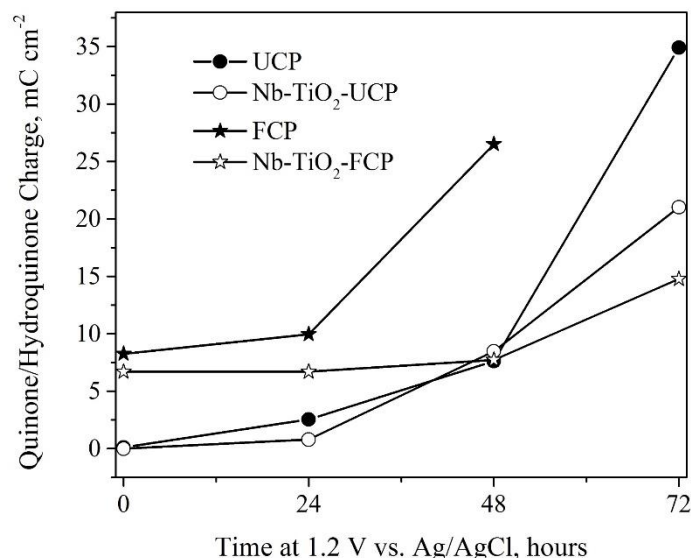


Figure 2.10. The amount of charge per cm² measured for the peaks of the Q/HQ redox couples as a function of time of electrochemical oxidation at 1.2 V.

The amount of electrochemical surface oxidation after 24 hours, 48 hours, and 72 hours at 1.2 V was estimated by comparing the peak areas of the Q/HQ redox couple after subtraction of the charges related to the pseudo-capacitive currents (Figs. 2.9 and 2.10) [27]. It is immediately obvious that FCP has the highest charge per cm² to start with and also shows the largest increase in charge per cm² from 8.23 to 26.52 mC·cm⁻² after 48 hours at 1.2 V, Table 2.1. In contrast, the charge per area values of the coated FCP sample (Nb-TiO₂-FCP) remain almost constant for 48 hours (increase from 6.71 to 7.74 mC·cm⁻²), even though the initial value is almost as high as for FCP, and reach a value of 14.78 mC·cm⁻² after 72 hours. Both UCP and Nb-TiO₂-UCP start at very low charge per area values of 0.12 mC·cm⁻² and 0 mC·cm⁻², respectively. These values increase for UCP and Nb-TiO₂-UCP with each 24 hour oxidation cycle to 7.63 mC·cm⁻² and 8.48 mC·cm⁻² after 48 hours and 34.92 mC·cm⁻² and 21.03 mC·cm⁻² after 72 hours, respectively.

Table 2.1. The amount of charge per cm² measured for the peaks of the Q/HQ redox couples after holding the potential at 1.2 V versus Ag/AgCl for 0, 24, 48, and 72 hours.

Sample Name	Q/HQ charge per unit area (mC·cm ⁻²)			
	0 hrs at 1.2 V vs. Ag/AgCl	24 hrs at 1.2 V vs. g/AgCl	48 hrs at 1.2 V vs. g/AgCl	72 hrs at 1.2 V vs. g/AgCl
UCP	0.12	2.55	7.63	34.92
Nb-TiO ₂ -UCP	0	0.79	8.48	21.03
FCP	8.23	9.97	26.52	-
Nb-TiO ₂ -FCP	6.71	6.71	7.74	14.78

Overall, the increase of charge per unit area for the Q/HQ redox couple produced by electrochemical surface oxidation after 72 hours is highest for UCP with 34.80 mC·cm⁻² (not considering FCP), the lowest for Nb-TiO₂-FCP with 8.07 mC·cm⁻², and in between for Nb-TiO₂-UCP with 21.03 mC·cm⁻². In other words, Nb-TiO₂-FCP is by factors of 2.61 and 4.31 more stable than Nb-TiO₂-UCP and UCP, respectively. Here the factor has been defined as a ratio of the increase in charge per unit area for the Q/HQ redox couple for either UCP or Nb-TiO₂-UCP to that for Nb-TiO₂-FCP.

The observed differences in CV agree well with the observed structural differences discussed above. Sample FCP contains many redox active surface sites right from the beginning that appears to promote the formation of more Q/HQ redox couples during electrochemical oxidation. UCP has only few redox active surface sites at the beginning but the number of Q/HQ redox couples increases exponentially during electrochemical oxidation. The initial large differences between UCP and FCP are likely exaggerated by their differences in wetting. Many redox sites of the hydrophobic UCP sample may initially

not be in contact with the electrolyte but the UCP sample is as hydrophilic as FCP after 48 hours of oxidation (surface contact angle with water is 0°). A similar but less drastic change in wettability may also affect the number of Q/HQ redox couples initially observed for Nb-TiO₂-UCP (surface contact angle with water changes from 85° to 0° after 48 hours of oxidation). However, electrochemical oxidation of Nb-TiO₂-UCP is slower than that of UCP at all intervals, which must result from a partial protection by the TiO₂ coating. This protection is much better in Nb-TiO₂-FCP because of the better coverage of the carbon fibers with Nb-doped TiO₂ and makes the material that is most stable to electrochemical oxidation.

Based on the assumption that Q/HQ redox couples covered with Nb-doped TiO₂ are not redox active, we can conclude that many Q/HQ redox couples in Nb-TiO₂-FCP are not covered by the coating as the initial current per unit area is still high. It is likely that most of these sites are located deep inside the carbon paper and are simply not reached by the coating solution. In fuel cell applications these inner uncovered sites may not be problematic as most of the chemistry on the oxygen electrode side occurs close (at distances of about 10 to 50 μm) to the interface with the bifunctional catalyst layer.

2.4 Conclusions

A new procedure for a simple wet coating of carbon paper with Nb doped TiO₂ is presented. A more uniform coating of the carbon fibers is achieved only if the carbon paper is oxidatively functionalized prior to coating. Cyclic voltammetry measurements on all samples reveal that the oxidatively functionalized carbon paper coated with Nb doped TiO₂ is by a factor of 4.31 more stable than untreated carbon paper to electrochemical oxidation in 0.5 M aqueous H₂SO₄ at 1.2 V versus Ag/AgCl. This is astonishing as the cyclic voltammetry data suggest that many of the redox active sites are not covered by the Nb-doped TiO₂ coating, probably because they are located deep inside the carbon paper. However, these sites are likely more than 10-50 μm away from the interface to the bifunctional catalyst layer in unitized regenerative fuel cells and, therefore, outside the reaction zone. Future work will focus on the adjustment of the hydrophobicity of the coated

carbon paper by chemical alterations to the TiO₂ layer for actual tests in unitized regenerative fuel cells.

2.5 Acknowledgments

The authors thank Prof. Ricardo F. Aroca and Ariel R. Guerrero for their help on Raman spectroscopy. The authors also thank Dr. Tricia Breen Carmichael and Mike Miller for their help on the contact angle measurements. The authors are also grateful for the financial supports from the Natural Sciences and Engineering Research Council of Canada (NSERC) and the University of Windsor.

References

1. Pettersson, J., B. Ramsey, and D. Harrison, *A review of the latest developments in electrodes for unitised regenerative polymer electrolyte fuel cells*. Journal of Power Sources, 2006. **157**(1): p. 28-34.
2. Hwang, C.M., et al., *Influence of properties of gas diffusion layers on the performance of polymer electrolyte-based unitized reversible fuel cells*. International Journal of Hydrogen Energy, 2011. **36**(2): p. 1740-1753.
3. Ioroi, T., et al., *Influence of PTFE coating on gas diffusion backing for unitized regenerative polymer electrolyte fuel cells*. Journal of Power Sources, 2003. **124**(2): p. 385-389.
4. Wittstadt, U., E. Wagner, and T. Jungmann, *Membrane electrode assemblies for unitised regenerative polymer electrolyte fuel cells*. Journal of Power Sources, 2005. **145**(2): p. 555-562.
5. Song, S., et al., *Bifunctional oxygen electrode with corrosion-resistive gas diffusion layer for unitized regenerative fuel cell*. Electrochemistry Communications, 2006. **8**(3): p. 399-405.
6. Huang, S.-Y., et al., *Development of supported bifunctional oxygen electrocatalysts and corrosion-resistant gas diffusion layer for unitized*

- regenerative fuel cell applications*. Journal of Power Sources, 2012. **198**(0): p. 23-29.
7. Chen, G., et al., *Gas diffusion layer with titanium carbide for a unitized regenerative fuel cell*. Electrochimica Acta, 2010. **55**(28): p. 8801-8807.
 8. Sharma, G.D., et al., *Effect of surface modification of TiO₂ on the photovoltaic performance of the quasi solid state dye sensitized solar cells using a benzothiadiazole-based dye*. Journal of Power Sources, 2010. **195**(9): p. 3011-3016.
 9. Huang, S.-Y., et al., *Development of a Titanium Dioxide-Supported Platinum Catalyst with Ultrahigh Stability for Polymer Electrolyte Membrane Fuel Cell Applications*. Journal of the American Chemical Society, 2009. **131**(39): p. 13898-13899.
 10. Oh, H.-J., et al., *Surface characteristics of porous anodic TiO₂ layer for biomedical applications*. Materials Chemistry and Physics, 2008. **109**(1): p. 10-14.
 11. Chen, X. and S.S. Mao, *Titanium Dioxide Nanomaterials: Synthesis, Properties, Modifications, and Applications*. Chemical Reviews, 2007. **107**(7): p. 2891-2959.
 12. Park, K.-W. and K.-S. Seol, *Nb-TiO₂ supported Pt cathode catalyst for polymer electrolyte membrane fuel cells*. Electrochemistry Communications, 2007. **9**(9): p. 2256-2260.
 13. Ruiz, A.M., et al., *Insights into the Structural and Chemical Modifications of Nb Additive on TiO₂ Nanoparticles*. Chemistry of Materials, 2004. **16**(5): p. 862-871.
 14. Huang, S.-Y., P. Ganesan, and B.N. Popov, *Electrocatalytic activity and stability of niobium-doped titanium oxide supported platinum catalyst for polymer electrolyte membrane fuel cells*. Applied Catalysis B: Environmental, 2010. **96**(1-2): p. 224-231.

15. Navaei Alvar, E., B. Zhou, and S.H. Eichhorn. *Effect of Reducing Agent on the Dispersion of Pt Nanoparticles on Electrospun Nb_{0.1}Ti_{0.9}O₂ Nanofibers*. in *Materials Research Society 2013*. 2013. San Francisco.
16. Liu, C., et al., *Synthesis, characterization, and its photocatalytic activity of double-walled carbon nanotubes-TiO₂ hybrid*. *Materials Research Bulletin*, 2013. **48**(4): p. 1499-1505.
17. Kim, S. and S.K. Lim, *Preparation of TiO₂-embedded carbon nanofibers and their photocatalytic activity in the oxidation of gaseous acetaldehyde*. *Applied Catalysis B: Environmental*, 2008. **84**(1–2): p. 16-20.
18. Dumitriu, D., et al., *Photocatalytic degradation of phenol by TiO₂ thin films prepared by sputtering*. *Applied Catalysis B: Environmental*, 2000. **25**(2–3): p. 83-92.
19. Lin, S.-S., Y.-H. Hung, and S.-C. Chen, *Optical properties of TiO₂ thin films deposited on polycarbonate by ion beam assisted evaporation*. *Thin Solid Films*, 2009. **517**(16): p. 4621-4625.
20. Akalework, N.G., et al., *Ultrathin TiO₂-coated MWCNTs with excellent conductivity and SMSI nature as Pt catalyst support for oxygen reduction reaction in PEMFCs*. *Journal of Materials Chemistry*, 2012. **22**(39): p. 20977-20985.
21. Avilés, F., et al., *Evaluation of mild acid oxidation treatments for MWCNT functionalization*. *Carbon*, 2009. **47**(13): p. 2970-2975.
22. Burghard, K.B.a.M., *Chemically Functionalized Carbon Nanotubes*. *Small*, 2005. **1**(2).
23. Hu, N., et al., *A Facile Route for the Large Scale Fabrication of Graphene Oxide Papers and Their Mechanical Enhancement by Cross-linking with Glutaraldehyde*. *Nano-Micro Letters*, 2011. **3**(4): p. 215-222.

24. Kessler, V., et al., *New insight in the role of modifying ligands in the sol-gel processing of metal alkoxide precursors: A possibility to approach new classes of materials*. Journal of Sol-Gel Science and Technology, 2006. **40**(2-3): p. 163-179.
25. Manole, A.V., et al., *Optical properties of Nb-doped TiO₂ thin films prepared by sol-gel method*. Ceramics International, 2013. **39**(5): p. 4771-4776.
26. Wang, J., et al., *Electrochemical durability investigation of single-walled and multi-walled carbon nanotubes under potentiostatic conditions*. Journal of Power Sources, 2008. **176**(1): p. 128-131.
27. Wang, J., et al., *Effect of carbon black support corrosion on the durability of Pt/C catalyst*. Journal of Power Sources, 2007. **171**(2): p. 331-339.
28. Kovtyukhova, N.I., et al., *Individual Single-Walled Nanotubes and Hydrogels Made by Oxidative Exfoliation of Carbon Nanotube Ropes*. Journal of the American Chemical Society, 2003. **125**(32): p. 9761-9769.
29. Yan, X.-b., B.K. Tay, and Y. Yang, *Dispersing and Functionalizing Multiwalled Carbon Nanotubes in TiO₂ Sol*. The Journal of Physical Chemistry B, 2006. **110**(51): p. 25844-25849.
30. Shaffer, M.S.P., X. Fan, and A.H. Windle, *Dispersion and packing of carbon nanotubes*. Carbon, 1998. **36**(11): p. 1603-1612.
31. Yu, R., et al., *Platinum Deposition on Carbon Nanotubes via Chemical Modification*. Chemistry of Materials, 1998. **10**(3): p. 718-722.
32. Li, Y.-H., et al., *Self-organized Ribbons of Aligned Carbon Nanotubes*. Chemistry of Materials, 2002. **14**(2): p. 483-485.
33. Dresselhaus, M.S., G. Dresselhaus, and M. Hofmann, *The big picture of Raman scattering in carbon nanotubes*. Vibrational Spectroscopy, 2007. **45**(2): p. 71-81.
34. Kudin, K.N., et al., *Raman Spectra of Graphite Oxide and Functionalized Graphene Sheets*. Nano Letters, 2007. **8**(1): p. 36-41.

35. Wang, Y., D.C. Alsmeyer, and R.L. McCreery, *Raman spectroscopy of carbon materials: structural basis of observed spectra*. Chemistry of Materials, 1990. **2**(5): p. 557-563.
36. Li, Z.Q., et al., *X-ray diffraction patterns of graphite and turbostratic carbon*. Carbon, 2007. **45**(8): p. 1686-1695.
37. Zhu, Y., et al., *The synthesis of nanosized TiO₂ powder using a sol-gel method with TiCl₄ as a precursor*. Journal of Materials Science, 2000. **35**(16): p. 4049-4054.
38. Falaras, P., et al., *Characterization by resonance Raman spectroscopy of sol-gel TiO₂ films sensitized by the Ru(PPH₃)₂(dcbipy)Cl₂ complex for solar cells application*. Solar Energy Materials and Solar Cells, 2000. **64**(2): p. 167-184.
39. Wen, Z., et al., *TiO₂ nanoparticles-decorated carbon nanotubes for significantly improved bioelectricity generation in microbial fuel cells*. Journal of Power Sources, 2013. **234**(0): p. 100-106.
40. Kangasniemi, K.H., D.A. Condit, and T.D. Jarvi, *Characterization of Vulcan Electrochemically Oxidized under Simulated PEM Fuel Cell Conditions*. Journal of The Electrochemical Society, 2004. **151**(4): p. E125-E132.
41. Yang, Y. and Z.G. Lin, *In situ FTIR characterization of the electrooxidation of glassy carbon electrodes*. Journal of Applied Electrochemistry, 1995. **25**(3): p. 259-266.
42. Ioroi, T., et al., *Sub-stoichiometric titanium oxide-supported platinum electrocatalyst for polymer electrolyte fuel cells*. Electrochemistry Communications, 2005. **7**(2): p. 183-188.
43. Százdi, L., J. Gulyás, and B. Pukánszky, *Surface characterization of electrochemically oxidized carbon fibers: surface properties and interfacial adhesion*. Composite Interfaces, 2002. **9**(2): p. 219-232.

44. Bhat, M.A., *Mechanistic, kinetic and electroanalytical aspects of quinone–hydroquinone redox system in N-alkylimidazolium based room temperature ionic liquids*. *Electrochimica Acta*, 2012. **81**(0): p. 275-282.
45. Yu, H., et al., *Cyclic voltammetry studies of TiO₂ nanotube arrays electrode: Conductivity and reactivity in the presence of H⁺ and aqueous redox systems*. *Electrochimica Acta*, 2011. **56**(18): p. 6498-6502.

CHAPTER 3

Effect of Reducing Agent on the Dispersion of Pt Nanoparticles on Electrospun Nb_{0.1}Ti_{0.9}O₂ Nanofibers for PEM Fuel Cell Application

3.1 Introduction

Polymer electrolyte membrane (PEM) fuel cells are a promising technology for power generation especially in portable devices. One of their main limitations is the degradation of the catalyst and catalyst support, which has particularly fueled the development of new catalyst supports to replace or modify the widely used carbon materials [1]. Carbon as catalyst support is primarily degraded by electro-oxidation [2, 3].

In recent years, several novel nanostructured materials based on tungsten oxides, indium-tin oxides, and titanium oxides have been introduced as possible catalyst supports [1, 4, 5]. Particularly intriguing has been the work on cost-effective TiO₂ materials. Huang et al. first reported on the high stability of Pt/TiO₂ electrocatalysts when compared to commercial Pt/C catalysts [3, 6]. The activity of the Pt nanoparticles could be increased when they were deposited onto nano-structured TiO₂ support materials such as nanofibers [7]. However, a major drawback of TiO₂ as catalyst support is its low electrical conductivity of only $10^{-13} \Omega^{-1} \cdot \text{cm}^{-1}$ at 298 K that is insufficient for fuel cell applications [8]. Increased electronic conductivity has been reported for non-stoichiometric TiO₂ compounds, such as magneli phase titanium dioxide, or TiO₂ that is doped with donor-type ions such as Nb⁺⁵ [9-11]. The presence of niobium also increases the stability of the Pt nanoparticles in comparison to undoped titanium dioxide or carbon support as demonstrated by Bauer et al. with Pt nanoparticles deposited onto niobium-doped titanium dioxide nanofibers [12].

In addition to alterations to the catalyst support material, activity of the catalyst is also increased when the size of the Pt nanoparticles is decreased [13, 14]. Consequently, many different methods for the deposition of Pt nanoparticles on carbon supports have been developed [15-18]. Straightforward chemical reduction methods have been most widely applied and are the main method for the deposition of Pt onto TiO₂ supports [6, 8, 10]. Ethylene glycol [19], sodium borohydride in ethylene glycol [11, 20], and sodium borohydride in an alcoholic surfactant solution [3] are the most widely used reducing agents but no comparative studies for depositions of Pt on TiO₂ nanofibers have been reported. .

Presented here is an extension of Bauer's work that studies the effect of two different reducing agents on the deposition of Pt nanoparticles onto niobium-doped titanium dioxide nanofibers as well as their activity and stability as catalyst for water reduction at low pH.

3.2 Experimental

3.2.1 Preparation of Nb_{0.1}Ti_{0.9}O₂ nanofibers

Polyvinyl pyrrolidone (0.45 g, Mw = 1,300,000 g/mol) was added to 7.5 mL of anhydrous ethanol and stirred until it was fully dissolved. A second solution was prepared by adding 1.6 mL of Ti(IV)-isopropoxide and 135 μ l of niobium ethoxide to a solution of 3 mL acetic acid in 3 mL anhydrous ethanol under N₂ atmosphere. The two solutions were mixed together and stirred for 3 hrs at room temperature under N₂ to generate a homogeneous viscous polymer solution. After degassing, the solution was loaded into a plastic syringe that was equipped with a 22-gauge stainless steel needle. Electrospinning of nanofibers was carried out with a standard setup consisting of a plastic syringe and a grounded aluminum collector plate. The distance between the needle tip and the collector was 12 cm and the voltage was 12 kV. The solution was supplied with a syringe pump (KDS scientific) at a constant rate of 0.35 mL/hr. The as-spun fibers were dried at room temperature for 24 hrs and then heated to 500°C under oxygen atmosphere to give crystalline Nb-doped TiO₂ nanofibers free of PVP and other organic compounds after about 4 hrs of heat treatment.

3.2.2 Pt nanoparticle deposition

Method 1: Nb_{0.1}Ti_{0.9}O₂ nanofibers (30 mg) were dispersed in 25 mL of a solution of H₂PtCl₆.6H₂O in ethylene glycol (1.5 mM) at room temperature, which corresponds to a final loading of 20wt% of Pt on nanofibers. The pH value of the suspension was adjusted to 10 by drop-wise addition of 0.1M NaOH in ethylene glycol. Stirring of the suspension for 1 hr at room temperature 3 hrs at reflux (about 160 °C), and finally overnight at room temperature generated the Pt coated nanofibers, which were separated from the reaction suspension by centrifugation. The nanofibers were suspended in de-ionized water and separated by centrifugation three times to completely remove the ethylene glycol and finally dried in vacuum at 80 °C overnight

Method 2: Nb_{0.1}Ti_{0.9}O₂ nanofibers (30 mg) were dispersed in a solution of 0.2 M sodium dodecyl sulphate in anhydrous ethanol and sonicated for 1 hr. H₂PtCl₆.6H₂O (20 mg; corresponding to a final loading of 20wt% of Pt on nanofibers) was added to the dispersion and stirred for 3 hrs. Reduction of the Pt salt to Pt nanoparticles was achieved by the addition of a 0.1 M solution of NaBH₄ in ethanol (40 equivalents of NaBH₄ with regard to Pt). The reaction mixture was stirred for 15 hrs and the Pt coated nanofibers were separated by centrifugation, washed with de-ionized water three times, and dried in vacuum at 80 °C overnight.

3.2.3 Physical Characterization of Nb_{0.1}Ti_{0.9}O₂ and Pt/Nb_{0.1}Ti_{0.9}O₂ nanofibers

X-ray diffraction was conducted with a Bruker D8 diffractometer equipped with a copper source. Diffraction patterns were recorded in transmission mode between $2\theta = 20^\circ$ - 80° . The apparent crystallite size was determined using the Scherrer equation [21]. Three diffraction lines (111), (200) and (220) were chosen for the measurements crystallite sizes and the mean average is reported. The morphology of synthesized nanofibers and Pt/Nb_{0.1}Ti_{0.9}O₂ catalysts were examined by scanning electron microscopy (FEI Quanta 200 FEG equipped with an energy-dispersive spectrometer EDAX SiLi Detector). For SEM specimen preparation, a small amount of powder was spread on a carbon tape adhered to an aluminum specimen holder. Transmission electron microscopy was conducted with a JEOL 2010F microscope operating at 200 kV.

3.2.3 Electrochemical characterization of Pt/Nb_{0.1}Ti_{0.9}O₂ nanofibers

Electrochemical characterizations were conducted in a conventional three-electrode system using a BASi RDE-2 Rotating Disk Electrode. Pt wire and saturated Ag/AgCl electrodes were used as counter and reference electrodes, respectively. A glassy carbon RDE tip (0.076 cm²) served as the working electrode. The catalyst ink was prepared as a dispersion of 2 mg of Pt/Nb_{0.1}Ti_{0.9}O₂ nanofibers in 1 mL ethanol by sonication for 20 mins. This catalyst ink (about 20 μ L for each coating) was then coated onto the glassy carbon working electrode and dried. Nafion solution (2 μ L of 5 wt.% Nafion solution, DuPont) was added on top of the catalyst layer to ensure better adhesion to the glassy carbon electrode. All electrochemical characterizations were based on cyclic voltammetry techniques in Ar saturated solution of 0.5 M H₂SO₄ in the range of 0.03 V to 1.4 V vs. RHE

at a scan rate of 100 mV.s⁻¹. An upper potential limit of 1.4 V was chosen because 1.4 is close to the cathode potential in the condition of current and local fuel starvation at which the corrosion of the carbon support is most severe [6]. The electrodes were cleaned from any contamination by cycling them 20 times from 0.03 V to 1.2 V vs. RHE at a scan rate of 100 mV s⁻¹ in Ar purged 0.5 M H₂SO₄ prior to coating. To investigate the catalyst stability, 1000 full cycles in the range of 0.03 V to 1.4 V vs. RHE at a scan rate of 100 mV s⁻¹ were performed and the electrochemical surface area (ECSA) was calculated based on H₂ desorption peaks observed between 0.3 and 0.35 V vs. RHE after 50 and 1000 cycles. The electrochemical surface areas (ECSA) of Pt nanoparticles were determined by integration of the hydrogen desorption peak of the 50th and 1000th full cycles according to Eq. (1) [6]:

$$\text{ECSA} = \frac{Q_{\text{H}}}{m \times q_{\text{H}}} \quad (3-1)$$

Q_{H} is the charge of hydrogen desorption in coulombs, m is the Pt metal loading in g, and q_{H} is the charge per unit area required for the desorption of a monolayer of hydrogen on a Pt surface (here set to 210 $\mu\text{C cm}^{-2}$) [22].

3.3 Results and discussion

Optimization of the electrospinning parameters, especially flow rate, nozzle to target distance, and voltage, reproducibly generates Nb-doped TiO₂ nanofibers with an average diameter of 70 nm after calcination as confirmed by FE-SEM images (Figure 3.1). These results agree with what has been reported for the electrospinning of similar fibers [23].

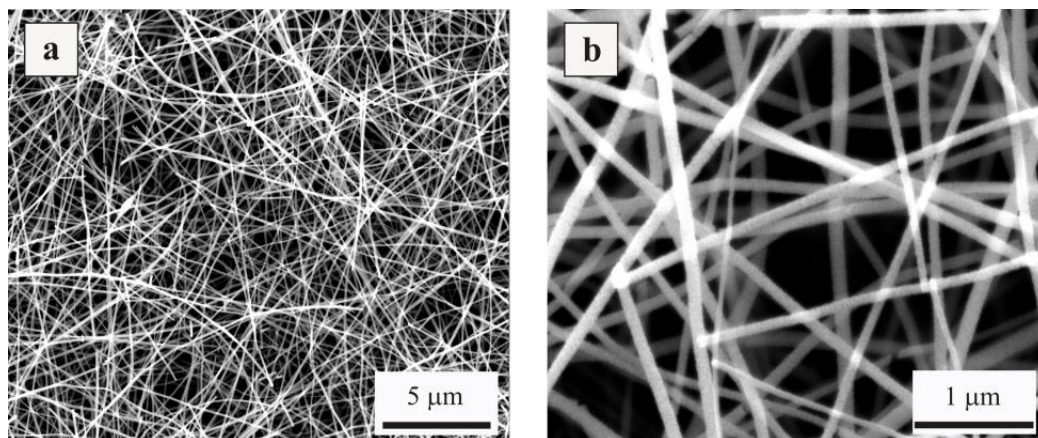


Figure 3.1. FE-SEM images of the Nb_{0.1}Ti_{0.9}O₂ nanofibers prepared at 1.25 KV/cm electric field.

Powder X-ray diffraction of the nanofibers before and after deposition of Pt nanoparticles confirms the presence of TiO₂ predominantly as anatase phase and the absence of reflections of Nb oxide (Figure 3.2). This confirms that Nb is fully incorporated into the TiO₂ structure. After deposition of Pt nanoparticles by either the ethylene glycol (EG) or the NaBH₄ reduction methods additional reflections occur in the XRD patterns that agree with the (111), (200), and (220) reflections of metallic Pt. The larger FWHM for the Pt reflections of the EG sample in comparison to the hydride sample suggests a smaller Pt particle size for the former. Estimations based on Scherrer's equation gives an average size of Pt crystallites of 5.4 nm and 7.6 nm for the EG and sodium borohydride reduction methods, respectively (Table 3.1).

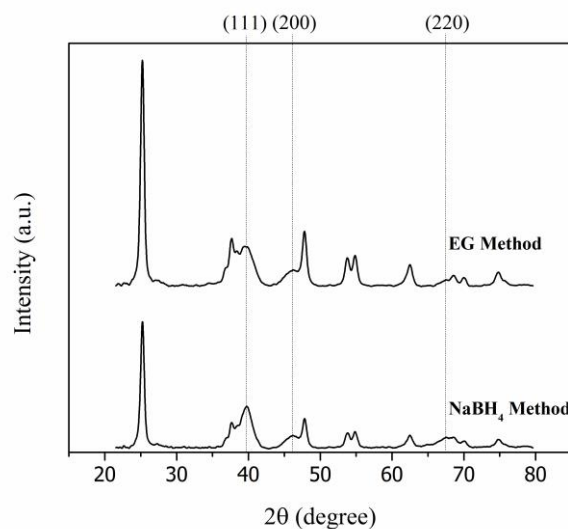


Figure 3.2. Powder X-Ray diffraction patterns of Pt-coated Nb_{0.1}Ti_{0.9}O₂ nanofibers with EG method and sodium borohydride (NaBH₄) method.

Table 3.1. Structural and electrochemical properties of Pt/Nb_{0.1}Ti_{0.9}O₂ catalysts at 50th and 1000th cycles after potential cycling in the range of 0.3 to 1.4V.

Catalyst	Crystallite size (nm) ^a	ECSA	ECSA
		(after 50 scans) (m ² /gPt) ^b	(after 1000 scans) (m ² /gPt) ^b
EG method	5.4, (SD=0.529)	5.45	3.43
NaBH ₄ method	7.6, (SD=0.556)	4.96	3.07

^a Scherrer equation; ^b Integration of H₂ desorption peak in cyclic voltammograms

Consequently, a larger surface area is expected for the sample generated by EG reduction and this was confirmed by cyclic voltammetry (Figure 3.3). The electrochemical results clearly show a larger electrochemical surface area (ECSA) of 5.45 m²/gPt

(voltammetric cycles between 0.03 and 1.4 V vs. RHE) for Pt nanoparticles reduced by EG in comparison to 4.96 m²/gPt for sodium borohydride reduction. Very similar ECSA values were reported for a Pt on Nb_{0.1}Ti_{0.9}O₂ nanofibers catalyst prepared with sodium borohydride in ethylene glycol [11].

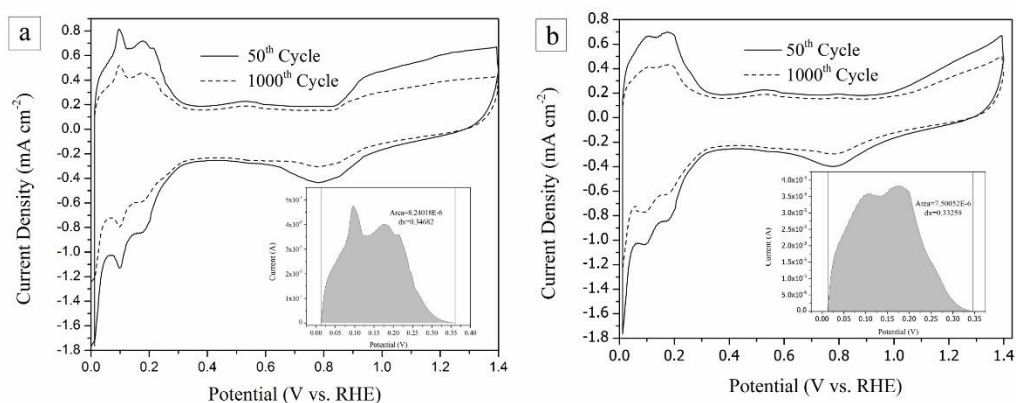


Figure 3.3. Cyclic voltammograms of (a) EG-reduced Pt/Nb_{0.1}Ti_{0.9}O₂ and (b) NaBH₄-reduced Pt/Nb_{0.1}Ti_{0.9}O₂ catalysts after 50 and 1000 cycles at a scan rate of 100 mV/s. The Pt loading was 100 μgPt.cm⁻² and the electrolyte was Ar purged 0.5 H₂SO₄. Insets show the charge integration of the H₂ desorption peaks for ECSA calculation.

The smaller size and the better dispersion of Pt nanoparticles on Nb_{0.1}Ti_{0.9}O₂ nanofibers when reduced with ethylene glycol is attributed to the stabilizing effect of glycolic acid, the oxidation product of ethylene glycol in the presence of OH⁻. Glycolic acid anions readily adsorb onto the surface of Pt nanoparticles that are then stabilized by charge repulsion [19], which apparently is more effective than dodecyl sulphate.

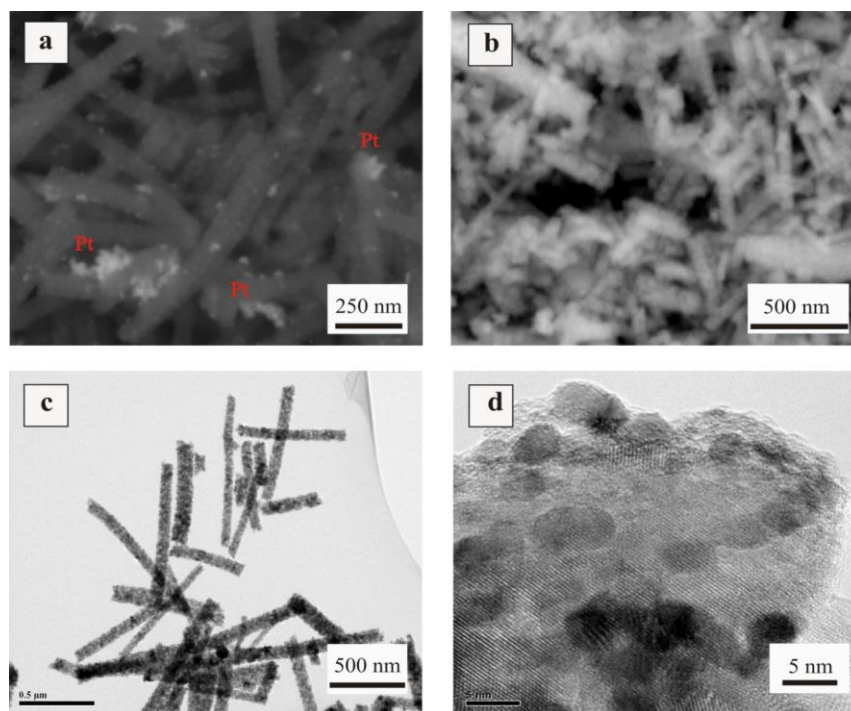


Figure 3.4. Back scattered FE-SEM images of catalysts reduced by NaBH₄ (a) and EG (b), respectively. TEM (c) and HRTEM (d) images of Pt nanoparticles on Nb/TiO₂ nanofibers prepared by the EG method.

The same differences in particle size and dispersion between the two samples prepared by EG and borohydride reductions are also visible in the SEM and TEM images (Figure 3.4). SEM images of samples prepared by borohydride reduction show larger aggregates and an uneven distribution of Pt nanoparticles (Figure 3.4a). In contrast, SEM images of samples reduced with EG have too low resolution to identify individual clusters of Pt nanoparticles (Figure 3.4b) but TEM images verify an average particle size of about 5 nm and an excellent dispersion on the nanofibers (Figures 3.4c, d). TEM images also confirm the crystalline nature of the Nb/TiO₂ nanofibers and an average diameter of the Pt nanoparticles of 4-5 nm.

Despite their differences in structure both Pt/Nb_{0.1}Ti_{0.9}O₂ catalyst samples show similar chemical stability. ECSA values calculated after 1000 potential cycles confirm an activity loss of 38% for both catalyst samples, which is a significant improvement in comparison to commercially used Pt/C catalysts that show a decrease in activity by 72% after 1000

potential cycles due to severe corrosion of the carbon support [6]. Similar activity losses of 40% have been reported for Nb-doped titanium dioxide nanofibers supported Pt catalysts that were prepared by reduction with NaBH₄ in ethylene glycol [11] and catalysts based on Pt nanoparticles coated onto TiO₂ nanotubes [24]. The better retention of activity for the Pt/Nb_{0.1}Ti_{0.9}O₂ catalyst system in comparison to Pt/C is reasoned with a strong metal support interaction (SMSI) between Pt nanoparticles and Nb_{0.1}Ti_{0.9}O₂ nanofibers [25].

3.4 Conclusions

The reductive deposition of Pt nanoparticles onto Nb_{0.1}Ti_{0.9}O₂ nanofibers generates highly active and stable catalyst systems for potential applications in PEM fuel cells. Reduction of the Pt salt with ethylene glycol generates smaller and better dispersed Pt nanoparticles on Nb/TiO₂ nanofibers than reduction with borohydride. This amounts to a higher catalytic activity for the sample reduced with ethylene glycol but, interestingly, the stability of both catalyst samples is equal with about 38% reduction in activity after 1000 voltammetric cycles.

3.5 Acknowledgments

The authors are grateful for the supports given by the Natural Sciences and Engineering Research Council of Canada (NSERC) and the University of Windsor.

References

1. Wang, Y.-J., D.P. Wilkinson, and J. Zhang, *Noncarbon Support Materials for Polymer Electrolyte Membrane Fuel Cell Electrocatalysts*. Chemical Reviews, 2011. **111**(12): p. 7625-7651.
2. Wang, X., et al., *Durability investigation of carbon nanotube as catalyst support for proton exchange membrane fuel cell*. Journal of Power Sources, 2006. **158**(1): p. 154-159.
3. Huang, S.-Y., et al., *Development of a Titanium Dioxide-Supported Platinum Catalyst with Ultrahigh Stability for Polymer Electrolyte Membrane Fuel Cell*

- Applications*. Journal of the American Chemical Society, 2009. **131**(39): p. 13898-13899.
4. Park, K.-W., et al., *PtRu Alloy and PtRu–WO₃ Nanocomposite Electrodes for Methanol Electrooxidation Fabricated by a Sputtering Deposition Method*. The Journal of Physical Chemistry B, 2004. **108**(19): p. 5989-5994.
 5. Chhina, H., S. Campbell, and O. Kesler, *An oxidation-resistant indium tin oxide catalyst support for proton exchange membrane fuel cells*. Journal of Power Sources, 2006. **161**(2): p. 893-900.
 6. Huang, S.-Y., P. Ganesan, and B.N. Popov, *Titania supported platinum catalyst with high electrocatalytic activity and stability for polymer electrolyte membrane fuel cell*. Applied Catalysis B: Environmental, 2011. **102**(1–2): p. 71-77.
 7. Cavaliere, S., et al., *Single step elaboration of size-tuned Pt loaded titania nanofibres*. Chemical Communications, 2011. **47**(24): p. 6834-6836.
 8. Hayden, B.E., D.V. Malevich, and D. Pletcher, *Electrode coatings from sprayed titanium dioxide nanoparticles – behaviour in NaOH solutions*. Electrochemistry Communications, 2001. **3**(8): p. 390-394.
 9. Ioroi, T., et al., *Stability of Corrosion-Resistant Magnéli-Phase Ti₄O₇-Supported PEMFC Catalysts at High Potentials*. Journal of The Electrochemical Society, 2008. **155**(4): p. B321-B326.
 10. Senevirathne, K., et al., *Electrocatalytic activity and durability of Pt/NbO₂ and Pt/Ti₄O₇ nanofibers for PEM fuel cell oxygen reduction reaction*. Electrochimica Acta, 2012. **59**(0): p. 538-547.
 11. Park, K.-W. and K.-S. Seol, *Nb-TiO₂ supported Pt cathode catalyst for polymer electrolyte membrane fuel cells*. Electrochemistry Communications, 2007. **9**(9): p. 2256-2260.
 12. Bauer, A., et al., *Pt nanoparticles deposited on TiO₂ based nanofibers: Electrochemical stability and oxygen reduction activity*. Journal of Power Sources, 2010. **195**(10): p. 3105-3110.

13. Kongkanand, A., et al., *Highly Dispersed Pt Catalysts on Single-Walled Carbon Nanotubes and Their Role in Methanol Oxidation*. The Journal of Physical Chemistry B, 2006. **110**(33): p. 16185-16188.
14. Antolini, E., *Carbon supports for low-temperature fuel cell catalysts*. Applied Catalysis B: Environmental, 2009. **88**(1–2): p. 1-24.
15. Endo, M., et al., *Selective and Efficient Impregnation of Metal Nanoparticles on Cup-Stacked-Type Carbon Nanofibers*. Nano Letters, 2003. **3**(6): p. 723-726.
16. Spinacé, E.V., et al., *Electro-oxidation of ethanol using PtRu/C electrocatalysts prepared by alcohol-reduction process*. Journal of Power Sources, 2004. **137**(1): p. 17-23.
17. Chu, Y.-Y., et al., *Performance of Pt/C catalysts prepared by microwave-assisted polyol process for methanol electrooxidation*. Journal of Power Sources, 2010. **195**(7): p. 1799-1804.
18. Zoval, J.V., et al., *Electrochemical Preparation of Platinum Nanocrystallites with Size Selectivity on Basal Plane Oriented Graphite Surfaces*. The Journal of Physical Chemistry B, 1998. **102**(7): p. 1166-1175.
19. Bock, C., et al., *Size-Selected Synthesis of PtRu Nano-Catalysts: Reaction and Size Control Mechanism*. Journal of the American Chemical Society, 2004. **126**(25): p. 8028-8037.
20. Kim, P., et al., *NaBH₄-assisted ethylene glycol reduction for preparation of carbon-supported Pt catalyst for methanol electro-oxidation*. Journal of Power Sources, 2006. **160**(2): p. 987-990.
21. Holzwarth, U. and N. Gibson, *The Scherrer equation versus the 'Debye-Scherrer equation'*. 2011, Nature Publishing Group. p. 534-534.
22. F. Nart, W. Vielstich, W. Vielstich, H.A. Gasteiger, A. Lamm (Eds), *Handbook of Fuel Cells – Fundamentals, Technology and Applications, Vol. 2. Electrocatalysis*, (John Wiley&Sons 2003).

23. Tekmen, C., A. Suslu, and U. Cocen, *Titania nanofibers prepared by electrospinning*. *Materials Letters*, 2008. **62**(29): p. 4470-4472.
24. Lim, D.-H., et al., *Electrochemical Characterization and Durability of Sputtered Pt Catalysts on TiO₂ Nanotube Arrays as a Cathode Material for PEFCs*. *Journal of The Electrochemical Society*, 2010. **157**(6): p. B862-B867.
25. Li, Q., et al., *Effect of photocatalytic activity of CO oxidation on Pt/TiO₂ by strong interaction between Pt and TiO₂ under oxidizing atmosphere*. *Journal of Molecular Catalysis A: Chemical*, 2006. **258**(1–2): p. 83-88.

CHAPTER 4

Carbon-Embedded Mesoporous Nb-doped TiO₂ Nanofibers as Catalyst Support for Oxygen Reduction Reaction in PEM Fuel Cell

4.1 Introduction

To take a notable step towards fuel cell commercialization, high cost and low durability are the most important challenges that have to be overcome [1]. Pt catalysts supported by carbon black are widely implemented as electrocatalyst for PEM fuel cells, yet they lose the performance with time due to the degradation of carbon blacks at high potentials [2-4]. This fact triggered numerous research activities in the following areas: understanding the degradation mechanisms [5-9]; and seeking up-scalable and promising mitigation strategies to develop more durable electrocatalysts for PEM fuel cells [1, 10-12]. In the search for an electrochemically durable noncarbon catalyst support, titanium dioxide (TiO₂) has shown to be very promising due to its exceptional chemical and thermal stability [2, 13-15]. However, inherently low electronic conductivity and surface area of titanium dioxide have been identified to be the two biggest challenges to utilize TiO₂ as a catalyst support for PEM fuel cells. It has been well recognized that electronic conductivity of TiO₂ can be increased either through the introduction of oxygen vacancies to form Ti₄O₇ via reductive heat treatment [16] or introduction of variable valence transition metals (e.g., Nb [17], Ta [18], Cr [19], and Mo [20]) via doping into TiO₂ lattice. Of these strategies, although the former can produce electronically conductive oxygen-deficient phases such as Ti₄O₇, it is not feasible for PEM fuel cell applications because Ti₄O₇ will be electro-oxidized back to TiO₂ polymorphs at the surface in fuel cell operating conditions [21, 22]. At the same time, the latter was not straightforward as high electronic conductivities (e.g., 1.11 S cm⁻¹) are only achievable after relatively high temperature reductive treatment, e.g., 900 °C, which results in nanoparticles with extremely low surface area (2 m² g⁻¹) [23, 24]. Recently, compositing or hybridizing transition metal-doped TiO₂ nanoparticles (NPs) with other conductive materials, e.g. graphitized carbon NPs [25-27] or palladium NPs [28], was employed to take the advantages of their high electronic conductivity and/or surface area [25-30]. However, high electronic conductivities of 2.4-4.88 S cm⁻¹ were only achieved through hybridizing/compositing the commercially available carbon NPs, at high contents (67-75 wt. %), that have high surface area with their in-house transition metal-doped TiO₂ NPs that featured with low surface area and low electronic conductivity. Catalysts made through depositing Pt or Pt alloys onto these composite supports, although

demonstrated significantly higher mass activities, their electrochemical durability was only slightly improved comparing with pure carbon black-supported catalysts. In addition, Senevirathne et al. [27] revealed that compositing Nb-doped TiO₂ with 75 wt. % carbon NPs could even result in lower electrochemical durability than pure carbon black-supported catalysts under certain synthesis conditions.

Moreover, due to their favorable structure and properties, metal oxide-based nanofibers (NFs) synthesized through easily up-scalable electrospinning method have been a research topic with considerable attention [22, 24, 30-32]. Recently, relatively conductive, 0.1 S cm⁻¹, Nb-doped TiO₂ NF based composite catalyst supports were also synthesized by compositing NFs with carbon NPs.[30] Although Bauer et al. [30] introduced carbon NPs into Nb-doped TiO₂ NFs through reductive treatment of an organic carbon source (not compositing with already graphitized carbon NPs), the final nanostructure of their synthesized composite catalyst support was still claimed to be only comprised from not evenly distributed carbon NPs (not embedded/doped) and Nb-doped TiO₂ NFs which are separately coated with Pt nanoparticles.

Overall to make transition metal doped titanium dioxide NPs/NFs feasible as a catalyst support for PEM fuel cell applications, to the best of the present authors' knowledge, first, synthesis conditions were shown to be very crucial [33]; second, the only alternative way which has been attempted to increase the electronic conductivity and surface area was to composite or hybridize carbon NPs with transition metal-doped TiO₂ NPs/NFs. Furthermore, it has been well-known that micropores (pores which are smaller than 2 nm,) are not easily accessible for Pt NPs and Nafion, whereas mesopores (pores with diameters in the range between 2-50 nm) are accessible and combined with a good electronic conductivity can lead to very appealing catalyst supports [31, 34].

Reported here is the first in-situ reductive embedment (ISRE) of carbon into mesoporous Nb-doped TiO₂ NFs. Pt catalysts supported by these NFs and those without embedded carbon (carbon-free) were synthesized and tested for ORR mass activity and durability under acidic conditions. Raman spectroscopy measurements were employed to identify the structure of carbon embedded in NFs and XPS measurements were employed

to investigate the elemental composition and chemical and electronic state of the surface of NFs under both oxidizing and reducing conditions.

4.2 Experimental

4.2.1 Synthesis of Nb-doped TiO₂ nanofibers with embedded carbon and carbon-free

In this study, for the purpose of synthesizing Nb-doped TiO₂, Nb_xTi_(1-x)O₂ ($x = 0.1$ and 0.25), NFs with embedded carbon or carbon-free through electrospinning, Polyvinylpyrrolidone (PVP), titanium tetraisopropoxide and niobium ethoxide were used as precursor materials. In a typical synthesis, 0.45g of PVP copolymer ($M_w = 1,300,000$) has been added into 7.5 mL of anhydrous ethanol and stirred until it completely dissolved and a clear polymer solution obtained. A second solution was prepared by adding 1.6 mL of Ti(IV)-isopropoxide and 0.14-0.44 mL of niobium ethoxide (corresponding to 10-25 at. % Nb doping level) into 6 mL of acetic acid and anhydrous ethanol mixture, with a 1:1 volumetric ratio. After stirring the second solution for an hour under Ar atmosphere, it has been added into the polymer solution and the mixture was stirred for another 3 hrs at room temperature to get a homogeneous viscous solution. After degassing the obtained viscous solution by sonication for 10 mins, it was loaded into a plastic syringe which was equipped with a 22-gauge blunt stainless steel needle. Electrospinning of NFs was carried out in an electrospinning apparatus developed in the Clean Powertrain Lab at the University of Windsor[35] with a syringe and grounded aluminum collector plate configuration. The distance between the needle tip and the collector was 12 cm and the voltage was 12 KV, the solution was fed at a constant rate of 0.35 mL hr⁻¹ by using a syringe pump (KDS scientific). The as-spun NFs were left at ambient environment with room temperature for 24 hours and then were treated under two different heating protocols as follow:

Protocol CF: First, calcined under air stream from room temperature up to 500 °C at a heating rate of 5 °C min⁻¹, kept at 500 °C for 6 hours and removed from the furnace after it has been cooled down to room temperature; second, the oxidized NFs were loaded into a tube furnace and reduced under pure hydrogen atmosphere from room temperature up to 800 °C at a heating rate of 5 °C min⁻¹ and kept at 800 °C for 2 hours.

Protocol CE: Calcined under pure hydrogen atmosphere from room temperature up to 500 °C at a heating rate of 5 °C min⁻¹ and kept at 500 °C for 2 hours; and then continuously heated up to 800 °C with the same heating rate and kept at that temperature for 6 hours.

Protocol CF was aimed to produce carbon-free Nb-doped TiO₂ nanofibers (CF-NFs) through oxidative removal of the carbon source (PVP), whereas Protocol CE was aimed to produce carbon-embedded Nb-doped TiO₂ nanofibers (CE-NFs) through in situ graphitization of carbon source (PVP) and crystallization of Nb-doped TiO₂ NFs at the same time. The electrospinning of nanofibers together with the heat treatment under Protocol CE is called in-situ reductive embedment (ISRE) strategy to produce carbon-embedded nanofibers.

In the following, each synthesized nanofiber sample will be given a name started by CF or CE standing for carbon-free or carbon-embedded NFs, respectively, followed by its Nb doping level. For instance, CF10 or CE10 represents carbon-free or carbon-embedded 10 at. % Nb-doped TiO₂ NFs, respectively.

4.2.2 Pt catalyst synthesis

All of 20 wt. % Pt deposited NFs were prepared by using microwave-assisted polyol technique[25]. We also used the same method to deposit 20 wt. % Pt onto conventional carbon black (Vulcan XC-72R, Cabot Corp.) catalyst supports. In a typical synthesis, 40 mg of the desired catalyst support was sonicated in 15 mL of ethylene glycol for ~ 2 hrs until it formed a well-dispersed support mixture. Separately, a Pt precursor solution was prepared by adding 27 mg of chloroplatinic acid hexahydrate (H₂PtCl₆.6H₂O) into 1 mL of Deionized water (DI) water and ethylene glycol solvent mixture, with a 1:1 volumetric ratio. Pt precursor solution was then added dropwise to the well-dispersed support mixture and stirred for 1 hr to form a uniform solution. Later using a micropipette, the pH value of the uniform solution was adjusted to 10 by adding 0.1 M NaOH solution in ethylene glycol, also stirred for another 2 hrs before introducing into the microwave reactor. This solution then was reduced at 185 °C for 2 mins in a Biotage[®] (Initiator Classic) microwave reactor. After cooling the reduced solution to 50 °C, the reduction treatment was repeated for another time to assure fully reduction of the Pt cations. The resulting suspension (catalyst + solvent) was centrifuged at 5000 rpm (Sorvall[™], ThermoScientific) for 30 mins and then

the solvent replaced by fresh DI water. The centrifuging and solvent-replacement cycle was repeated several times (3 to 5 times) until the washed-out DI water achieved pH of 7. The washed catalysts were finally vacuum-dried at 80°C for overnight.

In this paper Pt deposited catalysts were denoted as: 20 wt.% Pt/CF10, 20 wt.% Pt/CE10, 20 wt.% Pt/CF25, 20 wt.% Pt/CE25, and 20 wt.% Pt/Vulcan.

4.2.3 Physical characterizations

The micromorphology of synthesized NFs was examined by scanning electron microscopy (FEI Quanta 200 FEG equipped with an energy-dispersive spectrometer EDAX SiLi Detector) in secondary mode at 6 kV to get more details from the surface of NFs. Powder X-ray diffraction (PXRD) measurements were performed on a Bruker D8 Discover diffractometer equipped with a Vantec-500 area detector and GADDS software package. The X-ray tube was operated at 40 kV and 40 mA with CuK α 1 monochromatized radiation source (wavelength = 1.54187 Å) and an initial beam diameter of 0.5 mm was used. Any possible instrumental error in PXRD patterns were corrected according to the standard corundum reference sample with known diffraction peaks. Van der Pauw method[36] was used to measure the electronic conductivity of the samples. For conductivity measurements, the powder samples were made into pellets of 13 mm in diameter and about 3 mm in thickness using a stainless steel die in a hydraulic press under a pressure of 5000 pounds-force. To obtain reliable data, a liquid metal alloy (Gallium-Indium eutectic alloy, Sigma-Aldrich) was used at the interface between probes and pressed pellets. Multiple measurements have been made at different orientations and the average readings have been reported with a unit of S cm⁻¹. The pore size and surface area analyser (NOVA 1200e, Quantachrome Instruments) equipped with NovaWin software package used for surface area and average pore size measurement. The total amount of adsorbed nitrogen onto supports at relative pressures P/P₀ (adsorptive pressure/saturated vapour pressure) between 0.01 to 0.3 have been used for BET surface area measurements, the measurements were performed at a constant temperature of 77 °K (-196 °C). The t-method of de Boer [37], offered by NovaWin software [38, 39], used for the calculation of external surface area, i.e., the area of pores with diameters (D) larger than 2 nm. The slope and intercept of the obtained t-plots using NovaWin software correspond to external

surface area and micropore volume, respectively. Further, the pore size distributions were calculated from desorption branch of the isotherms using Barrett, Joyner and Halenda (BJH) method [38]. Raman spectroscopy measurements were conducted on an inVia Raman microscope (Reinshaw) by using an argon laser with an excitation wavelength of 514.5 nm and an objective lens of x50 magnification. Curve fittings for the determination of Raman spectra parameters were performed by using Origin software (OriginLab, Northampton, MA). Spectra were fitted by using Levenberg-Marquardt fit algorithm[40] with r-square values close to 1.

Thermogravimetric analyses (TGA) were performed on a thermal analysis (TA) instrument (SDT Q600) under air stream with a heating rate of 3 °C min⁻¹ from room temperature to 1050 °C. High resolution transmission electron microscopy (HRTEM) and scanning transmission electron microscopy (STEM) images were taken at an image-corrected low-base microscope (FEI Titan), operated at 300kV, equipped with an x-sight EDS detector with the INCA processing software (Oxford Instruments). X-ray photoelectron spectroscopy (XPS) measurements were performed on an Axis Ultra X-ray photoelectron spectrometer (Kratos analytical). Powder samples were pressed into indium foil using a clean glass slide before XPS measurements. Both survey scans and high resolution analyses were carried out with an analysis area of 300 × 700 microns and pass energies of 160 eV and 20 eV, respectively. The instrument work function was calibrated to give a binding energy (BE) of 83.96 eV for the Au 4f_{7/2} line for metallic gold and the spectrometer dispersion was adjusted to give a BE of 932.62 eV for the Cu 2p_{3/2} line of metallic copper. The Kratos charge neutralizer system was used on all specimens. Spectra were charge corrected so that the main line of the carbon 1s spectrum (adventitious carbon) set to 284.8 eV.

4.2.4 Electrochemical characterizations

Electrochemical characterizations were conducted in a conventional three-electrode system contained in a glass cell using a rotating disk electrode (BASi RDE-2). Pt wire and saturated Ag/AgCl electrodes were used as counter and reference electrodes, respectively. A 0.076 cm² (D = 3 mm) area glassy carbon (GC) rotating disk electrode (RDE) with a tip coated with a thin layer of catalyst served as the working electrode. Before coating the

catalyst onto GC electrode, the catalyst ink was prepared through sonicating 3 mg of the desired catalyst in 1.5 mL of isopropanol for 20 mins. Then, 5 μ L of the prepared catalyst ink, while it is sonicating, was taken by a micropipette and dropped onto pre-polished GC electrode. By doing so, the total catalyst loading onto the GC electrode would be 10 μ g (2 μ g of Pt). Afterwards, they were left at room temperature for solvent evaporation, and then were impregnated by 2 μ L of diluted Nafion ionomer solution (5 wt. % in aliphatic alcohols, Type: D-520 from DuPont) to form a thin protective layer on top of the coated catalyst layers. Finally, the prepared working electrodes were ambient-dried slowly at room temperature for overnight before any electrochemical tests.

After the dried working electrodes were introduced into the electrolyte for further electrochemical measurements, they were activated through applying cyclic voltammograms (CVs) on them until a steady CV was obtained. All CVs were performed in Ar saturated solutions of 0.5 M H₂SO₄ between 0 V to 1.2 V versus to the reversible hydrogen electrode (RHE) at a scan rate of 50 mV/s. To investigate the electrochemical durability of the catalysts, 1000 full potential cycles were performed in the range of 0 V to 1.2V vs. RHE at a scan rate of 50 mV s⁻¹. To check the electrochemical durability of the catalysts, the electrochemically active surface areas (ECSA) were calculated and compared for the fresh catalysts (those have been already activated) and potentially cycled catalysts after 100, 500, and 1000 cycles. The ECSAs were calculated through the charge integration under the hydrogen adsorption peaks appearing between 0.05 and 0.38 V (RHE) in the negative going potential sweep [41]. For ECSA calculations, a standard hydrogen monolayer desorption charge of 210 μ C cm⁻² on a pure Pt surface was assumed [41].

For Oxygen Reduction Reaction (ORR) mass activity measurements, linear sweep voltammograms were recorded at a scan rate of 5 mV s⁻¹ in O₂ saturated solutions of 0.5 M H₂SO₄ with a rotation speed of 1600 rpm at room temperature and ambient pressure. To check the durability of catalysts, the ORR mass activities were reported and compared for fresh catalysts and potentially cycled catalysts after 1000 cycles. The linear current-voltage curves at the negative sweep scan at the potential range of 0.4 V to 1.1 V were used for ORR measurements. The ORR mass activities, with a unit of mA mg_{Pt}⁻¹, were estimated

via calculation of I_k (kinetic current) using mass transport correction for thin-film RDEs (Eq. 4.1) and normalization to the Pt-loading of the working electrode [41]:

$$I_k(mA) = \frac{I_{lim}(mA) \times I(mA)}{(I_{lim}(mA) - I(mA))} \quad (4-1)$$

Where I is the measured current at 0.9 V vs. reversible hydrogen electrode (RHE), I_k is the kinetic current and I_{lim} is the measured diffusion limited current at 0.4V. All potentials were reported versus to RHE using Eq. 4.2 and all ORR polarization curves were corrected by subtracting background current under steady state and N₂ atmosphere.

$$E (RHE) = E \left(Ag/AgCl \right) + 0.197 + 0.0592 \times pH \quad (4-2)$$

Specific activities at 0.9 V, with a unit of A mPt⁻², were all reported through dividing corresponding mass activities (I_k) with ECSAs [42].

4.3 Results and discussion

4.3.1 Carbon-embedded/carbon-free Nb-doped TiO₂ nanofibers as catalyst supports

4.3.1.1 Micromorphology

Fig. 4.1 shows that all CF-NFs and CE-NFs at different doping levels of Nb, i.e. 10 and 25 at. %, were fabricated with diameters in the range of 70 – 100 nm. Scanning electron microscopy (SEM) studies also reveal an easily distinguishable difference between the surface morphology of the carbon-free and the carbon-embedded nanofibers. CF-NFs, as shown in Figs. 4.1a and 4.1b, are exhibiting pearl-like morphology with relatively smooth

surfaces whereas the surfaces of CE-NFs, as shown in Figs. 4.1c and 4.1d, resembles more likely a bumpy and porous surface.

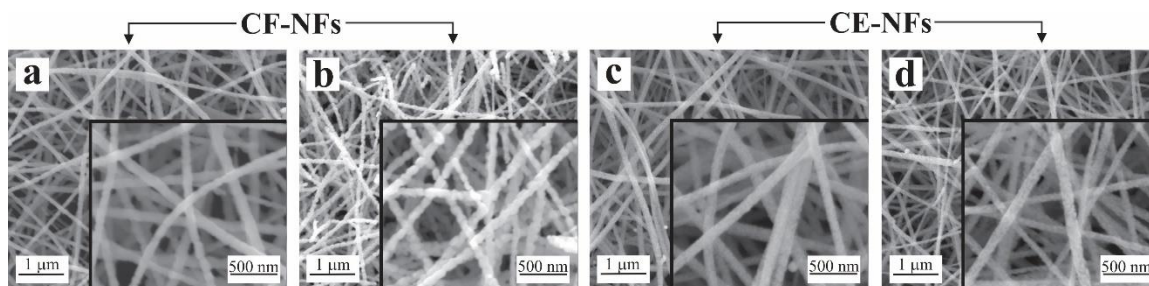


Figure 4.1. Field emission-SEM images of Nb_xTi_(1-x)O₂ (x= 0.1 and 0.25) NFs heat treated under either protocol CF or CE. (a) CF10; (b) CF25; (c) CE10; and (d) CE25.

4.3.1.2 Crystal structure, electronic conductivity and surface area

Table 4.1 summarizes the physical properties of CF and CE nanofibers which were subjected to different heat treatments. The results will be explained in sequence at the following paragraphs.

Table 4.1. Physical Properties of synthesized Nb_xTi_(1-x)O₂ nanofibers and Vulcan XC-72R as reference.

Heat Treatment Protocol	Catalyst Support Name	Rutile Crystallite Size ^a (nm)	Rutile Percentage (%)	Electronic Conductivity (S.cm ⁻¹)	BET Surface Area (m ² .g ⁻¹)	External Surface Area (m ² .g ⁻¹)	BJH Pore Volume (mL.g ⁻¹)	Average Pore Diameter (nm)
CF	CF10	15	94	5 × 10 ⁻⁶	17	17	0.03	6.5
	CF25	15	94	6 × 10 ⁻⁶	16	15	0.03	7
CE	CE10	8	85	0.12	102	86	0.19	7.5
	CE25	9	87	0.05	105	90	0.19	7
-	Vulcan XC-72R	-	-	4	225	105	0.25	4

^aFrom Scherrer equation

Powder X-ray diffraction (PXRD) analysis was used to investigate the crystal structure of the Nb_xTi_(1-x)O₂ (x = 0.1 and 0.25) nanofibers prepared in the Clean Powertrain Lab at the University of Windsor, Fig. 4.2.

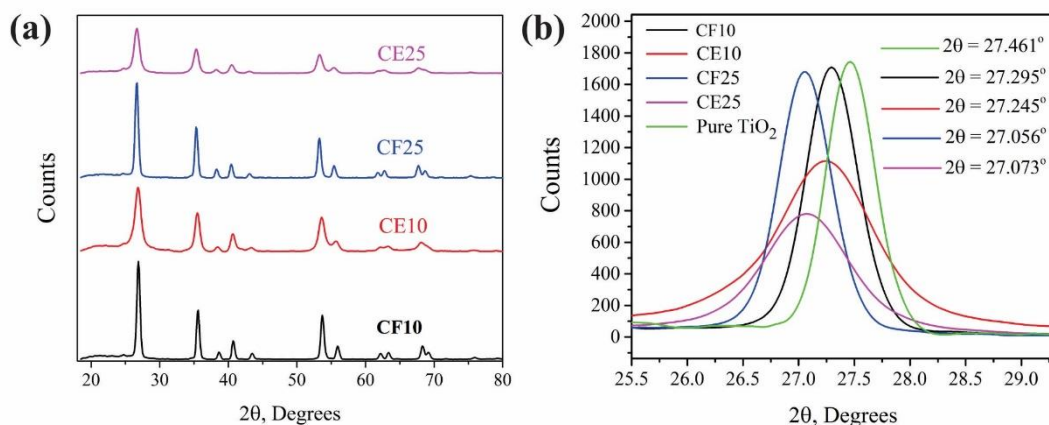


Figure 4.2. PXRD patterns collected from Nb_xTi_(1-x)O₂ (x = 0.1 and 0.25) NFs heat treated under either protocol CF or CE. (a) Wide-angle patterns; (b) magnified views of the rutile (110) peak.

Fig. 4.2a shows that all four types of nanofibers consist of anatase and rutile polymorphs of TiO₂, although the presence of strong reflection of rutile phase at 2θ values around 27.30 verifies the predominance of rutile phase; rutile phase percentages [43] are in the range of 85-94% (Table 4.1). Rutile phase crystallite sizes from the Scherrer equation [44] were smaller for CE-NFs than that for CF-NFs, as shown in Table 4.1. Furthermore, niobium incorporation into rutile lattice of all four samples has been confirmed by the following facts: first, no distinct features of niobium oxide or ternary phases in Fig. 4.2a; and second, observed significant shift of main rutile peaks to lower 2θ values, about 27.03-27.29°, while the reflection of a pure rutile phase was observed at 2θ = 27.46° very close to the reported value [43] of 2θ = 27.45° as shown in Fig. 4.2b. Accordingly, the observed shifts were caused most probably by doped Nb⁴⁺/Nb⁵⁺ into titania lattice due to their larger ionic radiuses versus Ti⁴⁺ (0.68/0.64 Å vs. 0.605 Å for Nb⁴⁺/Nb⁵⁺ vs Ti⁴⁺ for a coordination number of six) [45, 46].

Figure 4.3 shows, for all four Nb-doped TiO₂ NFs and a commercial Vulcan XC-72R carbon catalyst support, the nitrogen adsorption/desorption isotherms for surface area analysis, and the BJH pore size distributions. The extracted results from Fig. 4.3 are as summarized in Table 4.1. As shown in Fig. 4.3a, CF-NFs exhibited low sorption capacity for N₂ whereas CE-NFs exhibited N₂ adsorption/desorption isotherms which can be classified as type IV isotherm, typical of mesoporous materials with strong affinities based on international union for pure and applied chemistry (IUPAC) classification [47, 48].

The mesoporous structures of CE10 and CE25 NFs were further confirmed by their BJH pore size distributions centered around 10 nm despite their relatively high temperature reduction treatment at 800 °C. On the other hand, the positive intercept of the t-plots (Fig. SI-4.1) obtained for CE-NFs along with Vulcan XC-72R exhibits the presence of micropores (with diameters less than 2 nm) along with mesopores (with diameter between 2 to 50 nm). In fact, the relevant external surface area of the catalyst support is best estimated by subtracting the micropore area from the BET surface area as micropores are not beneficial to hold either Pt nanoparticles or Nafion [39, 49]. Comparing with commercial Vulcan XC-72R, as shown in Table 4.1, although CE-NFs showed just half the BET surface area (105/102 vs 225 m² g⁻¹) while their external surface area was only lower by about 10% (90/86 vs. 105 m² g⁻¹).

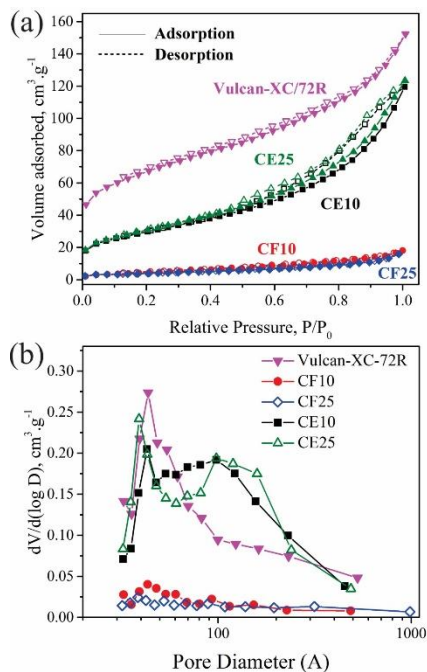


Figure 4.3. Surface area and pore size analysis of Nb_xTi_(1-x)O₂ (x = 0.1 and 0.25) NFs heat treated under either protocol CF or CE. (a) Nitrogen adsorption/desorption isotherms (BET); and (b) BJH pore size distribution plots.

Overall the physical properties summarized in Table 4.1, first, confirm the predominance of rutile phase in our Nb-doped TiO₂ nanofibers which agrees well with previously observed higher electronic conductivities for rutile phase titania than anatase [23, 33]; second, by showing higher external surface areas and smaller crystallite sizes for CE- than CF-NFs, agree well with more porous surface morphology observed for CE-NFs, as shown in Figs. 4.1c and 4.1d. Similarly, the surface smoothness and pearl like morphology of CF-NFs, as shown in Figs. 4.1a and 4.1b, correlates very well with their measured relatively low BET surface areas (Table 4.1) and this effect of high temperature reductive treatment is consistent with literature for CF-NFs [24]. Furthermore the mesoporous structure of CE-NFs combined with comparable external surface areas and electronic conductivities to those of Vulcan XC-72R suggests that the carbon embedment is critical for making practical catalysts supports.

4.3.1.3 Carbon content and thermal stability

TGA analysis was used to determine the content of carbon embedded in NFs by assuming that no carbon is lost below 400 °C and weight loss above 400 °C is exclusively due to oxidative loss of carbon [27]. As shown in Fig. 4.4, CE-NFs (CE10, CE25) are mainly losing weight, ~ 10-11%, after 300 °C along with less significant weight gains around 450 °C while CF-NFs (CF10, CF25) are exhibiting only weight gains. The observed weight gains, around 0.5-1% (the theoretical weight gains through complete oxidation of pure NbO₂ and Ti₄O₇ are 6.4% and 5.3%), at a temperature range of 250-550 °C, are most probably induced by the oxidation of small quantities of Ti₄O₇ and/or NbO₂ into most stable oxides TiO₂ and/or Nb₂O₅ at the surface of nanofibers [22]. The temperature that the weight gain started for CF25 NFs is well below than that for CF10. The observed lower phase transformation temperature for CF25 NFs could suggest that the CF25 has more of NbO₂ than Ti₄O₇ because Ti₄O₇ has higher phase transformation temperature [22], XPS measurement results also agree well with this statement as explained later. Moreover, the temperature that the embedded carbon initiated to oxidize is lower in CE-NFs than in graphitized carbon nanoparticles [27], 300 vs 450 °C. This observation could suggest either the embedment of carbon into NFs in the forms of smaller domains than carbon NPs (with a diameter in the range of 20-40 nm) or the presence of some quantities of amorphous carbon. Earlier studies on the thermal oxidation of carbon nanotubes observed lower decomposition temperatures for small- than larger-diameter nanotubes due to increased steric strain [50] or amorphous than graphitized nanotubes [51].

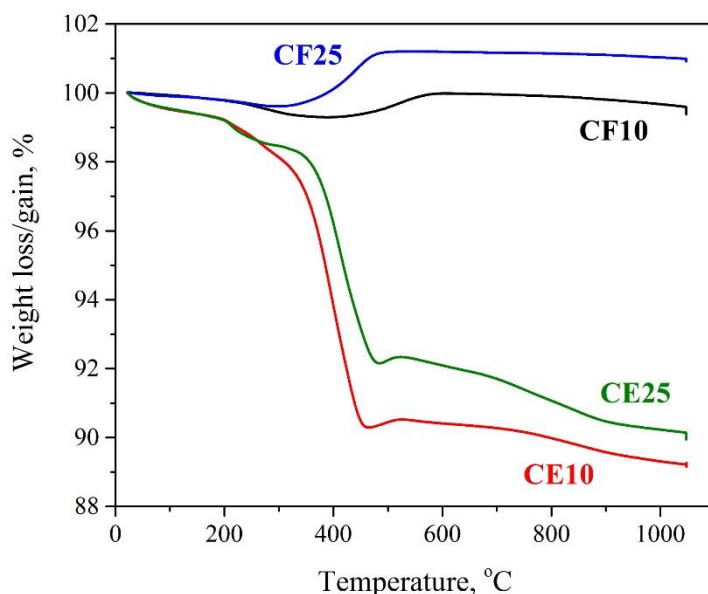


Figure 4.4. TGA data plots obtained for Nb_xTi_(1-x)O₂ (x = 0.1 and 0.25) NFs heat treated under either protocol CF or CE.

TGA data plots were also used to determine the thermal stability of synthesized CF and CE nanofibers. Fig. 4.4 clearly showed that any noticeable weight gain or weight loss happens at temperatures higher than 200 °C which makes the thermal stability of all of our synthesized NFs to be acceptable for PEM fuel cell applications operating at temperatures between 50 – 200 °C [52].

4.3.1.4 Atomic structure of embedded carbon

Raman spectroscopy was utilized as a standard method [53] to investigate the atomic structure of embedded carbon, Fig. 4.5a. Raman spectra of all four Nb-doped TiO₂ nanofibers (Table 4.1) show the characteristic first-order absorption bands of ordered/disordered graphite at frequencies between ~ 1200 to ~1650 cm⁻¹ [40, 54] along with three distinct rutile phase characteristic peaks at 244, 442, and 607 cm⁻¹ [55-57] for both CF- and CE-NFs, as shown in Fig. 4.5a. The observation of less intensive first order bands of ordered/disordered graphite for CF-NFs (CF10, CF25) could suggest incomplete oxidation of carbon source (PVP) even after air calcination treatment at 500 °C for 6 hrs (Protocol CF) and to complete the oxidation it needs either more time or higher

temperature. The combination of five bands were used for the analysis and determination of the peak parameters of characteristic first-order and second-order absorption bands of the embedded carbon in CE-NFs [40]. The complete list of these five bands, G and D1-D4, is shown in Table SI-4.1 along with their corresponding band positions and descriptions. The G-band is assigned to in-plane vibrations of the sp² carbon framework and the D-band (D1 - D4 bands) is associated with carbon atoms at edges, amorphous and sp³ carbons [40, 54, 58]. Figs. 4.5b and c shows the peak analysis results for CE10 and CE25 nanofibers, respectively. The higher D/G intensity (peak area) ratio (Table SI-4.2) generally interprets as distorted graphite lattice [40, 53]. As shown in Figs. 4.5b, 4.5c and Table SI-4.2, for both CE10 and CE25 nanofibers all of four D (D1-D4) bands have been observed and the highest band area ratio, $A_{DX\text{-band}}/A_{G\text{-band}}$ ($X = 1, 2, 3, 4$), belongs to D1 band known for vibrations of sp³ carbons at graphene layer edges with A_{1g} symmetry [53, 59]. In an early Raman work, D3 and D4 peaks were only assigned to the vibrations seen on soot [40] but later Hara et al. [59] observed them even in the Raman spectra collected from graphitized carbon blacks (GCB) used as a catalyst support for PEM fuel cells. However, the first-order DX/G band area ratios reported in Table SI-4.2 are relatively higher than reported ratios for GCB [59], by a factor around 4. This difference could be due to the relatively higher degree of distortion in the graphite lattice of the embedded carbons in our CE-NFs than that of GCB or the statistical uncertainty in relative intensities (peak area ratios DX/G) introduced by deconvolution of the broad signal peaks into multiple peaks through the peak analysis [40].

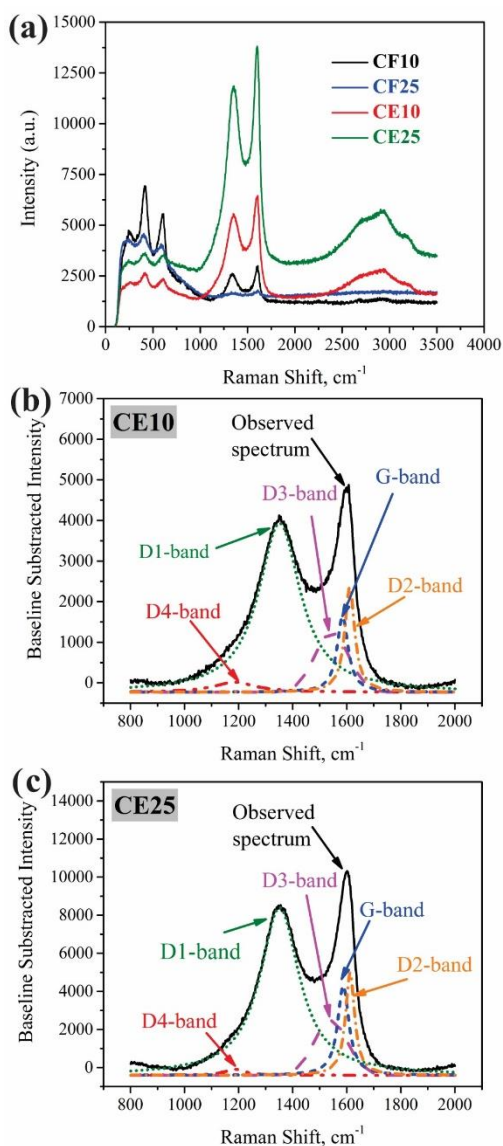


Figure 4.5. Raman Spectra of Nb_xTi_(1-x)O₂ (x = 0.1 and 0.25) NFs heat treated under either protocol CF or CE along with peak analyses of CE-NFs based on the combination of bands given in Table S1. (a) Raman spectra; (b) peak analyses of first-order bands of ordered/disordered graphite observed for CE10 and CE25.

Furthermore recorded Raman spectra of the CE-NFs depict pronounced second order characteristic bands for disturbed graphitic structures at frequencies around 2000 to 3500 cm⁻¹, as shown in Fig. 4.5a. Fig. SI-4.2 shows the peak analysis results for second order bands with a combination of four Lorentzian-shaped bands centered around 2700, 2900 and 3100 cm⁻¹ which are consistent with literature [40].

4.3.2 Pt catalysts supported by carbon-embedded/carbon-free Nb-doped TiO₂ nanofibers

4.3.2.1 Nanostructure and nanomorphology

20 wt. % Pt nanoparticles were deposited onto synthesized Nb-doped TiO₂ NFs through microwave-assisted polyol technique [25]. PXRD patterns of NFs after deposition of Pt nanoparticles are shown in Fig. SI-4.3. Comparing with Fig. 4.2, the additional reflections located at 2θ values of 39.80, 46.28, and 66.53° shown in Fig. SI-4.3 agree well with the reflections of metallic Pt at these 2θ values [60]. The size of Pt crystallites which have been deposited onto both CF- and CE-NFs were estimated to be in average of 6 nm, using Scherrer equation [44].

Figs. 4.6a and 4.6c show BF-TEM images of 20 wt. % Pt/CE10 nanofibers, while high-resolution images of the selected areas in Figs. 4.6a and 4.6c are shown in Figs. 4.6b, 4.6d, and 4.6e. As shown in Fig. 4.6a and low magnification TEM images in Fig. SI4.4, there is a high and uniform coverage of Pt NPs onto CE10 nanofibers. However, a few areas, i.e. Fig. 4.6c, are poorly coated and exhibiting different support morphology with relatively larger domains in the range of 30 to 40 nm. The predominance of rutile phase titania in CE10 nanofibers confirmed by correlation of both of the collected selected area diffraction (SAD) pattern from a single Pt deposited NF, inset of Fig. 4.6a, and interplanar spacings of 0.33 and 0.27 nm between lattice fringes, Figs. 4.6b and 4.6e, with the d-spacing between (110) and (101) planes in rutile lattice, matching the powder diffraction of file no. 01-089-554 from the international centre for diffraction data (ICDD). Furthermore the HRTEM images (Figs. 4.6b and SI-4.4c, showed that spherical Pt NPs are mostly single crystals with an interplanar spacing of 0.22 nm matching with the d-spacing between (111) planes in pure metallic Pt, diameters are between 3-5 nm shown in Fig. SI-4.4c.

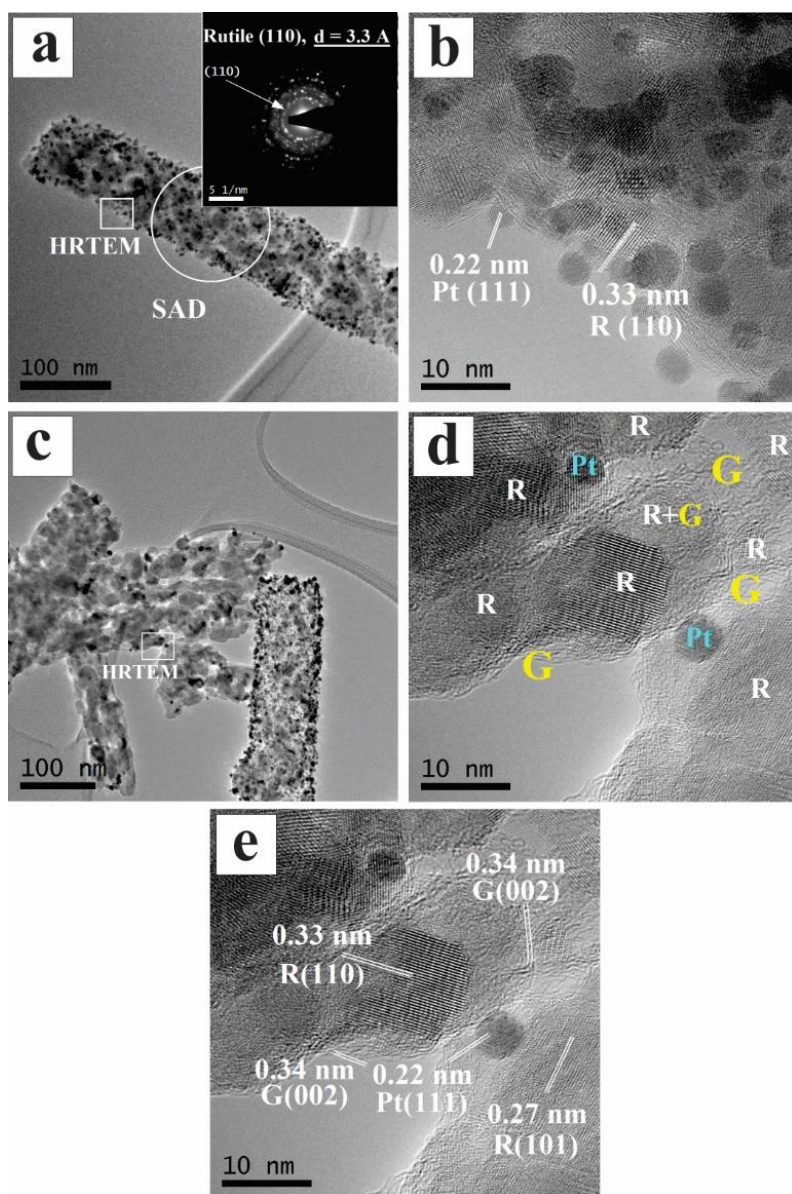


Figure 4.6. Bright field (BF) TEM and HRTEM images from 20 wt. % Pt deposited CE10 NFs. (a) TEM image from a single Pt deposited NF along with collected SAD pattern; (b) HRTEM image from a selected area shown in (a); (c) TEM image from Pt deposited nanofibers with relatively different morphologies; (d) HRTEM image from a selected area shown in (c).

We further observed that graphite-like crystalline domains containing turbostratically stacked graphene layers with interplanar d-spacing of 0.34 nm are either embedded in between rutile domains of NFs (as shown in Figs. 4.6d and 4.6e) or inlaid onto NFs (as in

Fig. SI4.4c). To be able to quantify both carbon content and bulk Ti:Nb atomic ratio, energy dispersive X-ray spectroscopy (EDX) measurements were taken in scanning transmission electron microscopy (STEM) mode. Dark field (DF) images along with collected EDX measurements from two areas with different Pt dispersions and support morphologies are shown in Fig. SI-4.5. The Ti:Nb atomic ratio calculated from EDX spectrum taken from a single Pt coated nanofiber, Figure SI-4.5a, which exemplifies the majority of the NFs, is 1:0.107, close enough to the targeted ratio of 1:0.11 for CE10 nanofibers. However, there are still a few areas with ratios of 1:0.19, which suggests the formation of domains (i.e. 16 at. % Nb-doped TiO₂) enriched with NbO₂, whereas the formation of larger crystalline domains in these areas remain uncertain. Furthermore presence of 22 at. % carbon in both taken EDX spectra, as shown in Fig. SI-4.5, suggests homogeneous embedment of carbon into CE10 nanofibers.

Overall TEM and HRTEM studies confirm the following facts: first, the crystal structure of nanofibers are mainly rutile which agrees well with PXRD patterns; second, the Pt nanoparticles are uniformly dispersed onto nanofibers in the form of single crystals which is critical for the increase of Pt utilization; third, the embedment of carbon into/onto NFs is relatively homogeneous in the form of stacked graphene layers with highly distorted graphitic structure, which correlates very well with Raman spectroscopy measurements as discussed in section 4.3.1.4.

4.3.2.2 Elemental composition, chemical and electronic state at the surface

X-ray photoelectron spectroscopy (XPS) measurements were used to further investigate the surface elemental composition and electronic state of the synthesized Pt catalysts supported by Nb-doped TiO₂ NFs. For Pt catalysts, the XPS survey spectra and the XPS high-resolution spectra at C, O, Ti, Nb, and Pt primary XPS regions are shown in Figs. SI-4.6 to SI-4.9, inclusive, and Figs. SI-4.10 to SI-4.14†, respectively. The peak deconvolution results obtained from these high resolution spectra were tabulated in Tables SI-4.3 to SI-4.7, inclusive.

From survey spectra, Figs. SI-4.6 to SI-4.9 inclusive, photoelectron peaks have been revealed for C 1s (284.35 eV), O 1s (530.75 eV), Ti 2p (458.65 eV), Nb 3d (207.35 eV), and Pt 4f (71.55 eV). The relative surface elemental composition of Pt catalysts supported

by both CF- and CE-NFs are shown in Table 4.2. The quantification of survey spectra were performed through integration of respective XPS peak for each element.

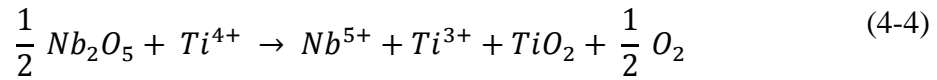
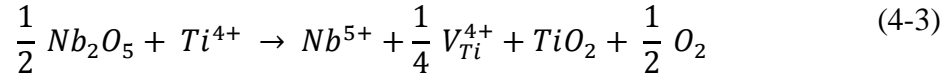
Table 4.2. Relative surface elemental composition of the synthesized Nb-doped TiO₂ nanofibers obtained from XPS survey spectra.

	20 wt.% Pt/CF10	20 wt.% Pt/CF25	20 wt.% Pt/CE10	20 wt.% Pt/CE25
Ti:Nb	1:0.08	1:0.32	1:0.12	1:0.35
Ti:Pt	1:0.67	1:0.88	1:0.70	1:0.49
Ti:C	1:1.14	1:1.53	1:4.82	1:4.07
Ti:O	1:3.09	1:3.92	1:3.5	1:3.62

The most obvious differences between the relative surface compositions of synthesized Pt catalysts were in the niobium and carbon relative atomic concentrations versus to titanium. As shown in Table 4.2, the obtained Ti:Nb ratios at the surface of Pt catalysts correlated very well with the corresponding doping ratios of Nb in their corresponding supporting NFs. We did not observed any considerable surface enrichment/depletion of the Nb versus to the bulk Ti:Nb ratios of 1:0.11 and 1:0.33 for any of supporting CE- or CF-NFs doped with different levels of Nb. We assumed that the niobium surface enrichment/depletion observed in other studies [61, 62] could be due to their relatively long time and high temperature oxidizing/reducing treatments (i.e. reduction at 900 °C for 50 hrs) [61]. Furthermore, the obtained Ti:C ratios at the surface of Pt-deposited NFs also correlated with the type of heat treatment of the corresponding supporting nanofibers. The detected carbon atoms at the surface of Pt-deposited CF-NFs are most probably adventitious carbons [63] (mainly Sp³ bonded carbon that comes from atmosphere) due to their extremely high Sp³/Sp² ratios obtained from their corresponding high resolution XPS spectra in C1s region, Fig. SI-4.10 and Table SI4.3.

In terms of the electronic state of chemical components at the surface, it has been well known that the evolution of the different oxidation states for titanium and niobium in Nb-doped TiO₂ nanoparticles depends on the synthesis condition [39, 46]. The solubility limit of Nb in rutile lattice exhibits high degree of dependency on the synthesis condition, heating temperature and oxygen partial pressure.[46, 64] It has been shown that excessive

Nb doing could lead to the formation of secondary oxides (NbO₂ and Nb₂O₅) or ternary phase of TiNb₂O₇ which are neither electronically conductive nor electrochemically stable [22, 46]. By assuming that the introduced Nb into TiO₂ lattice (within solubility limits) would prefer to stay in pentavalent oxidation state (Nb⁵⁺) rather than tetravalent oxidation state (Nb⁴⁺)- more similar relative radius of Ti⁴⁺ (0.0605 nm) and Nb⁵⁺ (0.064 nm) with the same coordination number of 6- one extra charge of Nb⁵⁺ vs. Ti⁴⁺ must be compensated for charge neutralization. Charge compensation could happen in two different ways depending on having oxidative or reductive condition in the environment (oxygen partial pressure). The two possible reactions can be described by Eqs. (4.3) and (4.4) :[46]



The above two equations were also shown using the Kroger-vink notations[65] in the ESI† (see Eqs. (SI-4.3) and (SI-4.4)). Oxidative condition would be in favour of Eq. (4.3) by preferably keeping cations in their higher oxidation states and compensating the extra charge via the introduction of one Ti⁴⁺ vacancy (V_{Ti}^{4+}) per four Nb⁵⁺ cations. On the contrast, reductive condition would be in favour of Eq. (4.4) by stoichiometrically reducing one Ti⁴⁺ to Ti³⁺ per each pentavalent Nb (Nb⁵⁺) introduced. In heating protocol CF the oxidative condition was provided first to oxidize carbon and then reductive condition was provided at 800 °C, whereas in protocol CE reductive condition was provided from room temperature up to 800 °C (without the introduction of any oxidative condition). In both protocols reductive condition was provided to introduce free electrons into TiO₂ lattice through charge compensation according to Eq. (4.4). Ideally if the charge compensation fully occurs through Eq. (4.4) (without any contribution from Eq.(4.3)) the atomic concentration of Nb⁵⁺ and Ti³⁺ should be equal at the surface, i.e., the compensation degree

($[\text{Ti}^{3+}]_{\text{at.}}/[\text{Nb}^{5+}]_{\text{at.}}$) should be equal to 1 [66]. But if the compensation degree deviates from 1, it suggests that both mechanisms as shown in Eqs. (4.3) and (4.4) contributed to the charge compensation at the same time and some other mechanisms maybe also involved as follow: compensation degree higher than 1 could suggest the direct reduction of Ti^{4+} into Ti^{3+} (e.g. formation of Ti_4O_7 domains) under reductive condition, whereas compensation degree less than 1 could suggest the formation of ternary phases such as TiNb_2O_7 [46] where there is no need for charge compensation.

On the other hand, the detection of any Nb^{4+} at the surface suggests the direct reduction Nb^{5+} into Nb^{4+} without any need for charge compensation (e.g. formation of NbO_2 domains). Here, a combination of three different atomic concentration ratios ($[\text{Ti}^{3+}]_{\text{at.}}/[\text{Nb}^{5+}]_{\text{at.}}$, $[\text{O}_{\text{oxide}}]_{\text{at.}}/[\text{Ti}]_{\text{at.}}$, and $[\text{Nb}^{5+}]_{\text{at.}}/[\text{Nb}^{4+}]_{\text{at.}}$) obtained from high resolution XPS spectra at Nb, Ti, and O regions (Figs. SI-4.11 to SI-4.13 inclusive) will be used to understand the surface electronic and chemical state of both CF- and CE-NFs doped with Nb at two different doping levels.

Table 4.3. Atomic concentration ratios for the supporting NFs obtained from high-resolution XPS spectra shown in Figs. SI-4.11 to SI-4.13, inclusive, and their tabulated peak parameters shown in Tables SI-4.5 to SI-4.7, inclusive.

	20 wt.% Pt/CF10	20 wt.% Pt/CF25	20 wt.% Pt/CE10	20 wt.% Pt/CE25
$[\text{Ti}^{3+}]_{\text{at.}}/[\text{Nb}^{5+}]_{\text{at.}}$	1.27	0.573	0.78	0.335
$[\text{O}_{\text{oxide}}]_{\text{at.}}/[\text{Ti}]_{\text{at.}}$ (Theor. value ^a)	1.76 (2.22)	2.14 (2.66)	2.20 (2.22)	2.75 (2.66)
$[\text{Nb}^{5+}]_{\text{at.}}/[\text{Nb}^{4+}]_{\text{at.}}$	14.6	9.20	18.6	13.5

^aTheoretical values were Calculated for supporting $\text{Nb}_x\text{Ti}_{(1-x)}\text{O}_2$ ($x = 0.1$ or 0.25) nanofibers.

With respect to the $[\text{Ti}^{3+}]_{\text{at.}}/[\text{Nb}^{5+}]_{\text{at.}}$, the higher doping level of Nb, the lower the value of the compensation degree. If we assume that all of Nb^{5+} ions have been doped into TiO_2 lattice (without forming ternary phase), lower compensation degree suggests Eq. (4.3) to be the dominant mechanism for charge compensation. Accordingly, this observation could suggest higher doping levels to be less effective in providing free electrons into TiO_2 lattice through Eq. (4.4). Moreover, the value of 1.27 (compensation degree higher than 1)

obtained for 20 wt. % Pt/CF10 catalyst suggests the direct reduction of Ti⁴⁺ into Ti³⁺ at the surface of CF10 supporting NFs.

With respect to $[O_{\text{oxide}}]_{\text{at.}}/[Ti]_{\text{at.}}$, the values for CF-NFs are lower than the theoretical values, whereas the values for CE-NFs are very close to the theoretical values. Lower values than theoretical values could suggest introduction of oxygen vacancies at the surface of NFs. Accordingly, this observation could suggest formation of more oxygen-deficient oxides at the surface of CF-NFs than CE-NFs. For instance, the $[O_{\text{oxide}}]_{\text{at.}}/[Ti]_{\text{at.}}$ value obtained for supporting CF10 nanofibers is very close to the theoretical value for oxygen-deficient Ti₄O₇ (the theoretical $[O_{\text{oxide}}]_{\text{at.}}/[Ti]_{\text{at.}}$ value for Ti₄O₇ is 1.75). The presence of oxygen-deficient oxides at the surface of CF-NFs also agrees well with the observed weight gains in their corresponding TGA data plots under air stream, as shown in Fig. 4.4.

With respect to $[Nb^{5+}]_{\text{at.}}/[Nb^{4+}]_{\text{at.}}$, the higher doping level of Nb, the lower the values. In addition, for the same doping levels, the values for CF-NFs are smaller than CE-NFs. Smaller $[Nb^{5+}]_{\text{at.}}/[Nb^{4+}]_{\text{at.}}$ value at the surface of NFs could suggest more of the direct reduction of Nb⁵⁺ into Nb⁴⁺ (formation of NbO₂ domains rather than doping into the titania lattice). Accordingly, Of the above two observations- with respect to keeping Nb in its pentavalent oxidation state rather than forming NbO₂ domains- the former suggests 10 at.% to be more effective than 25 at.% Nb doping level and the later suggests Protocol CE to be more efficient than Protocol CF. Formation of NbO₂ domains at the surface of NFs with smaller $[Nb^{5+}]_{\text{at.}}/[Nb^{4+}]_{\text{at.}}$ value also agrees well with the weight gain obtained in the TGA data plot of CF25 nanofibers (with smallest $[Nb^{5+}]_{\text{at.}}/[Nb^{4+}]_{\text{at.}}$ value of 9.2) under air stream, as shown in Fig. 4.4.

Overall, all of the above observations at the surface of supporting NFs suggest the followings: first, the Nb doping level of 10 at.% is more effective than 25 at.% in providing free electrons for TiO₂ lattice which is in agreement with electronic conductivity measurements, see Table 4.1; second, Protocol CE is more effective than Protocol CF in preventing the formation of electrochemically unstable oxygen-deficient oxides which will be discovered by doing electrochemical durability tests under acidic conditions in section 4.3.3.

To further investigate the structure of embedded carbon in CE-NFs, high-resolution XPS spectra at C 1s region, as shown in Fig. SI-4.10 and Table SI-4.3, have been used to calculate Sp³/Sp² hybridization ratios [63]. The main peak of XPS C 1s spectra were fitted by two peaks centred around 284.47 - 284.63 and 284.77 - 284.93 corresponding to Sp² and Sp³ bonded carbons [67]. Table SI-4.4 clearly showed that, in terms of predicting highly distorted graphitic structure, the calculated Sp³/Sp² hybridization ratios for both 20 wt. % Pt/CE10 and 20 wt. % Pt/CE25, 2.26 and 1.86 respectively, are in agreement with DX/G band area ratios (Table SI-4.2) obtained from the peak analysis of their corresponding Raman spectra. In addition, high-resolution XPS spectra collected from Pt catalysts supported by CE or CF nanofibers at Pt 4f region (Fig. SI-4.14 and Table SI-4.7), confirmed the presence of Pt NPs only in the form of metallic Pt at the surface of supporting NFs.

4.3.3 Electrochemical activity and durability of Pt catalysts for oxygen reduction reaction

The electrochemical characteristics of Pt catalysts supported by either Nb-doped TiO₂ NFs or Vulcan XC-72R were examined via potential cycling in a conventional three electrode system, the electrochemical characteristics of a commercial carbon black-based Pt catalyst (Hi Spec 40 wt. % Pt/C, Johnson Matthey) was also examined as a reference. Table 4.4 summarizes the electrochemical data (before and after durability tests) obtained from both cyclic and linear sweep voltammograms. The results will be explained in sequence at the following subsections.

Table 4.4. ECSA and ORR mass activities at 0.9 V measured for 20 wt. % Pt/Nb-doped TiO₂ nanofiber and 20 wt. % Pt/Vulcan catalysts before and after Durability Tests (potential cycling experiments).

Catalyst	Before Durability Tests			After Durability Tests	
	ECSA, m ² g ⁻¹	Mass activity @ 0.9 V, A g _{Pt} ⁻¹	Specific activity @ 0.9 V, A m _{Pt} ⁻²	ECSA, m ² g ⁻¹ (% of retention)	Mass activity @ 0.9 V, A g _{Pt} ⁻¹ (% of retention)
20 wt.% Pt/CF10	25	7	0.28	19.5 (78)	5.6 (80)
20 wt.% Pt/CF25	23	7	0.30	17.48 (76)	5.4 (79)
20 wt.% Pt/CE10	39	17	0.43	31.6 (81)	14.5 (85)
20 wt.% Pt/CE25	34	14	0.41	26.18 (77)	11.5 (82)
20 wt.% Pt/C	67	19	0.28	44.2 (66)	13.5 (71)
HiSpec 40 wt.% Pt/C	65	19	0.29	44 (68)	13.7 (72)

4.3.3.1 Electrochemical activity of Pt catalysts before durability tests

With respect to the electrochemically active surface areas (ECSAs) of fresh catalysts under acidic conditions, cyclic voltammograms were recorded in Ar-saturated solutions of 0.5M H₂SO₄ (shown in Fig. 4.7a). As shown in Fig. 7a, Pt catalysts supported by Vulcan XC-72R (20 wt.%Pt/C) or CE-NFs (20 wt.%Pt/CE10 and 20 wt.%Pt/CE25), were exhibited characteristic hydrogen adsorption/desorption (in the potential range 0.05-0.35 V) and Pt oxide formation (potentials larger than 0.75 V) and reduction (in potential range 0.5-1 V) peaks, whereas Pt catalysts supported by CF-NFs (20 wt.%Pt/CF10 and 20 wt.%Pt/CF25) were only exhibited much less significant hydrogen adsorption/desorption peaks. Among Pt catalysts supported by CF- or CE-NFs, the observed lower faradaic and nonfaradaic currents for those supported by CF-NFs than CE-NFs (as shown in Fig. 4.7a) was expected due to extremely lower electronic conductivities and lower external surface areas of CF-NFs, see Table 4.1. Accordingly, the obtained ECSA values were lower for Pt catalysts supported by CF-NFs than those supported by CE-NFs, as shown in Table 4.4. Moreover, despite having similar external surface areas, the ECSA values obtained for Pt catalysts supported by CE-NFs were still remarkably lower than those supported by carbon

blacks, most probably due to higher electronic conductivity of carbon blacks, i.e. 4 vs. 0.12 S cm⁻¹.

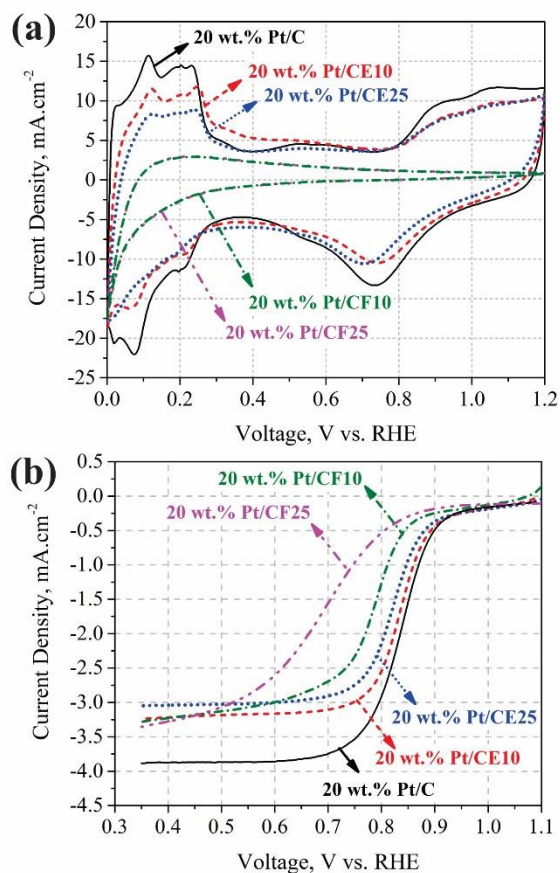


Figure 4.7. Cyclic voltammograms (CV) and linear sweep voltammograms (LSVs) obtained for different Pt catalysts. (a) CVs obtained in Ar-saturated aqueous solutions of 0.5M H₂SO₄ at a potential scan rate of 50 mV/s; and (b) LSVs obtained in O₂ saturated aqueous solutions of 0.5M H₂SO₄ with a potential sweep rate of 5 mV/s and rotation speed of 1600 rpm.

With respect to the electrochemical activity of fresh catalysts for oxygen reduction reaction (ORR), linear sweep voltammograms (LSVs) were recorded in O₂ saturated solutions of 0.5M H₂SO₄ (Shown in Fig. 4.7b). As shown in Fig. 4.7b, three diffusion limited (0.35 V to 0.7 V), mixed diffusion-kinetic limited (0.7 V to 0.9 V) and purely kinetically controlled (> 0.9V) regions which are relevant to ORR process have been observed in all of our synthesized Pt catalysts.[68, 69] Less purely diffusion limited region

(0.35 V to 0.7V) has been observed for Pt catalysts supported by CF-NFs which is most probably due to low electronic conductivity of CF-NFs. As shown in Table 4.4, ORR mass activities were also significantly lower for Pt catalysts supported by CF-NFs than those supported by CE-NFs. However, less notable difference can be noticed between fresh (before durability tests) ORR mass activities obtained for Pt catalysts supported by CE-NFs and those supported by carbon blacks, about 11-35% higher for carbon black, despite remarkably higher ECSAs obtained for Pt catalysts supported by carbon blacks (about 55-100%). The higher activity of Pt nanoparticles onto Nb-doped TiO₂ nanofibers have been best represented by their specific activities with a unit of A m_{Pt}⁻². Much higher specific activities of Pt nanoparticles supported by CF- or CE-NFs in comparison to commercial carbon black supports (0.43 vs. 0.28 A m_{Pt}⁻² for 20 wt.% Pt/CE10 vs. 20 wt.% Pt/C) is known to be due to synergetic interaction between Pt nanoparticles and metal-oxide based supports [2, 28, 70, 71].

Furthermore, to determine whether ORR reaction produces H₂O (4-electron pathway) or H₂O₂ (2-electron pathway), Koutecky-Levich equation [27, 72] (see SI Chapter 4) was used. The linear relationship between the reciprocal of the experimentally measured current densities at 0.4 V (j⁻¹) vs. ω^{1/2} in Fig. SI-4.15f can be taken as an indication of the first order reaction with respect to dissolved oxygen. The experimental value of the slopes (1/B) of the K-L plots for all Pt catalysts supported by CF- or CE-NFs were between 2.75 to 2.85 which agree, within experimental errors, with the theoretical slope value of 3.1 (B=0.32)[73] for 4-electron pathway. This suggests that the number of exchanged electrons in ORR reactions are close to 4 and as a result all of our synthesized 20 wt. % Pt catalysts supported by CF- or CE-NFs are mainly forming water without generating considerable amounts of hydrogen peroxide as side product.

4.3.3.2 Electrochemical activity of Pt catalysts after durability tests

To track the ECSAs, Pt catalysts were subjected to continuous potential cycling between 0 to 1.2 V and the obtained cyclic voltammograms after applying 100, 500 and 1000 full potential cycles were shown in Figs. 4.8a, 4.8b, and 4.8c; ECSA values after applying 1000 potential cycles (after durability tests) are shown in Table 4. At the same time, to track ORR mass activities, LSVs were also recorded in O₂ saturated solutions of 0.5M H₂SO₄

before and after durability tests as shown in Figs. 4.8d, 4.8e, 4.8f and SI-4.16; ORR mass activity values after durability tests are shown in Table 4.4.

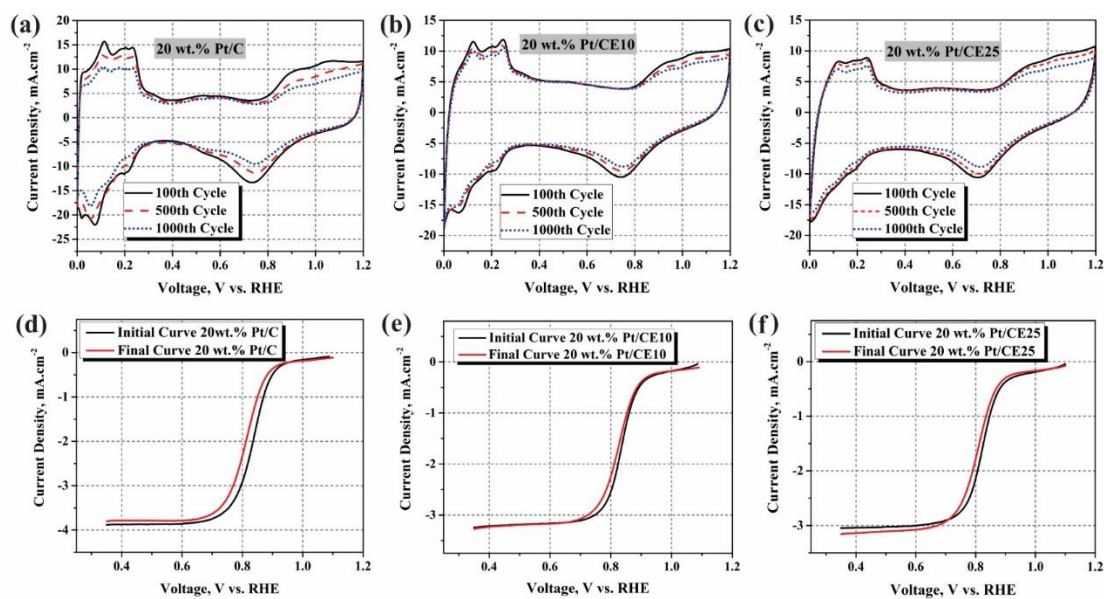


Figure 4.8. Series of CV and LSV plots obtained for different catalysts during durability experiments. (a, b, and c) Series of CV curves obtained after certain numbers of potential cycling between 0 to 1.2 V in Ar saturated aqueous solutions of 0.5M H₂SO₄ at a potential scan rate of 50 mV/s; (d, e, and f) Oxygen reduction LSVs obtained in O₂ saturated aqueous solutions of 0.5M H₂SO₄ with a potential sweep rate of 5 mV/s and rotation speed of 1600 rpm, before and after 1000 potential cycles.

As shown in Figs. 4.8 and Table 4.4, with respect to the retention of ECSAs and ORR mass activities after durability tests, both ECSA and ORR retentions are higher for Pt catalysts supported by CF- or CE-NFs than those obtained for Pt catalysts supported by carbon blacks. Among Pt catalysts supported by CF- or CE-NFs, the percentage of ECSA and ORR retentions are higher for those supported by CE-NFs than those supported by CF-NFs. Lower ECSA and ORR activity retentions for Pt deposited onto CF-NFs was to some extent expected due to their extremely lower surface areas which can facilitate the agglomeration of Pt nanoparticles during potential cycling tests [4, 6]. However, with respect to the low durability of Pt catalysts supported by CF-NFs, observed weight gains under oxidative conditions for CF-NFs (Figure 4.4), and the atomic concentration ratios

obtained from surface chemical components (Table 4.3), suggest electro-oxidation of oxygen-deficient surface oxides (e.g. Ti₄O₇ and/or NbO₂) to be mainly responsible. It has been shown that the electro-oxidation of any of these oxygen deficient surface oxides into more stable oxides (e.g. TiO₂ and/or Nb₂O₅) could lead to a poor interaction between the support and Pt nanoparticles and accordingly lower ORR activities [25, 74].

In addition under the same heat treatment, the percentage of ECSA and ORR retentions are slightly lower for Pt catalyst supported by CF25 (20 wt.% Pt/CE25) than that supported by CF10 (20 wt.% Pt/CE25), i.e. 82% vs. 85%. Based on XPS measurement results (Table 4.3), this observation can be speculated to be mainly due to the formation of more of not electrochemically stable NbO₂ domains at the surface of NFs doped with 25 at.% Nb than those doped with 10 at.% Nb.

4.4 Conclusions

An electrochemically durable and catalytically active catalyst support is presented as an alternative for conventionally used carbon black catalyst supports for PEM fuel cell applications. More electronically conductive and electrochemically durable catalyst support is only achieved if distorted graphite-like carbon domains are embedded in the Nb doped TiO₂ NFs. Doping the rutile phase of TiO₂ with 10 at. % Nb rather than 25 at. % Nb found, first, to be more effective in terms of providing free electrons to the ideal lattice of TiO₂; second, to make the surface less prone to the formation of secondary oxides. Future work will focus on the evaluation of the in-house prepared catalysts under real fuel cell conditions and propose an innovative strategy to prepare more electrochemically durable PEM fuel cells with optimized performances.

4.5 Acknowledgments

The authors thank Profs. Olivera Kesler (University of Toronto), Paul A. Charpentier (Western University), Tricia B. Carmichael (Chemistry and Biochemistry Dept.) Jeremy Rawson (Chemistry and Biochemistry Dept.) and Ricardo F. Aroca (Chemistry and Biochemistry Dept.) for providing access to their high temperature tube furnace, TA instrument, four-probe conductivity measurement setup, microwave reactor, or Raman

spectrometer. The authors thank Dr. Igor Osorio Roman (Chemistry and Biochemistry Dept.), Ms. Sharon Lackie (Great Lake Institute for Environmental Research), Dr. Mark C. Biesinger (Surface Science Western), Dr. Andreas Korinek (Canadian Centre for Electron Microscopy at McMaster University) for their help on the Raman spectroscopy, SEM, XPS, or TEM studies.

References

1. Debe, M.K., *Electrocatalyst approaches and challenges for automotive fuel cells*. Nature, 2012. **486**(7401): p. 43-51.
2. Wang, Y.-J., D.P. Wilkinson, and J. Zhang, *Noncarbon Support Materials for Polymer Electrolyte Membrane Fuel Cell Electrocatalysts*. Chemical Reviews, 2011. **111**(12): p. 7625-7651.
3. Zhang, S., et al., *A review of platinum-based catalyst layer degradation in proton exchange membrane fuel cells*. Journal of Power Sources, 2009. **194**(2): p. 588-600.
4. Huang, S.-Y., et al., *Development of a Titanium Dioxide-Supported Platinum Catalyst with Ultrahigh Stability for Polymer Electrolyte Membrane Fuel Cell Applications*. Journal of the American Chemical Society, 2009. **131**(39): p. 13898-13899.
5. Wu, J., et al., *A review of PEM fuel cell durability: Degradation mechanisms and mitigation strategies*. Journal of Power Sources, 2008. **184**(1): p. 104-119.
6. Yu, X. and S. Ye, *Recent advances in activity and durability enhancement of Pt/C catalytic cathode in PEMFC: Part II: Degradation mechanism and durability enhancement of carbon supported platinum catalyst*. Journal of Power Sources, 2007. **172**(1): p. 145-154.
7. Virkar, A.V. and Y. Zhou, *Mechanism of Catalyst Degradation in Proton Exchange Membrane Fuel Cells*. Journal of The Electrochemical Society, 2007. **154**(6): p. B540-B547.

8. Zhang, Y., et al., *Study of the degradation mechanisms of carbon-supported platinum fuel cells catalyst via different accelerated stress test*. Journal of Power Sources, 2015. **273**(0): p. 62-69.
9. Hitchcock, A.P., et al., *Carbon corrosion of proton exchange membrane fuel cell catalyst layers studied by scanning transmission X-ray microscopy*. Journal of Power Sources, 2014. **266**(0): p. 66-78.
10. Sharma, S. and B.G. Pollet, *Support materials for PEMFC and DMFC electrocatalysts—A review*. Journal of Power Sources, 2012. **208**(0): p. 96-119.
11. Shao, Y., et al., *Novel catalyst support materials for PEM fuel cells: current status and future prospects*. Journal of Materials Chemistry, 2009. **19**(1): p. 46-59.
12. Xie, T., et al., *Development of Highly Active and Durable Hybrid Cathode Catalysts for Polymer Electrolyte Membrane Fuel Cells*. Journal of The Electrochemical Society, 2014. **161**(14): p. F1489-F1501.
13. Chen, X. and S.S. Mao, *Titanium Dioxide Nanomaterials: Synthesis, Properties, Modifications, and Applications*. Chemical Reviews, 2007. **107**(7): p. 2891-2959.
14. Lv, H. and S. Mu, *Nano-ceramic support materials for low temperature fuel cell catalysts*. Nanoscale, 2014. **6**(10): p. 5063-5074.
15. Abdullah, N. and S.K. Kamarudin, *Titanium dioxide in fuel cell technology: An overview*. Journal of Power Sources, 2015. **278**(0): p. 109-118.
16. Ioroi, T., et al., *Stability of Corrosion-Resistant Magnéli-Phase Ti₄O₇-Supported PEMFC Catalysts at High Potentials*. Journal of The Electrochemical Society, 2008. **155**(4): p. B321-B326.
17. Park, K.-W. and K.-S. Seol, *Nb-TiO₂ supported Pt cathode catalyst for polymer electrolyte membrane fuel cells*. Electrochemistry Communications, 2007. **9**(9): p. 2256-2260.
18. Kumar, A. and V. Ramani, *Ta_{0.3}Ti_{0.7}O₂ Electrocatalyst Supports Exhibit Exceptional Electrochemical Stability*. Journal of The Electrochemical Society, 2013. **160**(11): p. F1207-F1215.

19. Kim, J.-H., et al., *Enhancement of Activity and Durability through Cr Doping of TiO₂ Supports in Pt Electrocatalysts for Oxygen Reduction Reactions*. ChemCatChem, 2014. **6**(11): p. 3239-3245.
20. Ho, V.T.T., et al., *Nanostructured Ti_{0.7}Mo_{0.3}O₂ Support Enhances Electron Transfer to Pt: High-Performance Catalyst for Oxygen Reduction Reaction*. Journal of the American Chemical Society, 2011. **133**(30): p. 11716-11724.
21. Chen, G., S.R. Bare, and T.E. Mallouk, *Development of Supported Bifunctional Electrocatalysts for Unitized Regenerative Fuel Cells*. Journal of The Electrochemical Society, 2002. **149**(8): p. A1092-A1099.
22. Senevirathne, K., et al., *Electrocatalytic activity and durability of Pt/NbO₂ and Pt/Ti₄O₇ nanofibers for PEM fuel cell oxygen reduction reaction*. Electrochimica Acta, 2012. **59**(0): p. 538-547.
23. Huang, S.-Y., P. Ganesan, and B.N. Popov, *Electrocatalytic activity and stability of niobium-doped titanium oxide supported platinum catalyst for polymer electrolyte membrane fuel cells*. Applied Catalysis B: Environmental, 2010. **96**(1–2): p. 224-231.
24. Savych, I., et al., *On the effect of non-carbon nanostructured supports on the stability of Pt nanoparticles during voltage cycling: A study of TiO₂ nanofibres*. Journal of Power Sources, 2014. **257**(0): p. 147-155.
25. Wang, Y.-J., et al., *Ta and Nb co-doped TiO₂ and its carbon-hybrid materials for supporting Pt-Pd alloy electrocatalysts for PEM fuel cell oxygen reduction reaction*. Journal of Materials Chemistry A, 2014. **2**(32): p. 12681-12685.
26. Ignaszak, A., et al., *Carbon–Nb_{0.07}Ti_{0.93}O₂ composite supported Pt–Pd electrocatalysts for PEM fuel cell oxygen reduction reaction*. Electrochimica Acta, 2012. **75**(0): p. 220-228.
27. Senevirathne, K., et al., *Nb-doped TiO₂/carbon composite supports synthesized by ultrasonic spray pyrolysis for proton exchange membrane (PEM) fuel cell catalysts*. Journal of Power Sources, 2012. **220**(0): p. 1-9.

28. Wang, Y.-J., et al., *Synthesis of Pd and Nb-doped TiO₂ composite supports and their corresponding Pt-Pd alloy catalysts by a two-step procedure for the oxygen reduction reaction*. Journal of Power Sources, 2013. **221**(0): p. 232-241.
29. Zana, A., et al., *Core-shell TiO₂@C: towards alternative supports as replacement for high surface area carbon for PEMFC catalysts*. Electrochimica Acta, 2014. **139**(0): p. 21-28.
30. Bauer, A., et al., *Application of a composite structure of carbon nanoparticles and Nb-TiO₂ nanofibers as electrocatalyst support for PEM fuel cells*. Journal of Power Sources, 2012. **210**(0): p. 15-20.
31. Bauer, A., et al., *Synthesis and characterization of Nb-TiO₂ mesoporous microsphere and nanofiber supported Pt catalysts for high temperature PEM fuel cells*. Electrochimica Acta, 2012. **77**(0): p. 1-7.
32. Bauer, A., et al., *Pt nanoparticles deposited on TiO₂ based nanofibers: Electrochemical stability and oxygen reduction activity*. Journal of Power Sources, 2010. **195**(10): p. 3105-3110.
33. Chhina, H., et al., *Transmission Electron Microscope Observation of Pt Deposited on Nb-Doped Titania*. Electrochemical and Solid-State Letters, 2009. **12**(6): p. B97-B100.
34. Chevallier, L., et al., *Mesoporous Nanostructured Nb-Doped Titanium Dioxide Microsphere Catalyst Supports for PEM Fuel Cell Electrodes*. ACS Applied Materials & Interfaces, 2012. **4**(3): p. 1752-1759.
35. Navaei Alvar, E., B. Zhou, and S.H. Eichhorn. *Effect of Reducing Agent on the Dispersion of Pt Nanoparticles on Electrospun Nb_{0.1}Ti_{0.9}O₂ Nanofibers*. in *Materials Research Society 2013*. 2013. San Francisco.
36. Ramadan, A.A., R.D. Gould, and A. Ashour, *On the Van der Pauw method of resistivity measurements*. Thin Solid Films, 1994. **239**(2): p. 272-275.

37. de Boer, J.H., et al., *Studies on pore systems in catalysts: VII. Description of the pore dimensions of carbon blacks by the t method*. Journal of Catalysis, 1965. **4**(6): p. 649-653.
38. Instruments, Q., *Gas Sorption System Operation Manual*. 2008-2012: USA.
39. Chhina, H., S. Campbell, and O. Kesler, *Ex Situ and In Situ Stability of Platinum Supported on Niobium-Doped Titania for PEMFCs*. Journal of The Electrochemical Society, 2009. **156**(10): p. B1232-B1237.
40. Sadezky, A., et al., *Raman microspectroscopy of soot and related carbonaceous materials: Spectral analysis and structural information*. Carbon, 2005. **43**(8): p. 1731-1742.
41. Garsany, Y., et al., *Experimental Methods for Quantifying the Activity of Platinum Electrocatalysts for the Oxygen Reduction Reaction*. Analytical Chemistry, 2010. **82**(15): p. 6321-6328.
42. Wilkinson, D.P., et al., *Proton Exchange Membrane Fuel cells: Materials Properties and Performances*, ed. S. Lee. 2010, United States of America: Taylor and Francis Group, LLC.
43. Depero, L.E., et al., *Niobium-titanium oxide powders obtained by laser-induced synthesis: Microstructure and structure evolution from diffraction data*. Journal of Materials Research, 1998. **13**(06): p. 1644-1649.
44. Holzwarth, U. and N. Gibson, *The Scherrer equation versus the 'Debye-Scherrer equation'*. 2011, Nature Publishing Group. p. 534-534.
45. Arashi, T., et al., *Nb-doped TiO₂ cathode catalysts for oxygen reduction reaction of polymer electrolyte fuel cells*. Catalysis Today, 2014. **233**(0): p. 181-186.
46. Ruiz, A.M., et al., *Insights into the Structural and Chemical Modifications of Nb Additive on TiO₂ Nanoparticles*. Chemistry of Materials, 2004. **16**(5): p. 862-871.
47. Balbuena, P.B. and K.E. Gubbins, *Theoretical interpretation of adsorption behavior of simple fluids in slit pores*. Langmuir, 1993. **9**(7): p. 1801-1814.

48. Alvar, E.N. and M. Rezaei, *Mesoporous nanocrystalline MgAl₂O₄ spinel and its applications as support for Ni catalyst in dry reforming*. Scripta Materialia, 2009. **61**(2): p. 212-215.
49. Soboleva, T., et al., *On the Micro-, Meso-, and Macroporous Structures of Polymer Electrolyte Membrane Fuel Cell Catalyst Layers*. ACS Applied Materials & Interfaces, 2010. **2**(2): p. 375-384.
50. Arepalli, S., et al., *Protocol for the characterization of single-wall carbon nanotube material quality*. Carbon, 2004. **42**(8-9): p. 1783-1791.
51. Landi, B.J., et al., *Thermal Oxidation Profiling of Single-Walled Carbon Nanotubes*. Chemistry of Materials, 2005. **17**(26): p. 6819-6834.
52. Wang, Y., et al., *A review of polymer electrolyte membrane fuel cells: Technology, applications, and needs on fundamental research*. Applied Energy, 2011. **88**(4): p. 981-1007.
53. Wang, Y., D.C. Alsmeyer, and R.L. McCreery, *Raman spectroscopy of carbon materials: structural basis of observed spectra*. Chemistry of Materials, 1990. **2**(5): p. 557-563.
54. Dresselhaus, M.S., G. Dresselhaus, and M. Hofmann, *The big picture of Raman scattering in carbon nanotubes*. Vibrational Spectroscopy, 2007. **45**(2): p. 71-81.
55. Wang, W., et al., *Synthesis of Rutile (α -TiO₂) Nanocrystals with Controlled Size and Shape by Low-Temperature Hydrolysis: Effects of Solvent Composition*. The Journal of Physical Chemistry B, 2004. **108**(39): p. 14789-14792.
56. Ocaña, M., J.V. Garcia-Ramos, and C.J. Serna, *Low-Temperature Nucleation of Rutile Observed by Raman Spectroscopy during Crystallization of TiO₂*. Journal of the American Ceramic Society, 1992. **75**(7): p. 2010-2012.
57. Arbiol, J., et al., *Effects of Nb doping on the TiO₂ anatase-to-rutile phase transition*. Journal of Applied Physics, 2002. **92**(2): p. 853-861.
58. Alvar, E.N., B. Zhou, and S.H. Eichhorn, *Oxidative Treatment to Improve Coating and Electrochemical Stability of Carbon Fiber Paper with Niobium Doped*

- Titanium Dioxide Sols for Potential Applications in Fuel Cells*. *Electrochimica Acta*, 2014. **132**(0): p. 347-355.
59. Hara, M., et al., *Electrochemical and Raman spectroscopic evaluation of Pt/graphitized carbon black catalyst durability for the start/stop operating condition of polymer electrolyte fuel cells*. *Electrochimica Acta*, 2012. **70**(0): p. 171-181.
60. Pecharsky, V.K. and P.Y. Zavalij, *Fundamentals of powder diffraction and structural characterization of materials*. 1 ed. 2005: Springer.
61. Sheppard, L.R., *Niobium Surface Segregation in Polycrystalline Niobium-Doped Titanium Dioxide*. *The Journal of Physical Chemistry C*, 2013. **117**(7): p. 3407-3413.
62. Atanacio, A.J., T. Bak, and J. Nowotny, *Niobium Segregation in Niobium-Doped Titanium Dioxide (Rutile)*. *The Journal of Physical Chemistry C*, 2014. **118**(21): p. 11174-11185.
63. Haerle, R., et al., *$\{sp\}^2\{sp\}^3$ hybridization ratio in amorphous carbon from C *1s* core-level shifts: X-ray photoelectron spectroscopy and first-principles calculation*. *Physical Review B*, 2001. **65**(4): p. 045101.
64. Antonio, M.R., I. Song, and H. Yamada, *Coordination and valence of niobium in TiO₂NbO₂ solid solutions through X-ray absorption spectroscopy*. *Journal of Solid State Chemistry*, 1991. **93**(1): p. 183-192.
65. Kröger, F.A. and H.J. Vink, *Relations between the Concentrations of Imperfections in Crystalline Solids*, in *Solid State Physics*, S. Frederick and T. David, Editors. 1956, Academic Press. p. 307-435.
66. Morris, D., et al., *Photoemission and STM study of the electronic structure of Nb-doped TiO₂*. *Physical Review B*, 2000. **61**(20): p. 13445-13457.
67. Jackson, S.T. and R.G. Nuzzo, *Determining hybridization differences for amorphous carbon from the XPS C *1s* envelope*. *Applied Surface Science*, 1995. **90**(2): p. 195-203.

68. Jung, H.-Y., S. Park, and B.N. Popov, *Electrochemical studies of an unsupported PtIr electrocatalyst as a bifunctional oxygen electrode in a unitized regenerative fuel cell*. Journal of Power Sources, 2009. **191**(2): p. 357-361.
69. Inoue, H., et al., *Oxygen reduction on bare and Pt monolayer-modified Ru(0001), Ru(1010) and Ru nanostructured surfaces*. Electrochimica Acta, 2002. **47**(22–23): p. 3777-3785.
70. Akalework, N.G., et al., *Ultrathin TiO₂-coated MWCNTs with excellent conductivity and SMSI nature as Pt catalyst support for oxygen reduction reaction in PEMFCs*. Journal of Materials Chemistry, 2012. **22**(39): p. 20977-20985.
71. Huang, S.-Y., P. Ganesan, and B.N. Popov, *Titania supported platinum catalyst with high electrocatalytic activity and stability for polymer electrolyte membrane fuel cell*. Applied Catalysis B: Environmental, 2011. **102**(1–2): p. 71-77.
72. Levich, V.G., *Physicochemical hydrodynamics*. Prentice-Hall international series in the physical and chemical engineering sciences. 1962, Englewood Cliffs, N.J.: Prentice-Hall. 700 p.
73. Gochi-Ponce, Y., G. Alonso-Nuñez, and N. Alonso-Vante, *Synthesis and electrochemical characterization of a novel platinum chalcogenide electrocatalyst with an enhanced tolerance to methanol in the oxygen reduction reaction*. Electrochemistry Communications, 2006. **8**(9): p. 1487-1491.
74. Avasarala, B. and P. Haldar, *Durability and degradation mechanism of titanium nitride based electrocatalysts for PEM (proton exchange membrane) fuel cell applications*. Energy, 2013. **57**(0): p. 545-553.

Supplementary Information (SI) Chapter 4

Carbon-Embedded Mesoporous Nb-doped TiO₂ Nanofibers as Catalyst Support for Oxygen Reduction Reaction in PEM Fuel Cell

Koutecky-Levich Equation

Furthermore, to determine whether ORR reaction produces H₂O (4-electron pathway) or H₂O₂ (2-electron pathway), Koutecky-Levich equation, Eq. (SI-4.1): [1, 2]

$$\frac{1}{j} = \frac{1}{j_k} + \frac{1}{B\omega^{1/2}} \quad (\text{SI-4.1})$$

Where j is the experimentally measured current density (mA.cm⁻²), j_k is kinetic current density (mA.cm⁻²), j_d is the diffusion limiting current density (mA.rad^{1/2}.s^{-1/2}.cm⁻²) and ω is the angular velocity frequency of rotation derived from $\omega=2\pi f/60$, f is the rotation rate in rpm. Constant B in Eq. (5) which is the simplified form of koutecky-Levich (K-L) equation by assuming the resistance of Nafion layer sufficiently small [3], can be expressed as follow:

$$B = 0.62nFD_{O_2}^{\frac{2}{3}} C_{O_2} \nu^{-\frac{1}{6}} \quad (\text{SI-4.2})$$

The theoretical values for 2-electron ($n=2$) and 4-electron ($n=4$) ORR pathways can be calculated by extracting diffusion coefficient of O₂ ($D_{O_2} = 1.4 \times 10^{-5}$ cm².s⁻¹), maximum solubility of O₂ ($C_{O_2} = 1.1 \times 10^{-6}$ mol.cm⁻³), and kinematic viscosity of O₂ ($\nu = 10 \times 10^{-3}$ cm².s⁻¹) in 0.5 M H₂SO₄ aqueous solution at room temperature from literature.[4]

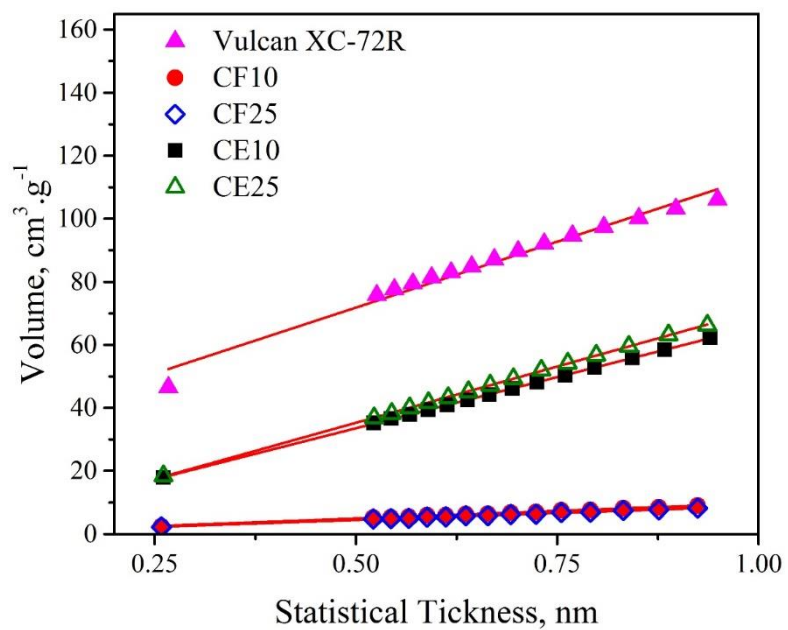
t-plots

Figure SI-4.1. t-plots of all synthesized Nb_xTi_(1-x)O₂ (x = 0.1 and 0.25) nanofibers and a Vulcan XC-72R.

Raman peak analysis parameters and results

Table SI-4.1. Sadezky et al.[5] reported vibration modes and line shapes for the best curve-fitting of first-order Raman bands for carbonaceous materials.

Band	Raman Shift (cm ⁻¹)	Vibration mode	Line shape
G	~ 1580 cm ⁻¹	Ideal graphitic lattice (E _{2g} -symmetry)	Lorentzian
D1	~ 1350 cm ⁻¹	Disordered graphitic lattice (graphene layer edges, A _{1g} symmetry)	Lorentzian
D2	~ 1620 cm ⁻¹	Disordered graphitic lattice (surface graphene layers, E _{2g} symmetry)	Lorentzian
D3	~ 1500 cm ⁻¹	Amorphous carbon	Gaussian
D4	~ 1200 cm ⁻¹	Disordered graphitic lattice (A _{1g} symmetry)	Lorentzian

Table SI-4.2. Relative band area ratios of the D1-D4 bands to G band, A_{DX-band}/A_{G-band} (X = 1, 2, 3, 4).

Nanofiber Name	Peak Area Ratio			
	D1/G	D2/G	D3/G	D4/G
CE10	8.478	1.244	1.609	0.500
CE25	6.56	0.923	1.200	0.1212

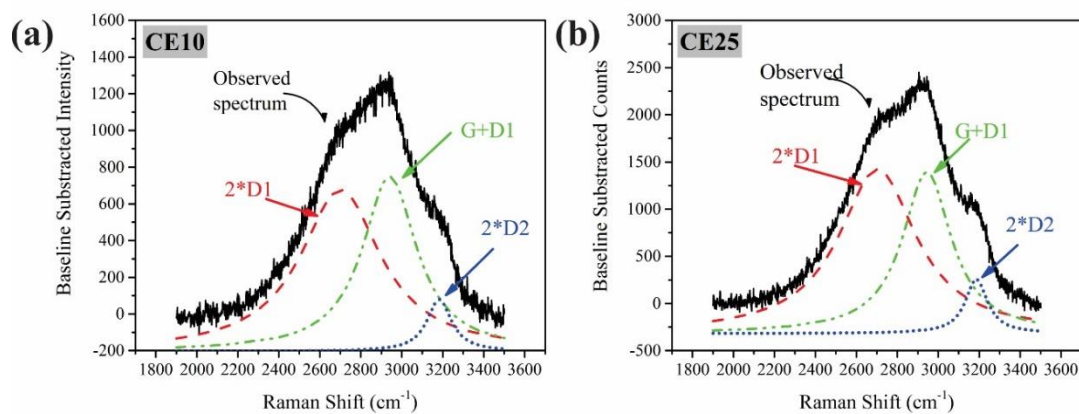


Figure SI-4.2. Peak analyses of the ordered/disordered graphite second-order bands observed in the Raman spectra of CE-NFs. (a) CE10; and (b) CE25.

PXRD patterns of Pt-deposited nanofibers

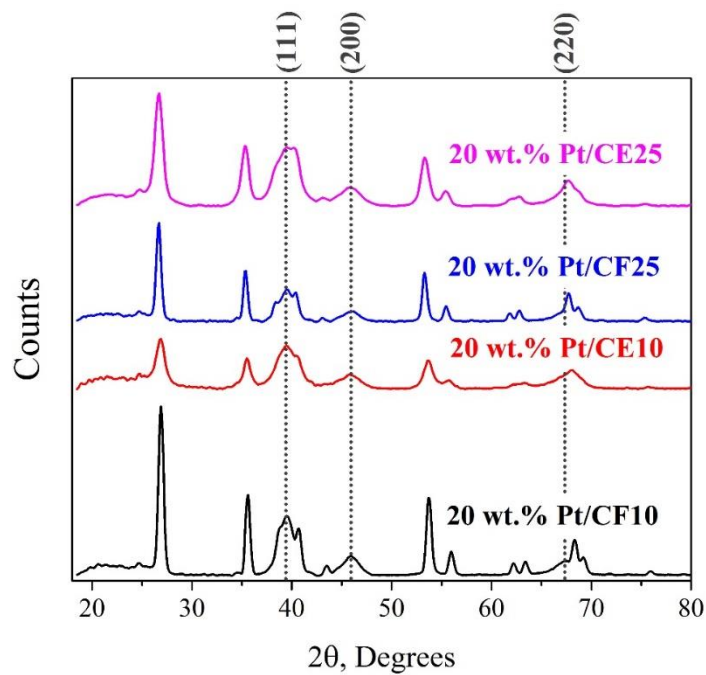


Figure SI-4.3. PXRD patterns of 20 wt. % Pt deposited Nb_xTi_(1-x)O₂ (x = 0.1 and 0.25) nanofibers.

Transmission electron microscopy (TEM) and energy dispersive X-ray spectroscopy (EDX) results

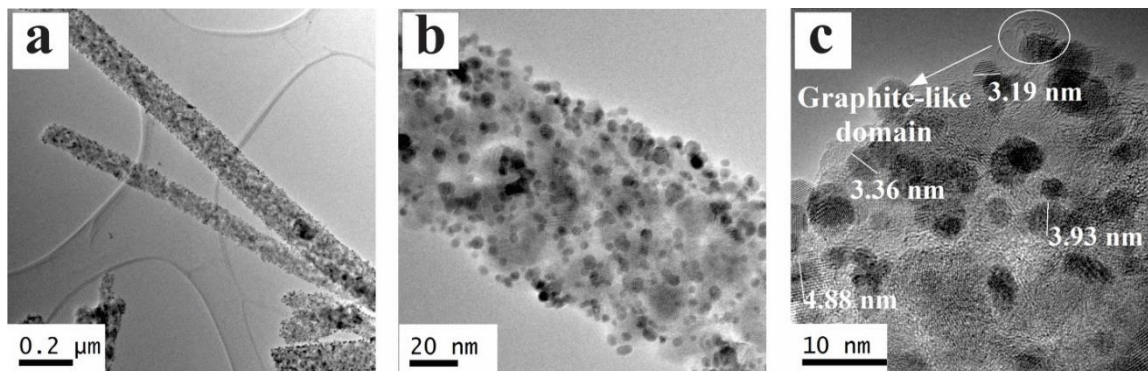


Figure SI-4.4. BF-TEM and HRTEM images of 20 wt. % Pt deposited CE10 nanofibers at different magnifications.

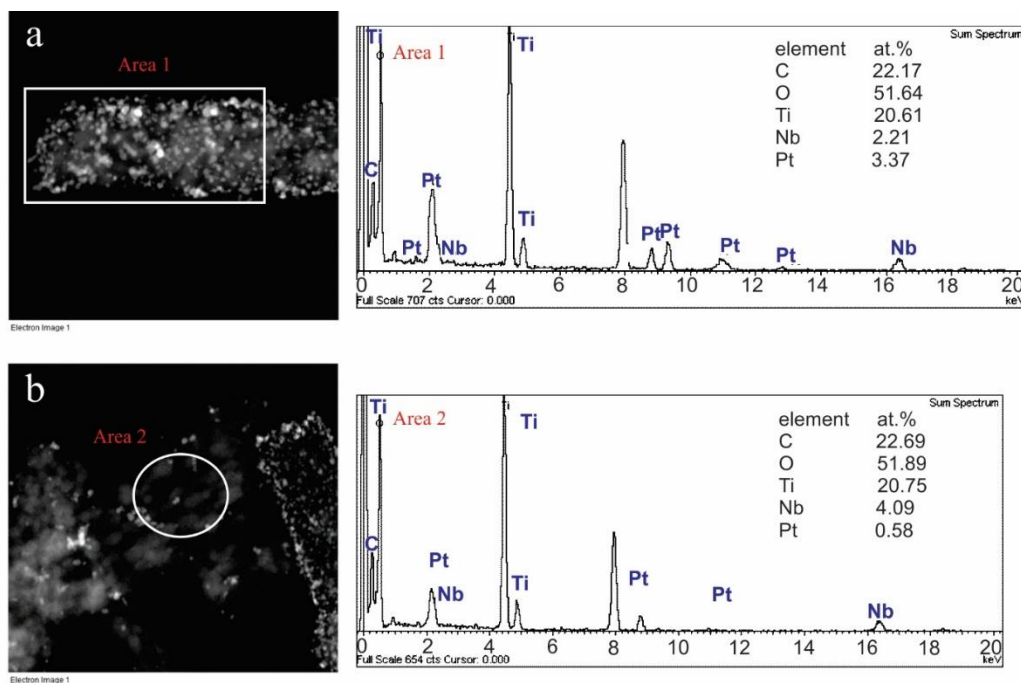


Figure SI-4.5. Dark field-TEM images and collected EDX spectra from 20 wt. % Pt deposited CE10 nanofibers.

X-ray photoelectron spectroscopy (XPS) survey scans

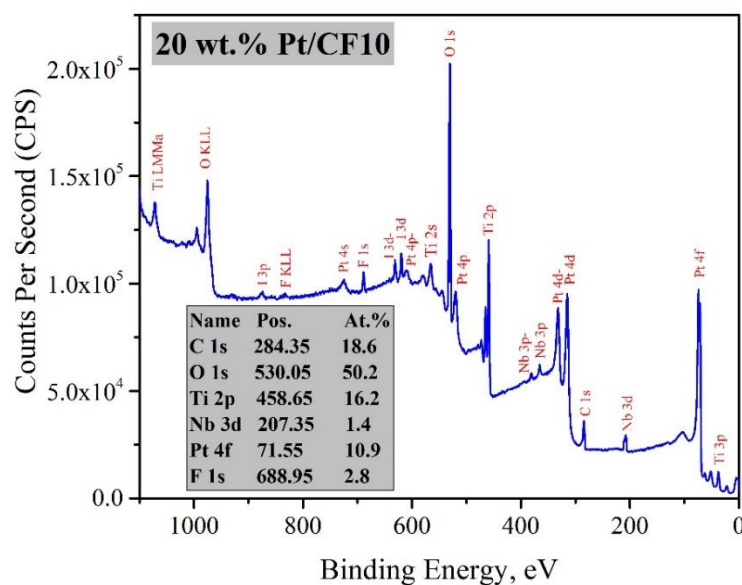


Figure SI-4.6. XPS survey spectra of 20 wt. % Pt deposited CF10 nanofibers.

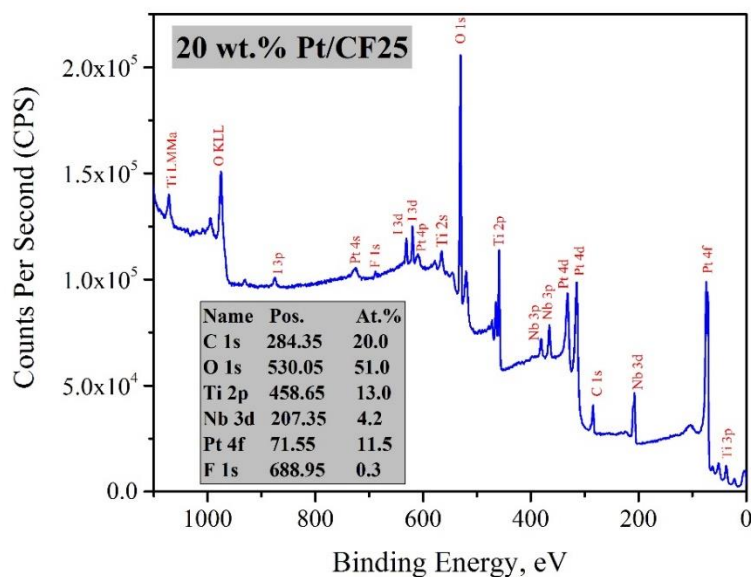


Figure SI-4.7. XPS survey spectra of 20 wt. % Pt deposited CF25 nanofibers.

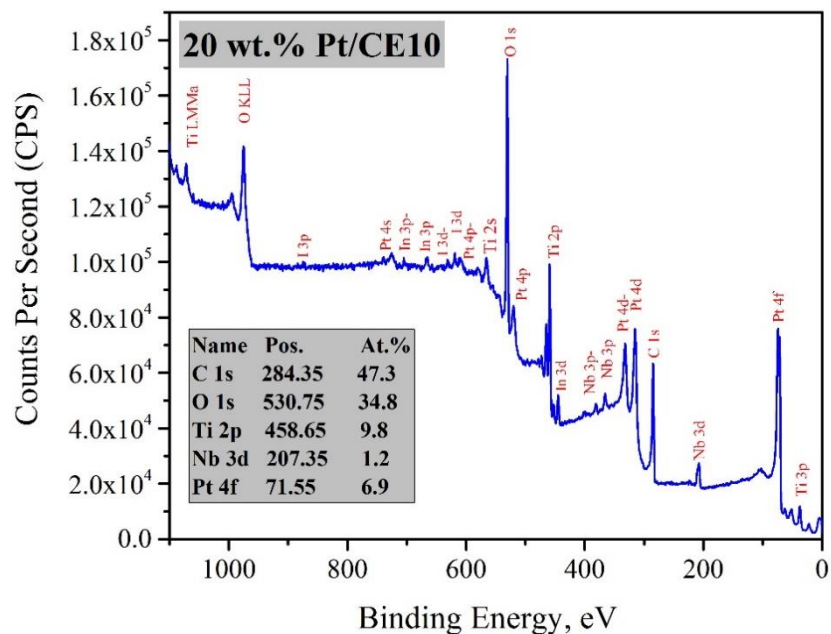


Figure SI-4.8. XPS survey spectra of 20 wt. % Pt deposited CE10 nanofibers.

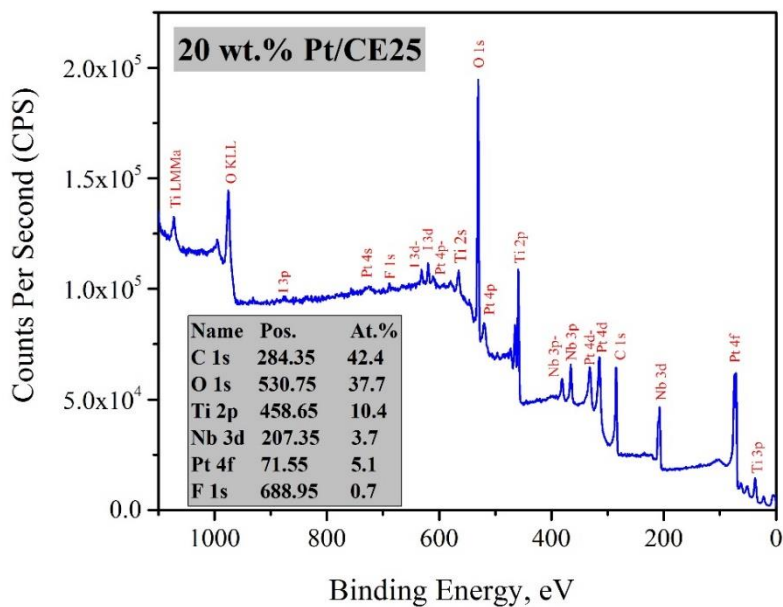


Figure SI-4.9. XPS survey spectra of 20 wt. % Pt deposited CE25 nanofibers.

High-resolution XPS scans in C 1s region

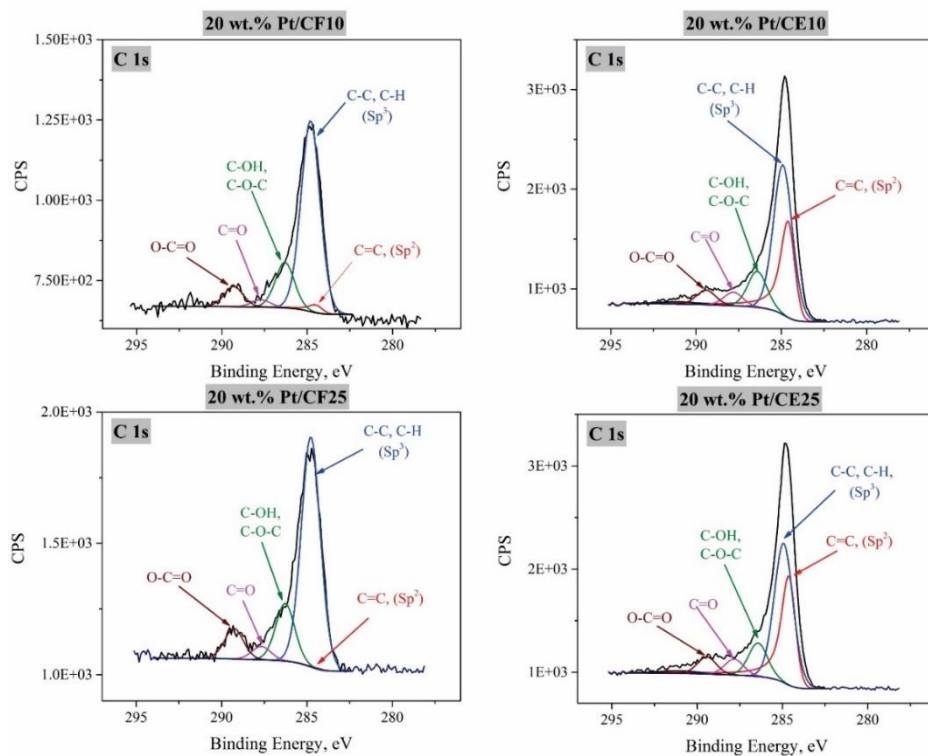


Figure SI-4.10. High resolution XPS spectra of different catalysts along with component fits in C 1s region.

High-resolution XPS scans in O 1s region

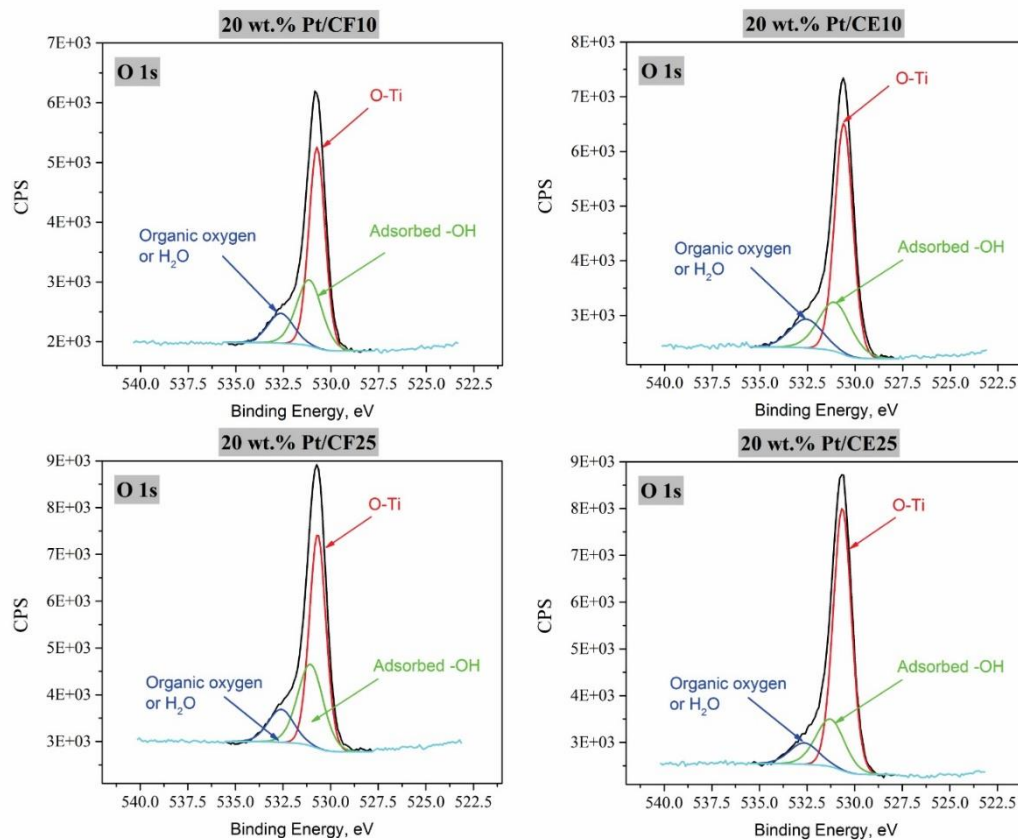


Figure SI-4.11. High resolution XPS spectra of different catalysts along with component fits in O 1s region..

Table SI-4.4. XPS peak parameters and Area % of different components in O 1s region.

Area %	FWHM	Peak Position, eV	Chemical State	At.% of O1s	Sample #
57.1	0.99	530.74	Oxide	50.2	CF10
29.6	1.57	531.14	Adsorbed -OH		
13.3	1.57	532.64	Organic oxygen		
62.2	2	530.59	Oxide	34.8	CE10
23.8	2	531.07	Adsorbed -OH		
14.0	1.11	532.57	Organic oxygen		
54.7	1.58	530.68	Oxide	51.0	CF25
32.3	1.58	531.05	Adsorbed -OH		
13.0	1.02	532.60	Organic oxygen		
76	1.22	530.64	Oxide	37.7	CE25
14.2	1.22	531.27	Adsorbed -OH		
9.8	1.50	532.65	Organic oxygen		

High-resolution XPS scans in Ti 2p region

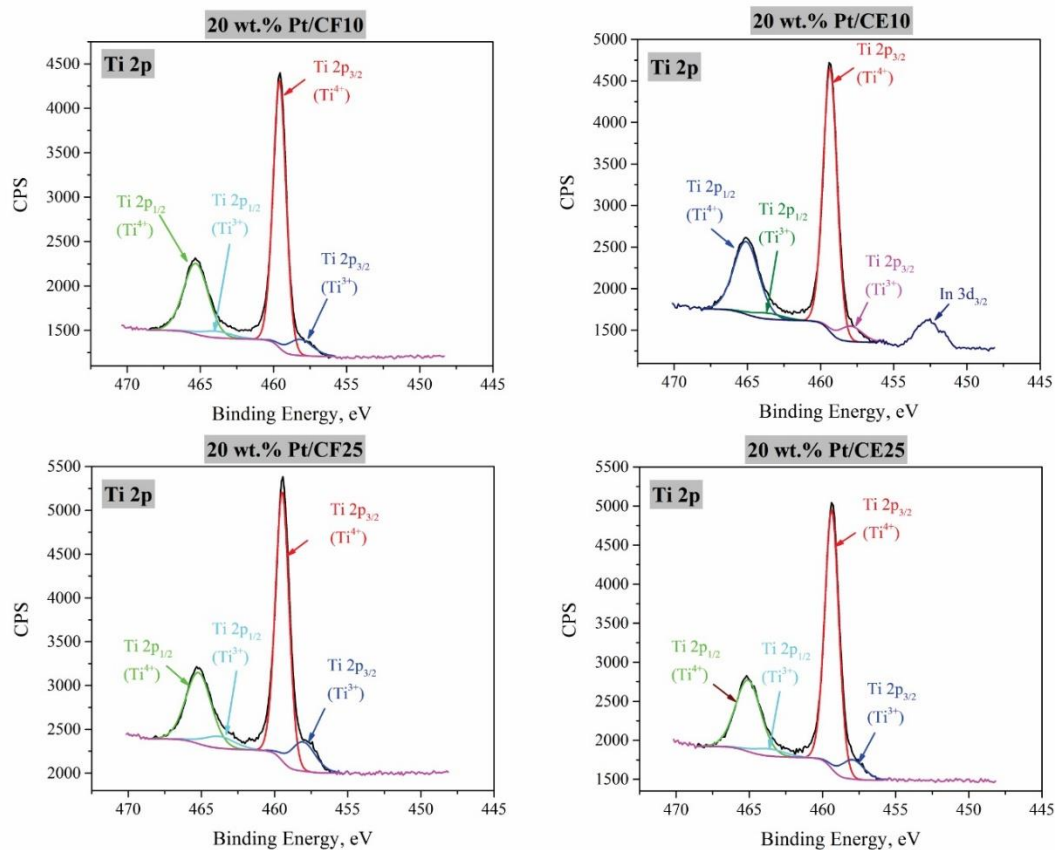


Figure SI-4.12. High resolution XPS spectra of different catalysts along with component fits in Ti 2p region..

Table SI-4.5. XPS peak parameters and Area % of different components in Ti 2p region.

Sample #	CF10		CE10		CF25		CE25	
At.% of Ti2p	16.2		9.8		13		10.4	
Chemical State	Ti 2p _{3/2} (Ti ⁴⁺)	Ti 2p _{3/2} (Ti ³⁺)	Ti 2p _{3/2} (Ti ⁴⁺)	Ti 2p _{3/2} (Ti ³⁺)	Ti 2p _{3/2} (Ti ⁴⁺)	Ti 2p _{3/2} (Ti ³⁺)	Ti 2p _{3/2} (Ti ⁴⁺)	Ti 2p _{3/2} (Ti ³⁺)
Peak Position, eV	459.59	463.91	459.35	457.95	459.47	458.07	459.36	457.96
FWHM	1.05	2.00	1.11	1.88	1.08	2.00	1.12	1.88
Area %	89.7	10.3	90.9	9.1	83.3	16.7	88.9	11.1

*Peak splitting value for Ti2p spin-orbit components is 5.72 eV.

High-resolution XPS scans in Nb 3d region

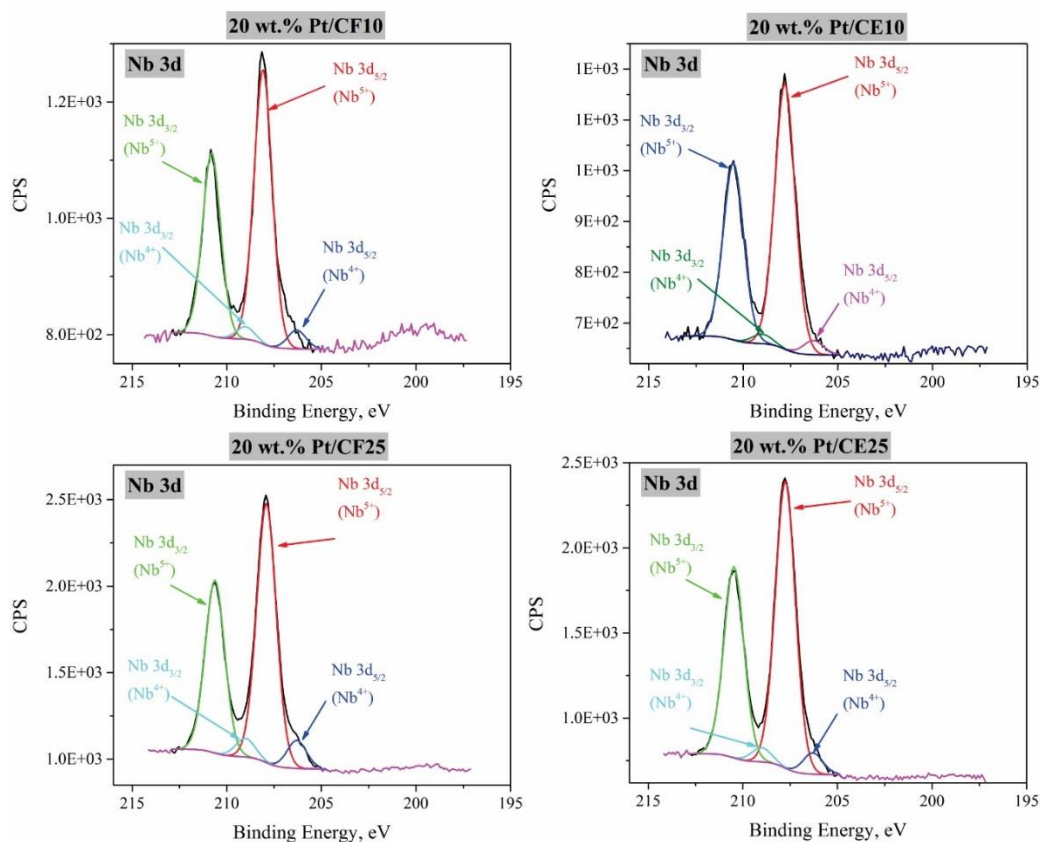


Figure SI-4.13. High resolution XPS spectra of different catalysts along with component fits in Nb 3d region..

Table SI-4.6. XPS peak parameters and Area % of different components in Nb 3d region.

Sample #	CF10		CE10		CF25		CE25	
At.% of Nb3d	1.4		1.2		4.2		3.7	
Chemical state	Nb 3d _{5/2} (Nb ⁵⁺)	Nb 3d _{5/2} (Nb ⁴⁺)	Nb 3d _{5/2} (Nb ⁵⁺)	Nb 3d _{5/2} (Nb ⁴⁺)	Nb 3d _{5/2} (Nb ⁵⁺)	Nb 3d _{5/2} (Nb ⁴⁺)	Nb 3d _{5/2} (Nb ⁵⁺)	Nb 3d _{5/2} (Nb ⁴⁺)
Peak Position, eV	208.08	206.30	207.80	206.30	207.91	206.30	207.75	206.30
FWHM	1.13	1.13	1.26	1.26	1.21	1.21	1.24	1.24
Area %	93.6	6.4	94.9	5.1	90.2	9.8	93.1	6.9

*Peak splitting value for Nb3d spin-orbit components is 2.72 eV.

High-resolution XPS scans in Pt 4f region

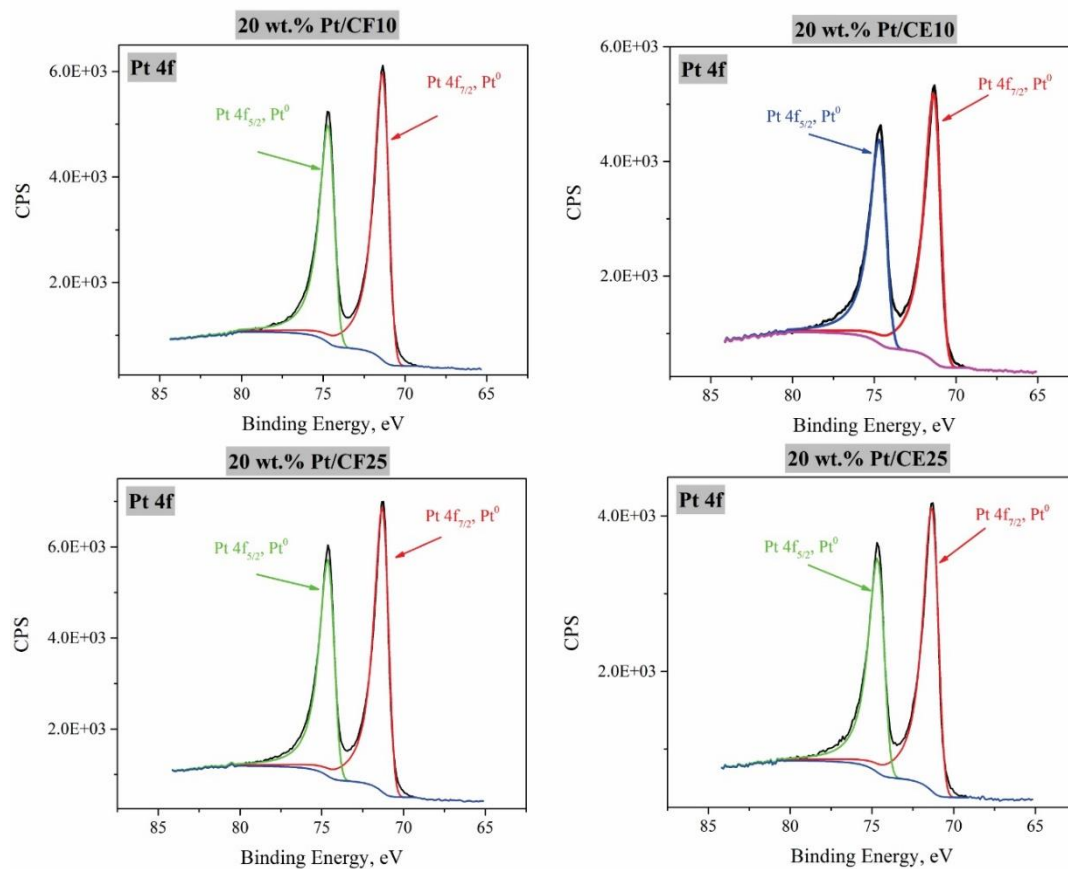


Figure SI-4.14. High resolution XPS spectra of different catalysts along with component fits in Pt 4f region..

Table SI-4.7. XPS peak parameters and Area % of different components in Pt 4f region.

Sample #	CF10	CE10	CF25	CE25
At.% of Pt4f	10.9	6.9	11.5	5.1
Chemical state	Pt 4f _{7/2} (Pt ⁰)			
Peak Position, eV	71.10	71.07	71.03	71.05
FWHM	0.90	0.96	0.88	0.93

*Peak splitting value for Pt4f spin-orbit components is 3.32 eV.

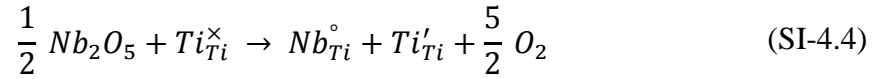
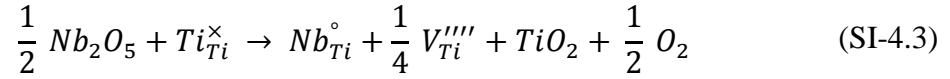
Kroger-vink notations

Table SI-4.8. Descriptions of Kroger-vink notations used in Eqs. (SI-4.3) and (SI-4.4).

Kroger-vink notation	Description	
Ti_{Ti}^{\times}	A titanium ion sitting on a titanium lattice site with neutral charge	(Ti^{4+})
Nb_{Ti}°	A niobium ion sitting on a titanium lattice site with single positive charge	(Nb^{5+})
$V_{Ti}^{''''}$	A titanium vacancy with quadruple negative charge	
Ti'_{Ti}	A titanium ion sitting on a titanium lattice site with single negative charge	(Ti^{3+})

Electrochemical characterization results

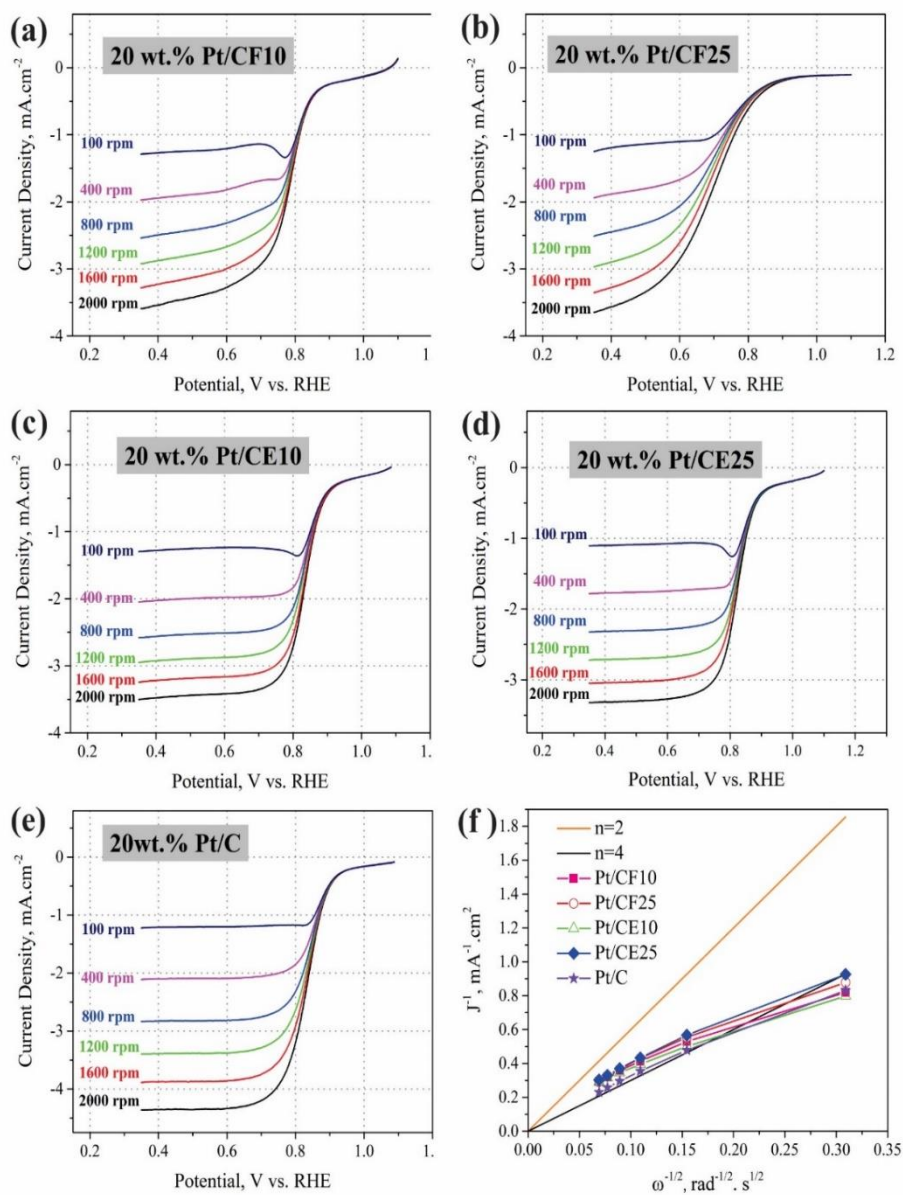


Figure SI-4.15. ORR Linear sweep voltammograms (LSVs) recorded at a potential scan rate of 5 mV s⁻¹ and various rotation speeds along with Koutecky-Levich plots at 0.7 V for different catalysts in O₂ saturated aqueous solution of 0.5M H₂SO₄. LSVs for (a) 20 wt.%Pt/CF10; (b) 20 wt.%Pt/CF25; (c) 20 wt.%Pt/CE10; (d) 20 wt.%Pt/CE25; (e) 20 wt.%Pt/Vulcan; and (f) K-L plots at 0.7V.

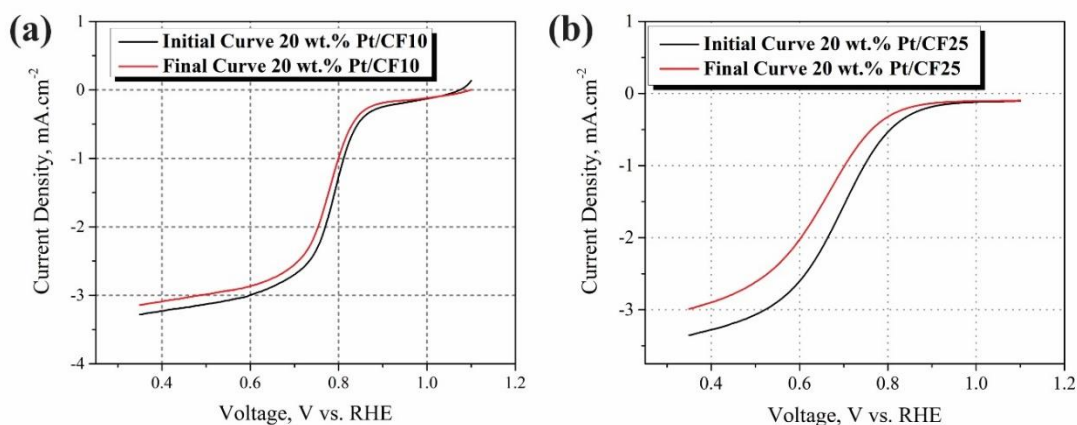


Figure SI-4.16. ORR linear sweep voltammograms of different catalysts recorded in O₂ saturated aqueous solutions of 0.5M H₂SO₄ with a potential sweep rate and rotation speed of 5 mV/s and 1600 rpm, respectively, before and after 1000 potential cycles.

(a) 20 wt.% Pt/CF10; (b) 20 wt.% Pt/CF25.

References

1. Senevirathne, K., et al., *Nb-doped TiO₂/carbon composite supports synthesized by ultrasonic spray pyrolysis for proton exchange membrane (PEM) fuel cell catalysts*. Journal of Power Sources, 2012. **220**(0): p. 1-9.
2. Levich, V.G., *Physicochemical hydrodynamics*. Prentice-Hall international series in the physical and chemical engineering sciences. 1962, Englewood Cliffs, N.J.: Prentice-Hall. 700 p.
3. Paulus, U.A., et al., *Oxygen reduction on high surface area Pt-based alloy catalysts in comparison to well defined smooth bulk alloy electrodes*. Electrochimica Acta, 2002. **47**(22–23): p. 3787-3798.
4. Song, C. and J. Zhang, *Electrocatalytic Oxygen Reduction Reaction*, in *PEM Fuel Cell Electrocatalysts and Catalyst Layers*, J. Zhang, Editor. 2008, Springer London. p. 89-134.
5. Sadezky, A., et al., *Raman microspectroscopy of soot and related carbonaceous materials: Spectral analysis and structural information*. Carbon, 2005. **43**(8): p. 1731-1742.

CHAPTER 5

Electrosprayed Cathode Catalyst Layer with Composite-supported Pt Catalyst and Nafion Loading Optimization Strategy for Polymer Electrolyte Membrane Fuel Cell

5.1 Introduction

Polymer electrolyte membrane fuel cells (PEMFCs) are regarded as a promising candidate for transportation and mobile electronics applications. Cost and durability have been identified as the major challenges that have to be met in order to commercialize fuel cell technology in these applications [1]. U.S. Department of Energy (DOE) has set the targets for 2020 in its most recent fuel cell technical plan as follows: less than 40% loss of initial mass activity under automotive load cycle and less than $0.125 \text{ mg}_{\text{Pt}} \cdot \text{cm}^{-2}$ total (anode + cathode) platinum group metal (PGM) loading [2]. Despite of the evolution of nanostructured carbon-based catalysts with outstanding catalytic properties [3-6], the electro-oxidation caused by carbon at high potentials [7, 8] is still inevitable with the state of the art commercial carbon black supports. This fact kept researchers to work hard to search for an electrochemically durable and active noncarbon catalyst supports [9-11] and to further investigate the degradation mechanisms [12-16]. Among several proposed noncarbon catalyst supports [17-20], titanium dioxide (TiO_2) is widely studied due to its high chemical stability and favorable strong metal-support interaction (SMSI) for PEMFC applications [21-27]. However, to make TiO_2 appealing for PEMFC catalyst support, its inherent low electronic conductivity and low surface area must be improved [28-31]. Recently it has been shown that blending transition-metal doped TiO_2 nanostructures with commercial carbon blacks can combine their advantages and make more appealing catalyst supports with much higher electronic conductivities and surface areas [32-39]. Commercial carbon blacks were mostly blended with titanium and doping element (e.g. niobium) containing precursor solutions and the final reduced blend was commonly referred as composite or hybrid catalyst support [34, 36]. The most important deficiency of catalysts supported by these composite or hybrid catalyst supports, despite much enhanced oxygen reduction reaction (ORR) mass activities, was their relatively lower [34] or just slightly improved [36] durability under acidic condition. The ORR mass activities of Pt alloy catalysts supported by hybrid supports were improved only by blending high contents of carbon NPs (75 wt.%) with transition metal-doped TiO_2 NPs [36]. Therefore, most probably due to the high contents of carbon NPs, the electrochemical durability was only slightly improved [36]. Furthermore, under certain synthesis conditions [34], blending high

contents of carbon NPs with Nb-doped TiO₂ nanocrystals even increased the ORR mass activity loss compared to pure carbon based Pt catalysts.

Additionally, despite large number of studies which were just relied on ex-situ measurements such as rotating disk electrode (RDE) measurements to evaluate the catalytic performances of catalysts supported by transition metal-doped TiO₂ or blended supports, only a few groups evaluated the in-situ performance of transition metal-doped TiO₂ supported Pt catalysts under real PEMFC operating conditions [10, 22, 23, 35, 40]. In fact the catalytic activity evaluation under real fuel cell conditions is more critical than simulated RDE conditions with pure oxygen saturated flooded electrolytes. In real fuel cell conditions, the sluggish ORR reaction will not occur unless triple phase boundary (TPB) condition satisfies in the catalyst layer (CL) [41-43]. Proton conducting ionomer phase (Nafion) incorporation into the CL under real fuel cell conditions was shown to be very critical in terms of providing enough proton conductive paths deep into the CL [44] whereas its excessive amount could either block the active sites or increase the resistivity [45]. Therefore many studies have been done to find a criterion to be able to formulate the required optimized Nafion amounts to be applied to the catalyst layers [46-49]. Despite widespread use of optimized Nafion weight percentages (NWP) in the range of 20 – 40% [45, 46, 50] for commercial pure carbon-based catalysts, it has been shown that optimized NWP are highly dependent on catalyst type (e.g. the type of catalyst support or metal percentages) and cannot be directly applied to any type of catalyst layer [51-53]. Recently, in comparison to the use of catalyst weight, the use of catalyst volume was shown to be more effective in predicting optimized Nafion loadings for Pd/C catalysts with different metal percentages [52]. However, the proposed volumetric ratios were only validated to pure carbon black supported Pd catalysts. Hence using volumetric ratios as a fixed value for any type of catalyst support (specifically for composite or hybrid supports) needs to be validated. Despite a few studies which were performed on the PEMFC performance evaluation of transition metal doped TiO₂ supports, to the best of the present author's knowledge, the optimization of Nafion amount to be applied to their corresponding CLs has not been investigated. The optimized Nafion loadings were also shown to be highly dependent on the catalyst layer preparation method [53]. Furthermore, electrospaying

technique has shown to be a very promising alternative way to make highly active CLs through improving the distribution and interaction of Nafion ionomer in the CL [53, 54].

Recently, using an in-situ reductive embedment (ISRE) strategy, the present authors have successfully synthesized carbon-embedded mesoporous Nb-doped TiO₂ nanofibers (NFs) as catalyst support, with relatively high electronic conductivity about 0.12 S·cm⁻¹ and high surface area of 102 m²·g⁻¹ [55]. In order to increase the electronic conductivity of Nb-doped TiO₂ nanomaterials (NFs or NPs), ISRE strategy using organic carbon sources (i.e. Polyvinylpyrrolidone) was shown to be more effective method than the one blending with already graphitized carbon NPs used in the literature [34], because the ISRE strategy used much less carbon amount (11 wt.% [55] vs. 25 wt.% [34]) to achieve sufficiently conductive catalyst supports. The Pt catalysts supported by carbon-embedded 10 at.% Nb-doped TiO₂ (C/Nb_{0.1}Ti_{0.9}O₂) NFs, evaluated through RDE measurements, have showed much enhanced durability with comparable ORR mass activity, when compared with pure carbon-based catalysts for oxygen reduction reaction (ORR) [55].

Our main goal here is to composite C/Nb_{0.1}Ti_{0.9}O₂ NFs with commercial carbon blacks to combine their advantages through physical mixing, and then evaluate the catalytic activity of the synthesized composite-supported Pt catalysts under both, acidic and real PEMFC operating conditions. To reach this goal, first, a new methodology is introduced to prepare CLs out of composite-supported Pt catalysts so that the PEMFC performances at optimized Nafion loadings can be compared; second, an optimized amount of carbon black which is needed to be composited with C/Nb_{0.1}Ti_{0.9}O₂ NFs is identified that balances performance and durability.

5.2 Experimental

5.2.1 Synthesis and characterization of composite supported Pt catalysts

5.2.1.1 Synthesis of carbon-embedded Nb-doped TiO₂ nanofibers

An electrospinning setup developed in the Clean Powertrain Lab at the University of Windsor [56] was used to fabricate carbon-embedded 10 at.% Nb-doped TiO₂ (C/Nb_{0.1}Ti_{0.9}O₂) nanofibers and the details of the synthesis processes are reported

elsewhere [55]. The heat treatment of the as-spun nanofibers described in this work is as follows: First, the as-spun fibers were left at ambient environment with room temperature for 24 hours, second, they were reduced under pure hydrogen atmosphere from room temperature up to 500°C at a heating rate of 5°C·min⁻¹ and kept at 500°C for 2 hours; and then continuously heated up to 800°C with the same heating rate and kept at that temperature for 6 hours.

5.2.1.2 Synthesis of composite catalyst supports

Before the composite catalyst supports can be made, the surface functionalization treatment on carbon blacks (Vulcan XC-72R, Cabot Inc.), shown to be in favor of uniform distribution of Pt nanoparticle [57-59], was performed by refluxing desired amounts of carbon blacks (4 mg·mL⁻¹) into aqueous solution of 0.5M HNO₃ at 100°C for 2 hours. Then, the pre-functionalized carbon blacks were washed with copious amount of deionized (DI) water until the washed-out water achieved pH of 7. Later Composite catalyst supports were prepared by physically mixing, using a mortar and pestle, pre-functionalized pure carbon blacks with C/Nb_{0.1}Ti_{0.9}O₂ nanofibers at four different weight percentages, i.e. 0, 25, 75 and 100 wt.%. In this study, two cases for pure C/Nb_{0.1}Ti_{0.9}O₂ nanofibers and pure carbon blacks were treated as composite catalyst supports, only for the convenience of discussion and fluency of reading, which are containing 0 and 100 wt.% carbon blacks.

5.2.1.3 Pt deposition

Using microwave-assisted polyol technique described in [55], Pt nanoparticles were deposited onto composite catalyst supports. In a typical catalyst synthesis, a desired amount of composite catalyst support was first dispersed into ethylene glycol. The Pt precursor solution was prepared separately by adding the desired amount of chloroplatinic acid hexahydrate (H₂PtCl₆·6H₂O), with a target Pt weight percentages of 20 wt.%, into the mixture of DI water and ethylene glycol as solvent. And then the above two solutions were mixed, and the pH value of this mixture was adjusted to 10 by adding 0.1 M NaOH solution in ethylene glycol. This solution then has been reduced at 185 °C for 2 minutes in a Biotage® (Initiator Classic) microwave reactor. After the reduced suspension (Pt catalyst + solvent) being cooled down to 50°C, the reduction step was repeated for one more time. Finally, Pt catalysts were separated from the solvent, washed with copious amounts of DI

water, and then vacuum dried at 80 °C for overnight. Table 5.1 shows corresponding abbreviated names and CBWPs (CBWPs) of all synthesized Pt catalysts along with commercial 40 wt.% Pt/C (HiSpec 4000, Johnson Matthey) catalyst used as a reference.

Table 5.1. List of investigated Pt catalysts. Samples TC, C25C, C75C and VC were prepared While JM was purchased from Johnson Matthey. CBWP=carbon black weight percentage.

Catalyst Name	Catalyst Composition	CBWPs in composite support, wt. %
TC	20 wt.% Pt/(C/Nb _{0.1} Ti _{0.9} O ₂)	0
C25C	20 wt.% Pt/(Vul. _{25wt.%} -(C/Nb _{0.1} Ti _{0.9} O ₂) _{75wt.%})	25
C75C	20 wt.% Pt/(Vul. _{75wt.%} -(C/Nb _{0.1} Ti _{0.9} O ₂) _{25wt.%})	75
VC	20 wt.% Pt/Vulcan XC-72R	100
JM	HiSpec 40 wt.% Pt/C	100

5.2.1.4 Material characterization of composite supported Pt catalysts

Powder X-ray diffraction (PXRD) measurements were performed on a Bruker D8 Discover diffractometer equipped with a Vantec-500 area detector and GADDS software package. For All PXRD measurements, the X-ray tube was operated at 40 kV and 40 mA with monochromatized radiation source of CuK α 1 (wavelength = 1.54187 Å) and an initial beam diameter of 0.5 mm was used. Van der Pauw method [60] was used to measure the electronic conductivity of composite catalyst supports, the details for the process of measurements were reported elsewhere [55]. Thermogravimetric analyses were performed using a Thermal analysis (TA) instrument (SDT Q-600) under air stream with 3°C/min heating rate from room temperature up to 1050 °C. The true densities of catalyst supports were measured using a gas pycnometer (Micromeritics Accupyc II 1340) at 25°C, and the average of last three measurements were reported with a standard deviations less than

0.0005. The NOVA 1200e pore size and surface area analyser (Quantachrome Instruments) equipped with NovaWin software package was used for surface area and average pore size measurements. The amount of adsorbed nitrogen onto different supports at constant temperature of 77°K (-196°C) have been used for Brunauer-Emmett-Teller (BET) surface area measurements. The t-plot of de Boer [61] offered by NovaWin software [40, 62] was used for the calculation of external surface area of different supports, i.e., the area of pores with diameters larger than 2nm. Further, the pore size distributions were calculated from desorption branch of the isotherms using Barrett, Joyner and Halenda (BJH) method [62]. High resolution transmission electron microscopy (HRTEM) images were taken at an image-corrected low-base microscope (FEI Titan), operated at 300kV, equipped with an Oxford x-sight energy dispersive spectrometer (EDS) detector (Oxford Instruments). X-ray photoelectron spectroscopy (XPS) measurements were performed on an Axis Ultra X-ray photoelectron spectrometer (Kratos Analytical). Powder samples were pressed into indium foil using a clean glass slide before XPS measurements. Both survey scan and high resolution analyses were carried out with an analysis area of 300 × 700 microns and pass energies of 160 eV and 20 eV, respectively. The instrument work function was calibrated to give a binding energy (BE) of 83.96 eV for the Au 4f_{7/2} line for metallic gold and the spectrometer dispersion was adjusted to give a BE of 932.62 eV for the Cu 2p_{3/2} line of metallic copper. The Kratos charge neutralizer system was used on all specimens. Spectra were charge corrected so that the main line of the C 1s spectrum (adventitious carbon) set to 284.8 eV.

5.2.1.5 Electrochemical characterization of composite-supported Pt catalysts

Electrochemical characterizations were conducted using a rotating disk electrode (BASi RDE-2) with a conventional three-electrode system contained in a glass cell and a potentiostat. Pt wire and saturated Ag/AgCl electrodes were used as counter and reference electrodes, respectively, and a 0.076 cm² (D = 3 mm) area glassy carbon (GC) rotating disk electrode (RDE) tip coated with a thin layer of catalyst served as a working electrode, the details of the catalyst coating method were described elsewhere [55]. The total catalyst mass coated onto the GC electrodes was 10 µg with 2 µg of Pt and then the catalyst coated GC electrodes were impregnated by 2 µL of diluted Nafion ionomer solution (5 wt.% in aliphatic alcohols, Type: D-520 from DuPont) before any electrochemical test.

All Cyclic Voltammograms (CVs) were performed in Ar saturated solutions of 0.5 M H₂SO₄ between 0 to 1.2 V versus to the reversible hydrogen electrode (RHE) at a scan rate of 50 mV/s. To investigate the electrochemical durability of the catalysts, the electrochemically active surface areas (ECSAs) were calculated and compared for the fresh catalysts and potentially cycled catalysts after 1000 full potential cycles between 0-1.2 V. The ECSAs were calculated through the charge integration under the hydrogen adsorption peaks appearing between 0.05 and 0.38 V (RHE) in the negative going potential sweep, a standard hydrogen monolayer full coverage charge of 210 $\mu\text{C}\cdot\text{cm}^{-2}$ was assumed on a pure Pt surface [63].

For Oxygen reduction reaction (ORR) mass activity measurements, linear sweep voltammograms were recorded at a scan rate of 5 mV/s in O₂ saturated solutions of 0.5 M H₂SO₄ with a rotation speed of 1600 rpm at room temperature and ambient pressure. Similarly to check the durability of synthesized catalysts, the ORR mass activities were reported and compared for fresh catalysts and potentially cycled catalysts after 1000 cycles. The linear current-voltage curves at the negative sweep scan at the potential range of 0.4 V to 1.1 V were used to estimate ORR mass activities at 0.9V with a unit of $\text{mA}\cdot\text{mg}_{\text{Pt}}^{-1}$ [55, 63].

5.2.2 Evaluation of composite supported Pt catalysts by optimized H₂-air PEMFC performance

Generally to be able to evaluate the H₂-air PEMFC performances with the synthesized Pt catalysts on the cathode side, first, they need to be mixed with other components (Nafion and solvent) at pre-determined relative amounts to form a catalyst ink precursor; second, the catalyst ink needs to be coated onto either gas diffusion layers or Nafion membranes in the form of a catalyst layer (CL). To be able to compare PEMFC performance of different catalysts at their highest PEMFC performance conditions, Nafion loading in the CL identified to be a key parameter which needs to be effectively optimized and correlated to either weight or volume of the catalyst (catalyst support + PGMs) in the CL. In the remaining of this section, the methodology that will be used to compare the PEMFC performance of synthesized composite supported Pt catalysts will be explained. The optimization of Nafion loading using Nafion Volume percentages (NVPs) will be defined

first and then catalyst layer preparation procedure through electrospray deposition technique will be explained.

5.2.2.1 NVP vs. NWP in the catalyst layer

In order to compare the performance of PEMFCs with different composite-supported Pt catalysts, Nafion volumetric percentage (NVP) is defined as the percentage of dry Nafion volume in the CL, as shown in Eq. (5-1):

$$\text{NVP} = \frac{\left(L_{\text{Nafion}} / \rho_{\text{Nafion}} \right)}{\left(L_{\text{Nafion}} / \rho_{\text{Nafion}} \right) + \left(L_{\text{Support}} / \rho_{\text{Support}} \right) + \left(L_{\text{Pt}} / \rho_{\text{Pt}} \right)} \times 100 \quad (5-1)$$

Where ρ_{Nafion} , ρ_{Support} , and ρ_{Pt} are the true densities, with units of $\text{mg}\cdot\text{cm}^{-3}$, and L_{Nafion} , L_{Support} , and L_{Pt} are the target loadings of dry Nafion, catalyst support, and platinum, with units of $\text{mg}\cdot\text{cm}^{-2}$, in the CL, respectively. The true densities for different types of composite catalyst supports (ρ_{Support}) were determined through gas pycnometry (Micromeritics Accupyc II 1340) measurements, as shown in Table 5.2, and a value of $21400 \text{ mg}\cdot\text{cm}^{-3}$ was used as the true density of metallic Platinum (ρ_{Pt}). The dry Nafion density (ρ_{Nafion}) is set to a value of $1134 \text{ mg}\cdot\text{cm}^{-3}$ that was reported by Bonifácio et al. [52] for the same type of Nafion solution employed in this study for catalyst ink preparation, i.e., Type D-520 from DuPont.

Table 5.2. True densities of composite catalyst supports measured through gas pycnometry.

	C/Nb _{0.1} Ti _{0.9} O ₂	Vul.25 wt.%- (C/Nb _{0.1} Ti _{0.9} O ₂) ₇₅ wt.%	Vul.75 wt.%- (C/Nb _{0.1} Ti _{0.9} O ₂) ₂₅ wt.%	Vulcan XC-72R
Density, $\text{mg}\cdot\text{cm}^{-3}$	4259	3737	2693	2171

To be able to compare the effectiveness and efficiency of working with NVPs rather than commonly used NWP, NWP were also reported in the present study. NWP were determined using the well-established equation proposed by Passalacqua et al. [46] as the percentage of dry Nafion Loading in the CL (previously known as NFP), as shown in Eq. (5-2):

$$\text{NWP} = \frac{L_{\text{Nafion}}}{L_{\text{Nafion}} + L_{\text{Support}} + L_{\text{Pt}}} \times 100 \quad (5-2)$$

5.2.2.2 Catalyst Layer preparation

Cathode Catalyst layers were prepared onto 24BC SIGRACET[®] carbon papers with an area of 5 cm² through only electrospray deposition technique, whereas anode CLs were prepared either by airbrush or electrospray deposition techniques. Before adopting any method to form a CL, desired amounts of catalysts and Nafions have to be dispersed homogeneously in a solvent to create target Pt loadings and NVPs in the CL. In this study, catalyst volumetric loading (CVL) with a unit of cm³·cm⁻², as defined in Eq. (5-3), was used to calculate the required Nafion loadings (mg·cm⁻²), defined in Eq. (5-4), to create the target NVPs in the CLs, as follows:

$$\text{Catalyst Volumetric Loading (CVL)} = (L_{\text{Support}} \times \rho_{\text{Support}}^{-1}) + (L_{\text{Pt}} \times \rho_{\text{Pt}}^{-1}) \quad (5-3)$$

$$L_{\text{Nafion}} = \left(\frac{\text{NVR}}{1 - \text{NVR}} \right) \times \text{CVL} \times \rho_{\text{Nafion}} \quad (5-4)$$

Where NVR stands for Nafion volumetric ratio (NVR), and it equals to NVP divided by 100. Isopropyl alcohol was used as solvent to prepare the catalyst inks and the

concentration of dry Nafion in the solvent was $0.6 \text{ mg}\cdot\text{mL}^{-1}$ for both airbrush and electro spray deposition techniques. After about 3 hours sonication of the catalyst inks at room temperature, the well-dispersed catalyst inks can be airbrushed (only used for anode CLs) using a commercial dual-action airbrush gun (VL-SET, Paasche) at a back pressure of 10 psig, or can be electro sprayed by an electro spinning apparatus with a heated aluminum collector. During catalyst layer deposition, the carbon paper substrates were always placed on the heated aluminum collector at 60°C to accelerate the solvent evaporation process. The amount of deposited catalyst onto dried carbon paper substrates were controlled by weighing them using a 5 digit accuracy balance (ACCULAB) before and after deposition.

As an example, Table SI-5.1 shows a typical series of calculations which are needed to be done to prepare an electro sprayed catalyst layer out of TC catalysts with a target Pt loading of $0.17 \text{ mgPt}\cdot\text{cm}^{-2}$ and NVP of 45%. Table SI-5.1 shows that typically to prepare an electro sprayed CL with the above specifications, 4.25 mg of TC catalysts will be dispersed into 1.29 mL of diluted Nafion ionomer solution in isopropanol (17 μL of 5 wt.% Nafion stock solution + 1.29 mL isopropanol). This suspension will be sonicated for at least 3 hours to form a well-dispersed catalyst ink. Then the well-dispersed catalyst ink will be loaded into a plastic syringe with a 22 gauge stainless steel blunt needle. After placing the loaded syringe into a syringe pump (KDS scientific), it will be electrodeposited by using a DC voltage of 8kV (ES50, Gamma high voltage research) at 1 mL/hr feeding rate while the substrate (carbon paper) is placed onto a heated aluminum collector. The distance between the thermostated collector at 60°C and needle tip will be 5 cm, and the catalyst ink has to be sonicated every 15 minutes to keep it homogenized during electrodeposition process.

5.2.2.3 Membrane electrode assembly (MEA) fabrication

By using an automatic hydraulic press (CARVER®) under 600 pounds force at 130°C for 3 minutes, MEAs have been prepared via sandwiching NRE212 (non-reinforced membrane with an equivalent weight of $1100 \text{ g}\cdot\text{eq}^{-1}$ and thickness of $50.8 \mu\text{m}$) type Nafion membrane between air-dried anode and cathode electrodes.

5.2.2.4 Polarization curves

PEMFC polarization curves have been recorded by using an entirely automatic fuel cell test station (FCTS) developed in the Clean Powertrain Lab (CTL) at the University of Windsor. The entirely automated fuel cell test station which have been used in our previous study [64] was upgraded by a 5 cm² research fuel cell with Pneumatic compression (TP5E, Tandem Technologies Inc.), standard back pressure unit (850BP Scribner Associates Inc.) and a house-made fully automated bubble humidifier with heated transfer lines. Both H₂ and air were saturated with water at 80°C and were provided with constant excess coefficients of 1.5 and 2.5 to anode and cathode compartments, respectively. Before recording polarization curves, as-fabricated MEAs were activated first in the constant voltage mode (through 6 cycles of alternating the voltage from 0.7 V for 20 minutes to 0.5 V for 20 minutes) and then in the constant current mode (at 0.5 A·cm⁻² for 12 hours). The polarization curves were recorded at the cell temperature of 80°C and back pressure of 30 psig.

5.3. Results and discussion

5.3.1. Development of composite-supported Pt catalysts

5.3.1.1 Physical characteristics of composite catalyst supports

Crystal structure

PXRD was employed to investigate the crystal structure of all proposed composite catalyst supports, C/Nb_{0.1}Ti_{0.9}O₂; physical mixture of 25 wt.% Vulcan XC-72R with 75 wt.% C/Nb_{0.1}Ti_{0.9}O₂ NFs (Vul._{25wt.%}-(C/Nb_{0.1}Ti_{0.9}O₂)_{75wt.%}); physical mixture of 75 wt.% Vulcan XC-72R with 25 wt.% C/Nb_{0.1}Ti_{0.9}O₂ NFs (Vul._{75wt.%}-(C/Nb_{0.1}Ti_{0.9}O₂)_{25wt.%}); and Vulcan XC-72R, and the PXRD patterns of these supports are shown in Fig. SI-5.1. As discussed in our previous study [55], C/Nb_{0.1}Ti_{0.9}O₂ nanofibers (the composite with 0 wt.% carbon black) were crystallized into a mixture of rutile and anatase polymorphs of TiO₂ lattice, predominantly 85% rutile, without any distinct features of niobium oxide or ternary phases. Both having rutile phase TiO₂ and Nb incorporation into the TiO₂ lattice, without forming any secondary oxide, are extremely critical in order to produce electronically

conductive Nb-doped TiO₂ as a catalyst support for PEMFC applications [65, 66]. Fig. SI-5.1 also showed that, after mixing 75 wt.% carbon black with C/Nb_{0.1}Ti_{0.9}O₂ NFs, Vul._{75wt.%(C/Nb_{0.1}Ti_{0.9}O₂)_{25wt.%}, composite support showed distinguishable feature of added Vulcan XC-72R at 24.9° which is in agreement with the predominance of graphitic carbon in this sample. Furthermore, the crystal structure of C/Nb_{0.1}Ti_{0.9}O₂ NFs was remained intact, evidenced by no shift in the peak positions of rutile structure after physically mixing with carbon blacks.}

Actual carbon content, electronic conductivity, and surface area

The physical properties of the synthesized catalyst supports are summarized in Table 5.3.

Table 5.3. Physical properties of in-house prepared catalyst supports and pure Vulcan XC-72R carbon blacks (purchased from Cabot Corporation).

Catalyst Support	CBWPs, wt.%	Actual Carbon Content ^a , wt.%	Electronic Conductivity, (S·cm ⁻¹)	BET Surface Area, (m ² ·g ⁻¹)	Micropore Area ^c , (m ² ·g ⁻¹)	External Surface Area ^d , (m ² ·g ⁻¹)
C/Nb _{0.1} Ti _{0.9} O ₂	0	11	0.12	102	16	86
Vul. _{25 wt.%(C/Nb_{0.1}Ti_{0.9}O₂)_{75 wt.%}}	25	30	1.2	130	35	95
Vul. _{75 wt.%(C/Nb_{0.1}Ti_{0.9}O₂)_{25 wt.%}}	75	77	3.3	189	80	100
Vulcan XC-72R	100	> 97.5% ^b	4	215	110	105

^aActual carbon contents were obtained from TGA data plots except for Vulcan XC-72R; ^bPhysical properties of Vulcan XC-72R is available from Cabot Corporation Website (<http://www.cabotcorp.com>); ^cMicropore areas were obtained from t-plots; ^dExternal surface areas were obtained by subtracting micropore areas from BET surface areas.

Thermogravimetric analyses (TGAs) were employed to verify the actual carbon content of composite catalyst supports that is represented by the weight loss percentage, assuming the only source of weight loss would be the carbon oxidation. TGA results are shown in Fig. 5.1. The composite catalyst supports with 25 or 75 wt.% carbon black clearly demonstrated much higher weight loss than that for C/Nb_{0.1}Ti_{0.9}O₂ NFs. It is important to note that the actual carbon content includes the carbon sources from both the carbon embedment and physically mixing. Therefore the actual carbon content of a composite catalyst support is higher than the CBWP for the same composite support, e.g 30 wt.% vs. 25wt.%. This difference correlates very well with the contribution from the oxidation of the embedded carbon in C/Nb_{0.1}Ti_{0.9}O₂ NFs, around 11%. Additionally, carbon decomposition temperature is higher for the composite catalyst supports with non-zero carbon black percentages than that for C/Nb_{0.1}Ti_{0.9}O₂ NFs which is with zero carbon black percentage, e.g, 500°C vs. 300°C, that is in agreement with less graphitization degree of the embedded carbon than that for the graphitized carbon blacks [67], the embedded carbon into Nb-doped TiO₂ NFs has been previously shown to exhibit highly distorted garphitic structure [55].

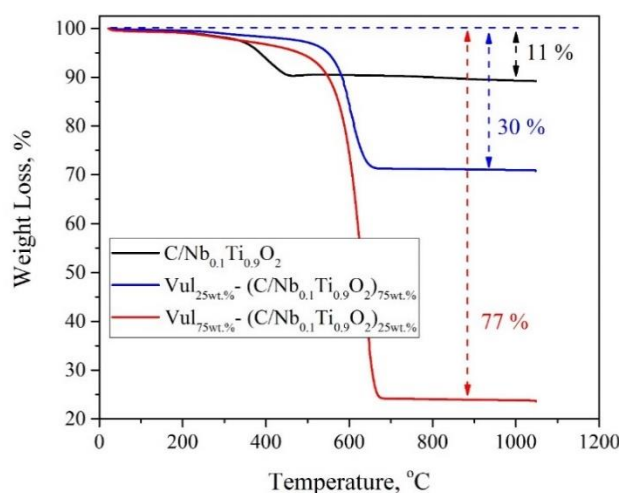


Figure 5.1. Weight loss vs Temperature from TGA tests for composite catalyst supports C/Nb_{0.1}Ti_{0.9}O₂, Vul_{25wt.%}-(C/Nb_{0.1}Ti_{0.9}O₂)_{75wt.%} and Vul_{75wt.%}-(C/Nb_{0.1}Ti_{0.9}O₂)_{25wt.%}.

As shown in Table 5.3, the electronic conductivity of the composite support Vul._{25wt.%}-(C/Nb_{0.1}Ti_{0.9}O₂)_{75wt.%}, formed by adding 25 wt.% carbon blacks (Vulcan XC-72R) to C/Nb_{0.1}Ti_{0.9}O₂ NFs, is 10 times higher than that of C/Nb_{0.1}Ti_{0.9}O₂, i.e., 1.2 vs 0.12 S·cm⁻¹. Adding more carbon black, e.g., 75 wt.%, the electronic conductivity of the composite support was further increased and only slightly lower than the electronic conductivity of pure carbon blacks, e.g., 3.3 vs. 4 S cm⁻¹. The observed as expected monotonic increase in the electronic conductivity of the composite supports by the increase of CBWP in the composite support most probably would favor the electron transfer from Pt nanoparticles to/through composite supports during the ORR in PEM fuel cells [27, 36].

Fig. SI-5.2 shows, for all synthesized composite supports, the nitrogen adsorption/desorption isotherms for surface area analysis, the BJH pore size distributions and t-plots for external surface area calculations. It has been shown that micropores (pore with diameter smaller than 2 nm) merely serve as active sites for platinum depositions [68], instead external surface areas (micropore surface area subtracted from BET surface area) is more representative of the area that can contribute to the enhanced fuel cell performances. As shown in Fig. SI-5.2c, by an increase in CBWP, t-plots are clearly demonstrating larger positive intercepts (an increase in micropore areas), because carbon blacks have much larger micropore area than C/Nb_{0.1}Ti_{0.9}O₂ NFs, as shown in Table 5.3. Accordingly, as shown in Table 5.3, although adding carbon blacks to C/Nb_{0.1}Ti_{0.9}O₂ NFs significantly improved BET surface areas (e.g. from 102 to 189 m².g⁻¹), the external surface areas of composite supports were only slightly improved (e.g. from 102 to 189 m².g⁻¹). Furthermore, pore size distribution curves, as shown in Fig. SI-5.2b, showed that pore diameters in Vulcan XC-72R support are more centered on around 40 Å (4 nm) rather than around 80 -100 Å (8-10 nm) for composite catalyst supports, that can be also correlated to having larger micropore area in pure Vulcan XC-72R supports.

It is noteworthy to see that, from Table 5.3, by increasing the CBWP in the composite supports, a monotonic increase in the electronic conductivity of the composite supports has been clearly observed, however, only slightly improved external surface areas could be achieved.

5.3.1.2 Physical characteristics of composite-supported Pt catalysts

Nanostructure and nanomorphology

Microwave-assisted polyol technique have been used to deposit 20 wt.% platinum NPs onto composite catalyst supports with different weight percentages of carbon blacks in the range of 0-100 wt.%. Fig. SI-5.3 shows the PXRD patterns of different composite supported-20 wt.% Pt catalysts. All samples are showing clear peaks of metallic Pt at 39.90°, 46.1°, and 67.5° with all other peaks identical to the ones shown in Fig. SI-5.1, confirmed that the deposition of Pt NPs onto NFs does not change the structure of catalyst supports.

TEM was used to investigate the structure and morphology of Vul.^{75wt.%}-(C/Nb_{0.1}Ti_{0.9}O₂)_{25wt.%} composite-supported 20 wt.% Pt catalyst. As shown in Figs. 5.2a and 5.2b, bright filed (BF) TEM images, the Pt nanoparticles are quite uniformly deposited onto both C/Nb_{0.1}Ti_{0.9}O₂ NFs and carbon blacks. This observation confirmed the effectiveness of the pre-functionalization treatment of carbon blacks in moderating their hydrophobicity to be able to compete with highly hydrophilic C/Nb_{0.1}Ti_{0.9}O₂ NFs in interaction with Pt nanoparticles, which is critical to create an active and durable composite catalyst. However at some areas in Fig. 5.2a, carbon blacks are heavily or less coated with Pt NPs that are consistent with previously observed relatively inhomogeneous coating of Pt onto commercial carbon blacks [65].

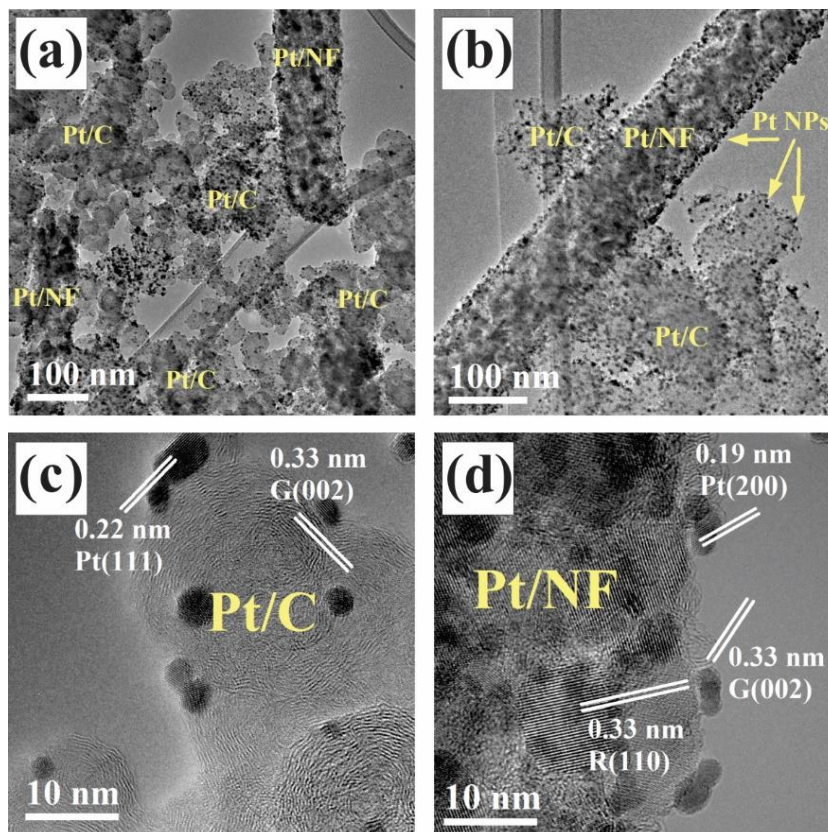


Figure 5.2. Bright filed (BF)-TEM and HRTEM images for the sample of C75C catalyst (20 wt.% Pt/ Vul.75wt.%(C/Nb_{0.1}Ti_{0.9}O₂)₂₅wt.%). (a) and (b) BF-TEM images from different areas; (c) HRTEM image from a representative Pt/C area; and (d) HRTEM image from a representative Pt/NF area. G stands for Graphite and R stands for Rutile.

HRTEM images which are taken from only Pt/Vulcan XC-72R, Fig. 5.2c, or Pt/C/Nb_{0.1}Ti_{0.9}O₂, Fig. 5.2d, areas are both confirming the deposition of Pt NPs mostly in the form of single crystals with diameters in the range of 3-5 nm, which is critical for having higher Pt utilization. The inter-planar spacings (d-spacing) of 0.22 and 0.19 nm between platinum lattice fringes are correlating very well with the distance between (111) and (200) crystallographic planes in the metallic platinum lattice, respectively. Moreover the d-spacings of 0.33 nm observed for both stacked graphene layers (Fig. 5.2c) and titania lattice fringes (Fig. 5.2d) agree well with the distance between (200) planes in graphite and (110) planes in rutile phase titania. We also observed inlaid graphite-like structures at

the surface of Pt deposited C/Nb_{0.1}Ti_{0.9}O₂ NFs (Fig. 5.2d), which could be originated from previously observed inlaid carbon onto C/Nb_{0.1}Ti_{0.9}O₂ NFs [55] or physically mixed carbon blacks.

3.1.2.2 Elemental composition and chemical state at the surface

XPS measurements were used to further study the surface elemental composition of 20 wt.% Pt catalyst supported by Vul.75wt.%(C/Nb_{0.1}Ti_{0.9}O₂)_{25wt.%} supports. The collected XPS survey spectra, as shown in Fig. SI-5.4, reveal that the majority of the atoms at the surface are carbon, around 88 at.%, which is in agreement with the high actual carbon content confirmed by TGA analysis (77 wt.%, see Fig. 5.1). The presence of more unprotected carbon at the surface may lead to higher corrosion rates and lower durability which will be investigated in the next section. The high-resolution XPS spectra at C 1s, O 1s, Ti 2p, Nb 3d, and Pt 4f regions were deconvoluted using different chemical states (Fig. SI-5.5), the XPS peak parameters for different chemical state fits are tabulated in Tables SI-5.2a-e. The obtained high-resolution XPS spectra at different regions, first, showed that the detected carbon at the surface is mostly graphitized carbon black represented by Sp² and it is in agreement with high weight percentage of graphitized carbon blacks; and second, confirmed the presence of Pt NPs only in the form of metallic Pt, rather than having Pt oxide, at the surface of supporting composite catalyst support.

5.3.1.3 Electrochemical activity and durability of Pt catalysts for oxygen reduction reaction

Electrochemical cell with a three electrode system with RDE was employed to investigate the electrochemical activity and durability of our in-house prepared 20 wt.% Pt catalysts with composite catalyst supports and a commercial catalyst (HiSpec 40 wt.% Pt/C, Johnson Matthey) as the reference. Fig. SI-5.6 shows both cyclic and linear-sweep voltammograms obtained from Pt catalysts supported by composite supports before and after applying 1000 potential cycles between 0 to 1.2 V vs. RHE. The obtained electrochemical data were summarized in Table SI-5.3.

As shown in Fig. 5.3, except for the case with CBWP of 100 wt% (i.e., pure carbon black), increasing the CBWP (equivalent to increasing actual carbon content) of the composite catalyst supports, both ORR mass activities and ORR losses were increased.

Accordingly, among the cases studied here, the most durable but least active catalyst is the Pt catalyst supported by $C/Nb_{0.1}Ti_{0.9}O_2$ NFs with 0 wt.% carbon black, and the most active and least durable catalyst is C75C with 75 wt.% carbon black. Furthermore, in both cases of before and after durability tests, it is very interesting to note that, for C75C and C25C catalysts, the incorporation of mesoporous $C/Nb_{0.1}Ti_{0.9}O_2$ NFs into carbon blacks improved not only the durability but also the catalytic activity, comparing with the VC catalyst.

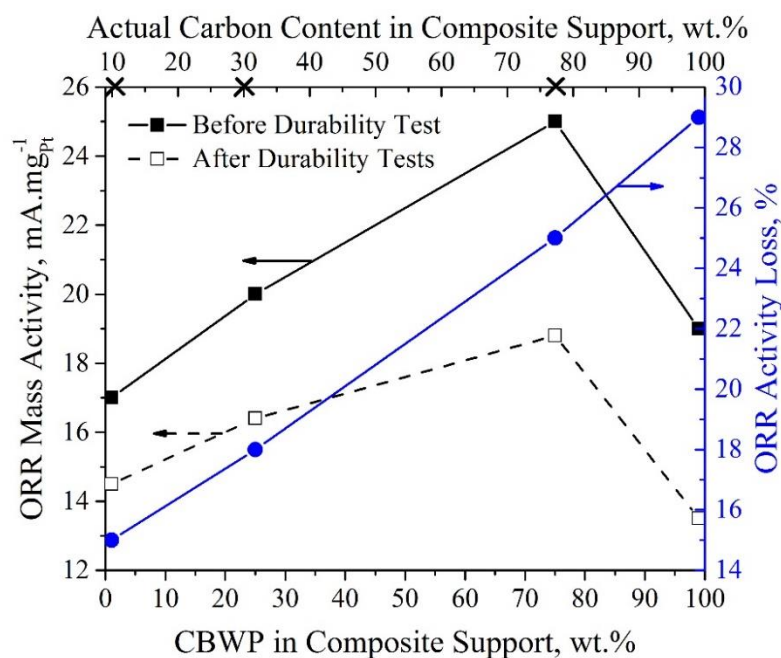


Figure 5.3. ORR mass activities and ORR activity losses for in-house synthesized Pt catalysts versus the CBWP in composite catalyst supports. The actual carbon contents were obtained from TGA data plots represented in Fig. 5.1.

The monotonic increase in the ORR mass activities caused by adding carbon blacks is most probably due to a monotonic increase in the electronic conductivity of the composite catalyst supports as shown in Table 5.3; the enhancement of the electrocatalytic activity (ORR mass activity) of C25C and C75C catalysts versus VC catalyst can be reasoned by the partial charge transfer from metal oxide supports onto Pt NPs [26, 69] induced by

C/Nb_{0.1}Ti_{0.9}O₂ NFs in the composite catalyst supports which is in agreement with the results from literature [27, 36]. However, composite catalyst supports with lower CBWP (higher weight percentage of C/Nb_{0.1}Ti_{0.9}O₂ NF) showed less mass activity than those with higher carbon blackweight percentage (i.e. mass activity of TC < C25C < C75C). This observation suggests the electron transfer between Pt NPs to/through supports to be the limiting factor for the ORR mass activity of the catalyst supports with lower CBWPs [27], because electronic conductivity of composite catalyst supports is significantly lower for the ones with lower CBWP, as shown in Table 5.3.

As shown in Fig. 5.3, increase in the ORR losses was observed with the increase of the CBWP or actual carbon content of the composite catalyst supports. However, after durability tests, TC, C25C, and C75C catalysts exhibited higher ORR mass activities and less ORR losses than those of VC catalyst, which effectively demonstrated the role of C/Nb_{0.1}Ti_{0.9}O₂ NFs in the composite supports.

5.3.2 H₂-Air PEMFC performance evaluations

The ORR mass activity and ORR losses reported in the above section are the ex-situ performance of the Pt catalysts supported by these composite supports. In order to evaluate the in-situ performance, PEMFC with Pt catalysts supported by these composite supports have to be evaluated and compared.

If NWP is used, before being able to compare the performance of PEMFCs with electrospayed cathode catalyst layers that have different composite-supported Pt catalysts, the Nafion loading would have to be optimized for each case independently. Here, experimentally optimized fixed value of NVP was used to predict optimized Nafion loading for electrospayed cathode catalyst layers that have different composite-supported Pt catalysts. The efficiency of using fixed NVP value rather than fixed NWP value will be also demonstrated.

To be able to use fixed NVP value to predict optimized Nafion loadings, initially, optimized NVP has to be experimentally found for electrospayed (ES) cathode CLs, as demonstrated in section 5.3.2.1.

5.3.2.1 Optimized NVP for electrosprayed catalyst layers

From literature [53, 54], optimized NVPs were found between 15% to 35%, based on Table SI-5.4 where the conversion between NWP and NVP has been demonstrated, the equivalent optimized NVPs were found to be in the range of 29% to 57%. Fig. 4 shows the polarization curves (Fig.5.4a) and power density curves (Fig. 5.4b) obtained from single cells with different ES cathode CLs that have different NVP values with same Pt loading of $0.2 \text{ mgPt}\cdot\text{cm}^{-2}$; all anode CLs were fabricated by airbrushing JM catalyst with same Pt loading of $0.4 \text{ mgPt}\cdot\text{cm}^{-2}$ and same NWP of 30%. Fig. 5.4c shows the maximum power density versus NVP, constructed from Fig. 5.4b, clearly showing that ES cathode CLs obtained their maximum power density of $0.49 \text{ W}\cdot\text{cm}^{-2}$ at NVP of 43.7%, or equivalently NWP of 25%.

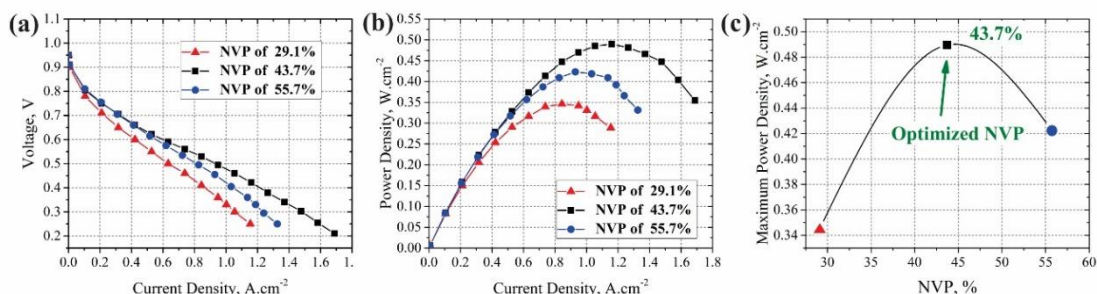


Figure 5.4. Effect of NVP of the cathode CL on H_2/Air PEMFC performance. (a) Polarization curve; (b) Power density curve; and (c) Maximum power density versus NVP values.

Furthermore, in order to reach the goal set by DOE to lower total PGM (anode+cathode) loadings, the effect of Pt loading on the performance of H_2/Air PEMFCs at optimized NVP was investigated. Fig. 5.5 depicts the polarization curves (Fig. 5.5a) and power density curves (Fig. 5.5b) corresponding to single cells with different ES cathode CLs that have different loadings of Pt in the range between 0.05 to $0.40 \text{ mgPt}\cdot\text{cm}^{-2}$ with same NVP of 43.7%; all anode CLs were fabricated by airbrushing JM catalyst with same Pt loading of $0.4 \text{ mgPt}\cdot\text{cm}^{-2}$ and same NWP of 30%. Fig. 5.5c shows the maximum power density versus Pt loading, constructed from Fig. 5.5b, showing that Pt loading of $0.17 \text{ mgPt}\cdot\text{cm}^{-2}$ can be

suggested as an optimized Pt loading for ES CLs within the work presented here. The decrease in the maximum power densities of the ES CLs with Pt loadings beyond $0.2 \text{ mg}_{\text{Pt}}\cdot\text{cm}^{-2}$, that is consistent with literature [53], can be reasoned by the decrease of the Pt utilization efficiency with the increase of the Pt loading. On the other hand, the remarkable decrease in the maximum power densities of the ES CLs with Pt loadings lower than $0.17 \text{ mg}_{\text{Pt}}\cdot\text{cm}^{-2}$, especially in the case of $0.05 \text{ mg}_{\text{Pt}}\cdot\text{cm}^{-2}$ (slightly lower than DOE target for 2020), further confirmed that the mass activity of the state of the art Pt catalysts (e.g. VC catalyst) also have to be improved to reach DOE goals.

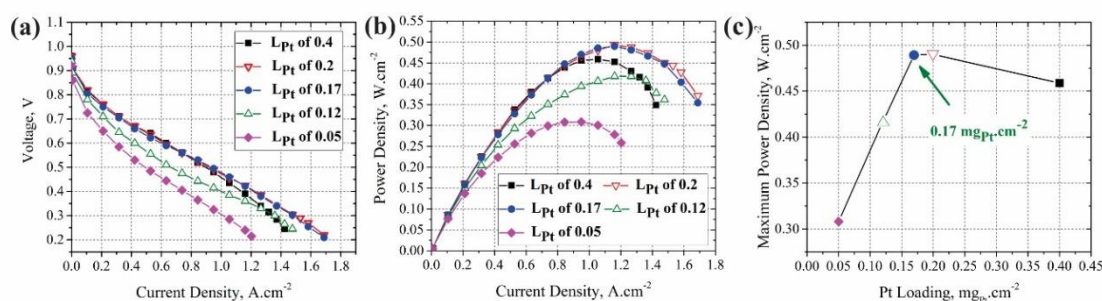


Figure 5.5. Effect of Pt loading of the ES cathode CL on H₂/Air PEMFC performance at optimized NVP. (a) Polarization curves; (b) Power density curves; and (c) Maximum power density versus Pt loading.

To compare our optimized Nafion loadings with the values reported in the literature, Fig. 5.6 compares the H₂/Air PEMFC performance of ES CL of this work (at optimized Pt and Nafion loadings) with the H₂/O₂ PEMFC performance reported by Chaparro et al. [54] with the same Pt loading of $0.17 \text{ mg}_{\text{Pt}}\cdot\text{cm}^{-2}$ and optimized NWP of 15%. Our results for H₂/O₂ PEMFCs were estimated based on the H₂/Air PEMFC performance obtained in our lab and an unsteady model of single PEMFC developed in Dr. Zhou's previous's work as shown in [70] for the sake of comparison of the present work with the available literature. This estimation is needed because that H₂/Air PEMFC performance similar to our work is not available in the literature, and, in our lab, H₂/O₂ PEMFC tests were not doable for safety concerns. Despite using higher value of optimized NWP than that reported by Chaparro et

al. [54] (25% vs. 15%), Fig. 5.6b clearly shows a higher peak power density for the estimated H₂/O₂ PEMFC performance of this work, comparing with that from [55].

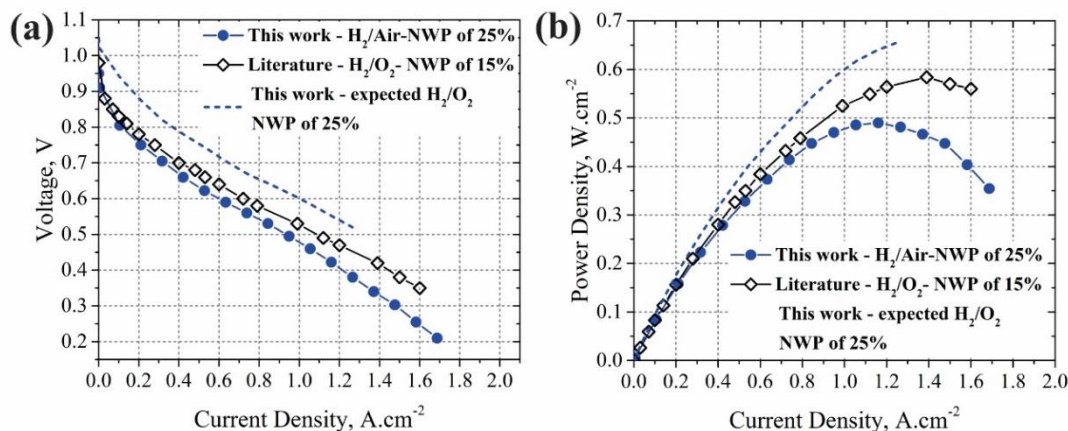


Figure 5.6. Performance comparison for PEMFCs with the house-made ES CL (VC catalyst) at optimized NVP with ES CL (E-tek catalyst) reported in literature [54] with the same Pt loading of 0.17 mg_{Pt}·cm⁻². The dashed lines represent the expected H₂/O₂ PEMFC performance based on the model in [70].

The obtained higher value of the optimized NVP for our in-house synthesized Vulcan XC-72R supported Pt catalysts (VC catalyst) than that reported for commercial 20 wt.% Pt/C (E-tek) catalyst is most probably due to the previously observed dissimilarity between the densities of the catalysts [52]. Recently, gas pycnometry measurements revealed a significant difference between the Vulcan XC-72 used in commercial Pt/C catalysts (sold by BASF) and that available for synthesis (as purchased from Cabot Inc.) [51]. This observation further suggested the fact that using NVP as a criterion is more effective and efficient than NWP to report optimized Nafion loadings for even commercial Pt/C catalysts.

As shown in Fig. SI-5.7, in an attempt to decrease the total PGM loadings, we also used electrospayed CL with a Pt loading of 0.17 mgPt·cm⁻² on the anode side. As expected due to the higher kinetics of hydrogen oxidation reaction (HOR) on the anode side, by lowering the Pt loading even slightly increased the performance at high current density region.

5.3.2.2 Predicted optimized Nafion loadings for composite-supported Pt catalysts

Table 5.4 shows the predicted optimized Nafion loadings for ES CLs employing composite-supported Pt catalysts listed in Table 1. The predictions were done by taking the assumption that the experimentally optimized NVP for ES CL employing VC catalysts would be valid for Pt catalyst with any catalyst supports.

Table 5.4. Predicted optimized Nafion loadings, according to experimentally optimized NVPs, for ES catalyst layers that are employing different catalyst supports.

Catalyst Type	NVP (%)	CVL ^a (cm ³ ·cm ⁻²)	Predicted optimized L _{Nafion} ^b (mg _{Na} ·cm ⁻²)	NWP ^c
C75C	43.7	26×10 ⁻⁵	0.229	21.3
C25C	43.7	19×10 ⁻⁵	0.167	16.4
TC	43.7	16.8×10 ⁻⁵	0.147	14.8

^a CVLs were calculated according to Eq. (3); ^b L_{Nafion}s were calculated according to Eq. (4); ^c NWPs were calculated according to Eq. (2).

As shown in Table 5.4, using fixed optimized NVP obtained experimentally for ES CL employing VC catalysts as the criterion to predict the optimized Nafion loadings led to different NWPs corresponding to each catalyst. This is because of the difference in the densities of these catalyst supports.

To be able to evaluate the effectiveness of using fixed optimized NVP in predicting optimized Nafion loadings for composite-supported Pt catalysts, the case with ES CL employing TC catalyst was chosen to validate the prediction of Nafion loadings using fixed optimized NVP. This is done because the catalyst type of TC catalyst (the density of catalyst support) is totally different than that of VC catalyst which was used to find the optimized NVP value of 43.7%.

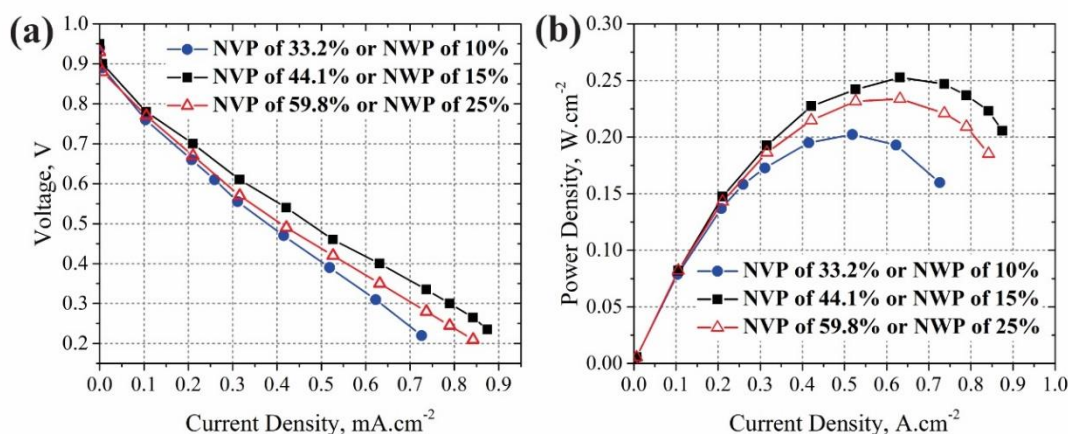


Figure 5.7. Polarization and power density curves of H₂/Air PEMFCs employing electrospayed VC CL on the anode side, with a Pt loading of 0.17 mg_{Pt}·cm⁻² and NVP of 43.7%, and electrospayed TC CL on the cathode side prepared with a Pt loading of 0.17 mg_{Pt}·cm⁻² at different NVPs or NWPs. (a) Polarization curves; (b) Power density curves.

Fig. 5.7 shows the effect of Nafion loading (represented by NWPs on the cathode side) on the PEMFC performance of TC catalysts. Fig. 5.7 clearly demonstrated that experimentally optimized NWP for TC catalyst (15%) is correlating very well with predicted L_{Nafion} of 14.8% through using fixed NVP value as shown in Table 5.4. This observation strongly suggests that using fixed NVP instead of fixed NWP in predicting optimized L_{Nafion} is more efficient and more effective. Accordingly through using fixed NVP, the tedious experimentation for finding optimized Nafion loadings (e.g. typical experiments that were done on TC catalyst in Fig. 5.7) can be avoided and simply the fixed experimentally optimized NVP can be used for predicting optimized L_{Nafion} for catalysts with different catalyst supports.

In the following, the methodologies of using fixed NVP versus fixed NWP will be further evaluated by comparing the performances of PEMFCs with different composite-supported Pt catalysts.

5.3.2.3 PEMFC performances at fixed NVP versus fixed NWP

Figure SI-5.8 compares the H₂/Air PEMFC performances of ES cathode CLs that are employing composite-supported Pt catalysts. In an attempt to further investigate the

effectiveness of using fixed NVP rather than fixed NWP values to predict the optimized Nafion loadings, the H₂/Air PEMFC performances of ES cathode CLs were reported for both fixed NVP and NWP values of 43.7% and 25%, respectively.

Figure 5.8 shows Peak power densities of ES CLs that are employing composite-supported Pt catalysts prepared under both fixed NVP and NWP values versus actual carbon contents or CBWPs of the composite catalyst supports. The ORR losses of composite-supported Pt catalysts obtained under acidic conditions were also reported. The employed fixed NVP and NWP values were 43.7% and 25%, respectively, and the actual carbon contents were obtained from TGA data plots as shown in Fig. 5.1. As shown in Figure 5.8, it is very clear that pure carbon black-based Pt catalyst (VC) outperformed all other composite-supported Pt catalysts, under real fuel cell conditions, despite much-enhanced mass activity obtained for C75C than VC catalyst under acidic conditions (see Fig. 5.2). Moreover, excluding VC catalyst which has 100 wt% of carbon black, by an increase in the CBWP in composite supports, the rate of increase in the peak power densities of ES CLs can be broken up into two sections, despite exhibiting a continuous rise in the ORR mass activities at a fixed rate as shown Fig. 5.3. The maximum peak power densities of ES CLs were significantly improved at 25 wt.% carbon black in the composite catalyst support, whereas the increase in the peak power densities was much less significant after adding more of carbon black (i.e. 75 wt.%). As a result, the hatched area in Fig. 5.8 could resemble an optimum range of the weight percentage of carbon black that should be composited with C/Nb_{0.1}Ti_{0.9}O₂ NFs. Because compositing more carbon blacks (e.g. 75 wt.%) with C/Nb_{0.1}Ti_{0.9}O₂ NFs increased more of the ORR loss (less durability) rather than a noticeable increase in the maximum power density. Furthermore, excluding VC catalyst which has 100 wt% of carbon black, it is apparent that PEMFC performances with the ES CLs prepared at fixed NVP are higher than those prepared at fixed NWP.

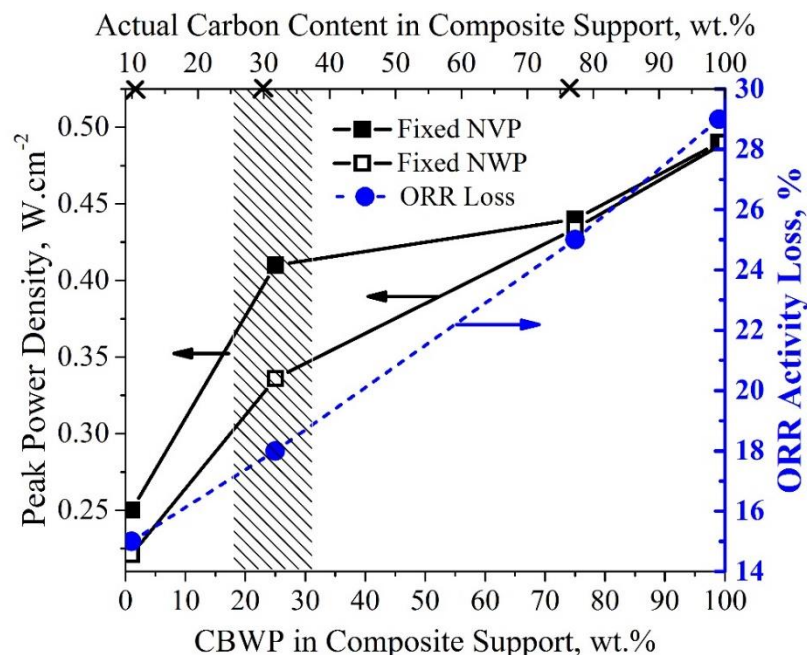


Figure 5.8. Peak Power densities and ORR activity losses for Pt catalyst with different composite supports.

Higher PEMFC performance obtained for ES carbon black-based Pt CL, despite having lower ORR mass activity under acidic conditions when compared with composite-supported Pt catalysts with 25 wt.% and 75 wt.% carbon black, further suggests the fact that real fuel cell conditions are different than that in simulated flooded electrolytes in RDE measurements that were used to measure ORR mass activities [3]. On the other hand, by the increase of CBWP in composite catalyst supports, the change in the rate of PEMFC performance gain (as shown in Fig. 5.8), despite a continuous increase in the ORR mass activities (Fig. 5.3), can be reasoned by a trade-off between the decrease in the electronic conductivity of catalyst layer by an increase in the optimized Nafion loadings (see Table 5.4) and an increase in the electronic conductivity of catalyst supports (see Table 5.3) at 75 wt.% versus 25 wt.% CBWPs. Increasing the CBWP of composite catalyst supports shown to be very critical in terms of improving the electron transfer between Pt NPs to/through supports whereas it could be also detrimental due to an increase in the volume of the catalyst and accordingly an increase in the required Nafion loading to have sufficient proton conductivity. It has been well understood that an increase in the concentration of Nafion (Nafion loading) on the cathode CL will have a profound effect on the proton

transport to Pt clusters, on the one hand, and on the oxygen diffusivity and the internal resistance of the catalyst layer, on the other [53]. Accordingly less significant increase in the PEMFC performance of ES CLs with higher CBWPs (i.e. 75 wt.%) suggest internal resistance of the catalyst layer to be the limiting factor due to the incorporation of higher content of electronically nonconductive Nafion in the catalyst layer (0.229 vs. 0.167 $\text{mg}_{\text{Nafion}}\cdot\text{cm}^{-2}$, see Table 5.4), despite higher electronic conductivity of the composite catalyst supports. However, future works are needed to focus on discovering the effect of either carbon black/ C/Nb_{0.1}Ti_{0.9}O₂ NFs content on other relevant catalyst layer properties such as pore and Nafion distributions.

Additionally, with respect to the advantage of using fixed NVP rather than fixed NWP for comparing PEMFC performances of different catalysts, it can be concluded that the optimized Nafion loadings are more sensitive to and directly affected by the catalyst volumes rather than catalyst weights. Accordingly fixed NVPs could be used for the comparison between PEMFC performances of catalysts with different densities at their highest PEMFC performance conditions without any need for tedious Nafion loading optimization experiments.

5.4 Conclusions

Electrocatalytically more active and more durable composite-supported Pt catalysts were synthesized through depositing Pt nanoparticles onto composite catalyst supports obtained through physically mixing Vulcan XC-72R carbon blacks with carbon-embedded 10 at.% niobium-doped titanium dioxide nanofibers (C/Nb_{0.1}Ti_{0.9}O₂). HRTEM results confirmed the relatively uniform deposition of Pt nanoparticles with an average particle size of 3-5 nm onto both Vulcan XC-72R and C/Nb_{0.1}Ti_{0.9}O₂ supports. By an increase in the carbon black content in the composite catalyst supports, despite having a monotonic rise in the ORR mass activities and ORR losses, PEMFC performance results suggested that adding 25 wt.% carbon black to the composite catalyst supports is more effective than 75 wt.% to create sufficiently active and more durable cathode catalyst layers. Furthermore using fixed NVP in predicting optimized Nafion loadings for catalyst layers employing different catalyst supports was also validated and showed to be more efficient than using fixed NWP. Future work will focus on performing catalyst durability tests under actual fuel

cell conditions and the effects of either carbon black or C/Nb_{0.1}Ti_{0.9}O₂ NFs content on the catalyst layer properties.

5.5 Acknowledgments

The authors thank Profs. Olivera Kesler (University of Toronto), Paul A. Charpentier (Western University), Tricia B. Carmichael (Chemistry and Biochemistry Dept.) and Jeremy Rawson (Chemistry and Biochemistry Dept.) for providing access to their high-temperature tube furnace, TA instrument, four-probe conductivity measurement setup, and microwave reactor, respectively. The authors thank, Ms. Sharon Lackie (GLIER at the University of Windsor), Dr. Mark C. Biesinger (Surface Science Western at Western University), Dr. Andreas Korinek (Canadian Centre for Electron Microscopy at McMaster University) for their help on the SEM, XPS and TEM studies, respectively.

References

1. Debe, M.K., *Electrocatalyst approaches and challenges for automotive fuel cells*. Nature, 2012. **486**(7401): p. 43-51.
2. DOE, *Fuel cell technologies office multi-year research, development, and demonstration plan*. 2014. <http://energy.gov/eere/fuelcells/downloads/fuel-cell-technologies-office-multi-year-research-development-and-22>.
3. Xie, T., et al., *Development of Highly Active and Durable Hybrid Cathode Catalysts for Polymer Electrolyte Membrane Fuel Cells*. Journal of The Electrochemical Society, 2014. **161**(14): p. F1489-F1501.
4. Liu, J., et al., *High-Performance Oxygen Reduction Electrocatalysts based on Cheap Carbon Black, Nitrogen, and Trace Iron*. Advanced Materials, 2013. **25**(47): p. 6879-6883.
5. Shao, Y., et al., *Novel catalyst support materials for PEM fuel cells: current status and future prospects*. Journal of Materials Chemistry, 2009. **19**(1): p. 46-59.

6. Sun, S., et al., *A Highly Durable Platinum Nanocatalyst for Proton Exchange Membrane Fuel Cells: Multiarmed Starlike Nanowire Single Crystal*. *Angewandte Chemie International Edition*, 2011. **50**(2): p. 422-426.
7. Zhang, S., et al., *A review of platinum-based catalyst layer degradation in proton exchange membrane fuel cells*. *Journal of Power Sources*, 2009. **194**(2): p. 588-600.
8. Darling, R.M. and J.P. Meyers, *Kinetic Model of Platinum Dissolution in PEMFCs*. *Journal of The Electrochemical Society*, 2003. **150**(11): p. A1523-A1527.
9. Antolini, E. and E.R. Gonzalez, *Ceramic materials as supports for low-temperature fuel cell catalysts*. *Solid State Ionics*, 2009. **180**(9–10): p. 746-763.
10. Wang, Y.-J., D.P. Wilkinson, and J. Zhang, *Noncarbon Support Materials for Polymer Electrolyte Membrane Fuel Cell Electrocatalysts*. *Chemical Reviews*, 2011. **111**(12): p. 7625-7651.
11. Lv, H. and S. Mu, *Nano-ceramic support materials for low temperature fuel cell catalysts*. *Nanoscale*, 2014. **6**(10): p. 5063-5074.
12. Wu, J., et al., *A review of PEM fuel cell durability: Degradation mechanisms and mitigation strategies*. *Journal of Power Sources*, 2008. **184**(1): p. 104-119.
13. Yu, X. and S. Ye, *Recent advances in activity and durability enhancement of Pt/C catalytic cathode in PEMFC: Part II: Degradation mechanism and durability enhancement of carbon supported platinum catalyst*. *Journal of Power Sources*, 2007. **172**(1): p. 145-154.
14. Virkar, A.V. and Y. Zhou, *Mechanism of Catalyst Degradation in Proton Exchange Membrane Fuel Cells*. *Journal of The Electrochemical Society*, 2007. **154**(6): p. B540-B547.
15. Zhang, Y., et al., *Study of the degradation mechanisms of carbon-supported platinum fuel cells catalyst via different accelerated stress test*. *Journal of Power Sources*, 2015. **273**(0): p. 62-69.

16. Hitchcock, A.P., et al., *Carbon corrosion of proton exchange membrane fuel cell catalyst layers studied by scanning transmission X-ray microscopy*. Journal of Power Sources, 2014. **266**(0): p. 66-78.
17. Lo, C.-P. and V. Ramani, *SiO₂-RuO₂: A Stable Electrocatalyst Support*. ACS Applied Materials & Interfaces, 2012. **4**(11): p. 6109-6116.
18. Yin, S., et al., *A highly stable TiB₂-supported Pt catalyst for polymer electrolyte membrane fuel cells*. Journal of Power Sources, 2011. **196**(19): p. 7931-7936.
19. Liu, Y. and W.E. Mustain, *High Stability, High Activity Pt/ITO Oxygen Reduction Electrocatalysts*. Journal of the American Chemical Society, 2012. **135**(2): p. 530-533.
20. Avasarala, B. and P. Haldar, *Durability and degradation mechanism of titanium nitride based electrocatalysts for PEM (proton exchange membrane) fuel cell applications*. Energy, 2013. **57**(0): p. 545-553.
21. Neophytides, S.G., et al., *Composite Hypo-Hyper-d-Intermetallic and Interionic Phases as Supported Interactive Electrocatalysts*. The Journal of Physical Chemistry B, 2006. **110**(7): p. 3030-3042.
22. Huang, S.-Y., et al., *Development of a Titanium Dioxide-Supported Platinum Catalyst with Ultrahigh Stability for Polymer Electrolyte Membrane Fuel Cell Applications*. Journal of the American Chemical Society, 2009. **131**(39): p. 13898-13899.
23. Huang, S.-Y., P. Ganesan, and B.N. Popov, *Electrocatalytic activity and stability of niobium-doped titanium oxide supported platinum catalyst for polymer electrolyte membrane fuel cells*. Applied Catalysis B: Environmental, 2010. **96**(1-2): p. 224-231.
24. Rajalakshmi, N., N. Lakshmi, and K.S. Dhathathreyan, *Nano titanium oxide catalyst support for proton exchange membrane fuel cells*. International Journal of Hydrogen Energy, 2008. **33**(24): p. 7521-7526.

25. Abdullah, N. and S.K. Kamarudin, *Titanium dioxide in fuel cell technology: An overview*. Journal of Power Sources, 2015. **278**(0): p. 109-118.
26. Lewera, A., et al., *Metal–Support Interactions between Nanosized Pt and Metal Oxides (WO₃ and TiO₂) Studied Using X-ray Photoelectron Spectroscopy*. The Journal of Physical Chemistry C, 2011. **115**(41): p. 20153-20159.
27. Wang, Y.-J., D.P. Wilkinson, and J. Zhang, *Synthesis of conductive rutile-phased Nb_{0.06}Ti_{0.94}O₂ and its supported Pt electrocatalysts (Pt/Nb_{0.06}Ti_{0.94}O₂) for the oxygen reduction reaction*. Dalton Transactions, 2012. **41**(4): p. 1187-1194.
28. Park, K.-W. and K.-S. Seol, *Nb-TiO₂ supported Pt cathode catalyst for polymer electrolyte membrane fuel cells*. Electrochemistry Communications, 2007. **9**(9): p. 2256-2260.
29. Kumar, A. and V. Ramani, *Ta_{0.3}Ti_{0.7}O₂ Electrocatalyst Supports Exhibit Exceptional Electrochemical Stability*. Journal of The Electrochemical Society, 2013. **160**(11): p. F1207-F1215.
30. Kim, J.-H., et al., *Enhancement of Activity and Durability through Cr Doping of TiO₂ Supports in Pt Electrocatalysts for Oxygen Reduction Reactions*. ChemCatChem, 2014. **6**(11): p. 3239-3245.
31. Ho, V.T.T., et al., *Nanostructured Ti_{0.7}Mo_{0.3}O₂ Support Enhances Electron Transfer to Pt: High-Performance Catalyst for Oxygen Reduction Reaction*. Journal of the American Chemical Society, 2011. **133**(30): p. 11716-11724.
32. Zana, A., et al., *Core-shell TiO₂@C: towards alternative supports as replacement for high surface area carbon for PEMFC catalysts*. Electrochimica Acta, 2014. **139**(0): p. 21-28.
33. Wang, Y.-J., et al., *Synthesis of Pd and Nb–doped TiO₂ composite supports and their corresponding Pt–Pd alloy catalysts by a two-step procedure for the oxygen reduction reaction*. Journal of Power Sources, 2013. **221**(0): p. 232-241.

34. Senevirathne, K., et al., *Nb-doped TiO₂/carbon composite supports synthesized by ultrasonic spray pyrolysis for proton exchange membrane (PEM) fuel cell catalysts*. *Journal of Power Sources*, 2012. **220**(0): p. 1-9.
35. Bauer, A., et al., *Application of a composite structure of carbon nanoparticles and Nb–TiO₂ nanofibers as electrocatalyst support for PEM fuel cells*. *Journal of Power Sources*, 2012. **210**(0): p. 15-20.
36. Wang, Y.-J., et al., *Ta and Nb co-doped TiO₂ and its carbon-hybrid materials for supporting Pt-Pd alloy electrocatalysts for PEM fuel cell oxygen reduction reaction*. *Journal of Materials Chemistry A*, 2014. **2**(32): p. 12681-12685.
37. Qu, W.-L., et al., *Titanium compounds TiC–C and TiO₂–C supported Pd catalysts for formic acid electrooxidation*. *International Journal of Hydrogen Energy*, 2012. **37**(20): p. 15096-15104.
38. von Kraemer, S., et al., *Evaluation of TiO₂ as catalyst support in Pt-TiO₂/C composite cathodes for the proton exchange membrane fuel cell*. *Journal of Power Sources*, 2008. **180**(1): p. 185-190.
39. Ruiz-Camacho, B., et al., *Electrochemical and XAS investigation of oxygen reduction reaction on Pt-TiO₂-C catalysts*. *International Journal of Hydrogen Energy*, 2013. **38**(28): p. 12648-12656.
40. Chhina, H., S. Campbell, and O. Kesler, *Ex Situ and In Situ Stability of Platinum Supported on Niobium-Doped Titania for PEMFCs*. *Journal of The Electrochemical Society*, 2009. **156**(10): p. B1232-B1237.
41. O'Hayre, R., D.M. Barnett, and F.B. Prinz, *The Triple Phase Boundary: A Mathematical Model and Experimental Investigations for Fuel Cells*. *Journal of The Electrochemical Society*, 2005. **152**(2): p. A439-A444.
42. Steele, B.C.H. and A. Heinzel, *Materials for fuel-cell technologies*. *Nature*, 2001. **414**(6861): p. 345-352.

43. Tabe, Y., H. Takamatsu, and T. Chikahisa, *Analysis of Dominant Parameters in Structure and Properties of Cathode Catalyst Layer on PEM Fuel Cell Performance*. ECS Transactions, 2009. **25**(1): p. 39-47.
44. Costamagna, P. and S. Srinivasan, *Quantum jumps in the PEMFC science and technology from the 1960s to the year 2000: Part I. Fundamental scientific aspects*. Journal of Power Sources, 2001. **102**(1–2): p. 242-252.
45. Qi, Z. and A. Kaufman, *Low Pt loading high performance cathodes for PEM fuel cells*. Journal of Power Sources, 2003. **113**(1): p. 37-43.
46. Passalacqua, E., et al., *Nafion content in the catalyst layer of polymer electrolyte fuel cells: effects on structure and performance*. Electrochimica Acta, 2001. **46**(6): p. 799-805.
47. Curnick, O.J., B.G. Pollet, and P.M. Mendes, *Nafion[registered sign]-stabilised Pt/C electrocatalysts with efficient catalyst layer ionomer distribution for proton exchange membrane fuel cells*. RSC Advances, 2012. **2**(22): p. 8368-8374.
48. Xing, L., et al., *Numerical investigation of the optimal Nafion® ionomer content in cathode catalyst layer: An agglomerate two-phase flow modelling*. International Journal of Hydrogen Energy, 2014. **39**(17): p. 9087-9104.
49. Siddique, N.A. and F. Liu, *Process based reconstruction and simulation of a three-dimensional fuel cell catalyst layer*. Electrochimica Acta, 2010. **55**(19): p. 5357-5366.
50. Litster, S. and G. McLean, *PEM fuel cell electrodes*. Journal of Power Sources, 2004. **130**(1–2): p. 61-76.
51. Bonifácio, R.N., A.O. Neto, and M. Linardi, *Influence of the relative volumes between catalyst and Nafion ionomer in the catalyst layer efficiency*. International Journal of Hydrogen Energy, 2014. **39**(27): p. 14680-14689.
52. Bonifácio, R.N., A.O. Neto, and M. Linardi, *Comparative analysis between mass and volume of catalysts as a criterion to determine the optimal quantity of Nafion*

- ionomer in catalyst layers*. International Journal of Hydrogen Energy, 2015. **40**(6): p. 2840-2849.
53. Chaparro, A.M., et al., *PEMFC electrode preparation by electrospray: Optimization of catalyst load and ionomer content*. Catalysis Today, 2009. **143**(3–4): p. 237-241.
54. Chaparro, A.M., et al., *Properties of Catalyst Layers for PEMFC Electrodes Prepared by Electrospray Deposition*. Journal of The Electrochemical Society, 2010. **157**(7): p. B993-B999.
55. Navaei Alvar, E., b. Zhou, and S.H. Eichhorn, *Carbon embedded Nb-doped TiO₂ nanofiber catalyst supports for PEM fuel cell applications*. Journal of Materials Chemistry A, 2015.
56. Navaei Alvar, E., B. Zhou, and S.H. Eichhorn. *Effect of Reducing Agent on the Dispersion of Pt Nanoparticles on Electrospun Nb_{0.1}Ti_{0.9}O₂ Nanofibers*. in *Materials Research Society 2013*. 2013. San Francisco.
57. Akalework, N.G., et al., *Ultrathin TiO₂-coated MWCNTs with excellent conductivity and SMSI nature as Pt catalyst support for oxygen reduction reaction in PEMFCs*. Journal of Materials Chemistry, 2012. **22**(39): p. 20977-20985.
58. Guha, A., et al., *Surface-modified carbons as platinum catalyst support for PEM fuel cells*. Carbon, 2007. **45**(7): p. 1506-1517.
59. Kumar, S.M.S., et al., *Efficient tuning of the Pt nano-particle mono-dispersion on Vulcan XC-72R by selective pre-treatment and electrochemical evaluation of hydrogen oxidation and oxygen reduction reactions*. International Journal of Hydrogen Energy, 2011. **36**(9): p. 5453-5465.
60. Van Der Pauw, L.J., *A Method of Measuring Specific Resistivity and Hall Effect of Discs of Arbitrary Shape*. Philips Research Reports, 1958. **13**: p. 1-9.
61. de Boer, J.H., et al., *Studies on pore systems in catalysts: VII. Description of the pore dimensions of carbon blacks by the t method*. Journal of Catalysis, 1965. **4**(6): p. 649-653.

62. Instruments, Q., *Gas Sorption System Operation Manual*. 2008-2012: USA.
63. Garsany, Y., et al., *Experimental Methods for Quantifying the Activity of Platinum Electrocatalysts for the Oxygen Reduction Reaction*. *Analytical Chemistry*, 2010. **82**(15): p. 6321-6328.
64. Chen, J. and B. Zhou, *Diagnosis of PEM fuel cell stack dynamic behaviors*. *Journal of Power Sources*, 2008. **177**(1): p. 83-95.
65. Chhina, H., et al., *Transmission Electron Microscope Observation of Pt Deposited on Nb-Doped Titania*. *Electrochemical and Solid-State Letters*, 2009. **12**(6): p. B97-B100.
66. Ruiz, A.M., et al., *Insights into the Structural and Chemical Modifications of Nb Additive on TiO₂ Nanoparticles*. *Chemistry of Materials*, 2004. **16**(5): p. 862-871.
67. Ma, J., et al., *Functionalizing Effect of Increasingly Graphitic Carbon Supports on Carbon-Supported and TiO₂-Carbon Composite-Supported Pt Nanoparticles*. *The Journal of Physical Chemistry C*, 2012. **116**(41): p. 21788-21794.
68. Soboleva, T., et al., *On the Micro-, Meso-, and Macroporous Structures of Polymer Electrolyte Membrane Fuel Cell Catalyst Layers*. *ACS Applied Materials & Interfaces*, 2010. **2**(2): p. 375-384.
69. Kumar, A. and V. Ramani, *Strong Metal-Support Interactions Enhance the Activity and Durability of Platinum Supported on Tantalum-Modified Titanium Dioxide Electrocatalysts*. *ACS Catalysis*, 2014. **4**(5): p. 1516-1525.
70. Huang, W., B. Zhou, and A. Sobiesiak, *Steady and Unsteady Modeling of Single PEMFC with Detailed Thermochemical Model*. *Journal of The Electrochemical Society*, 2006. **153**(10): p. A1945-A1954.

Supplementary Information (SI) Chapter 5

Electrosprayed Cathode Catalyst Layer with Composite-supported Pt Catalyst and Nafion Loading Optimization Strategy for Polymer Electrolyte Membrane Fuel Cell

Typical Series of Calculations for Catalyst Ink Preparation

Table SI-5.1. Typical series of calculations to prepare electrosprayed catalyst layers with predetermined Pt loadings and NVPs.

Pre-determined Parameters	
Active area, cm ²	5
Catalyst Type	20 wt. % Pt deposited C/Nb _{0.1} Ti _{0.9} O ₂ nanofibers
Catalyst support density (ρ_{support}), mg·cm ⁻²	4259
Target Pt loading (L_{Pt}), mg·cm ⁻²	0.17
Target Nafion volume percentage (NVP), %	45
Target Nafion volume ratio (NVR)	= 45/100 = 0.45
Calculated parameters	
Support loading (L_{support}), mg·cm ⁻²	= ((0.17 × 0.2))/0.8 = 0.68
Required amount of 20 wt. % Pt deposited catalyst, mg	= $\frac{(0.17 \times 5)}{0.2} = 4.25 \text{ mg}$
Catalyst volumetric loading (CVL), cm ⁻¹	= (0.68 × 4259 ⁻¹) + (0.17 × 21400 ⁻¹) = 168 × 10 ⁻⁶
Nafion Loading (L_{Nafion}), mg·cm ⁻³	= $\left(\frac{0.45}{1-0.45}\right) \times 168 \times 10^{-6} \times 1134 = 0.155$
Required amount of Dry Nafion, mg	= 0.155 × 5 = 0.775 mg
Required amount of Nafion stuck solution, μL	= $\frac{0.755}{0.05 \times 0.875} = 17.25 \mu\text{L}$
Required solvent, mL	= 0.775 × 0.6 = 1.29 mL
Equivalent NWP, %	= $\left(\frac{0.155}{0.68+0.17+0.155}\right) \times 100 = 15.5$

PXRD Patterns of Composite Catalyst Supports

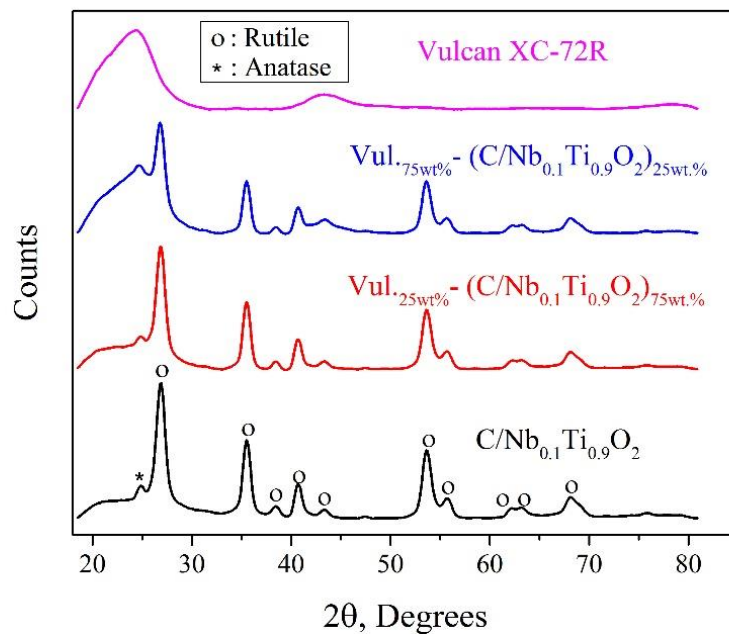


Figure SI-5.1. Powder X-ray Diffraction patterns of different catalyst supports. C/Nb_{0.1}Ti_{0.9}O₂; Vul.25wt%-(C/Nb_{0.1}Ti_{0.9}O₂)75wt.%; Vul.75wt%-(C/Nb_{0.1}Ti_{0.9}O₂)25wt.%; and Vulcan XC-72.

Surface Area Analysis and Pore Size Distributions

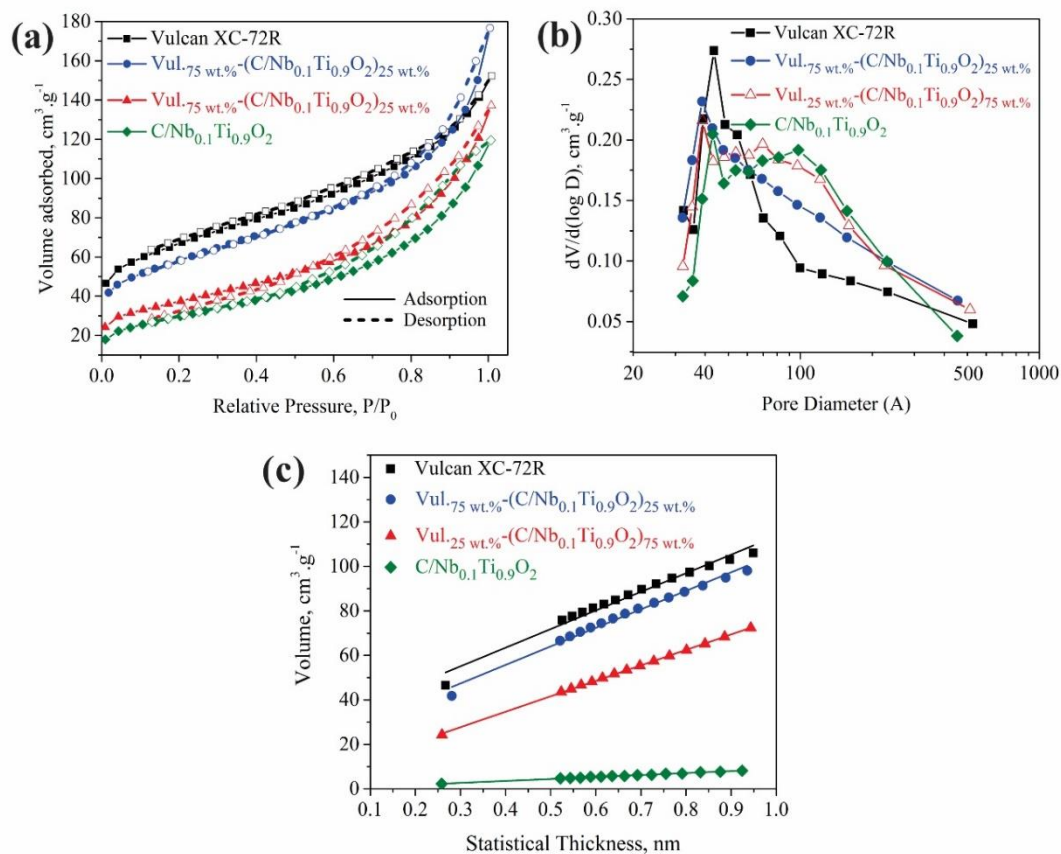


Figure SI-5.2. Surface area, pore size analysis and t-plots of different catalyst supports; (a) Nitrogen adsorption/desorption isotherms; (b) BJH pore size distribution plots; and (c) t-plots.

PXRD Patterns of Composite-supported Pt Catalysts

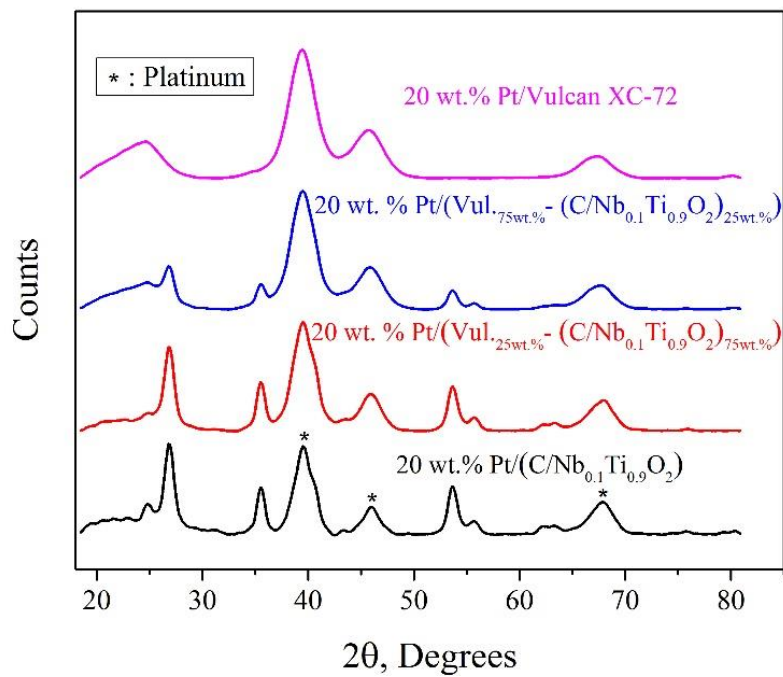


Figure SI-5.3. PXRD patterns of different composite supported-20 wt.% Pt catalysts.

Survey and High Resolution X-ray Photoelectron Spectroscopy (XPS) Results

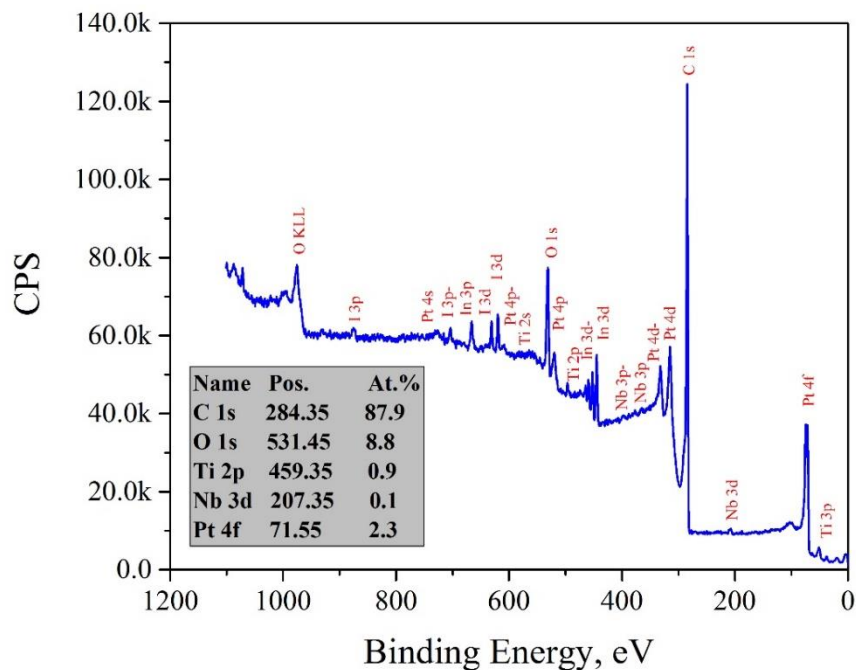


Figure SI-5.4. XPS survey spectra of 20 wt. % Pt/Vul.75 wt. %-(C/Nb_{0.1}Ti_{0.9}O₂)₂₅ wt. % catalyst.

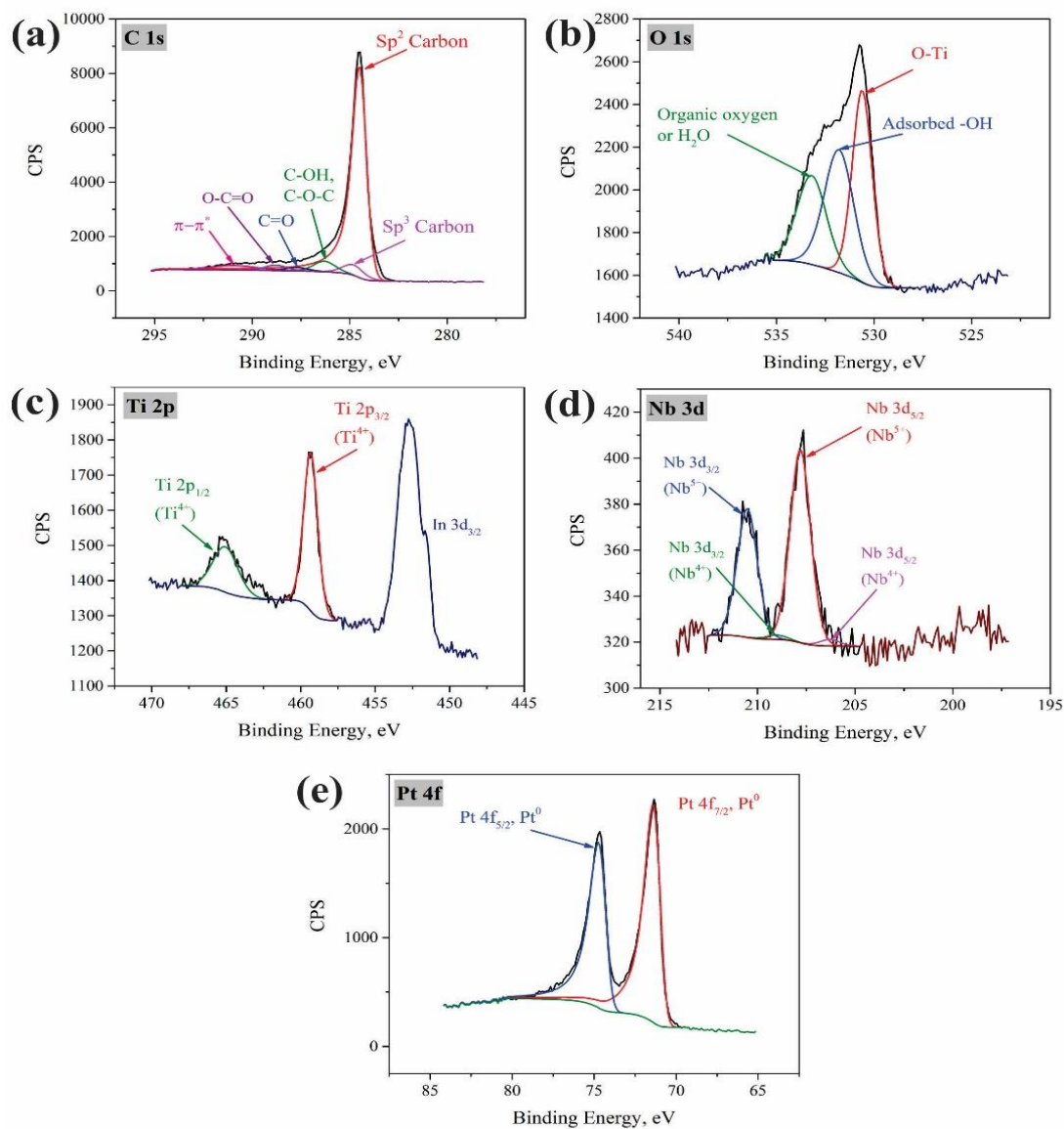


Figure SI-5.5. High resolution XPS spectra of 20 wt.% Pt/Vul.75 wt.%(C/Nb_{0.1}Ti_{0.9}O₂)₂₅ wt.% catalyst with Chemical state fits at different regions. (a) C 1s region; (b) O 1s region; (c) Ti 2p region; (d) Nb 3d region; and (e) Pt 4f region.

Table SI-5.2a. XPS peak parameters and % Area of different chemical states in C 1s region for 20 wt.% Pt/Vul.75 wt.%(C/Nb_{0.1}Ti_{0.9}O₂)₂₅ wt.% catalyst.

Chemical state	Sp ² carbon (C=C)	Sp ³ carbon (C-C, C-H)	C-OH, C-O-C	C=O	O-C=O	$\pi-\pi^*$
Position	284.5	284.8	286.30	287.70	288.80	290.91
FWHM	0.82	1.30	1.30	1.30	1.30	2.70
Line shape	A(0.4, 0.38, 20) GL(20)	GL(30)	GL(30)	GL(30)	GL(30)	GL(30)
Area%	81.7	6.4	6.5	2.1	3.4	0

Table SI-5.2b. XPS peak parameters and % Area of different Chemical states in O 1s region for 20 wt.% Pt/Vul.75 wt.%(C/Nb_{0.1}Ti_{0.9}O₂)₂₅ wt.% catalyst.

Chemical state	Oxide	Hydroxide	Water, Organic Oxygen
Position	530.61	531.80	533.20
FWHM	1.20	1.78	1.78
Area%	37.9	36	26.1

Table SI-5.2c. XPS peak parameters and % Area of different Chemical states in Ti 2p region for 20 wt.% Pt/Vul.75 wt.%(C/Nb_{0.1}Ti_{0.9}O₂)₂₅ wt.% catalyst.

Chemical state	Ti 2p _{3/2} Ti ⁴⁺	Ti 2p _{1/2} Ti ⁴⁺
Position	459.33	465.05
FWHM	1.11	1.95
Line shape	GL(30)	GL(30)
Area%	100.0	-

Table SI-5.2d. XPS peak parameters and % Area of different Chemical states in Nb 3d region for 20 wt.% Pt/Vul.75 wt.%(C/Nb_{0.1}Ti_{0.9}O₂)₂₅ wt.% catalyst.

Chemical state	Nb 3d _{5/2} Nb ⁴⁺	Nb 3d _{3/2} Nb ⁴⁺	Nb 3d _{5/2} Nb ⁵⁺	Nb 3d _{3/2} Nb ⁵⁺
Position	206.30	209.02	207.81	210.53
FWHM	1.22	1.22	1.22	1.22
Line shape	GL(30)	GL(30)	GL(30)	GL(30)
Area%	3.3	-	96.7	-

Table SI-5.2e. XPS peak parameters and % Area of different Chemical states in Pt 4f region for 20 wt.% Pt/Vul.75 wt.%(C/Nb_{0.1}Ti_{0.9}O₂)₂₅ wt.% catalyst.

Chemical state	Pt 4f _{7/2} Pt ⁰	Pt 4f _{5/2} Pt ⁰
Position	71.10	74.42
FWHM	0.98	1.01
Line shape	LA(1.2,85,70)	LA(1.2,85,70)
Area%	100.0	-

Electrochemical Activity and Durability Measurements

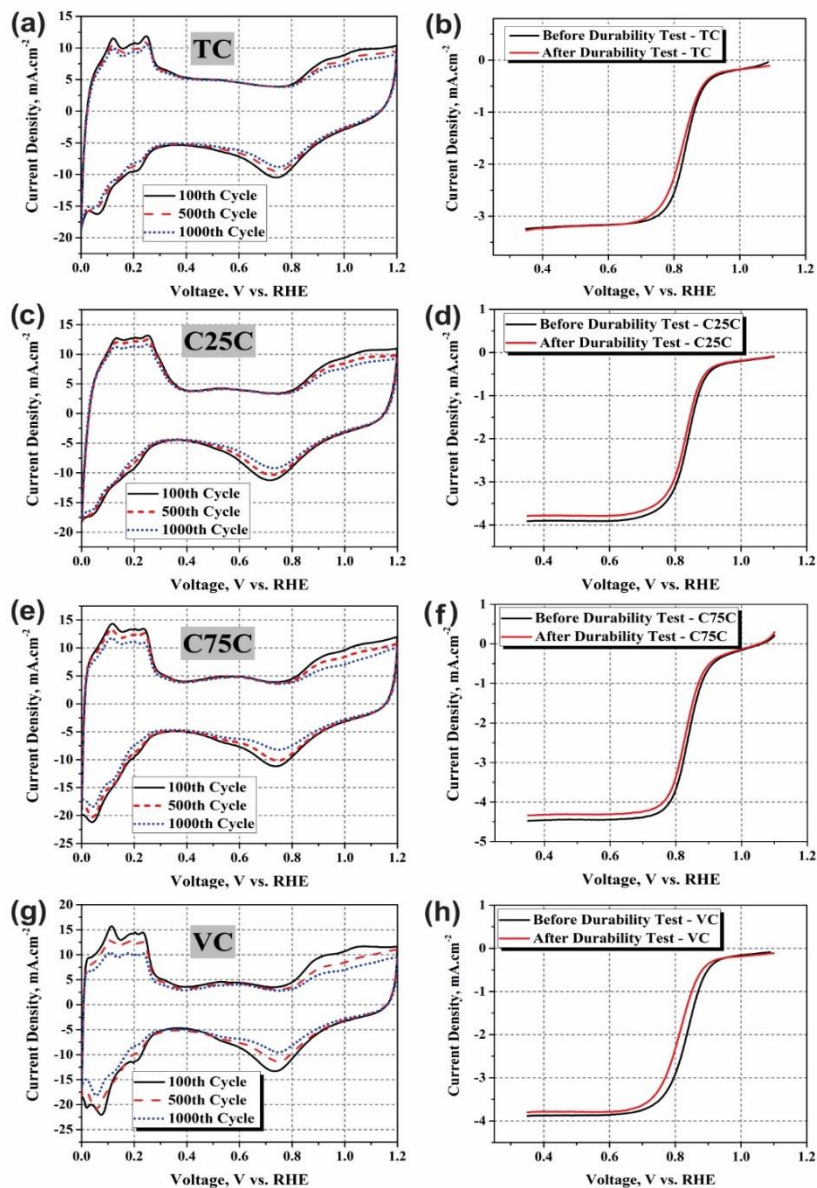


Figure SI-5.6. Cyclic and linear-sweep voltammograms obtained from Pt catalysts supported by different composite supports before and after durability test. (before and after applying 1000 potential cycles). (a, c, e, g) Series of CV curves obtained after certain numbers of potential cycling between 0 to 1.2 V. (b, d, f, h) linear sweep voltammograms (LSVs) obtained in O₂ saturated aqueous solutions of 0.5M H₂SO₄.

Table SI-5.3. ECSA and ORR mass activities at 0.9 V measured for different catalysts before and after durability test (1000 full potential cycling experiments).

Catalyst Formula	Catalyst Name	Before Durability Test		After durability Test			
		ECSA (m ² .g ⁻¹)	Mass activity @ 0.9 V (mA.mgPt ⁻¹)	ECSA (m ² .g ⁻¹)	ECSA loss (%)	Mass activity @ 0.9 V (mA.mgPt ⁻¹)	Mass activity loss (%)
20 wt.% Pt/(C/Nb _{0.1} Ti _{0.9} O ₂)	TC	43	17	34	22	14.5	15
20 wt.% Pt/Vul. _{25wt.%} -(C/Nb _{0.1} Ti _{0.9} O ₂) _{75wt.%}	C25C	51	20	40	22	16.4	18
20 wt.% Pt/Vul. _{75wt.%} -(C/Nb _{0.1} Ti _{0.9} O ₂) _{25wt.%}	C75C	59	25	42.5	28	18.8	25
20 wt.% Pt/Vulcan XC-72R	VC	68	19	44	35	13.5	29
HiSpec 40 wt.% Pt/C	JM	65	20	44	33	14.6	27

PEM Fuel Cell Evaluation Tests

Table SI-5.4. Converting NWP to NVP for electrosprayed catalyst layers using 20 wt.% Pt catalysts supported by carbon blacks. The calculations were performed for a Pt loading of $0.2 \text{ mg}_{\text{Pt}} \cdot \text{cm}^{-2}$.

Proposed NWP in the literature [1, 2], %	$L_{\text{Nafion}}^{\text{a}}$, $\text{mg} \cdot \text{cm}^{-2}$	NVP ^b , %
15	$= \frac{1 \times 0.15}{0.85}$ $= 0.176$	$= \frac{(0.176 \times 1134^{-1})}{(0.8 \times 2171^{-1}) \times (0.2 \times 21400^{-1}) \times (0.176 \times 1134^{-1})} \times 100 = 29.1$
25	$= \frac{1 \times 0.25}{0.75}$ $= 0.333$	$= \frac{(0.333 \times 1134^{-1})}{(0.8 \times 2171^{-1}) \times (0.2 \times 21400^{-1}) \times (0.333 \times 1134^{-1})} \times 100 = 43.7$
35	$= \frac{1 \times 0.35}{0.65}$ $= 0.538$	$= \frac{(0.538 \times 1134^{-1})}{(0.8 \times 2171^{-1}) \times (0.2 \times 21400^{-1}) \times (0.538 \times 1134^{-1})} \times 100 = 55.6$

^a L_{Nafions} were calculated according to Eq. (2). $L_{\text{Nafion}} = (L_{\text{Pt}} + L_{\text{support}}) \times \left[\frac{(NWP/100)}{(1 - (NWP/100))} \right]$

^b NVPs were calculated according to Eq. (1).

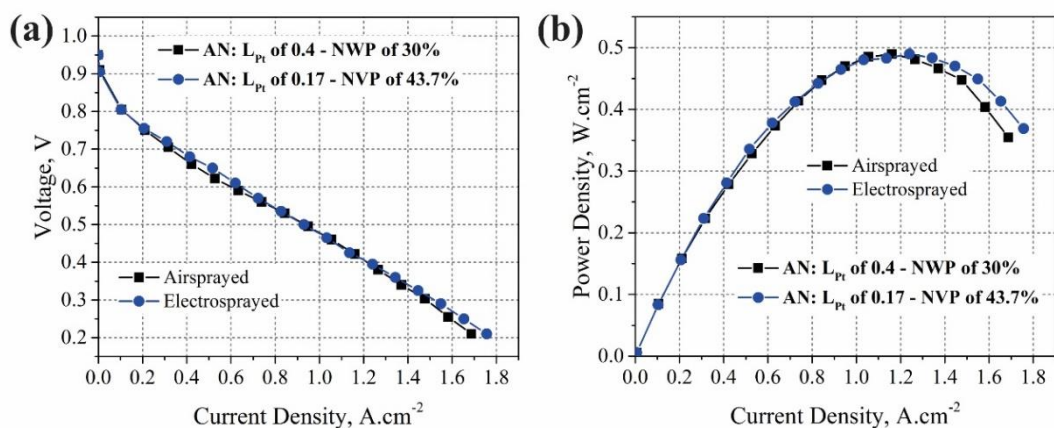


Figure SI-5.7. Effect of lowering Pt on the anode side on the H₂/Air PEMFC performances of MEAs prepared using electrospayed VC catalyst on the cathode side, with a Pt loading of 0.17 mgPt·cm⁻².

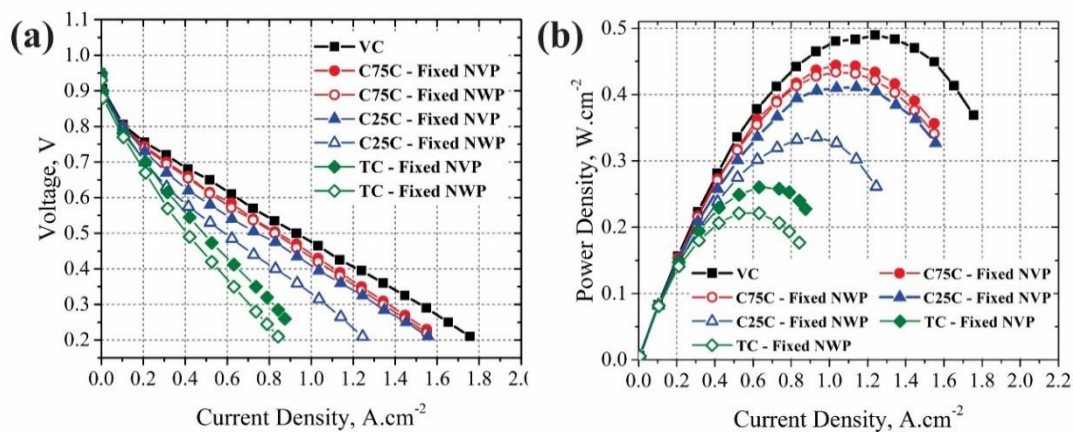


Figure SI-5.8. Polarization and power density curves of the H₂/Air PEMFCs employing different electrospayed CLs in their cathode compartments with optimized NVP of 43.7.

References

1. Chaparro, A.M., et al., *Properties of Catalyst Layers for PEMFC Electrodes Prepared by Electrospray Deposition*. Journal of The Electrochemical Society, 2010. **157**(7): p. B993-B999.
2. Chaparro, A.M., et al., *PEMFC electrode preparation by electrospray: Optimization of catalyst load and ionomer content*. Catalysis Today, 2009. **143**(3–4): p. 237-241.

CHAPTER 6

Electrosprayed vs Airsprayed Catalyst Layers with Composite-Supported Pt Catalysts at Optimized Nafion Volume Percentages

6.1 Introduction

Polymer electrolyte membrane fuel cells (PEMFCs) are regarded as a promising technology for both automotive and stationary applications [1, 2]. However, they are not still reasonably cost competitive and sufficiently durable for automotive applications [3]. Catalyst layer (the region where fuel and oxidant convert to products) was received more attention than other components, to mitigate the challenges above [4, 5]. Generally to have maximum PEMFC performance, catalyst layer should facilitate the transport of reactant gases and protons to the catalyst site and remove the product water, on the one hand, and facilitate the electrical current flow to and from reaction sites, on the other hand. It is well-known that the effectiveness of the catalyst layer in providing active sites, known as triple phase boundaries (TPBs) [6], depends heavily on the individual materials chemistry of its components, i.e. the catalyst [7, 8], the support [9] and the ionomer [10, 11]. However, the interplay and distribution of those components was also shown to be equally important [12-14]. Furthermore, among catalyst layer components, despite the evolution of ultrathin ionomer-free catalyst layers [15, 16] and overriding role of catalyst in the electrochemical kinetics of PEMFCs, ionomer (e.g. Nafion) incorporation and its well distribution in the state-of-the-art catalyst layers was shown to be very critical [4]. Therefore, finding an optimized Nafion loading for the catalyst layers received the researcher's attention as it is crucial to keep it as low as possible to have unimpeded gas transport (sufficient void space or porosity) and on the contrary it should create a connected network to create proton conductivity [17-21]. The state-of-the-art catalyst layers are commonly formed from a catalyst ink dispersions that comprise a catalyst (Pt + catalyst support), ionomer (e.g. Nafion), and dispersing solvent, initially, and subsequent layer formation onto either membrane or gas diffusion layers (GDLs) [22]. Therefore, apart from the influence of catalyst ink dispersing media (e.g. dielectric constant of dispersing solvent [23]) or aggregation processes that could happen during mixing [24-26], catalyst layer preparation method has shown to have a vital role in determining the catalyst layer properties and Pt utilization [17, 27-29]. For instance, through using electrospray deposition technique instead of commonly used airspray technique, optimized Nafion loadings have been demonstrated to be lower due to improvements in Nafion distribution and pore structure of

the catalyst layers [30-33]. Higher PEMFC performances obtained for electro sprayed catalyst layers rather than air sprayed catalyst layers was shown to be mainly due to lower internal electrical resistance and higher Pt utilization obtained for electro sprayed catalyst layers [30].

Recently, the present authors recommended compositing 25 wt.% carbon blacks with carbon-embedded Nb-doped TiO₂ NFs [34] to be in favor of a reasonable trade-off between high PEMFC performance and less oxygen reduction reaction (ORR) activity loss, through assessing the PEMFC performances of the electro sprayed catalyst layers [35]. Additionally a new strategy to optimize the Nafion loading of composite-supported Pt catalysts was also proposed by using fixed Nafion volume percentage (NVP) [35]. However, the validity of using fixed NVP for other catalyst layer preparation methods (e.g. air spraying) and the distribution of Nafion in the catalyst layers comprised from composite-supported Pt catalysts have not been investigated. Additionally, catalyst support properties (e.g. hydrophilicity/hydrophobicity [4, 36], and pore structure [37]) were also shown to affect the required optimum Nafion loading and water sorption property in the catalyst layer [13]. This observation further necessitated investigating the properties of catalyst layers employing composite-supported Pt catalysts.

The objectives of this work are, first, validating using fixed NVPs rather than fixed NWP for different catalyst layer preparation methods and comparing the resultant performances; and second, assessing the distribution of catalyst layer components employing composite-supported Pt catalysts at their corresponding NVPs.

6.2 Experimental

6.2.1 Synthesis of composite catalyst supports

The composite catalyst supports were physical mixtures of pre-functionalized Vulcan XC-72R carbon blacks (Cabot Corporation) and carbon-embedded 10 at. % Nb doped TiO₂ nanofibers (C/Nb_{0.1}Ti_{0.9}O₂) at two different weight percentages (i.e. 25 and 75 wt. %), the details of the synthesis have been reported elsewhere [34, 35]. In the following, the synthesized composite catalyst supports with 25 wt. % and 75 wt. % carbon black weight

percentages (CBWPs) will be denoted as Vul._{25wt.%}/ (C/Nb_{0.1}Ti_{0.9}O₂)_{75wt.%} and Vul._{75wt.%}/ (C/Nb_{0.1}Ti_{0.9}O₂)_{25wt.%}, respectively.

6.2.2 Synthesis of Pt catalysts

Microwave-assisted polyol technique, described in [35], was used to deposit 20 wt.% Pt nanoparticles (NPs) onto either composite catalyst supports or pure carbon blacks or pure C/Nb_{0.1}Ti_{0.9}O₂ NFs, hexachloroplatinic acid hexahydrate (H₂PtCl₆.6H₂O) from Sigma-Aldrich was used as Pt precursor. Table 6.1 shows corresponding abbreviated names and CBWPs of all synthesized Pt catalysts.

Table 6.1. List of synthesized Pt catalysts.

Catalyst Name	Catalyst Type	CBWP in Composite Support, wt. %
TC	20 wt. % Pt/(C/Nb _{0.1} Ti _{0.9} O ₂)	0
C25C	20 wt. % Pt/Vul. _{25wt.%} -(C/Nb _{0.1} Ti _{0.9} O ₂) _{75wt.%}	25
C75C	20 wt. % Pt/Vul. _{75wt.%} -(C/Nb _{0.1} Ti _{0.9} O ₂) _{25wt.%}	75
VC	20 wt. % Pt/Vulcan XC-72R	100

6.2.3 Catalyst layer preparation

Catalyst layers (CLs) were prepared onto 24BC SIGRACET[®] carbon papers with an area of 5 cm² through either airspray or electrospray deposition techniques. Before adopting any method to form a CL, catalyst inks were prepared by dispersing desired amounts of catalyst (Pt + catalyst support) and Nafion in isopropyl alcohol, the required quantities of each component was determined based on targeted Pt loading and NVP [34]. NVPs were determined as the percentage of dry Nafion volume in the catalyst layer using Eq. (6.1), as follow [34]:

$$\text{NVP} = \frac{\left(L_{\text{Nafion}} / \rho_{\text{Nafion}} \right)}{\left(L_{\text{Nafion}} / \rho_{\text{Nafion}} \right) + \left(L_{\text{Support}} / \rho_{\text{Support}} \right) + \left(L_{\text{Pt}} / \rho_{\text{Pt}} \right)} \times 100 \quad (6-1)$$

Where ρ_{Nafion} , ρ_{Support} , and ρ_{Pt} are the true densities, with units of $\text{mg}\cdot\text{cm}^{-3}$, and L_{Nafion} , L_{Support} , and L_{Pt} are the target loadings of dry Nafion, catalyst support, and platinum, with units of $\text{mg}\cdot\text{cm}^{-2}$, in the CL, respectively. The true densities for different types of composite catalyst supports (ρ_{Support}) were determined through gas pycnometry (Micromeritics Accupyc II 1340) measurements, as shown in Table 6.2, and a value of $21400 \text{ mg}\cdot\text{cm}^{-3}$ was used as the true density of metallic Platinum (ρ_{Pt}). The dry Nafion density (ρ_{Nafion}) is set to a value of $1134 \text{ mg}\cdot\text{cm}^{-3}$ [20].

Table 6.2. True densities of composite catalyst supports measured through gas pycnometry.

	C/Nb _{0.1} Ti _{0.9} O ₂	Vul.25 wt.%- (C/Nb _{0.1} Ti _{0.9} O ₂) _{75 wt.%}	Vul.75 wt.%- (C/Nb _{0.1} Ti _{0.9} O ₂) _{25 wt.%}	Vulcan XC-72R
Density, $\text{mg}\cdot\text{cm}^{-3}$	4259	3737	2693	2171

To be able to compare the effectiveness and efficiency of working with NVPs rather than commonly used NWP, NWP were also reported. NWP were determined using the well-established equation proposed by Passalacqua et al. [36] as the percentage of dry Nafion Loading in the CL.

After about 3 hrs sonication of the catalyst inks at room temperature, the well-dispersed catalyst inks can be airsprayed (AS) using a commercial dual-action airbrush gun (VL-SET, Paasche) at a back pressure of 10 psig, or can be electrospayed (ES) by an electrospinning apparatus with a heated aluminum collector, the details of the employed electrospaying technique can be found in [34]. The amount of deposited catalyst onto dried

carbon paper substrates were controlled by weighing them, before and after deposition, using a 5 digit accuracy balance (ACCULAB).

6.2.4 Membrane Electrode Assembly (MEA) fabrication

MEAs have been prepared via sandwiching NRE212 type Nafion membrane between air-dried anode and cathode electrodes. An automatic hydraulic press (CARVER®) with 600 pounds force at 130 °C for 3 mins was used to hot press the sandwiched layers.

6.2.5 Polarization Curves

An automatic fuel cell test station developed in the Clean Powertrain Lab at the University of Windsor (CPL-FCTS) [34] was used to record PEMFC Polarization curves. Before recording polarization curves, as-fabricated MEAs were activated first in the constant voltage mode (through 6 cycles of alternating the voltage from 0.7V for 20 mins to 0.5V for 20 mins) and then in the constant current mode (at 0.5 A·cm⁻² for 10 hours). Both 100% humidified H₂ and air were provided with constant excess coefficients of 1.5 and 2.5 to anode and cathode compartments, respectively. The polarization curves were recorded at the cell temperature of 80°C and back pressure of 30 psig.

6.2.6 AS and ES catalyst layer properties

The morphology and elemental X-ray mappings of the airsprayed/electrosprayed catalyst layers were examined by scanning electron microscopy (FEI Quanta 200 FEG) equipped with an energy-dispersive spectrometer (EDAX SiLi Detector) in secondary and back-scattered modes operated at 15 kV and 20 KV, respectively. Mercury porosimetry (AutoPore IV 9500 V1.07), using Washburn equation for cylindrical pores [39, 40], was employed to analyze the pore structure of the airsprayed and electrosprayed catalyst layers. In the Washburn equation, $\theta = 140.0^\circ$ was used for both advancing and receding contact angles and $\gamma = 480 \text{ dyn}\cdot\text{cm}^{-1}$ was used as the mercury surface tension. Raman spectroscopy measurements were conducted on an ALPHA300 Raman system (WITec GmbH) using a laser excitation source with a wavelength of 532 nm and a laser power lower than 1 mW to avoid laser-induced local heating. A 100× objective lens with a numerical aperture (NA) of 0.95 was used for Raman mappings. The acquisition time was chosen to be 2 s for each

pixel ($0.0057 \mu\text{m}^2$) for an optimum of mapping time and detected Raman signal in a scan area of $3.8 \mu\text{m} \times 3.8 \mu\text{m}$.

6.3 Results and discussion

6.3.1 H₂-Air PEMFC performance evaluation

6.3.1.1 Optimized NVP for airsprayed cathode catalyst layers

Before using fixed NVP [35] to compare the PEMFC performances of airsprayed cathode catalyst layers that are employing different composite-supported Pt catalysts, the optimized NVP needs to be experimentally found for VC catalyst as a reference. To be able to compare optimized NVP with previously reported optimized NVPs for carbon black-based Pt catalysts, NVPs were chosen to fall within the range of previously proposed NVPs [19, 38], Table 6.2.

Table 6.3. Converting proposed NVPs [19, 38] in the literature to NVPs for airsprayed catalyst layers using 20 wt. % Pt catalysts supported by pure carbon blacks. The calculations were performed for a Pt loading of $0.2 \text{ mg}_{\text{Pt}} \cdot \text{cm}^{-2}$.

Proposed NVPs in the literature, %	$L_{\text{Nafion}}^{\text{a}}, \text{ mg} \cdot \text{cm}^{-2}$	NVP ^b , %
25	$= \frac{1 \times 0.25}{0.75} = 0.333$	43.7
30	$= \frac{1 \times 0.30}{0.70} = 0.428$	50
35	$= \frac{1 \times 0.35}{0.65} = 0.538$	55.7
45	$= \frac{1 \times 0.45}{0.55} = 0.818$	65.6

^aNafion loading: $L_{\text{Nafion}} = (L_{\text{Pt}} + L_{\text{support}}) \times \left[\frac{(NVP/100)}{(1 - (NVP/100))} \right]$.

^bNVPs were calculated according to the equation proposed in [35].

Fig. 6.1 shows the polarization curves (Fig. 6.1a) and power density curves (Fig. 6.1b) obtained from single cells with different AS cathode CLs that have different NVP values with same Pt loading of $0.2 \text{ mgPt}\cdot\text{cm}^{-2}$; all anode CLs were fabricated by airspraying JM catalyst with same Pt loading of $0.4 \text{ mgPt}\cdot\text{cm}^{-2}$ and same NWP of 30%. Fig. 1c shows the maximum power density versus NVP that is constructed from Fig. 1b. Fig. 1c clearly shows that AS cathode CLs obtained their maximum power density of $0.43 \text{ W}\cdot\text{cm}^{-2}$ at NVP of 55.7%, equivalently at NWP of 35% that is in the range of previously reported optimized NWPs for carbon black-based Pt catalysts [18, 36].

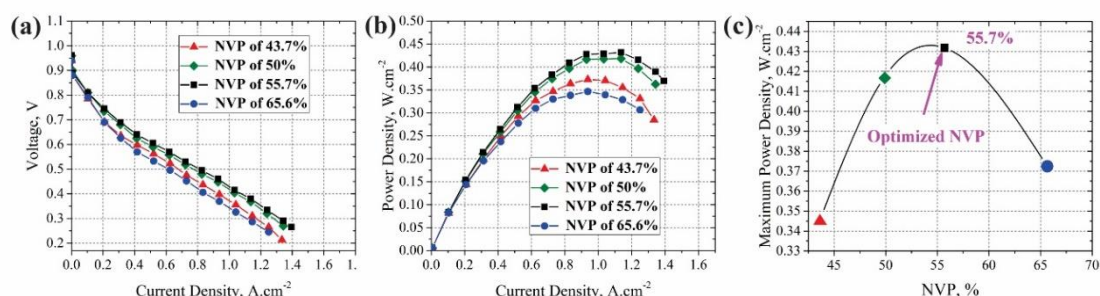


Figure 6.1. Effect of NVP of the air sprayed cathode CL (VC catalyst) on H_2/Air PEMFC performance. (a) Polarization curve; (b) Power density curve; and (c) Maximum power density versus NVP values.

Fig. 6.1c clearly showed that airsprayed cathode catalyst layers obtained their maximum power density of $0.43 \text{ W}\cdot\text{cm}^{-2}$ at NVP of 55.7% (equivalent to NWP of 35%), that is in the range of previously reported optimized NWPs for carbon black-based Pt catalysts [19, 38].

After experimentally optimizing NVP, as shown in Fig. 6.1, the obtained optimized NVP value can be used to predict the optimized Nafion loadings for the other three composite catalysts, as shown in Table 6.2. The optimized Nafion loadings can be predicted by taking the assumption that fixed NVP can predict the Nafion loadings effectively through correlating the Nafion volume with the volume of the catalyst [35].

Table 6.4. Predicted optimized Nafion loadings, according to experimentally optimized NVP, for airsprayed catalyst layers that are employing different catalyst supports.

Catalyst Type	NVP	Predicted mg _{Na} ·cm ⁻²	L _{Nafion} ^a ,	NWP
C75C	55.7	0.436		30.4
C25C	55.7	0.318		24.1
TC	55.7	0.281		21.9

$$^a\text{Nafion loading: } L_{Nafion} = (L_{Pt} + L_{support}) \times \left[\frac{(NWP/100)}{(1 - (NWP/100))} \right]$$

Furthermore, the predicted optimized NWP for C75C was chosen to be validated experimentally. Fig. 6.2 shows the effect of Nafion loading on the PEMFC performances of airsprayed cathode catalyst layers that are employing C75C catalyst; all anode CLs were fabricated by airbrushing VC catalyst with same Pt loading of 0.17 mg_{Pt}·cm⁻² and same NVP of 55.7%. Fig. 6.2b clearly shows that the highest peak power density (among the three cases) happened at NWP of 30% that is in a good agreement with predicted Nafion loadings through using fixed NVPs.

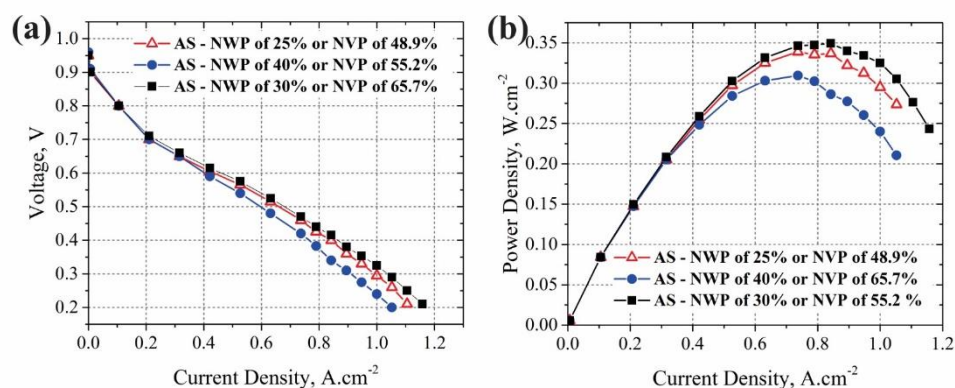


Figure 6.2. Effect of NVP of the AS cathode CL (C75C catalyst) on H₂/Air PEMFC performance. (a) Polarization curve; (b) Power density curve; and (c) Maximum power density versus NVP values.

6.3.1.2. Fixed NVP versus fixed NWP for airsprayed catalysts layers

To further confirm the effectiveness of fixed NVP rather than fixed NWP to predict optimized Nafion loading of catalyst layers with different composite-supported Pt catalysts, the PEMFC performances of airsprayed cathode catalyst layers prepared with either fixed NVP or fixed NWP were compared. Fig. 6.3 compares the PEMFC performances of airsprayed cathode catalyst layers prepared using Fixed NVP and fixed NWP values of 55.7% and 35%, respectively. In Fig. 6.3, all anode CLs were fabricated by airbrushing VC catalyst with same Pt loading of 0.2 mg_{Pt}·cm⁻² and same NVP of 55.7%.

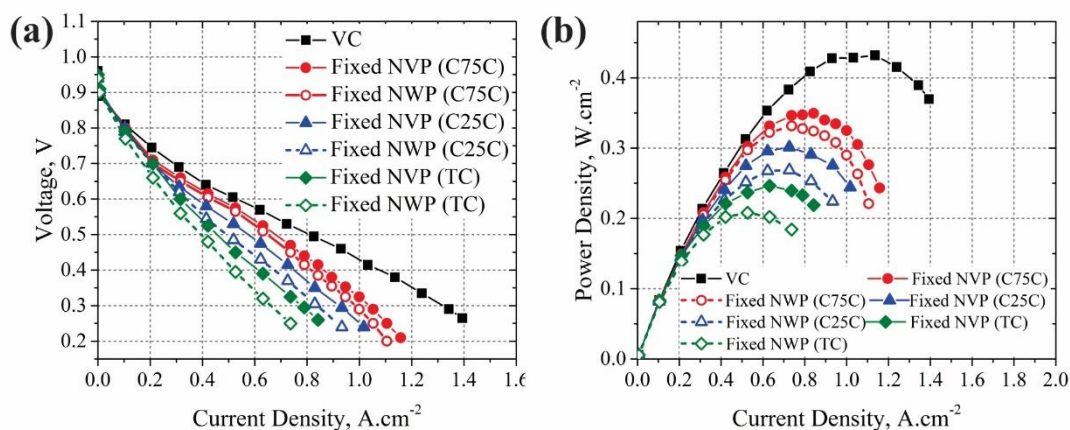


Figure 6.3. Comparison of effectiveness in predicting the optimized Nafion loadings through using fixed NVP vs. fixed NWP values. (a) Polarization curve; (b) Power density curve.

As shown in Figure 6.3, the PEMFC performances are clearly higher at fixed NVP than fixed NWP. This observation strongly confirms the effectiveness of using fixed NVP over using fixed NWP to compare the PEMFC performances of AS cathode CLs. However, the optimized NVP value for AS cathode CLs (i.e. 55.7%) is significantly higher than the optimized NVP value obtained for ES cathode CLs at a value of 43.7% [34]. This is in a good agreement with the literature [30], and it suggests a more uniform distribution of Nafion in ES than AS CLs.

6.3.1.3 AS vs. ES CLs at corresponding optimized NVPs

Figure 6.4 compares the PEMFC performances of airsprayed and electrospayed cathode catalyst layers which were prepared at their corresponding optimized NVPs, the peak power densities for electrospayed catalyst layer were reproduced from [35].

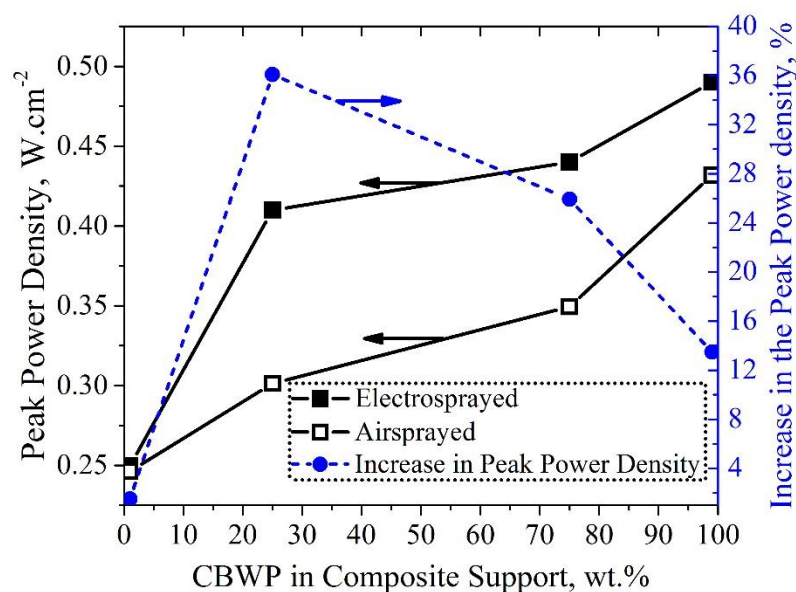


Figure 6.4. Effect of catalyst layer preparation methods on the peak power densities of MEAs employing different composite-supported Pt catalysts (Black curves). The increase in the peak power densities through using electro spraying rather than air spraying method were also shown versus CBWP in composite supports (Blue curve).

As illustrated in figure 6.4, it is immediately apparent that using electro spraying method rather than air spraying is very critical to have high performance composite-supported Pt catalysts (i.e. C25C and C75C catalysts). The peak power densities for electro sprayed catalyst layers employing composite-supported Pt catalysts were significantly improved (e.g. 26% to 36%), when compared with air sprayed catalyst layers, whereas for those employing pure carbon-based or pure C/Nb_{0.1}Ti_{0.9}O₂ nanofiber-based Pt catalysts were less significantly improved (e.g. 13.5% for VC catalyst) or remained the same (e.g. TC catalyst). In other words, from 100 wt.% to 25 wt.% CBWP, Fig. 6.4 suggests an increase in the effectiveness of electro spraying technique showing by the percentage of increase in peak power densities of ES than AS CLs. This observation could recommend the incorporation of hydrophilic C/Nb_{0.1}Ti_{0.9}O₂ nanofibers in the composite supports to be in favor of an improvement in the interaction of Nafion in the catalyst layers. Recently, Paul

et al. [35] observed a bimodal surface wettability (thickness-dependent wettability) for self-assembled Nafion films. They found Nafion films thinner than 55 nm to have hydrophilic surface whereas thicker Nafion films found to have a hydrophobic surface. Given that the thickness of self-assembled Nafion films on aggregated Pt/C catalysts during the catalyst layer formation is found to be around 10 nm [12, 35], the self-assembled Nafion films inside the catalyst layers can be assumed to be hydrophilic based on Paul et al. [35] observation. Accordingly, the incorporation of hydrophilic C/Nb_{0.1}Ti_{0.9}O₂ nanofibers into composite catalyst supports can be speculated to improve the interaction between the hydrophilic sulfonate groups with catalytically active sites that can yield into higher proton-donating characteristic [35].

Generally Fig. 6.4 suggested the incorporation of hydrophilic C/Nb_{0.1}Ti_{0.9}O₂ nanofibers in composite catalyst supports to be beneficial in terms of Nafion interaction with catalyst while the overall performance is still lower than pure carbon black-based Pt catalysts. Lower overall performance for composite-supported Pt catalysts suggests lower electronic conductivity of the composite catalyst supports to be still the limiting factor.

6.3.2 AS or ES Catalyst layer Characteristics at optimized NVPs

To explore the effect of catalyst preparation method on the H₂/Air PEMFC performances, catalyst layer relevant characteristics, i.e. porosity and Nafion distribution, were studied for both airsprayed and electrosprayed catalyst layers.

6.3.2.1 Morphology and Porosity

Figure 6.5 compares the morphologies of different catalyst layers prepared onto 24BC SIGRACET® carbon papers through airspray or electrospray deposition techniques at their corresponding optimized NVPs (Optimized NVP values are 43.7% and 55.6% for ES and AS CLs, respectively). Dendritic morphologies of the electrosprayed catalyst layers are clearly distinct from dense and flat morphologies of the airsprayed catalyst layers at 10 μm scale, which is in agreement with literature [31].

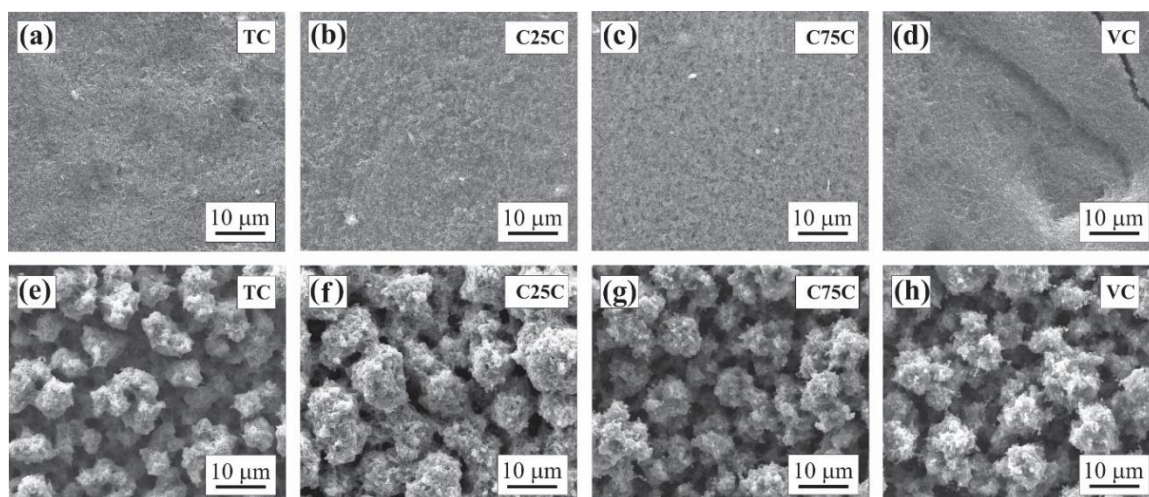


Figure 6.5. Field emission-SEM images of different AS/ES cathode CLs at their corresponding optimized NVPs at 10μm scale. a, b, c, and d are for AS CLs; e, f, g, and h are for ES CLs.

Figure 6.6 shows the meso- and macropore distribution curves obtained for airsprayed and electrospayed CLs employing C25C catalyst measured through mercury porosimetry.

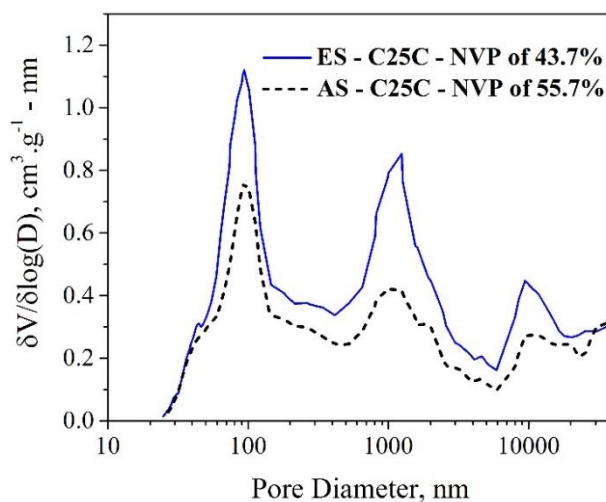


Figure 6.6. Pore size distributions for airsprayed/electrospayed catalyst layers employing C25C catalyst at their corresponding optimized NVPs.

As shown in Fig. 6.6, there are two main peaks as follows: so called “primary porosity” peak centered in pore diameters less than 100 nm and “secondary porosity” centered around

1000. It has been shown that the first peak centred ~ 100 nm can be ascribed to the voids in and between the primary catalyst particles and aggregates whereas the second peak ~ 1 μm is more associated with the voids between the agglomerates, the pores larger than 50 μm are mostly arising from carbon paper [31, 37, 41]. Figure 6 clearly suggested that airspraying method reduced more of both primary and secondary pores than electro spraying method, which is in agreement with the literature [31]. However, pore size distributions are not remarkably different between ES and AS CLs. This demonstrates that the pore size distribution alone cannot be responsible for the remarkable increase in the peak power densities of ES CLs, when compared with AS CLs (Fig. 6.4).

6.3.2.2 Nafion, Carbon and TiO₂ distributions

To evaluate the Nafion distribution in the prepared CLs, the color coded (red) fluorine X-ray mappings were used as a fingerprint of the PTFE backbone of the ionomer phase, as shown in Fig. 6.7. The color coded (red) fluorine X-ray mappings with scale of 250 μm clearly demonstrates more uniform Nafion distribution in ES CLs than AS ones, especially for the CLs that are employing composite-supported Pt catalysts with 25 and 75 wt. % carbon blacks (C25C and C75C catalyst), as shown in Figs. 6.7b and 6.7c, 6.7f and 6.7g.

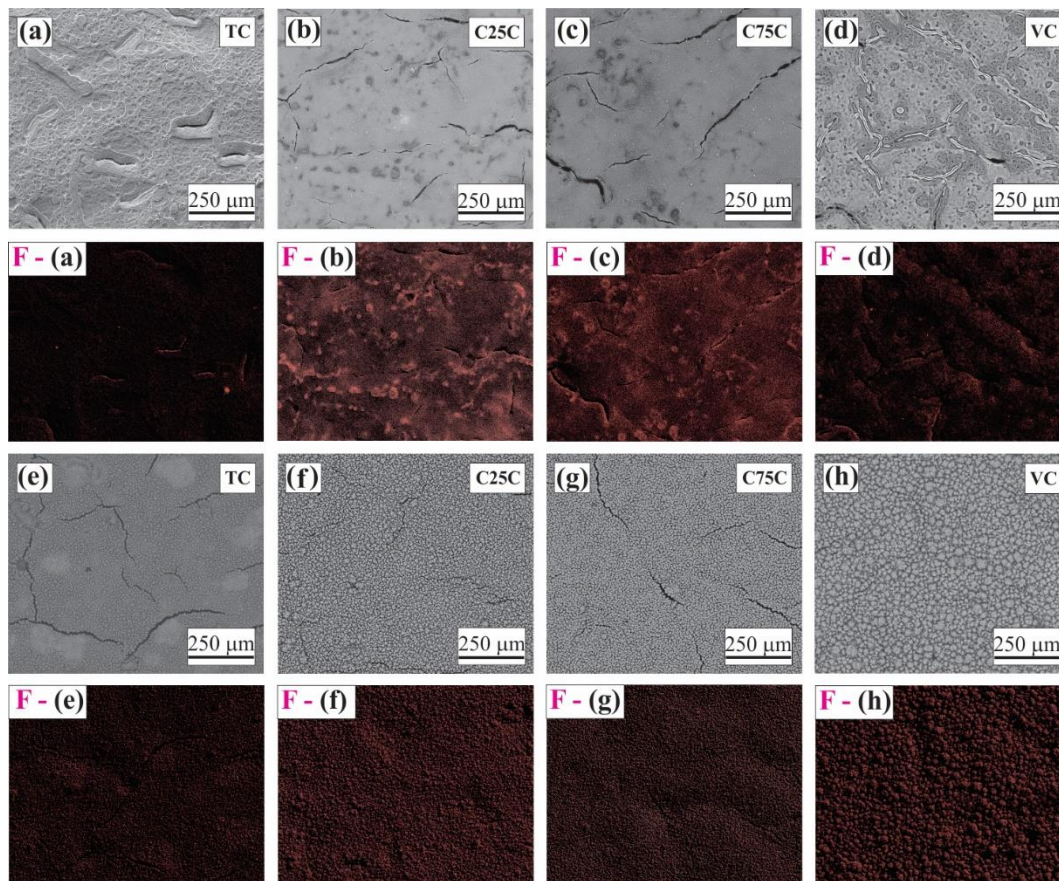


Figure 6.7. Back-scattered SEM images and Fluorine X-ray mapping of different AS/ES cathode CLs at their corresponding optimized NVPs. a, b, c, and d are for AS CLs; e, f, g, and h are for ES CLs.

Figs. 6.8 compares the color coded, red for fluorine, orange for titanium, and green for carbon, X-ray mappings collected from airsprayed and electrosprayed C25C catalyst layers with a scale of 25 μm .

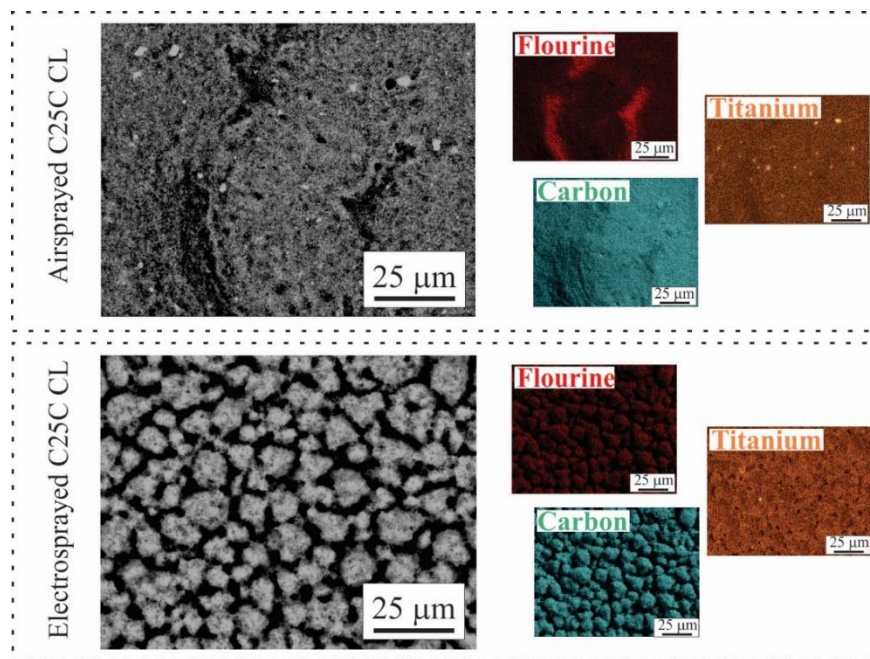


Figure 6.8. Back-scattered SEM images and elemental X-ray mappings of AS and ES catalyst layers employing C25C catalyst at their corresponding optimized NVPs.

As shown in Figure 6.8, it is immediately apparent that, despite nonuniform distribution of flourine (fingerprint of Nafion) in AS CL, both carbon (fingerprint of carbon blacks) and titanium (fingerprint of $C/Nb_{0.1}Ti_{0.9}O_2$ NFs) are uniformly distributed in both AS and ES CLs. Using Raman intensity mappings were identified to be a more effective tool than microscopic mappings to investigate the distribution of the composites containing carbon nanoparticles [40]. Because Raman spectra of TiO_2 and graphitic carbon nanoparticles show non-overlapping well-defined features, their Raman intensity mappings were used to further investigate rutile phase TiO_2 and carbon black distributions in AS or ES C25C CLs with a scale of $< 1 \mu m$, as shown in Fig. 6.9.

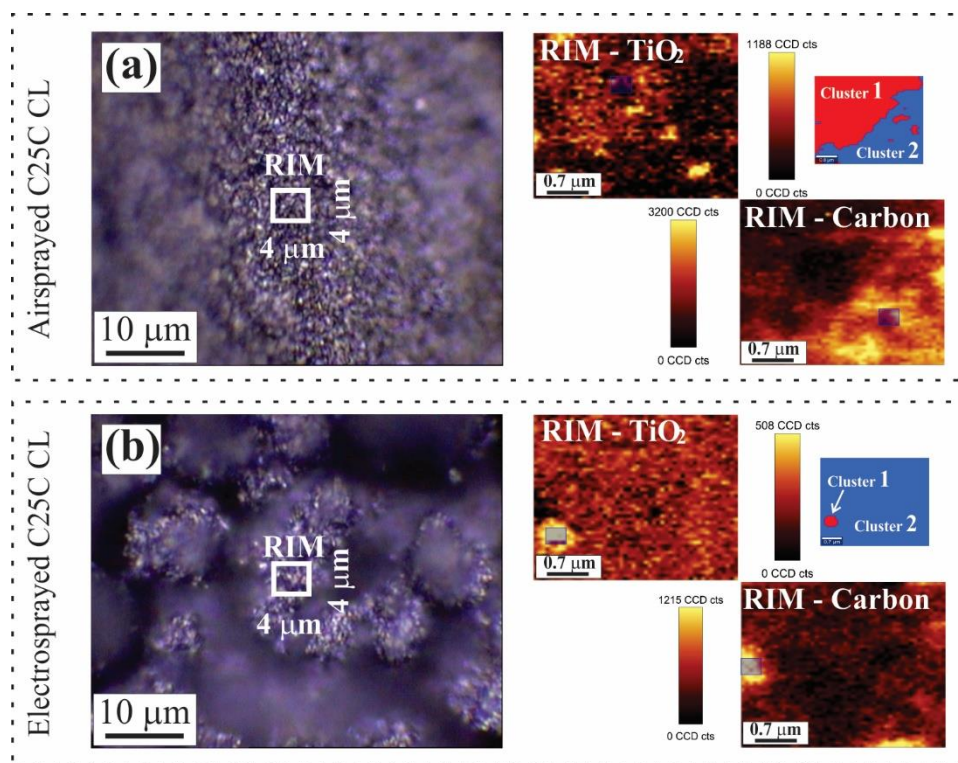


Figure 6.9. Optical images and Raman intensity mappings collected from AS and ES catalysts layers employing C25C catalyst at their corresponding optimized NVPs. Optical images of (a) airsprayed and (b) electrospayed C25C CLs along with Raman intensity maps of TiO₂ and carbon.

The integrated Raman spectra in the wavenumber range of 400-450 cm⁻¹ was used as a fingerprint of rutile phase C/Nb_{0.1}Ti_{0.9}O₂ NFs [33, 41], whereas the wavenumber in the range of 1280-1610 cm⁻¹ [42] was chosen as Vulcan XC-72R fingerprint. The scale bars next to Raman mappings are indicating the relative intensity of each color. The cluster analysis on collected Raman Intensity mappings, represented in Fig. 6.9 as blue and red colors, was used to identify the areas which may have concentrated TiO₂ or carbon blacks. These analyses clearly showed that AS CLs even have nonuniform distributions of carbon and C/Nb_{0.1}Ti_{0.9}O₂ NFs whereas ES CLs are more uniform except for a single C/Nb_{0.1}Ti_{0.9}O₂ nanofiber concentrated area with a dimension < 1 μm.

Overall the combination of X-ray and Raman intensity mappings revealed that the distribution of the catalyst layer components have been significantly improved in ES CLs

that are employing composited-supported Pt catalysts when compared to AS CLs. The nonuniformity observed for AS composite-supported Pt catalyst layers can be explained as follows: in airspraying method, hydrophilic C/Nb_{0.1}Ti_{0.9}O₂ NFs and relatively hydrophobic carbon nanoparticles could create a preferential interaction of Nafion with either C/Nb_{0.1}Ti_{0.9}O₂ NFs or carbon blacks; whereas in electrospraying method, the electrostatic force between catalyst layer components will supersede that preferential interaction of Nafion and will dominate the distribution processes of catalyst layer components.

6.4 Conclusions

Both of airspray and electrospray deposition methods were used to prepare cathode catalyst layers employing composite-supported Pt catalysts, and their PEMFC performances were evaluated. Although using fixed NVP was shown to be more efficient than using fixed NWP in predicting the optimized Nafion loadings for both airsprayed and electrosprayed composite-supported Pt catalysts, the optimized values were shown to be highly dependent on the catalyst layer preparation methods. The comparisons of PEMFC performances at fixed NVPs revealed that electrospray deposited catalyst layers significantly outperformed airsprayed catalyst layers, which is most probably due to the much more uniform distribution of Nafion in the electrosprayed catalyst layers. Incorporation of hydrophilic carbon-embedded Nb-doped TiO₂ nanofibers in the composite catalyst supports was speculated to be in favor of better interaction between self-assembled Nafion layers and catalyst sites. Future work will focus on to get more insights from the possible interaction between self-assembled Nafion layers and the carbon-embedded Nb-doped TiO₂ nanofibers-based Pt catalysts.

References

1. Mehta, V. and J.S. Cooper, *Review and analysis of PEM fuel cell design and manufacturing*. Journal of Power Sources, 2003. **114**(1): p. 32-53.
2. Debe, M.K., *Electrocatalyst approaches and challenges for automotive fuel cells*. Nature, 2012. **486**(7401): p. 43-51.

3. de Bruijn, A.F. and G.M. Janssen, *PEM Fuel Cell Materials: Costs, Performance and Durability*, in *Encyclopedia of Sustainability Science and Technology*, R. Meyers, Editor. 2012, Springer New York. p. 7694-7730.
4. Holdcroft, S., *Fuel Cell Catalyst Layers: A Polymer Science Perspective*. Chemistry of Materials, 2014. **26**(1): p. 381-393.
5. Tabe, Y., et al., *Effects of Cathode Catalyst Layer Structure and Properties Dominating Polymer Electrolyte Fuel Cell Performance*. Journal of The Electrochemical Society, 2011. **158**(10): p. B1246-B1254.
6. O'Hayre, R., D.M. Barnett, and F.B. Prinz, *The Triple Phase Boundary: A Mathematical Model and Experimental Investigations for Fuel Cells*. Journal of The Electrochemical Society, 2005. **152**(2): p. A439-A444.
7. Nørskov, J.K., et al., *Origin of the Overpotential for Oxygen Reduction at a Fuel-Cell Cathode*. The Journal of Physical Chemistry B, 2004. **108**(46): p. 17886-17892.
8. Stamenkovic, V., et al., *Changing the Activity of Electrocatalysts for Oxygen Reduction by Tuning the Surface Electronic Structure*. Angewandte Chemie International Edition, 2006. **45**(18): p. 2897-2901.
9. Zhang, S., et al., *Recent progress in nanostructured electrocatalysts for PEM fuel cells*. Journal of Materials Chemistry A, 2013. **1**(15): p. 4631-4641.
10. Elabd, Y.A. and M.A. Hickner, *Block Copolymers for Fuel Cells*. Macromolecules, 2011. **44**(1): p. 1-11.
11. Mauritz, K.A. and R.B. Moore, *State of Understanding of Nafion*. Chemical Reviews, 2004. **104**(10): p. 4535-4586.
12. More, K., R. Borup, and K. Reeves, *Identifying Contributing Degradation Phenomena in PEM Fuel Cell Membrane Electride Assemblies Via Electron Microscopy*. ECS Transactions, 2006. **3**(1): p. 717-733.

13. Soboleva, T., et al., *PEMFC Catalyst Layers: The Role of Micropores and Mesopores on Water Sorption and Fuel Cell Activity*. ACS Applied Materials & Interfaces, 2011. **3**(6): p. 1827-1837.
14. Berejnov, V., et al., *3D Chemical Mapping of PEM Fuel Cell Cathodes by Scanning Transmission Soft X-ray SpectroTomography*. ECS Transactions, 2013. **50**(2): p. 361-368.
15. Gancs, L., et al., *Crystallographic Characteristics of Nanostructured Thin-Film Fuel Cell Electrocatalysts: A HRTEM Study*. Chemistry of Materials, 2008. **20**(7): p. 2444-2454.
16. Chan, K. and M. Eikerling, *Impedance Model of Oxygen Reduction in Water-Flooded Pores of Ionomer-Free PEFC Catalyst Layers*. Journal of The Electrochemical Society, 2011. **159**(2): p. B155-B164.
17. Yu, H., et al., *Influence of the ionomer/carbon ratio for low-Pt loading catalyst layer prepared by reactive spray deposition technology*. Journal of Power Sources, 2015. **283**(0): p. 84-94.
18. Song, D., et al., *A method for optimizing distributions of Nafion and Pt in cathode catalyst layers of PEM fuel cells*. Electrochimica Acta, 2005. **50**(16–17): p. 3347-3358.
19. Litster, S. and G. McLean, *PEM fuel cell electrodes*. Journal of Power Sources, 2004. **130**(1–2): p. 61-76.
20. Qi, Z. and A. Kaufman, *Low Pt loading high performance cathodes for PEM fuel cells*. Journal of Power Sources, 2003. **113**(1): p. 37-43.
21. Bonifácio, R.N., A.O. Neto, and M. Linardi, *Comparative analysis between mass and volume of catalysts as a criterion to determine the optimal quantity of Nafion ionomer in catalyst layers*. International Journal of Hydrogen Energy, 2015. **40**(6): p. 2840-2849.

22. Wilson, M.S. and S. Gottesfeld, *High Performance Catalyzed Membranes of Ultra-low Pt Loadings for Polymer Electrolyte Fuel Cells*. Journal of The Electrochemical Society, 1992. **139**(2): p. L28-L30.
23. Shin, S.J., et al., *Effect of the catalytic ink preparation method on the performance of polymer electrolyte membrane fuel cells*. Journal of Power Sources, 2002. **106**(1–2): p. 146-152.
24. Xu, F., et al., *Investigation of a Catalyst Ink Dispersion Using Both Ultra-Small-Angle X-ray Scattering and Cryogenic TEM*. Langmuir, 2010. **26**(24): p. 19199-19208.
25. Malek, K., et al., *Self-Organization in Catalyst Layers of Polymer Electrolyte Fuel Cells*. The Journal of Physical Chemistry C, 2007. **111**(36): p. 13627-13634.
26. Lee, S.-J., et al., *Solution properties of nafion in methanol/water mixture solvent*. Polymer, 2004. **45**(8): p. 2853-2862.
27. Negro, E., et al., *Pt electrodeposited over carbon nano-networks grown on carbon paper as durable catalyst for PEM fuel cells*. Applied Catalysis B: Environmental, 2015. **166–167**(0): p. 155-165.
28. Morikawa, H., et al., *Preparation of Membrane Electrode Assembly for Fuel Cell by Using Electrophoretic Deposition Process*. Journal of The Electrochemical Society, 2004. **151**(10): p. A1733-A1737.
29. O'Hayre, R., et al., *A sharp peak in the performance of sputtered platinum fuel cells at ultra-low platinum loading*. Journal of Power Sources, 2002. **109**(2): p. 483-493.
30. Chaparro, A.M., et al., *PEMFC electrode preparation by electrospray: Optimization of catalyst load and ionomer content*. Catalysis Today, 2009. **143**(3–4): p. 237-241.
31. Chaparro, A.M., et al., *Properties of Catalyst Layers for PEMFC Electrodes Prepared by Electrospray Deposition*. Journal of The Electrochemical Society, 2010. **157**(7): p. B993-B999.

32. Chaparro, A.M., et al., *Catalyst layers for proton exchange membrane fuel cells prepared by electrospray deposition on Nafion membrane*. Journal of Power Sources, 2011. **196**(9): p. 4200-4208.
33. Martin, S., P.L. Garcia-Ybarra, and J.L. Castillo, *Electrospray deposition of catalyst layers with ultra-low Pt loadings for PEM fuel cells cathodes*. Journal of Power Sources, 2010. **195**(9): p. 2443-2449.
34. Navaei Alvar, E., b. Zhou, and S.H. Eichhorn, *Carbon embedded Nb-doped TiO₂ nanofiber catalyst supports for PEM fuel cell applications*. Journal of Materials Chemistry A, 2015, *To be submitted*.
35. Navaei Alvar, E., B. Zhou, and S.H. Eichhorn, *Electrosprayed Cathode Catalyst layer with Composite-supported Pt Catalyst and Optimized Nafion Volume Percentage for Polymer Electrolyte Membrane Fuel Cell* Applied Catalysis B: Environmental, 2015, *To be submitted*.
36. Paul, D.K., et al., *Characteristics of Self-Assembled Ultrathin Nafion Films*. Macromolecules, 2013. **46**(9): p. 3461-3475.
37. Soboleva, T., et al., *On the Micro-, Meso-, and Macroporous Structures of Polymer Electrolyte Membrane Fuel Cell Catalyst Layers*. ACS Applied Materials & Interfaces, 2010. **2**(2): p. 375-384.
38. Passalacqua, E., et al., *Nafion content in the catalyst layer of polymer electrolyte fuel cells: effects on structure and performance*. Electrochimica Acta, 2001. **46**(6): p. 799-805.
39. Washburn, E.W., *Note on a Method of Determining the Distribution of Pore Sizes in a Porous Material*. Proceedings of the National Academy of Sciences, 1921. **7**(4): p. 115-116.
40. Giesche, H., *Mercury Porosimetry: A General (Practical) Overview*. Particle & Particle Systems Characterization, 2006. **23**(1): p. 9-19.
41. Uchida, M., et al., *Investigation of the Microstructure in the Catalyst Layer and Effects of Both Perfluorosulfonate Ionomer and PTFE-Loaded Carbon on the*

- Catalyst Layer of Polymer Electrolyte Fuel Cells*. Journal of The Electrochemical Society, 1995. **142**(12): p. 4143-4149.
42. Liu, Y., et al., *Influence of interface combination of reduced graphene oxide/P25 composites on their visible photocatalytic performance*. RSC Advances, 2014. **4**(82): p. 43760-43765.
43. Wang, W., et al., *Synthesis of Rutile (α -TiO₂) Nanocrystals with Controlled Size and Shape by Low-Temperature Hydrolysis: Effects of Solvent Composition*. The Journal of Physical Chemistry B, 2004. **108**(39): p. 14789-14792.
44. Sadezky, A., et al., *Raman microspectroscopy of soot and related carbonaceous materials: Spectral analysis and structural information*. Carbon, 2005. **43**(8): p. 1731-1742.

CHAPTER 7

Conclusions and Recommendations

7.1 Conclusions

Making Nb-doped TiO₂ nanofibers feasible for PEM fuel cells (PEMFCs) as a durable catalyst support, requires not only high electronic conductivity and high surface area but also a control on their doping level, crystallinity and heat treatment environment. For example, the adjustment of doping level is essential for the control over surface chemistry of nanofibers, crystallinity affects the electronic conductivity remarkably, and heat treatment environment may affect electronic conductivity and surface area. Furthermore, the well distribution of catalyst layer components (in particular hydrophilic metal oxide-based Pt catalyst and Nafion) is essential to have higher performances under real PEMFC operating conditions.

The objective of the studies described in *Chapter 2* was to find a simple way to protect the interface between catalyst layer and gas diffusion backing layer for unitized regenerative fuel cell applications. The resistance towards oxidation of coated and uncoated carbon papers was probed by cyclic voltammetry for up to 72 hours to mimic the conditions in a unitized regenerative fuel cell. Cyclic voltammetry measurements revealed that oxidatively functionalized carbon paper coated with a relatively uniform layer of anatase phase Nb-doped TiO₂ is more stable than uncoated carbon papers by a factor of 4.3, whereas many of the redox active sites deep inside the carbon paper were not covered yet.

In *chapters 3 and 4*, the use of Nb-doped TiO₂ nanofibers as a catalyst support for PEMFCs was systematically investigated. Although using ethylene glycol as a reducing agent produced smaller sized Pt nanoparticles onto anatase phase Nb-doped TiO₂ nanofibers (*Chapter 3*), their oxygen reduction reaction (ORR) mass activities were extremely lower than pure carbon based Pt catalysts. In contrast, rutile phase Nb-doped TiO₂ nanofibers showed to have much higher electronic conductivity, but still both of surface area and ORR mass activity of Pt catalysts supported by rutile phase nanofibers were not competitive to pure carbon based Pt catalysts. The embedment of carbon at the amount of about 11 wt. % with highly distorted graphitic structure into rutile phase Nb-doped TiO₂ nanofibers was shown to be very promising as it featured nanofibers with much

enhanced electronic conductivity and surface area, when compared with carbon-free rutile phase nanofibers (*Chapter 4*). Furthermore Nb doping level also shown to be very critical. Doping rutile phase TiO₂ with 10 at. % Nb rather than 25 at. % Nb found, first, to be more effective in terms of providing free electrons to the ideal lattice of TiO₂ (higher electronic conductivity); second, to make the surface less prone to the formation of electrochemically unstable oxides (higher electrochemical stability/durability). Although Pt catalysts supported by carbon-embedded nanofibers have showed much enhanced ORR specific activity and much-improved durability than those supported by carbon black (Vulcan XC-72R), the ORR mass activities were still slightly lower than pure carbon black based Pt catalysts.

Chapter 5 mainly focused on compositing carbon-embedded 10 at. % Nb-doped TiO₂ nanofibers with commercial carbon blacks to combine their advantages under real PEMFC operating conditions. Additionally using fixed Nafion volume percentage (NVP) rather than commonly used fixed Nafion weight percentage (NWP) was shown to be more efficient in predicting optimized Nafion loadings for electrospayed cathode catalyst layers. By an increase in the carbon black weight percentage of composite supports, there was a monotonic rise in both ORR mass activities and ORR losses at the same time. However, among the optimized cases of composite catalyst supports with different carbon black weight percentages (0 wt.% to 100 wt.%), considering both the performance and durability, the PEMFCs with electrospayed catalyst layers clearly showed that there exist an optimum zone around 25 wt.% carbon blacks that features higher fuel cell performance with lower ORR loss.

The objective of the studies described in *Chapter 6* was to validate using fixed NVP for different catalyst layer preparation methods and further investigate the catalyst layer properties employing composite-supported Pt catalysts. Although the value of optimized NVP was higher for airsprayed catalyst layers when compared with electrospayed catalyst layers, using fixed NVP was still more efficient than using fixed NWP regardless of the method that used for catalyst layer preparation. Comparing the PEMFC performances at fixed NVPs revealed that electrospay deposited catalyst layers are remarkably outperforming airsprayed catalyst layers due to much uniform distribution of catalyst layer

components (Nafion + composite-supported Pt catalysts) in the electro sprayed catalyst layers.

7.2 Recommendations

Electronic conductivity measurements in *Chapters 3 and 4* revealed that rutile phase Nb-doped TiO₂ nanofibers that have been reduced under pure hydrogen atmosphere are much more conductive than anatase phase Nb-doped TiO₂ nanofibers. Therefore, an obvious extension of the work presented in *Chapter 2* is to reduce coated carbon papers at higher temperatures under a pure hydrogen atmosphere. More conductive coatings can decrease the overall internal resistance of the cell in unitized regenerative fuel cells because the interface between catalyst layer and gas diffusion layer should not impede the electron flow.

The methodology for carbon-embedment that has been presented in *Chapter 4* can be easily applied to any metal oxide nanofibers. Hence, an extension of this work is to use other doping elements such as Ta, Cr, F, and even co-doping to produce more conductive and still durable metal-oxide based nanofibers. Furthermore, both of atomic structure and amount of carbon embedment can be manipulated to increase the electronic conductivity and surface area of nanofibers.

The catalytic performance evaluations under real PEMFC operating condition presented in *Chapters 5 and 6* revealed how important is the distribution of catalyst layer components and the catalyst layer composition, regardless of the type of catalyst and catalyst support. More specifically Nafion incorporation is extremely vital to create more catalytically active triple phase boundaries (TPBs) and increase the overall performance without impeding gas transport at the same time. Accordingly coating electro sprayed catalyst layers directly onto Nafion membranes [1] could enhance more the PEMFC performances of composite-supported Pt catalyst layers by creating a better connection between the proton conducting media and catalysts. Moreover, incorporation of Pt nanoparticles into the near-surface area of Nafion membranes (100-200 nm) has been also introduced a new avenue in being able to increase the Pt utilization in the catalyst layer [2].

To eliminate carbon corrosion, on top of finding corrosion-resistant alternatives, the investigation on the distribution and interaction of catalyst layer components has a vital importance to achieve higher performances under real PEMFC operating condition. This investigation should lead or be fruitful for the preparation of ultrathin catalyst layers (with extremely lower Nafion loadings) that could feature sufficient proton conductivity and the minimum impediment in the flow of electrons and reactant gases to/from catalyst sites.

References

1. Chaparro, A.M., et al., *Catalyst layers for proton exchange membrane fuel cells prepared by electrospray deposition on Nafion membrane*. *Journal of Power Sources*, 2011. **196**(9): p. 4200-4208.
2. Ingle, N.J.C., et al., *Synthesis and Characterization of Diverse Pt Nanostructures in Nafion*. *Langmuir*, 2014. **30**(7): p. 1871-1879.

APPENDICES

APPENDIX A

Basic Operation Principles of various Fuel Cell Types

Table A-1. Basic operation principles of various fuel cell types ((Source: <http://americanhistory.si.edu/fuelcells/basics.htm>)

Fuel Cell Type	Electrolyte	Electrochemical reactions	Operating Temp. (°C)
	Charge carrier		Fuel/Oxidant
Alkaline (AFC)	KOH, NaOH solution	<u>AN</u> ^a : $2OH^- + H_2 \rightarrow 2H_2O + 2e^-$	50-200
	OH ⁻	<u>CA</u> ^b : $\frac{1}{2}O_2 + 2H_2O + 2e^- \rightarrow 2OH^-$	H ₂ /O ₂
Proton Exchange Membrane (PEM)	Nafion	<u>AN</u> : $H_2 \rightarrow 2H^+ + 2e^-$	50-200
	H ⁺	<u>CA</u> : $\frac{1}{2}O_2 + 2H^+ + 2e^- \rightarrow H_2O$	H ₂ /O ₂ , Air
Phosphoric acid (PAFC)	H ₃ PO ₄	<u>AN</u> : $H_2 \rightarrow 2H^+ + 2e^-$	170-210
	H ⁺	<u>CA</u> : $\frac{1}{2}O_2 + 2H^+ + 2e^- \rightarrow H_2O$	H ₂ , natural gas/O ₂ , Air
Molten Carbonate (MCFC)	Na ₂ CO ₃ , Li ₂ CO ₃ or K ₂ CO ₃	<u>AN</u> : $H_2 + CO_3^{2-} \rightarrow H_2O + CO_2 + 2e^-$	600-700
	CO ₃ ²⁻	<u>CA</u> : $\frac{1}{2}O_2 + CO_2 + 2e^- \rightarrow CO_3^{2-}$	H ₂ , CH ₄ /Air, O ₂
Solid Oxide (SOFC)	Solid ZrO ₂	<u>AN</u> : $H_2 + O^{2-} \rightarrow H_2O + 2e^-$	650-1000
	O ²⁻	<u>CA</u> : $\frac{1}{2}O_2 + 2e^- \rightarrow O^{2-}$	H ₂ , CH ₄ , CO/Air, O ₂

^aAnode; ^bCathode.

APPENDIX B

Copyright Permissions

6/4/2015

Rights link® by Copyright Clearance Center



Home Account Info Help



Title: Oxidative Treatment to Improve Coating and Electrochemical Stability of Carbon Fiber Paper with Niobium Doped Titanium Dioxide Sols for Potential Applications in Fuel Cells

Author: Esmail Navaei Alvar, Biao Zhou, S. Holger Eichhorn

Publication: Electrochimica Acta

Publisher: Elsevier

Date: 20 June 2014

Copyright © 2014 Elsevier Ltd. All rights reserved.

Logged in as:
Esmail Navaei Alvar

LOGOUT

Order Completed

Thank you very much for your order.

This is a License Agreement between Esmail Navaei Alvar ("You") and Elsevier ("Elsevier"). The license consists of your order details, the terms and conditions provided by Elsevier, and the [payment terms and conditions](#).

[Get the printable license.](#)

License Number	3642241000769
License date	Jun 04, 2015
Licensed content publisher	Elsevier
Licensed content publication	Electrochimica Acta
Licensed content title	Oxidative Treatment to Improve Coating and Electrochemical Stability of Carbon Fiber Paper with Niobium Doped Titanium Dioxide Sols for Potential Applications in Fuel Cells
Licensed content author	Esmail Navaei Alvar, Biao Zhou, S. Holger Eichhorn
Licensed content date	20 June 2014
Licensed content volume number	132
Licensed content issue number	n/a
Number of pages	9
Type of Use	reuse in a thesis/dissertation
Portion	full article
Format	both print and electronic
Are you the author of this Elsevier article?	Yes
Will you be translating?	No
Title of your thesis/dissertation	Innovative Membrane Electrode Assemblies for Polymer Electrolyte Membrane Fuel Cells
Expected completion date	Aug 2015
Estimated size (number of pages)	120
Elsevier VAT number	GB 494 6272 12
Permissions price	0.00 CAD
VAT/Local Sales Tax	0.00 CAD / 0.00 GBP
Total	0.00 CAD

ORDER MORE...

CLOSE WINDOW

Copyright © 2015 Copyright Clearance Center, Inc. All Rights Reserved. [Privacy statement](#), [Terms and Conditions](#). Comments? We would like to hear from you. E-mail us at customer care@copyright.com

https://s100.copyright.com/AppDispatchServlet

1/2

6/4/2015

Rights link® by Copyright Clearance Center



RightsLink®

Home

Account
Info

Help



Title: Effect of Reducing Agent on the Dispersion of Pt Nanoparticles on Electrospun Nb_{0.1}Ti_{0.9}O₂ Nanofibers

Author: Esmail Navaei Alvar, Biao Zhou and S. Holger Eichhorn

Publication: MRS Online Proceedings Library

Publisher: Cambridge University Press

Date: Jun 4, 2013

Copyright © Materials Research Society 2013

Logged in as:
Esmail Navaei Alvar

[LOGOUT](#)

Order Completed

Thank you very much for your order.

This is a License Agreement between Esmail Navaei Alvar ("You") and Cambridge University Press ("Cambridge University Press"). The license consists of your order details, the terms and conditions provided by Cambridge University Press, and the [payment terms and conditions](#).

[Get the printable license.](#)

License Number	3642241189591
License date	Jun 04, 2015
Licensed content publisher	Cambridge University Press
Licensed content publication	MRS Online Proceedings Library
Licensed content title	Effect of Reducing Agent on the Dispersion of Pt Nanoparticles on Electrospun Nb _{0.1} Ti _{0.9} O ₂ Nanofibers
Licensed content author	Esmail Navaei Alvar, Biao Zhou and S. Holger Eichhorn
Licensed content date	Jun 4, 2013
Volume number	1542
Issue number	-1
Start page	0
End page	0
Type of Use	Dissertation/Thesis
Requestor type	Author
Portion	Full article
Author of this Cambridge University Press article	Yes
Author / editor of the new work	Yes
Order reference number	None
Territory for reuse	World
Title of your thesis / dissertation	Innovative Membrane Electrode Assemblies for Polymer Electrolyte Membrane Fuel Cells
Expected completion date	Aug 2015
Estimated size(pages)	120
Billing Type	Invoice
Billing address	Esmail Navaei Alvar Apt. 10, 3150 Peter St windsor, ON N9C 1H3 Canada

<https://s100.copyright.com/AppDispatchServlet>

1/2

VITA AUCTORIS

NAME: Esmail Navaei Alvar

PLACE OF BIRTH: Tabriz, IRAN

YEAR OF BIRTH: 1985

EDUCATION:

- Sahand University of Technology, B.Sc.-Materials Engineering, Tabriz, IRAN, 2006
- AmirKabir University of Technology, M.Sc.-Materials Engineering, Tehran, IRAN, 2009
- University of Windsor, Ph.D.-Mechanical Engineering, Windsor, Canada, 2015